TU Delft

Delft University of Technology

Tuning the surface properties of polymer microspheres by means of atomic layer deposition in fluidized beds

Kamphorst, R.

DOI
10.4233/uuid:3d80026b-2eec-4b3a-a839-59c396f03a84

Publication date
2025

Document Version
Final published version

Citation (APA)
Kamphorst, R. (2025). *Tuning the surface properties of polymer microspheres by means of atomic layer deposition in fluidized beds*. [Dissertation (TU Delft), Delft University of Technology]. https://doi.org/10.4233/uuid:3d80026b-2eec-4b3a-a839-59c396f03a84

Important note
To cite this publication, please use the final published version (if applicable).
Please check the document version above.

Copyright
Other than for strictly personal use, it is not permitted to download, forward or distribute the text or part of it, without the consent of the author(s) and/or copyright holder(s), unless the work is under an open content license such as Creative Commons.

Takedown policy
Please contact us and provide details if you believe this document breaches copyrights.
We will remove access to the work immediately and investigate your claim.

This work is downloaded from Delft University of Technology.
For technical reasons the number of authors shown on this cover page is limited to a maximum of 10.

Tuning the surface properties of polymer microspheres

by means of atomic layer deposition in fluidized beds

Rens Kamphorst



TUNING THE SURFACE PROPERTIES OF POLYMER MICROSPHERES BY MEANS OF ATOMIC LAYER DEPOSITION IN FLUIDIZED BEDS

TUNING THE SURFACE PROPERTIES OF POLYMER MICROSPHERES BY MEANS OF ATOMIC LAYER DEPOSITION IN FLUIDIZED BEDS

Proefschrift

ter verkrijging van de graad van doctor
aan de Technische Universiteit Delft,
op gezag van de Rector Magnificus prof.dr.ir. T.H.J.J. van der Hagen,
voorzitter van het College voor Promoties,
in het openbaar te verdedigen op

dinsdag 18 maart 2025
om 12.30

door

Rens KAMPHORST

Master of Science in Chemical Engineering,
Delft University of Technology, Delft, The Netherlands,
Born in Spijkenisse, The Netherlands.

Dit proefschrift is goedgekeurd door de promotoren

promotor: prof. dr. ir. J.R. van Ommen
copromotor: dr. G.M.H. Meesters

Samenstelling promotiecommissie:

Rector Magnificus,	Voorzitter
Prof. dr. ir. J.R. van Ommen,	Technische Universiteit Delft, promotor
Dr. ir. G.M.H. Meesters,	Technische Universiteit Delft, copromotor
Onafhankelijke leden:	
Prof. dr. ir. W. de Jong	Technische Universiteit Delft
Prof. dr. S.J. Picken	Technische Universiteit Delft
Prof. dr. J. Bachmann	Universiteit van Erlangen-Nürnberg
Prof. dr. ir. A.J.M. Mackus	Technische Universiteit Eindhoven
Dr. ir. M.A. van der Veen	Technische Universiteit Delft

Cover design: R. Kamphorst
Printed by: Ridderprint
ISBN 978-94-6522-100-7

Copyright © 2025 by R. Kamphorst

This work is part of the Advanced Research Center for Chemical Building Blocks, ARC CBBC, which is co-founded and co-financed by the Dutch Research Council (NWO) and the Netherlands Ministry of Economic Affairs and Climate Policy.

An electronic version of this dissertation is available at
`http://repository.tudelft.nl/`.

Dedicated to An Kamphorst

CONTENTS

Summary **ix**

Samenvatting **xi**

1 Introduction **1**
1.1 Substrate and colloids 1
1.2 Thin film deposition 3
1.3 Fluidization 4
1.4 Thesis objectives and outline 5
References 6

2 On the fluidization of cohesive powders **9**
2.1 Introduction 11
2.2 Powder classification 11
2.3 Forces acting on particles 16
2.4 Agglomeration in fluidized beds 24
2.5 Modelling agglomeration 27
2.6 Conclusions and outlook 35
References 36

3 On the structure of nanoparticle clusters **47**
3.1 Introduction 49
3.2 Methods 51
3.3 Results and discussion 55
3.4 Conclusion 58
References 59
3.5 Sensitivity of van der Waals interactions 63
3.6 2D model 66
3.7 Additional 3D model output 67

4 The Mechanism behind Vibration Assisted Fluidization **69**
4.1 Introduction 71
4.2 Assistance mechanism 72
4.3 Experimental and methodology 73
4.4 Results and discussion 77
4.5 Conclusions 84
References 85

5 Effect of vibrational modes on fluidization characteristics of cohesive powders 89
5.1 Introduction . . . 91
5.2 Materials and Methods . . . 92
5.3 Results and Discussion. . . . 95
5.4 Conclusion . . . 106
References . . . 107
5.5 Coefficients of variation within pressure drop data . . . 111

6 Stirrer design for improving fluidization of cohesive powder 113
6.1 Introduction . . . 115
6.2 Experimentation and methodology. . . . 117
6.3 Results and discussion . . . 123
6.4 Conclusions. . . . 139
References . . . 140
6.5 Validation of two-point calibration . . . 143
6.6 Validation of single angle projection . . . 143
6.7 Stirred fluidized beds with vibration initialization . . . 144

7 Effects ALD coatings on particle-water affinity 147
7.1 Introduction . . . 149
7.2 Methods and Materials . . . 150
7.3 Results and discussion . . . 153
7.4 Conclusion . . . 163
References . . . 165
7.5 SEM . . . 169
7.6 XPS . . . 172

8 Research implications and outlook 175
8.1 Aggregate and agglomerate formation . . . 175
8.2 Mechanism of assistance methods . . . 176
8.3 Scale-up potential of assistance methods . . . 177
8.4 Improved colloid stability by surface modification . . . 178
References . . . 178

Acknowledgements 181

Curriculum Vitæ 185

List of Publications 187

SUMMARY

Chocolate milk, paint and snow globes are all examples of solid-liquid suspensions found in daily life. In industry, colloids are also commonly used to process solids, as liquids are typically easier to handle than powders. Given the environmental concerns surrounding the usage of organic solvents, which are often evaporated and released during the process, water-based colloids are preferred. However, not all particles have a natural affinity with water. When particles have insufficient affinity for water, the solid and liquid phases segregate. To enable such particles to still form stable water-based suspensions, their surface properties can be modified.

Of the various techniques that can tune surface properties, atomic layer deposition (ALD) is favorable, as it can modify surfaces without affecting bulk properties. With ALD, ultra-thin coatings can be deposited by sequential introduction of chemicals to the substrate surface that react in a self-limiting way, separated by a purge step. When choosing the right coating material, one can provide a substrate with favorable surface properties, such as hydrophilicity. For optimal results, the entire surface area of each particle should be coated. To maximize the interaction between the solid surface and the chemicals that build the coating layer, fluidized bed reactors can be employed. In this work we use ALD in fluidized bed reactors with the goal of tuning the surface properties of particles with a naturally low water affinity, allowing for stable water-based solid-liquid suspensions to be formed.

Surface modification of the small particles considered in this research presented significant challenges. As the individual particles were small ($< 30\,\mu m$), they were cohesive. This meant that during the fluidization process, they tended to form clusters and channels, making most of their surface area unavailable for direct interaction with the chemicals that build up the coating layers. This required the aid of additional methods to adequately fluidize the powder. A significant portion of the research was dedicated to study scalable assistance methods.

In Chapter 2, we explored the literature on the fluidization of cohesive micro- and nanoparticles. We found that the behaviour of powders in these respective size ranges in fluidized beds can differ significantly. In particular, the sizes and structures of formed agglomerates differ.

The modelling work presented in Chapter 3 demonstrates how long-range interparticle forces alter the structure of nanoparticle clusters, whereas micro-sized particles are mostly unaffected by this phenomenon. This effect may explain the differences in macro-scale agglomerates, formed by particles in the respective size ranges.

Chapter 4 and Chapter 5 are concerned with mechanical vibration as a method to improve fluidization quality of cohesive powders. The mechanism of the improvement is identified and the applicability for both micro- and nanoparticles is explored. One of the main drawbacks of this method is the sustained presence of compacted sections in the bed. As gas-solid interactions are limited in these regions, this mitigates applications like film deposition.
In Chapter 6, an alternative assistant method for the fluidization of cohesive powders, mechanical agitation, is studied. Various impeller designs are tested, based on which design criteria for usage within fluidized beds are identified. Additionally it is shown that stirring can result in high degrees of fluidization, with no compacted sections.
The effect of deposited SiO_2 films on the wettability of polymer microspheres is discussed in Chapter 7. Films were deposited by ALD in mechanically vibrated fluidized beds. As we dealt with a sensitive substrate, relatively low temperatures were maintained during the coating. This led to an increased growth per deposition cycle, caused by incomplete purging of physisorbed reactants. As a result, already after two coating cycles, full surface coverage was attained. It is demonstrated that surface coverage is more important than coating thickness, when trying to improve substrate-water affinity.
Finally, in Chapter 8, we conclude that stable solid-liquid suspensions can indeed be attained after modification of particle surfaces by ALD in fluidized bed reactors. We also discuss the scale-up potential of the various techniques we studied. Additionally, we show that our work may serve as the initial step towards complete understanding of agglomeration types, exhibited by micro- and nanoparticles. Furthermore, we highlight that assistance methods work by breaking up channels within the powder bed. Based on our studies, we argue that mechanical vibration is an inadequate assistance method when considering larger-scale operations. Additionally, we argue that mechanical agitation has the highest potential to aid in the fluidiziation of cohesive powders on large scales. Finally, we recommend future research into controlled physisorption for single-cycle film deposition, which could enable single cycle deposition of coatings with a predetermined film thickness.

SAMENVATTING

Chocolademelk, verf en sneeuwbollen, het zijn allemaal voorbeelden van suspensies, bestaande uit vaste deeltjes in water, die we in het dagelijkse leven tegenkomen. In de industrie worden zulke colloïden gebruikt om vaste stoffen te verwerken, dit omdat vloeistoffen vaak makkelijker in gebruik zijn dan poeders. Het gebruik van organische vloeistoffen in zulke suspensies staat onder druk, aangezien deze schadelijk zijn voor het milieu en vaak vrijkomen tijdens deze processen. Idealiter zouden uitsluitend suspensies op waterbasis gebruikt worden. Echter, veel stoffen vormen van nature instabiele colloïden met water waardoor een fase scheiding optreedt. De oorzaak hiervan is een gebrek aan affiniteit tussen de deeltjes en het water. Om het vormen van stabiele suspensies desondanks mogelijk te maken kunnen de oppervlakte eigenschappen van zulke deeltjes gemodificeerd worden.

Er bestaan verschillende technieken waarmee oppervlakte eigenschappen kunnen worden bewerkt. Van deze technieken is atomaire-laag-depositie (ALD) aantrekkelijk, omdat het oppervlakt van deeltjes kan worden gepast zonder dat daarbij de bulkeigenschappen worden beïnvloed. Tijdens het ALD-proces wordt een ultradunne coating op een substraat aangebracht door het afwisselend introduceren van chemicaliën, gescheiden door een zuiveringsstap. De reactanten reageren met de oppervlaktegroepen van het substraat op zelflimiterende wijze, waardoor controle over de dikte van de filmlaag behouden blijft. Door het juiste materiaal aan te brengen kan een oppervlakte worden voorzien van nuttige eigenschappen, zoals hydrofiliteit. Voor optimaal resultaat moet het gehele oppervlakte van elk deeltje gecoat worden. Om het contact tussen reactanten die de coating deponeren en de deeltjes te maximaliseren kunnen fluïde-bed-reactoren gebruikt worden. In ons project hebben we ALD in fluïde-bed-reactoren toegepast met als doel de oppervlakte-eigenschappen van deeltjes die van nature weinig affiniteit met water hebben zo te bewerken dat stabiele suspensies op waterbasis gevormd kunnen worden.

Het modificeren van oppervlakten van kleine deeltjes die in ons onderzoek gebruikt zijn, bracht aanzienlijke uitdagingen met zich mee. De individuele deeltjes waren erg klein (< 30 µm), waardoor ze cohesief zijn. Dit houdt in dat vaak clusters en kanaaltjes gevormd werden tijdens het fluïdiseren. Dit had als gevolg dat het grootste deel van het te coaten oppervlak niet direct bereikbaar was voor de chemicaliën. Om dit te verhelpen waren assistentie-methoden nodig. Een groot deel van het onderzoek is besteed aan het vinden van assistentie-methoden die, in potentie, opgeschaald kunnen worden.

In Hoofdstuk 2 hebben we de literatuur op het gebied van fluïdisatie van cohe-

sieve deeltjes van micro- en nano-grootte bestudeerd. Hieruit bleek onder meer dat het gedrag in fluïde bedden van deeltjes van de genoemde grootten significant kan verschillen. In het bijzonder verschillen de grootte en structuren van de agglomeraten die deze deeltjes vormen.
Het modelleer werk dat in Hoofdstuk 3 beschreven is laat zien hoe krachten die over lange afstanden op deeltjes werken de structuren van de clusters die door nanodeeltjes gevormd worden kunnen beïnvloeden. Diezelfde krachten bleken een minimaal effect op deeltjes van microgrootte te hebben. Dit zou als uitleg kunnen dienen voor de eerder genoemde verschillen in agglomeraten die door beide deeltjes worden gevormd.
Hoofdstuk 4 en 5 gaan over mechanische vibratie, wat als assistentie-methode gebruikt kan worden om cohesieve poeders te fluïdiseren. Hier laten we zien hoe deze techniek de fluïdisatie van poeders kan initiëren. Een van de nadelen van deze techniek is het ontstaan van compacte zones in het poederbed. Op deze plekken is de interactie tussen gassen en deeltje belemmerd, wat toepassingen zoals film depositie bemoeilijkt.
In Hoofdstuk 6 is mechanische agitatie, een alternatieve assistentie, methode bestudeerd. Gebaseerd op het testen van verschillende roerder-ontwerpen, worden ontwerprichtlijnen gegeven voor gebruik in fluïde bedden. Daarbij wordt ook gepresenteerd dat mechanische agitatie kan leiden tot een hoge fluïdisatiegraad zonder compacte zones.
Het effect van gedeponeerde SiO_2-lagen op de deeltjes-water affiniteit van polymeren microbollen wordt behandeld in Hoofdstuk 7. De ALD coatings werden aangebracht in mechanisch gevibreerde fluïde bedden. Omdat het substraat kwetsbaar is, werden lage temperaturen gehanteerd tijdens het coaten. Als gevolg hiervan nam de depositie per coating cyclus toe, veroorzaakt door fysisch geadsorbeerd water, wat niet effectief verwijderd kon worden in de zuiveringsstappen. Hierdoor werd al na twee cycli eend dichte filmlaag over het gehele oppervlak aangebracht. Voor het verbeteren van substraat-water-affiniteit, blijkt het beslaan van het volledige oppervlak belangrijker te zijn dan de dikte van de aangebrachte coating.
Tot slot concluderen we in Hoofdstuk 8 dat stabiele water-gebaseerde suspensies verkregen kunnen worden na het modificeren van de oppervlakten van deeltjes door ALD in fluïde bedden. Ook zetten we de opschaalmogelijkheden van de bestudeerde technieken uiteen. Verder laten we zien hoe ons werk dient als eerste stap om agglomeratie typen van micro- en nanopoeders te begrijpen. We laten zien hoe assistentie-methoden werken, door het opbreken van kanaaltjes in het poederbed. Gebaseerd op ons gepubliceerde werk betogen we dat mechanische vibratie geen adequate assistentie-methode is voor het fluïdiseren van cohesieve poeders op grote schaal. Verder adviseren we onderzoeksrichtingen voor toe-

komstig werk. Met name werk aan gecontroleerde fysische adsorptie van waterlagen waarmee een filmlaag van vooraf bepaalde dikte in een enkele depositiecyclus gedeponeerd kan worden heeft, in onze ogen, hoge potentie.

1

INTRODUCTION

While not always obvious, micro- and nano-sized particles play a crucial role in every day life. They find applications in electronic devices [1, 2], medication [3, 4], and construction materials [5–7], to only name a few. Many of these applications benefit on the high surface-to-volume ratio of these small particles. Given this high surface area, major advantages can be attained if one would be able to provide this surface with favorable properties. Modifying characteristics like catalytic activity or electric conductivity allows for the creation of tailormade materials, specifically tuned with an application in mind. In this work, we are interested in tuning hydrophilicity of micro-sized particles.

Many particles are, by their nature, hydrophobic, making it troublesome to form stable water-based colloids with them. Processing handling such powder therefore often include the use of organic solvents, which are evaporated later. Apart from the inconvenience of not being able to use water for these processes, volatile organic compounds (VOCs) have high greenhouse potentials. The IPCC estimates the contribution of VOCs to the total greenhouse effect to be about 11 % [8]. Since colloid stability for particles in the given size range is primarily influenced by the characteristics of the particle surface, modifying this surface to enhance hydrophilicity can stabilize water-based colloids [9].

In our work we modified hollow polymer microspheres, utilizing the atomic layer deposition (ALD) coating technique in fluidized bed reactors, with the aim of improving affinity with water.

1.1. SUBSTRATE AND COLLOIDS

Among a vast portfolio of advanced materials, Nouryon produces hollow polymer microspheres under the brand-name Expancel®. This versatile powder finds applications in artificial leather, paints and shoe soles, to only name a few [10, 11]. In their current form however, no stable colloids of Expancel® particles in water can be made. Nouryon is a founding partner of the advanced research center chemical building blocks consortium (ARC-CBBC). This consortium aims to advance green chemistry and lead the transition towards a waste-free society, in light of which this research project was funded.

1

1.1.1. SUBSTRATE PROPERTIES

The particle shell consists of a methylmethacrylate-acrylonitrile co-polymer and encapsulates a driving gas. Upon heating the particles beyond the glass-transition temperature of the co-polymer, which lies at 90 °C, the shell becomes elastic. Furthermore, as a result of expansion of the driving gas, heating leads the particles to inflate by up to 60 times their original volume [12]. Upon sequential cooling the particles down, the shell solidifies and the expanded volume is retained. Figure 1.1 shows SEM images of Expancel® particles before and after exposition to elevated temperatures.

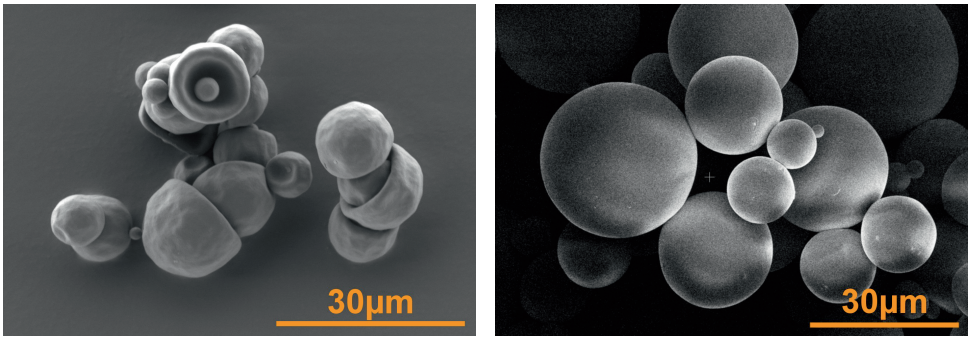


Figure 1.1: SEM images of pristine (left) and heated (right) Expancel® particles.

1.1.2. COLLOID STABILITY

Pristine Expancel® particles in water form unstable colloids. Over time, the particles cluster together, reaching a size where buoyancy becomes dominant and induces segregation. This phenomenon is typically described by the DLVO model [13]. This model describes the forces acting between hydrated surfaces: attractive van der Waals forces and repulsive electric double layer forces [14, 15]. While the former are always present, the latter depend on the the existence of charged surface groups [16]. Such groups arise as a result of hydration, in hydroxide groups for instance H^+ will dissociate, leaving a charged oxygen group at the surface, as per Equation (1.1). Counter-ions will then cover the charged surface, creating what is called the electric double layer. As two particles of the same material will develop a double layer of like charges, a repelling force arises between them. Colloids are considered to be stable when this repelling force exceeds the attractive van der Waals forces, keeping particles from clustering. In our work we will attempt to stabilize water-Expancel® colloids by increasing the amount hydrophilic surface groups on the particles, making the repellent forces potent

enough to mitigate clustering.

$$||-O-H \quad \rightleftharpoons \quad ||-O^- + H^+ \tag{1.1}$$

1.2. THIN FILM DEPOSITION

Coating techniques can generally be divided into two categories: physical deposition and chemical deposition. The former encompasses paints, lacquers and sputter coatings, all of which rely on adhesive forces or mechanical interlocking to stick to a substrates surface [17]. In contrast, chemical deposition methods, including chemical vapor deposition (CVD), sol-gel coating and atomic layer deposition (ALD), employ chemicals which react with a substrate's surface and thus attach by forming covalent bonds. Additionally, where physical deposition can typically only coat exposed surfaces, chemical deposition methods are not restrained by line of sight [18]. When working with particles in the size-range we are considering, this brings major advantages, as particles tend to form cluster, rendering a significant amount of surface inaccessible by line of sight coating techniques. Additionally, CVD and ALD can produce films free of defects like nano-pores [18, 19].

1.2.1. CHEMICAL VAPOR DEPOSITION

In chemical vapor deposition a film is formed by chemical reactions of gaseous reactants at or near the substrates surface [20]. It is a fairly mature technique, its first patent dating back to 1893 [21] and has since become part of industrial scale processes such as the production of semiconductors. A typical CVD process consists of a couple of steps [20, 22, 23]. First reactant gasses, typically two, are introduced to a substrate in an isolated chamber, with favorable reaction conditions. The reactants can diffuse onto the substrate surface and react with active groups present there. Alternatively reactants can undergo a gas-phase reaction, forming intermediate products which in turn diffuse onto the surface and react. Unreacted species and by-products subsequently desorb, making way for new reactants or intermediate products can take their place to react again. By allowing this process to repeat itself for a given time a film is built up, its thickness being controlled by reaction time. Depending on the chemical surface groups present on pristine substrate, surface activation may be required prior to deposition. This refers to the process of pre-treating the substrate, altering, or 'activating' the surface, allowing for subsequent reactions with the precursors to take place. Common activation treatments include those by ozone [24] or plasma [25].

1

1.2.2. ATOMIC LAYER DEPOSITION

A special case of CVD is atomic layer deposition [22]. Rather than the typical simultaneous introduction of reactants, in this process they are provided sequentially, separated by a purge. By selecting the reactants such that they exclusively react with the surface groups that are at the substrate upon their introduction, and not with formed groups after reacting, each step becomes self-limiting by virtue of running out of reactive surface groups. Purging ensures no direct reactions between precursor and oxidizer in the gas phase, such that, under ideal conditions, a full cycle results in the deposition of no more than one mono-layer [26]. In the archetypical ALD deposition of Al_2O_3, about a third of a mono-layer is deposited upon a complete cycle [27]. This provides control over coating thickness on an atomic level and results in more uniform and conformal deposition compared to CVD, though at the cost of a slower growth rate [28].

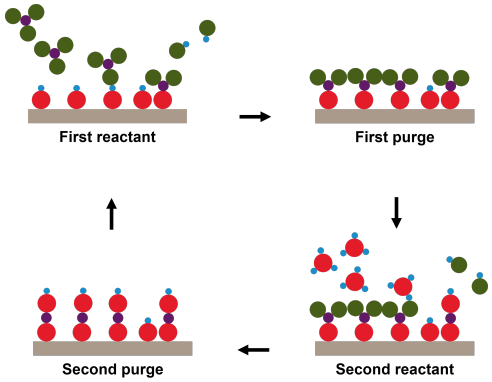


Figure 1.2: Schematic overview of the cyclic atomic layer deposition process

1.3. FLUIDIZATION

For a conformal coating on granular material by ALD, the entire surface area of each individual particle needs to be exposed to the gas, containing the precursors. Minimizing particle-particle contact, requires some form of aeration. Spacial coating systems incorporating vibration [29] or pneumatic transport [30] for aeration have seen recent interest, however, the most used and best understood method to aerate particles for temporal ALD is fluidization [31]. In this process, a gas flow is introduced from the bottom of the powder bed that creates drag. At a sufficient gas velocity, the drag overcomes the gravitational pull, and particles start to hover. At this point the powder bed mimics typical characteristics of a liquid and is considered 'fluidized'. When considering powders consisting of small particles, like Expancel®, the gravitational force is less significant, and

inter-particle forces start dominating the powder behaviour. Attractive van der Waals forces induce particle-particle clustering and leads to the formation of agglomerates, trapping a significant amount of particle surface area within these clusters. Additionally, upon the introduction of a gas flow to the powder back, cracks, or channels, may appear within it, allowing the gas to bypass without significant interaction with the particles. Both agglomeration and channeling complicate the application of fluidized beds of small, cohesive powders.
To mitigate these phenomena and improve the gas-solid interaction of fluidized beds of cohesive powders, assistance methods have been developed. These methods include mechanical vibration [32, 33], (micro-)jets [34, 35], pulsed flow [36, 37] and acoustic vibration [38, 39]. Assistance methods aim to agitate the powder bed, by the introduction of additional motion or forces, typically aimed at breaking up agglomerates. They have been shown to initiate and improve the fluidization of both cohesive micro- and nano-powders.

1.4. THESIS OBJECTIVES AND OUTLINE

The goal of our work was to develop a scalable production method to modify polymer microsphere particle surface properties. In particular, surface properties should be tuned such that stable water-based colloids with the particles can be formed. To achieve this, atomic layer deposition in fluidized bed reactors was employed to tune particle wettability. As we aimed to provide a process with the potential to be implemented on an industrial scale, a significant amount of work was dedicated to finding scalable assistance methods for fluidized beds of cohesive powders. Each chapter of this dissertation addresses a sub-objective, required to reach our final goal.
In Chapter 2, an in-depth literature review of the fluidization of cohesive powders is provided. As this group incorporates both nano- and micro-sized particles, we specifically sought to find whether an additional distinction between them should be made. We found the main difference between the two to be the way in which they agglomerate, where micro-sized particle form single-stage agglomerates, nano-sized particles cluster by forming multi-stage structures.
In Chapter 3 we took the first steps towards understanding the difference in cluster formation identified in Chapter 2. We built a 3D model, which allowed to show the van der Waals froces to significantly alter the structures produced by diffusion limited aggregation as a function of primary particle size. Additionally, we showed that this effect cannot be adequately studied by 2D models, which are the most commonly found ones in literature.
As our substrate is cohesive, and therefore unable to be fluidized under standard conditions, assistance methods were required. Many of such methods have been

proposed in literature, however the mechanisms by which these improve fluidization remained mostly unexplored. Moreover, studies have primarily been performed on small-scale equipment. To develop or improve methods, especially in the context of scalablility, we assessed the mechanisms by which such methods work. In Chapter 4, we used X-ray imaging to show that the disruption of gas channels is the cause of enhanced fluidization quality of mechanically vibrated fluidized beds of cohesive micro-silica. Where many publications had previously stated that the breakage of agglomerates was the cause of improved fluidization, we show this to be a result of initiated fluidization in stead.
In Chapter 5, we explored the influence of vibration orientation within mechanically vibrated fluidized beds. We hypothesized that a horizontal component would aid the disruption of channels, compared to sole vertical motion. However, we found this not to be the case, additionally we identified densified regions within all vibrated beds, complicating the potential of scaling up this assistance method.
An under-explored assistance method is mechanical agitation, or stirring. As the abundance of this technique in industrial processes proves, this technique is evidently applicable on large scale for liquid systems. In Chapter 6 we assessed the effectiveness of a vast range of stirrer designs on initiating fluidization of cohesive micro-silica. We identified favorable design parameters, and showed that homogeneous fluidization can be attained when using this method.
In Chapter 7, we used an ALD setup with a mechanically vibrated bed to deposit -Si-OH surface groups on Expancel® particles. We show that a drastic improvement in water-substrate colloid stability is obtained, even after a single coating cycle. Furthermore, it is demonstrated that surface coverage is more important than surface thickness for our application.
Finally, in Chapter 8 a summary of results and conclusions from the thesis is presented. We discuss the implications of our findings and provide recommendations for the direction future research on the respective topics may take.

REFERENCES

[1] I. Matsui, *Nanoparticles for electronic device applications: A brief review,* Journal of Chemical Engineering of Japan **38**, 535 (2005).

[2] N. A. Lah, M. N. Zubir, and M. A. Samykano, *Chapter 20 - engineered nanomaterial in electronics and electrical industries,* in *Handbook of Nanomaterials for Industrial Applications*, Micro and Nano Technologies, edited by C. Mustansar Hussain (Elsevier, 2018) pp. 324 – 364.

[3] A. Haleem, M. Javaid, R. P. Singh, S. Rab, and R. Suman, *Applications of nanotechnology in medical field: a brief review,* Global Health Journal **7**, 70 (2023).

[4] A. Z. Wang, R. Langer, and O. C. Farokhzad, *Nanoparticle delivery of cancer drugs,* Annual Review of Medicine **63**, 185 (2012).

[5] A. Mohajerani, L. Burnett, J. Smith, H. Kurmus, J. Milas, A. Arulrajah, and K. Abdul Kadir, *Nanoparticles in construction materials and other applications, and implications of nanoparticle use,* Materials **12** (2019), 10.3390/ma12193052.

[6] W. Li, Z. Luo, C. Long, C. Wu, W. H. Duan, and S. P. Shah, *Effects of nanoparticle on the dynamic behaviors of recycled aggregate concrete under impact loading,* Materials & Design **112**, 58 (2016).

[7] G. Goel, P. Sachdeva, A. K. Chaudhary, and Y. Singh, *The use of nanomaterials in concrete: A review,* Materials Today: Proceedings **69**, 365 (2022).

[8] Intergovernmental Panel on Climate Change, *Solvent and other products,* (1996).

[9] J. Schubert and M. Chanana, *Coating matters: Review on colloidal stability of nanoparticles with biocompatible coatings in biological media, living cells and organisms,* Current medicinal chemistry **25** (2018), 10.2174/0929867325666180601101859.

[10] AkzoNobel, *Expancel microspheres - the multi-performance additive,* (2013).

[11] Nouryon, *Expancel microspheres - the world's favorite secred ingredient,* (2019).

[12] Nouryon, *Expancel microspheres - your engineered solution,* (2019).

[13] H. Butt and M. Kappl, *Surface and Interfacial Forces,* 2nd ed. (John Wiley & Sons, Ltd, 2010).

[14] B. Derjaguin and L. Landau, *Theory of the stability of strongly charged lyophobic sols and of the adhesion of strongly charged particles in solutions of electrolytes,* Progress in Surface Science **43**, 30 (1993).

[15] E. J. W. Verwey, *Theory of the stability of lyophobic colloids.* The Journal of Physical and Colloid Chemistry **51**, 631 (1947).

[16] J. Israelachvili and H. Wennerström, *Role of hydration and water structure in biological and colloidal interactions,* Nature **379**, 219–225 (1996).

[17] H. Weiss, *Adhesion of advanced overlay coatings: mechanisms and quantitative assessment,* Surface and Coatings Technology **71**, 201 (1995).

[18] X. Wang and G. Yushin, *Chemical vapor deposition and atomic layer deposition for advanced lithium ion batteries and supercapacitors,* Energy Environ. Sci. **8**, 1889 (2015).

[19] D. J. Emslie, P. Chadha, and J. S. Price, *Metal ald and pulsed CVD: Fundamental reactions and links with solution chemistry,* Coordination Chemistry Reviews **257**, 3282 (2013).

[20] K. Choy, *Chemical vapour deposition of coatings,* Progress in Materials Science **48**, 57 (2003).

[21] A. D. Lodyguine, *Illuminant for incandescent lamps,* (No.575,002 Patented-Jan.12,1897).

[22] L. Sun, G. Yuan, L. Gao, J. Yang, M. Chhowalla, K. Heydari Gharahcheshmeh, M.and Gleason, Y. Choi, B. Hong, and Z. Liu, *Chemical vapour deposition,* **1**, 5 (2021).

[23] K. Yan, L. Fu, H. Peng, and Z. Liu, *Designed CVD growth of graphene via process engineering,* Accounts of chemical research **46** (2013), 10.1021/ar400057n.

[24] K. Kawase, S. Noda, T. Nakai, and Y. Uehara, *Densification of chemical vapor deposition silicon dioxide film using ozone treatment,* Japanese Journal of Applied Physics **48**, 101401 (2009).

[25] D. E. Carlson and C. R. Wronski, *Amorphous silicon solar cell,* Applied Physics Letters **28**, 671 (1976).

[26] R. W. Johnson, A. Hultqvist, and S. F. Bent, *A brief review of atomic layer deposition: from fundamentals to applications,* Materials Today **17**, 236 (2014).

[27] J. R. van Ommen, A. Goulas, and R. L. Puurunen, *Atomic layer deposition,* in *Kirk-Othmer Encyclopedia of Chemical Technology* (John Wiley & Sons, Ltd, 2021) pp. 1–42.

[28] D. Muñoz-Rojas, V. Nguyen, C. Masse de la Huerta, S. Aghazadehchors, C. Jiménez, and D.Bellet, *Spatial atomic layer deposition (sald), an emerging tool for energy materials. application to new-generation photovoltaic devices and transparent conductive materials,* Comptes Rendus Physique **18**, 391 (2017), demain l'énergie.

[29] F. N. Inc., *Manufacturing processes to synthesize, functionalize, surface treat and/or encapsulate powders, and applications thereof - 20190062914,* (2018), c23C 16/455 (20060101).

[30] J. van Ommen, *Integrated manufacturing of core-shell particles for li-ion batteries,* (2020).

[31] A. Goulas and J. R. Van Ommen, *Atomic layer deposition on particulate materials,* Materials Today Chemistry **14**, 100183 (2019).

[32] Y. Mawatari, Y. Hamada, M. Yamamura, and H. Kage, *Flow pattern transition of fine cohesive powders in a gassolid fluidized bed under mechanical vibrating conditions,* Procedia Engineering **102**, 945 (2015).

[33] D. Barletta and M. Poletto, *Aggregation phenomena in fluidization of cohesive powders assisted by mechanical vibrations,* Powder Technology **225**, 93 (2012).

[34] J. van Ommen, D. King, A. Weimer, R. Pfeffer, and B. van Wachem, *Experiments and modelling of micro-jet assisted fluidization of nanoparticles,* The 13th International Conference on Fluidization (2010).

[35] K. An and J. M. Andino, *Enhanced fluidization of nanosized tio2 by a microjet and vibration assisted (mva) method,* Powder Technology **356**, 200 (2019).

[36] E. Ireland, K. Pitt, and R. Smith, *A review of pulsed flow fluidisation; the effects of intermittent gas flow on fluidised gas–solid bed behaviour,* Powder Technology **292**, 108 (2016).

[37] E. AL-Ghurabi, M. Shahabuddin, N. Siva Kumar, and M. Asif, *Deagglomeration of ultrafine hydrophilic nanopowder using low-frequency pulsed fluidization,* Nanomaterials **10**, 388 (2020).

[38] P. Ammendola and R. Chirone, *Aeration and mixing behaviours of nano-sized powders under sound vibration,* Powder Technology **201**, 49 (2010).

[39] A. Langde, R. Sonolikar, and D. Tidke, *Effect of variable acoustic field and frequency on gas-solid suspension of fine powder: A review,* Chemical Engineering Communications **199**, 384 (2012).

2

On the fluidization of cohesive powders: Differences and similarities between micro- and nano-sized particle gas–solid fluidization

As our substrate is cohesive, we began by reviewing the literature on the fluidization of cohesive micro- and nanoparticles. In this chapter we elaborate on the forces acting on these particles, and show how their magnitudes are typically determined through models. Additionally, we discuss the differences between the sizes and structures of agglomerates formed by micro- and nanoparticles. Finally, we identify research gaps in the considered area and provide recommendations for future research within this field.

This chapter has been published as "On the fluidization of cohesive powders: Differences and similarities between micro- and nano-sized particle gas–solid fluidization" by R. Kamphorst, K. Wu, S. Salameh G.M.H. and J.R. van Ommen, The Canadian Journal of Chemical Engineering **101**, 227 (2023)

2

The fluidization of cohesive powders has been extensively researched over the years. When looking at literature on the fluidization of cohesive particles, one will often find papers concerned with only micro- or only nano-sized powders. It is, however, unclear whether they should be treated differently at all. In this paper, we look at differences and similarities between cohesive powders across the size range of several nanometres to 10s of micrometres. Classification of fluidization behaviour based on particle size was found to be troublesome since cohesive powders form agglomerates and using the properties of these agglomerates introduces new problems. When looking at inter-particle forces, it is found that van der Waals forces dominate across the entire size range that is considered. Furthermore, when looking into agglomeration and modelling thereof, it was found that there is a fundamental difference between the size ranges in the way they agglomerate. Where the transition between the types of agglomeration is located is, however, unknown. Finally, how models are made and agglomerate sizes are measured is currently insufficient to accurately predict or measure their sizes consistently.

2.1. INTRODUCTION

The applications of micro- and nano-sized particles are widespread: food [1–4], biomedical applications [5, 6], water treatment [7, 8], sensors, [9, 10] and electronic devices [11, 12] to name only a few. With even more possible applications being researched, the processing of these powders is a field worth looking into. Gas–solid fluidization is often the preferred option for processing powders [13, 14]. In this system, a gas flows through a bed of powder, creating drag, which lifts the particles, resulting in a liquid-like phase [15, 16]. This process is relatively straightforward when considering particles in a range of roughly 30 µm to 1 mm, but becomes tougher when using smaller particles due to cohesive inter-particle forces starting to dominate. A lot of studies have been published on the fluidization of cohesive powders, but most of them are focused on either micro- or nano-sized particles. It is unclear, however, whether a sharp distinction should be made between the two and, if so, what the differences in their fluidization behaviour are and what causes these differences.

In this study, a review of literature on the characteristics of cohesive powders in a fluidized bed is given, with a focus on studies published in the last 20 years. We touch upon the classification of fluidization behaviour based on particle properties and inter-particle forces. We look at which forces dominate for micro- and nano-sized particles as well as which equations are typically used to describe the forces on both scales. Additionally, formed agglomerates from powders in the two size ranges are compared and models to predict their sizes are discussed.

2.2. POWDER CLASSIFICATION

Over the years, many ways of classifying powders, with respect to their fluidization behaviour, have been developed. For the completeness of this work, a brief overview is given of the classifications of non-cohesive powders.

2.2.1. PARTICLE SIZE

Before any classification with respect to fluidization behaviour can be done, we need to establish when a powder is called 'micro' or 'nano'. Wang et al. defined nanoparticles as 'powdered materials with individual particles in nanometer scale' [17]. This definition becomes problematic, however, when considering a 3-dimensional particle with a high aspect ratio, resulting in the particle having dimensions in both micro- and nanoscale. Examples of this include carbon nanotubes [18, 19] and asbestos [20, 21].
In their 2011 report, the European Commission stated: 'nanomaterial means a natural, incidental or manufactured material containing particles, in an un-

bound state or as an aggregate or as an agglomerate and where, for 50 % or more of the particles in the number size distribution, one or more external dimensions is in the size range 1–100 nm' [22]. This definition addresses both the aspect ratio of individual particles, as well as particle size distribution. It is known that powder consisting of particles of different size ranges exhibits distinct, usually improved, fluidization behaviour, not only for cohesive powders that consist of both nano- and, cohesive, micro-sized particle [23, 24], but also of non-cohesive powders mixed with fine powder [25–29]. For this paper we will use the following definition for nanopowder: a powder that consists of primary particles of which at least one external dimension is smaller than 100 nm, where it is assumed that the average particle size can be used to describe all particles the powder consists of.

A definition like this for micropowders is not as simple, since it is not their size but their behaviour upon fluidization which is of interest. We are only considering cohesive particles, to avoid tediously restating this over and over, the term 'microparticles' will, in this work, exclusively refer to particles in the micro-size range that fall in the Geldart type C classifiaction (see Section 2.2.2), typically being smaller than 30 µm. When trying to fluidize these powders, they agglomerate and form channels, often requiring additional equipment to initiate fluidization.

2.2.2. GELDART DIAGRAM

The most well-known classification for the fluidization of powders, based on size and density, was proposed by Geldart in 1973 [30]. He performed fluidization experiments with sieve fractions of several powders and looked at minimum fluidization velocity, minimum bubble velocity, bed voidage, and bed height expansion to find the influence of particle properties on fluidization behaviour. The resulting classification is shown in Figure 2.1. Powders are classified as type A when they fluidize easily, give large bed expansions and start bubbling at a superficial gas velocity far above the minimum fluidization velocity. Type B powders are also easy to fluidize but start bubbling at, or close to, the minimum fluidization velocity. Type C powders tend to stick together and form plugs, agglomerates (sometimes called clusters), and channels. In general, these powders cannot be fluidized without the aid of assistance methods. Type D powders are spoutable materials: upon the introduction of a gas flow a spouted bed can be formed. This is not considered fluidization, since the particles do not form a consistent phase with bed expansion and/or bubbling. Whereas the boundaries between Type A and B and Type B and D were calculated, the shaded line, separating Type A and Type C powders, is drawn based on empirical data [30]. The Geldart diagram is still widely used, since it gives a reasonable prediction of fluidization behaviour based on few, and easily accessible, properties.

Particles of interest for this paper are all Type C and should therefore, according to the diagram, have the same fluidization behaviour. However, the smallest sieve fraction used by Geldart was 10–20 µm [30], meaning smaller particles could show different behaviour upon fluidization. This would then require an extension of the diagram to make accurate prediction of fluidziation behaviour of powders within the Type C size range possible.

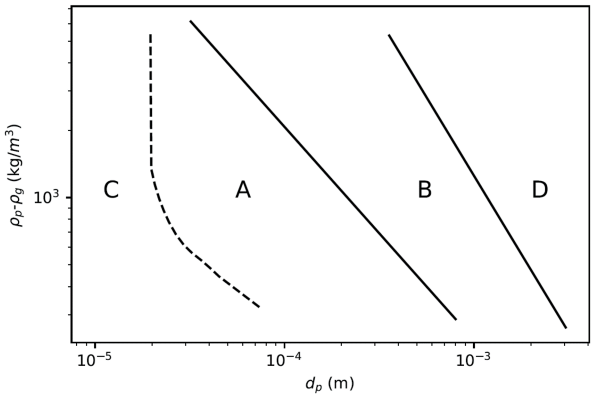


Figure 2.1: Geldart diagram (recreated from the work of Geldart[30])

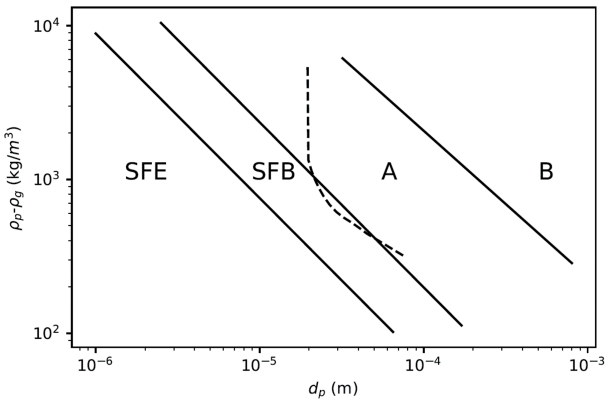


Figure 2.2: Extended Geldart diagram, SFB: solidlike-to-fluidlike-to-bubbling, SFE: solidlike-to-fluidlike-to-elutriation (recreated from the work of Valverde and Castellanos[31])

2.2.3. EXTENSION OF THE GELDART CLASSIFICATION

Although Geldart's diagram is a useful tool, it is not always applicable for fine (micro-sized) and ultra-fine (nano-sized) powders, some of which can be fluidized without using assistance methods, despite the diagram predicting the op-

posite [32–34]. Valverde and Castellanos developed an extension of the Geldart diagram, as shown in Figure 2.2. Solid-like to bubbling (SFB) and solid-like to fluid-like to elutriation (SFE) are identified as distinct regimes [31]. It is important to note here that the d_p on the x-axis of Figure 2.2 is not the diameter of the primary particle, but of pre-existing simple agglomerates. The graph therefore uses the well-known phenomena in fluidization of fine powders, that not the primary particles but the formed agglomerates dominate the fluidization behaviour [32, 35].

2.2.4. CLASSIFICATION BASED ON INTER-PARTICLE FORCES

The diagram proposed by Geldart shows the type of fluidization that is expected to happen when air at atmospheric pressure and ambient temperature is used as the fluidizing gas. Grace was among the first to propose using a generalization based on the Archimedes number [36] Ar (the ratio between gravitational and viscous forces) in order to include different gasses and pressures, which was later adopted by several other studies [37, 38]. Using Ar, the viscosity of the fluidization medium is included.

$$Ar = \frac{g d^3 \rho_f (\rho_p - \rho_f)}{\mu^2} \tag{2.1}$$

For the calculation of Ar for cohesive powders using d and ρ_p as constants of the primary particle or of the formed agglomerates will change the result. Most studies do not explicitly mention which one to take [37–39], some use the primary particle properties [36, 40] . Since the fluidization behaviour of fine powders is known to be dominated by the formed agglomerates [32, 35] one could argue that, for fine powders, the properties of agglomerates should be taken instead.
Recently, Mostoufi proposed a generalization that includes predictions of the type of fluidization that should be expected when assistance methods are used. This diagram is based on the dimensionless inter-particle force (φ) and Ar [39], see Figure 2.3.
where φ is defined as:

$$\varphi = \frac{F_{IP}}{F_W - F_B} \tag{2.2}$$

where F_{IP} is the sum of all attractive inter-particle forces minus the repulsive inter-particle forces which include forces that are introduced by assistance methods. This is however not straightforward, since there is a discussion on which forces are relevant on which scale and on how they should be calculated, as will

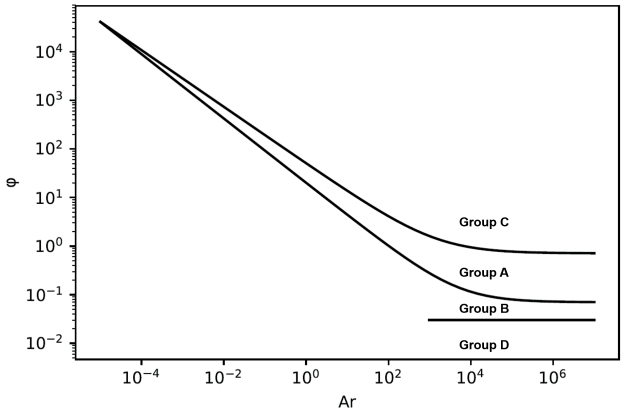


Figure 2.3: Geldart classification based on Ar and dimensionless inter-particle forces (recreated from the work of Mostoufi[39])

be discussed in Section 2.3. F_W and F_B are the forces resulting from the weight of the particle and the buoyancy, respectively. From this, it can be seen that using assistance methods to fluidize cohesive powders will decrease the value of φ by introducing a repulsive force that reduces the value of F_{IP} and therefore causes a transition from Type C to Type A fluidization when enough repulsive force is introduced. It is important to note that in Figure 2.3, the correlation between primary particle size and fluidization type is indirectly found in the Ar since agglomerate size depends on primary particle size, as will be discussed in Section 2.4. The dimensionless interparticle force (Equation (2.2)) is also a function of primary particle size, as will be discussed in Section 2.3.

2.2.5. LIMITATIONS OF CLASSIFICATION OF COHESIVE POWDERS

Since cohesive powders form agglomerates, it is often unclear whether the agglomerate size or the primary particle size should be used for predicting the fluidization behaviour. Considering that the agglomerates dominate the fluidization behaviour [32, 35], taking the agglomerate properties seems to be the best option. This does however introduce other complications. First of all, agglomerates have large size distributions [41–45]. This might seem trivial to point out since one can just use the average agglomerate size when classifying the powder; however, it is also known that mixtures of powders with different sizes significantly change the fluidization behaviour [46–48]. Second, using agglomerate size to predict fluidization behaviour is complicated further since agglomerates are not evenly spread through the bed but larger ones are more often found at the bottom whereas smaller ones are found at the top [49, 50]. Third, agglom-

erate size was found to depend on fluidization time [51] (see Section 2.4.2). Another complication appears when looking at Equation (2.1) and Equation (2.2). It is important to be aware that assistance methods are commonly thought to break up agglomerates (see Section 2.4.4), therefore decreasing the value of Ar. Assistance methods are also introducing repulsive forces which will decrease the value of φ. Looking at Figure 2.3, this makes assistance methods effective in two ways when it comes to making Type C powders behave like Type A ones. This can mean one of two things: either the introduction of assistance methods has a high effectiveness for improvement of fluidization by decreasing both Ar and φ aspects, or the effect of the assistance method is overestimated since it is introduced twice using this method. This can either mean that the primary particle size should be used to calculate Ar, which contradicts the idea that agglomerates dominate fluidization behaviour, or this method is not valid for accurately predicting assisted fluidization behaviour of particles that form agglomerates.

2.3. FORCES ACTING ON PARTICLES

The different forces acting on particles in a fluidized bed are the cause of the fluidization behaviour and resulting agglomeration [34, 52]. Therefore, we will highlight these forces in this chapter. Forces acting between particles directly, Figure 2.4, ones acting between particles and fluidization gas, and collisions are considered.

Agglomeration is the result of the interplay of cohesive and repulsive forces [41]. The forces that are typically considered to act between particles that form the agglomerates are [53, 54]: gravity, drag force, van der Waals forces, capillary force, electrostatic force, and forces due to collisions. They will all be introduced shortly in this review; for more extensive descriptions of the forces that dominate fluidization see the works of Ommen et al., Tahmasebpoor et al., Leroch and Wendland, and Endres et al.[13, 54–58]

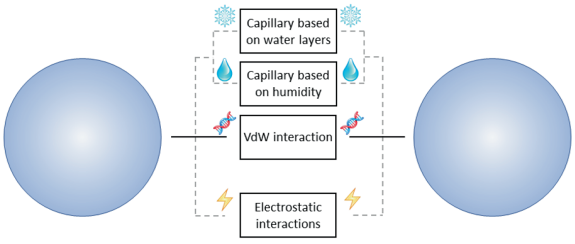


Figure 2.4: Forces acting between particles

2.3.1. GRAVITATIONAL FORCE

The most obvious force which must be overcome to fluidize a powder is gravity or weight force. Since gravity acts on the volume of a body, it can mostly be neglected for fine powders whereas inter-particle attraction which works on the particle surfaces becomes much more important. Basically at a scale of hundreds of micrometres, this surface/volume effect becomes relevant, meaning that the formed agglomerates have enough mass to experience gravity as a significant force counteracting the gas flow. For a spherical particle, the gravitational force can be calculated by:

$$F_W = \frac{\pi}{6}\rho_p g d_p^3 \tag{2.3}$$

Note that in Equation (2.3), ρ_p and d_p are the density and diameter of the primary particle, respectively. When calculating F_W for agglomerates, the density and diameter of the agglomerate should be taken instead.

Buoyancy is sometimes used in relation to agglomerate size, but due to the low density of the fluidizing gas compared to that of the particles, the effect of buoyancy is low. When considering agglomerates, one could argue that the buoyancy should be taken into account, since the agglomerates have an open structure and therefore a low density. However, buoyancy usually is neglected when it comes to particles/agglomerates in a gas.

A relation that is commonly used in literature related to the weight force to the inter-particle force is the Bond number.

$$Bo = \frac{\Sigma F_{cohesive}}{F_W} \tag{2.4}$$

When $Bo > 1$, the powder is considered cohesive [59]. Note here that, since F_W scales with d_p to the power 3 and cohesive forces typically scale with a lower power, the Bond number decreases with increasing particle size, meaning the particles become less cohesive, which is in agreement with the classifications discussed in earlier.

2.3.2. DRAG FORCE

The drag force creates lift which, when exceeding the gravitational pull, makes particles or agglomerates fluidize. While particles or agglomerates are fluidized, the drag force is usually assumed to be equal to the buoyant weight [60, 61].

The general expression for drag force, using Stokes law in the laminar regime, is given by:

$$F_D = 3\pi\mu d_p u \tag{2.5}$$

For particles lifted by a gas flow in the laminar regime in a suspension of alike particles, the equation can be generalized [62]:

$$F_D = 3u\pi\mu\varepsilon^{-3.8}d_p \tag{2.6}$$

where ε is the void fraction of the bed, which is assumed to be independent of u [62]. This equation is semi-empirical and was confirmed by experiments. The inclusion of ε is needed to correct for the change in interstitial gas velocity due to the presence of particles.
Apart from creating the needed lift for the particles to fluidize, drag can also break larger agglomerates into smaller ones [63].

2.3.3. VAN DER WAALS FORCE

The van der Waals forces are caused by electric dipoles in atoms/molecules, which result in an adhesive force [54, 64]. To describe this attraction for particles, Hamaker developed a simple model for two spheres of equal radius, which is frequently used today:

$$F_{vdW} = \frac{A_H \cdot d_p}{24H_0^2} \tag{2.7}$$

where A_H is the Hamaker constant, d_p is the primary particle size, and H_0 is the minimum inter-particle distance. This distance varies from different sources and assumptions while values between~ 0.17 nm [65] to ~ 0.4 nm [66] and even larger can be found in the literature.

It is important to note that the Hamaker constant, and therefore the resulting van der Waals force, is a function of particle size, particle geometry, material, and temperature [67]. This means that for processes at elevated temperatures, like particle coating [68], the fluidization behaviour might be affected. This effect has been shown in publications, although it can not account for all of the differences found in fluidization behaviour at high temperatures [69, 70].

When talking about van der Waals forces between formed agglomerates, Equation (2.7) cannot be applied directly. However, several approaches to calculate F_{vdW} between agglomerates are found in the literature. First of all, when one assumes agglomerates are very dilute and only a few particles are in direct contact, the van der Waals force between them can be calculated as [71]:

$$F_{vdW} = N \cdot \frac{A_H \cdot d_p}{24H_0^2} \tag{2.8}$$

where N is the number of shared particles. The fact that Equation (2.8) predicts a stronger van der Waals force for bigger particles is however inconsistent with the observation made by Matsuda et al. that agglomerates made up of smaller primary nanoparticles are stronger than ones made up of larger nanoparticles [41, 72]. However, it is important to note that the number of particles in contact is not equal for different-sized nanoparticles but depends on multiple factors of agglomerate formation.
The second approach is to assume agglomerates are microsized particles with asperities d_{asp}, giving the relation [61, 73]:

$$F_{vdW} = \frac{A_H \cdot d_{asp}}{24 H_0^2} \tag{2.9}$$

where d_{asp} is usually taken as 0.1–0.2 µm [60, 61]. Equation (2.9) is known to overestimate the attractive force between agglomerates made up of nanoparticles due to the assumption that the asperity has no porosity [41].

To address the shortcomings of the other equations, de Martín et al. proposed Equation (2.10) to calculate the van der Waals force between two porous agglomerates made up of nanoparticles [41], which they use to calculate the size of complex agglomerates (see Section 2.5).

$$F_{vdW} = \frac{A_H \cdot d_a (\rho_a / \rho_p)^2}{24 z_{eq}^2} \tag{2.10}$$

where d^* and ρ^* are the diameter and density of the agglomerates, respectively. z_{eq} represents an equivalent distance defined as:

$$z_{eq} = H_0 + k_1 \cdot rms \tag{2.11}$$

where k_1 is a coefficient relating the maximum vertical distance between any point of the asperity and the horizontal plane to rms and rms is the root mean square of the surface roughness [74].

In conclusion, for calculation of the van der Waals force between agglomerates, Equation (2.9) is thought to be suitable for agglomerates made up of micro-sized primary particles and Equation (2.10) is likely most suited for agglomerates made up of nanoparticles. It is important to note that these equations consider the fact that agglomerates are built up out of smaller particles, but do not take the structure of formed agglomerates into account. Rather, they describe that fact by general property values such as density or porosity.

The influence of van der Waals forces depends strongly on the surface properties of the particles. Powders with polar (hydrophilic) surfaces strongly bind water to their surface, resulting in a strong attractive van der Waals force which is determined by their surface hydroxyl groups [54, 56, 75]. For the most commonly used nanopowders in research (TiO_2, SiO_2 and Al_2O_3) a significant increase in minimum fluidization velocity is found when polar powder is used instead of apolar powder, which can be attributed to the strong van der Waals interactions of the hydroxyl groups and water molecules [56]. In addition, surface roughness of the contact area is considered essential to evaluate van der Waals force between particles [58, 76]. For numerical simulations, the Hamaker model is vastly extended to address effects of surface roughness, such as modifications for asperities on a flat rough surface [77] or submerged below the surface [74], and a generic model incorporating asperities at multiple scales [78].

For simulating the dynamics of cohesive particles, due to the presence of singularity in the Hamaker model, certain modified forms have been proposed to avoid the numerical divergence. As aforementioned, it generally assumes that adhesion force plateaus at a minimum contact distance in the order of asperity, that is $f_{vdW} = f(H_0)$ for $H \leq H_0$. More rigorously, the Hamaker correlation can be modified assuming the deformation is negligible. For example, Galvin and Benyahia [79] proposed an alternative to the Hamaker model that allows to avoid the numerical singularity:

$$F_{vdW} = \frac{A_H 2 r_i r_j (r_i + r_j + s)}{3 s^2 (r_i + r_j + s)^2} \left[\frac{s(2r_i + 2r_j + s)}{(r_i + r_j + s)^2 - (r_i - r_j)^2} - 1 \right]^2 \tag{2.12}$$

where s is defined as the distance between their surface, r_i and r_j are the radius of paired particle i and j, respectively

For softer particles bigger than 10 µm, Johnson et al.[80] proposed the JKR (Johnson-Kendall-Roberts) model that accounts for the influence of van der Waals forces with a surface energy density γ_s. Different from the Hamaker model, in which particle deformation during contact is negligible when sufficiently small particles are concerned, the JKR model is contact-dependent and used for the modelling of adhesive granular flows where agglomeration occurs:

$$F_{JKR} = 4\sqrt{\pi \gamma_s E^* a^3} \tag{2.13}$$

$$\delta = \frac{a^2}{R^*} - 4\sqrt{\frac{\pi a \gamma_s}{E^*}} \tag{2.14}$$

where γ_s is surface energy, E^* and R^* are the equivalent Young's modulus and equivalent radius, respectively, and a is the contact radius. The Hamaker constant is material-specific and can be correlated to the surface energy γ_s through the force required to break an adhesive contact:

$$A_H = 24\pi\gamma_s H_0^2 \tag{2.15}$$

The JKR model has also shown to be sufficient to predict the dynamics of relatively large primary particles [81, 82]. Besides, according to the JKR theory, a "pull-off" force, F_p, can be derived for the adhesion between particles.

van der Waals forces can be also modelled semi-empirically. To reduce computational cost in numerical simulations, Weber et al. simplified the van der Waals forces with a square-well potential and validated using a hard-sphere discrete framework to capture rapid granular flows [83]. Nevertheless, mappings between the constructed square-well and the particle properties are required to enable more generic applications. Similarly, Liu et al. proposed a square-force model which conserves the characteristic cohesive energy and maximal cohesive force over the Hamaker model, as a simple yet reasonable substitute of more rigorous models [84].

2.3.4. CAPILLARY FORCES

For polar particles, water molecules will adsorb to the particle surfaces. When these particles get close to each other, the water on their surfaces will form a meniscus between them, which introduces an additional attractive force, the capillary force. Hydrophobic particles will have less water adsorbed on their surface leading to a smaller capillary force [85].
The capillary force, for a simple two-sphere case, can be expressed as [86]:

$$F_{cap} = 2\pi\gamma l - \pi l^2 \Delta P \tag{2.16}$$

where γ is the surface tension of the liquid, l is the azimuthal radius, and ΔP is the pressure difference between the phases. This pressure difference is often calculated using the Young–Laplace and Kelvin equations [57, 86, 87]. The Kelvin equation was however found to only be valid for particles larger than 1 µm [88]. For smaller particles, some of the assumptions made are no longer valid and new models are needed to describe the forces. The reason for this is twofold. First of all, for micro-sized particles, it can be assumed that the radius of the water meniscus is constant since the radius of the particle is significantly larger than that of the meniscus [88]. For particles smaller than 1 µm this assumption no

longer holds. Also, for nanoparticles, the distance between the particles significantly influences the resulting capillary force [89] whereas this is not so much the case for microparticles. Second, at the nano-scale, the adsorbed water on the particle surface can no longer be treated as a continuum, but individual water molecules should be considered [88, 90]. This also means there is no distinct phase boundary between the water and surrounding gas anymore when one considers this small scale, making accurate modelling of capillary forces on nano-sized particles difficult. Simulations using LAMMPS [91] have shown good results to estimate the capillary force of nanoparticles [57, 90]. Alternatively, attempts carried out to indirectly account for the impacts of capillary force by applying a "wet" restitution coefficient to address the energy dissipation during the contact of wet particles [92, 93]. However, such a simple alternative cannot model agglomeration [94] and this "wet" restitution coefficient varies largely with particle properties and operating conditions.

F_{cap} is, among other variables such as temperature or shape of the particles, a function of relative humidity. Interestingly, the humidity dependency is still today a debate since the literature lists contradictory results which are not fully understood yet [95–98]. Nevertheless, we can say that for micro-sized particle F_{cap} will be the dominant force at higher humidities. Since in most studies dry nitrogen or dry air is used as a fluidizing gas, the powder will be dried and capillary forces can be assumed to be insignificant. However, for nano-sized particles, the adsorbed water layers do not disappear in a dry environment, as long as they are not heated [85], and the capillary forces still play a significant role. At what scale this effect is no longer relevant is currently unknown.

For dynamic particles linked via liquid bridges, a dynamic dissipative (or viscous) force arises from liquid viscosity, in parallel to capillary forces. It is modelled based on lubrication theory:

$$F_{\mu,n} = \frac{3\pi\mu R^2}{2s} v_n \tag{2.17}$$

where μ is the liquid viscosity, v_n is the normal component of the relative velocity between particles, R is the particle radius, and s is the separation distance. In a similar fashion to the van der Waals force, the dissipative force reaches a singularity when the two concerned particles are in contact ($s = 0$). Similar to the Hamaker model, a minimum separation distance is assumed on the length scale of surface asperities to prevent any singularity [99].

2.3.5. ELECTROSTATIC FORCES

The electrostatic forces that are typically discussed in literature on fluidization of fine and ultra-fine powders are the ones generated through triboelectrification. These charges are built up through charge separation, typically associated with the rubbing together of dissimilar or similar surfaces [100–102]. Since the fluidized bed is a highly dynamic system, this charge generation occurs constantly. This results in particles having a similar charge and therefore, in principle, repulsing each other, meaning a higher electrostatic force favours deagglomeration. At the same time, however, charged powder will tend to stick to the column walls, meaning that some of the powder will not be part of the bed anymore. Unlike the other forces acting on particles, the electrostatic force is heavily influenced by the handling of the powder, even before the fluidization starts [103]. Note here that the presence of water or an alcohol on a particle surface will mitigate this effect, meaning electrostatic forces are typically only present for hydrophobic particles. This also means that the electrostatic forces can usually be nullified by running the fluidizing gas through a bubbler with water or an alcohol before letting it enter the bed. The introduction of a saturated gas into the system does of course come at the cost of introducing, or increasing, capillary forces in the system. Also, when applied in a reactor, the introduction of water or alcohol vapour can harm the process by introducing undesired side reactions. Electrostatic forces are typically considered to not be relevant for both nanopowders [13, 61, 104] or micropowders [105], although studies have also shown the inclusion of alcohol vapour in fluidized beds to reduce these forces and improve fluidization [56, 100].

2.3.6. COLLISION FORCE

The final considered force is introduced by collisions between agglomerates. In contrast to the adhesion forces, the collision is described mostly empirical and a fundamental physical understanding is missing. To calculate this force, the following expression was proposed by Zhou et al. [48, 106] for the collision force between two agglomerates of equal size:

$$F_C = 0.166\left(\frac{\pi V^6 \rho_a^6}{k^2}\right)^{\frac{1}{5}} \cdot d_a^2 \tag{2.18}$$

where k is a function of Poisson's ratio and Young's modulus and V is the relative velocity of the agglomerates, which is a function of agglomerate density, bed voidage, and bubble diameter [106, 107]. It is assumed here that the agglomerates are elastic bodies.

When simply including this equation as a repulsive force in a balance, one would implicitly assume that all collisions lead to the breakage of the agglomerates. The

way for small agglomerates to grow however is also due to collisions, meaning not all the forces introduced will lead to breakage. Some particles that collide will just bounce off, some will merge, and others will break.

2.3.7. DOMINANT INTER-PARTICLE FORCES

Some publications on inter-particle forces include graphs where the forces are plotted as functions of particle size to show in which size range which forces are dominant [13, 108]. While useful for an indication, such graphs could be misleading since particle size is not the only relevant parameter that influences the respective forces. The most significant variable is the humidity in combination with a hydrophilic or hydrophobic surface; if under the given conditions capillary forces play a role, they are usually dominant and will stay dominant over the entire range of sizes relevant for this study. In absence of capillary forces, van der Waals forces are typically dominant. Electrostatic forces are usually thought to only become significant at larger particle sizes [109, 110] than considered in this study. With increasing particle size, gravity will eventually become the dominant force. In conclusion, for the size range considered in this study, the van der Waals force will be the dominant inter-particle force in the absence of moisture. Especially for hydrophilic particles, where the van der Waals forces are relatively large due to hydrogen bond formation.
When comparing micro- and nano-sized powders, one finds that the same forces are dominant for both powders. The way to calculate the values of these forces does differ, but based on this alone one cannot conclude these powders to behave differently or the same when fluidized.

2.4. AGGLOMERATION IN FLUIDIZED BEDS

Fine and ultra-fine powders fluidize as agglomerates. Larger particles, falling in the Geldart Type A, are also known to sometimes form agglomerates, or clusters, upon fluidization [111–113]. The observed fluidization behaviour is dominated by the nature of the agglomerates and not so much by the primary particles directly [32, 35]. Therefore, it is interesting to look at the agglomerates formed by powders with primary particle sizes in the nano- and micrometre range and find their similarities and differences, since these could explain differences in fluidization behaviour.

2.4.1. PARTICLE STRUCTURE

For complete understanding, a distinction needs to be made between agglomeration and aggregation. Though these terms are sometimes used interchangeably

in literature, they refer to different phenomena. Agglomeration is the process where bodies cluster together as a result of attractive inter-particle forces, forming agglomerates. Agglomerates are fragile by nature [114] and will constantly break and reform in the fluidized bed [34, 115, 116]. Aggregation is the process where primary particles form solid bridges, resulting in aggregates. The solid bridges are formed by surface diffusion or sintering [117–120]. This takes place at elevated temperatures and pressure [121], which are the conditions under which nanoparticles are typically produced. Aggregates cannot be easily split back into their primary particles, making them different than agglomerates. Aggregates have net-like structures, sizes in the hundreds of nanometres, and low densities due to the porous structure [34]. Aggregates are the smallest durable entities existing in the fluidized bed of nanopowders. As a result of inter-particle forces, aggregates can cluster together and form agglomerates during storage and fluidization.

Since micropowders are mostly produced by milling [122, 123] and spray drying [124, 125], typically no aggregation takes place. This means that the smallest particles present in the bed are the micro-sized primary particles themselves. Note here that the building blocks of agglomerates formed by micro- and nanopowders are thus significantly different in structure and density; agglomerates from micropowders being formed by primary micro-sized particles and those from nanoparticles by the sintered aggregates.

2.4.2. AGGLOMERATION IN PRACTICE

When we look at the modelling done on agglomeration, some knowledge from experimental studies is required. From experiments, it is known that agglomerates are not homogeneously distributed in the fluidized bed [49]. They are segregated based on their size: the larger ones are found at the bottom of the bed whereas the smaller ones are found at the top [49]. This makes accurately measuring agglomerate sizes tougher since results will be influenced by the height at which measurements are taken. Furthermore, agglomerates are constantly breaking and reforming [34, 115, 116], meaning that, if any equilibrium can be reached, this is a dynamic equilibrium and agglomerates do not stop interacting when reaching an equilibrium size.

Another aspect of agglomeration is that there are signs that it is dependent on fluidization time. Mogre et al. found that agglomerate size and bed height, of 21 nm TiO_2, decreased over time [51]. Nam et al. also found a decrease in bed height with time for nanopowder [115], but did not measure agglomerate size. The small number of studies that show this does not, however, mean that this effect is limited to nanoparticles (unlike Ali et al. claim in their study [126]). When considering the observation by Matsuda et al., that agglomerates made

up of smaller nanoparticles are stronger than those made up of larger ones [72], one should expect most, if not all, agglomerates to decrease in size with longer time spent in the fluidized bed. This would mean that reported agglomerate sizes should be considered with care since the measured size is unlikely to be the equilibrium size if the measurements were taken under the assumption that there is no time dependency. This in turn would affect proposed models based on these measurements. It is therefore crucial that the effect of time spent in the fluidized bed on agglomerate size, and other features, are tested and reported upon.

2.4.3. MEASURING AGGLOMERATE SIZE

Several measurement techniques to determine the size of agglomerates in a fluidized bed have been applied in publications. Measuring agglomerate size can be done either in-situ or ex-situ. Due to the fragile nature of agglomerates, ex-situ techniques have the inherent risk of changing the agglomerates before measuring them. Both removing the agglomerates from the bed, as well as the sample preparation thereafter, are likely to influence the acquired results. Therefore only in-situ techniques will be discussed here.

A way to measure the agglomerate size that is commonly found in literature is by obtaining images of the agglomerates at the surface of the bed. For this, a laser, a source for illumination, a camera, and software to process the images and estimate the size are used [35, 127]. The benefits of this technique are that the agglomerates are not damaged and that the bed is not disturbed. A downside is that only agglomerate sizes at the surface of the bed (the splash zone) can be measured since the lower region of the bed is too dense. As mentioned before, agglomerates tend to segregate based on size, meaning the splash zone is not representative of the whole bed.
A similar technique was proposed by Quevedo et al. Here a probe was placed inside the bed, allowing to obtain images from below the splash zone [128]. The advantage is that a more representative result can be obtained. The downside, however, is that the bed is disturbed by the presence of the probe, which could influence the results.

Another in-situ measurement technique was developed by de Martín et al. They placed a settling tube in the fluidized bed and measured the terminal velocity of agglomerates falling inside the tube by filming them with a borescope [129]. Apart from the advantage that agglomerate sizes are not only measured in the splash zone, another advantage is that the density of the agglomerates can be calculated from their velocity. The main disadvantage of the technique is that

the bed is disturbed by the presence of the tube, which might affect the results.

All three mentioned methods have their pros and cons, and until more is known about how representative the splash zone is for the entire bed, the methods by Quevedo and de Martín should be concluded to be most accurate. Since models to predict agglomeration are validated by comparing their output with measured agglomerate sizes, it is crucial that the most accurate measurement methods are used to prevent artefacts from influencing the evaluation of model validity. Furthermore, since multiple measurement procedures are used, it is currently not possible to directly compare results, even if all other conditions are equal. It would be interesting to see a study where the methods are compared to see how their results differ.

2.4.4. ASSISTANCE METHODS

Fluidization of powders, consisting of cohesive particles, can be drastically improved when using assistance methods. It is hard to definitively say whether a method is effective over a large range of particle sizes since studies rarely show unsuccessful applications of methods. The number of publications spanning a size range can however be an indication of a method being more effective. For instance, of the studies published on the effectiveness of a (micro)jet, one was found for 30 µm powder [130], whereas multiple were found in the range of 12–25 nm [128, 131–133]. For robust proof of limitations in particle sizes for which methods are applicable, more research is required.
The way most studies conclude assistance methods to work is by introducing additional repulsive forces that counteract the van der Waals force, reducing channelling and agglomeration (mechanical vibration [115], acoustic vibration [134], magnetic field [71], stirring [46], microjet [128, 132], and pulsed flow [135–137]). This additional force can be included in a force balance when modelling agglomerate size [105]. For a comparison of multiple methods and their effectiveness see [138]; note that only one micro-sized powder is used here, meaning it is unknown to what extent results can be generalized.

2.5. MODELLING AGGLOMERATION

Throughout the years, many models for the estimation of agglomerate sizes have been proposed. In this paper, we will focus on some recent models.
In a force balance, cohesive and repulsive forces considered are assumed to be in balance and the found equation is then solved for agglomerate size, d_a.

2.5.1. CONSIDERATIONS FOR MODELLING

For nanoparticles, it was found that agglomeration takes place in distinctive steps: primary particles to aggregates (sometimes called sub-agglomerates) to primary agglomerates to complex agglomerates, which is a phenomenon that was discovered by Yao et al. [34]. Where each stage of the multi-stage agglomeration (MSA) has its own density and fractal dimension [139]. The latter is a more recent insight since a fractal dimension of 2.5 was earlier used for all stages of nanoparticle agglomeration [115, 140, 141]. No MSA has been described for microparticles, making the final agglomerates present in the fluidized bed of microparticles significantly different.

2.5.2. MODELLING NANOPARTICLE AGGLOMERATION

For nanopowders, models were found based on MSA. These models propose ways to calculate the size of the complex agglomerates. Usually, the ratio between the densities of each of the respective stages is taken [41, 115, 142]:

$$\frac{\rho_x}{\rho_y} \propto \left(\frac{d_y}{d_x}\right)^{f(D)} \tag{2.19}$$

where x and y denote the stages, x being the larger one, and the exponent to the ratio of sizes being a function of the fractal dimension of stage x. The nanoparticles first form aggregates with a fractal dimension of ~2 [41], which combine into primary agglomerates with a fractal dimension of 2.5–2.6 [115, 140, 143], which then merge to form complex agglomerates with a fractal dimension of 2.3 [143]. One of the models based on MSA was proposed by Valverde et al. [144]. In their model, they equate the ratio between the diameter of each stage of agglomeration to the Bond number. Solving this for each of the stages results in a relation for the diameter of the complex agglomerates:

$$d_a = d_p^{0.679} \cdot d_{asp}^{0.321} \cdot Bo^{0.365} \tag{2.20}$$

Note here that the primary particle size, d_p, pops up twice, once explicitly and once hidden in the Bond number. Rewriting the equation to make the d_p completely explicit results in:

$$d_a = d_p^{-0.051} \cdot d_{asp}^{0.321} \cdot \left(\frac{A_H}{4\pi\rho_p g z_0^2}\right)^{0.365} \tag{2.21}$$

From Equation (2.21) it can be seen that a slight decrease in agglomerate size is predicted with an increase in primary particle size. The dependency on d_p arises from the van der Waals force and gravity. The power of −0.051 resulting from size

ratios and fractal dimensions of the steps in the multi-stage agglomerates.

Another model based on multi-stage agglomeration was proposed by de Martín et al. which, for hydrophobic powder, reduces to [41]:

$$d_a = \left(\frac{\hat{N} A_H d_{sa}^{D_1+D_0-5}}{(H_0 + 0.063 d_p)^2 g_{eff} d_p^{D_0-3} \rho_p} \right)^{\frac{1}{D_1}} \tag{2.22}$$

This model is derived by equating the global inter-agglomerate forces to the global drag force [41]. Note that, since drag force is equal to weight force [60, 61], this means that the model is essentially solving $Bo = 1$. When using Equations (2.3) and (2.10) in Equation (2.4), setting Bo = 1, taking $z_{eq} = H_0 + 0.063 d_p$, and substituting Equations (2.23) and (2.24) (assuming k_0 and k_1 to both be constants equal to 1) [41] one finds Equation (2.22), where $\hat{N}$ is a fitting parameter [41].

$$\frac{\rho_{sa}}{\rho_p} = k_0 \cdot \left(\frac{d_{sa}}{d_p} \right)^{D_0-3} \tag{2.23}$$

$$\frac{\rho_a}{\rho_{sa}} = k_1 \cdot \left(\frac{d_a}{d_{sa}} \right)^{D_1-3} \tag{2.24}$$

Note that in the final equation d_a scales with d_p twice; one term is left over from the ratio in density of simple agglomerates and primary particles in Equation (2.10), and the other one comes from the used equation for z_{eq}. Since $D_0 < 3$ it cannot be easily seen what the effect of d_p will be on the predicted d_a. Doing a sensitivity analysis reveals that the denominator grows with an increasing value for d_p and therefore the d_a is predicted to decrease. This will be discussed further in Section 2.5.4.

The model by de Martín and van Ommen (Equation (2.22)) was later modified by Tahmasebpoor et al. to include differences in polarity of materials; [54] this model does however require some empirical data. Tahmasebpoor et al. also proposed that electrostatic forces can play a significant role in the equilibrium size of agglomerates, whereas most found models neglect this force. They try to support their claim with data of fluidized beds where alcohol vapour is introduced, which reduces the repulsive electrostatic force. One could however argue that the introduction of attractive capillary forces during such experiments can also explain the data, without the need to include electrostatics.
In the same paper, Tahmasebpoor et al. propose a simplified model, which does not require data from experiments [54]. Assuming hydrophobic particles, no liq-

uid present, and rewriting the equation, one finds the following equation[1], which can be directly compared to the other discussed models:

$$d_a = \left(\frac{A_H d_{asp}}{4\pi z_0^2 (\rho_a - \rho_f) g} \right)^{\frac{1}{3}} \tag{2.25}$$

where the assumption is made that $\rho_a = \rho_b$, the bulk density of the powder. This equation is a result of equating drag force and the van der Waals force; this approach is once more the same as saying $Bo = 1$ (assuming $\rho_f \ll \rho_a$) and solving for d_a. This is essentially the same as shown in the study by de Martín et al.; [41] the difference in their results stems from the way the van der Waals force is calculated. Tahmasebpoor et al. use Equation (2.9), taking a constant value for H_0, which results in Equation (2.25) being independent of primary particle size completely.

2.5.3. MODELLING MICROPARTICLE AGGLOMERATION

For the prediction of the agglomerate size of powders made up of micro-sized particles, Castellanos et al. proposed a balance equating the shear acting on the agglomerate to the van der Waals forces [145]:

$$\frac{\pi}{6} d_p^3 \rho_p g \left(\frac{d_a}{d_p} \right)^{D_a+2} = \frac{A_H d_p}{24 z_0^2} \tag{2.26}$$

Rewriting Equation (2.26) gives:

$$d_a = \left(\frac{A_h d_p^{D_a}}{4\pi \rho_p g z_0^2} \right)^{\frac{1}{D_a+2}} \tag{2.27}$$

Note that, since D_a has a positive value, this model predicts larger agglomerate sizes with an increase in primary particle size. It can also be seen that for this model single step agglomeration is assumed to take place; agglomerates are directly made up of primary particles.

Mawatari et al. modelled agglomerate size of micro-sized powders in a vibro-fluidized bed [105]. Ignoring the effect of vibration, their model can be used to predict agglomerate sizes for micro-sized particles under unassisted conditions. The model is based on a balance between F_{vdW}, F_D, and F_g; when rewriting it to exclude the influence of vibration their balance reduces to:

[1] Note that Equation (2.25) differs from Eq. 16 in [54], even using the additional assumptions listed here. This is a result of Tahmasebpoor et al. missing a factor of $\frac{\pi}{6}$ in their calculation of the drag force.

$$\frac{A_H}{12z_0^2}\left(1+\frac{A_H}{6\pi z_0^3 \cdot H_r}\right)\cdot d_{asp} = \frac{\pi}{6}d_a^3(\rho_a-\rho_f)g + 3\pi\mu d_a u_{cha}\varepsilon_{cha}^{-3.8} \tag{2.28}$$

where H_r is the hardness of particle, taken to be $10^8 \mathrm{N\,m^{-2}}$ [146], u_{cha} is the superficial gas velocity at which channels are broken, and ε_{cha} is the bed voidage at u_{cha}.

When looking at Equation (2.28) one can see it is derived by balancing F_{vdW} and $F_W + F_{drag}$, using Equation (2.6) and where F_W is corrected for buoyancy. One can also see that the primary particle size is not present in the equation, although it is known that it will influence the value of ρ_a [145]. Furthermore, when comparing Equation (2.28) to Equation (2.26) it can also be seen that the calculation for F_{vdW} differs; Mawatari et al. used an equation for the van der Waals force from Krupp [66, 105], whereas Castellanos et al. used Equation (2.7). Also, Equation (2.28) is set up including both gravity and drag instead of just one of the two. The gravity needs to be overcome by the drag force in order to get the agglomerate to fluidize. When fluidization is taking place the forces are assumed equal; [60, 61] one would therefore expect only one of the two to be present in the equation. Furthermore, the u_{cha} is a function of the cohesiveness of the powder, and therefore, indirectly, of d_p. Since no expression for u_{cha} was given, a sensitivity analysis could only be done with the assumption u_{cha} is constant with respect to d_p. For earlier discussed models the density of the agglomerates was also a function of primary particle size, but Matawari et al. assumed the density to be constant, based on a study by Zhou and Li [105, 106]

2.5.4. EFFECT OF PRIMARY PARTICLE SIZES

Agglomerates are known to be formed by powders containing primary particles from a couple of nanometers up to tens of micrometers [147], the latter sometimes falling in Geldart Type A classification [30]. This means that these agglomerates of larger primary particles fluidize easily whereas the agglomerates made up of smaller primary particles usually do not. Therefore, the primary particle size must influence features of the formed agglomerates, causing the difference in fluidization behaviour. Differences in agglomerate size will be discussed in this section.

In the previous section, we discussed some models to predict agglomerate size based on, among other things, primary particle size. Not all papers specified a range in which their models are thought to be accurate, but when plotting the predicted agglomerate sizes by the models developed for nano-sized primary

particles in the range of 7–40 nm (the range in which the model by de Martín et al. is accurate [41]) their results can be compared. From Figure 2.5 it can be seen that the models differ significantly in predicted agglomerate sizes. Furthermore, it can be seen that, whereas the model by Tahmasebpoor et al. is insensitive with respect to primary particle size, both the model by de Martín and van Ommen and by Valverde et al. predict a decrease in agglomerate size with increased primary particle size, though the slopes of the curves differ significantly.
The same was done for the models developed for agglomerates made up of micro-sized primary particles, shown in Figure 2.6. Here it can be seen that the model by Castellanos et al. predicts an increase in agglomerate size with increasing primary particle size, contrary to the models developed for nano-sized particles. None of the models can be correct throughout the entire size range in which agglomerates are formed. When extrapolating the models for nanoparticles they will end up predicting agglomerate sizes smaller than the primary particle size. Looking at the model by Castellanos et al., it predicts a decrease of agglomerate for smaller primary particles, whereas the value at 10 µm is already lower than the ones predicted by models for nanoparticles. The differences in the found trends are a result of the assumptions made in the models, specifically whether MSA is assumed to take place or not.

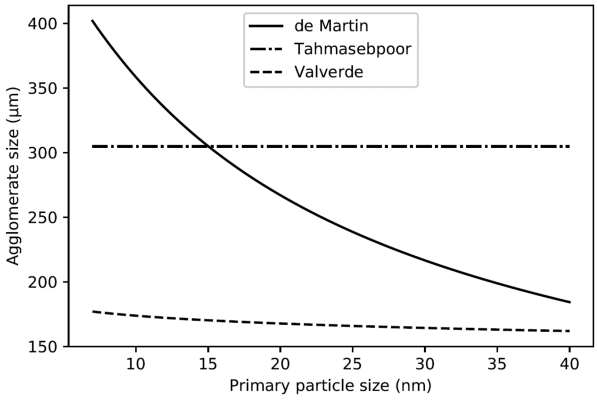


Figure 2.5: Predicted agglomerate size versus primary particle size; using parameters for hydrophobic SiO_2: $A_H = 1.5 \cdot 10^{-19} J$, $z_0 = 4 \cdot 10^{-10} m$, $d_{sa} = 3.5 \cdot 10^{-5} m$, $d_{asp} = 2 \cdot 10^{-7} m$, $\rho_p = 2560 kg/m^3$, $\rho_b = 55 kg/m^3$, $g = 9.81 m/s^2$, $D_0 = 2.6$, $D_1 = 2.3$, $\hat{N} = 1.2$

2.5.5. DISCUSSION

In order to develop a model, making assumptions is inevitable. However, one can argue not all assumptions to be equally valid.
The most common, usually implicit, assumption is that agglomerates are per-

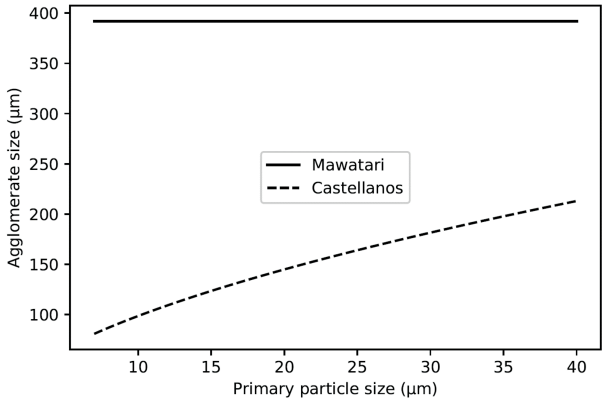


Figure 2.6: Predicted agglomerate size versus primary particle size; using parameters for hydrophobic SiO_2:$A_H = 1.5 \cdot 10^{-19} J$, $z_0 = 4 \cdot 10^{-10} m$, $D_a = 2.5$, $d_{asp} = 2 \cdot 10^{-7} m$, $\rho_p = 2560 kg/m^3$, $\rho_a = 55 kg/m^3$, $\rho_f = 1.25 kg/m^3$, $g = 9.81 m/s^2$,$u_{cha} = 5 \cdot 10^-3 m/s$, $\varepsilon_{cha} = 0.75$, $H_r = 10^8 N/m^2$

fectly spherical. From studies on this subject it is known that the actual sphericity of agglomerates is about 0.7 [127]. This assumption will change the drag force due to an underestimation of $A_\perp$. It will also change the effect of the van der Waals and capillary forces, although it is not easy to say what the effect is exactly.

Another thing to consider is that most models equate attractive forces to repulsive ones to calculate agglomerate size. Furthermore, models tend to use the van der Waals force as the only cohesive force and the drag force, which is equal to the weight force, as the only repulsive one. This means the models are, either explicitly or implicitly, assuming that an equilibrium is reached when the bond number is equal to 1. The result of taking Bo = 1 and solving Equation (2.4) using Equation (2.3) and Equation (2.9) is plotted in Figure 2.7. It can be seen that the solution to this equation falls well within the range of Type A fluidization, whereas one would expect the powder to start fluidizing smoothly at the boundary between C to A already. Rhodes and colleagues proposed that the ratio between inter-agglomerate forces and the buoyant weight is larger than 40 for cohesive particles [148]. Note that, although Rhodes et al. did not use the term, this is the same as saying the Bond number is equal to 40. The solution to Bo = 40 is also plotted in Figure 2.7. It can be seen that this line is reasonably close to the boundary between Type A and type C fluidization, meaning that solving Bo = 40 could give more representative results than solving Bo = 1. This could however change when other inter-particle forces, namely those due to collisions, are taken into account.

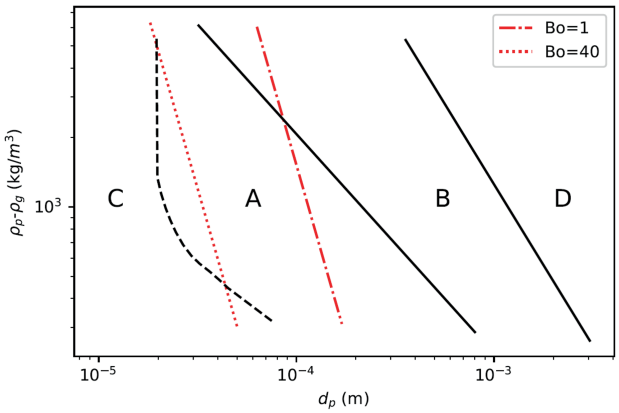


Figure 2.7: Geldart diagram with Bo = 1 plotted in red

One should also realize that the smallest freely moving entities present in the fluidized bed of nanopowders are aggregates, not the primary particles. Realizing that aggregate formation is dominated by production conditions [149], not by particle properties, models based on aggregate features are likely to give more accurate results. Some of the found models did use the primary particle features to predict the aggregate size (often called sub-agglomerates), however, the properties of aggregates are a result of the production process and cannot be easily predicted based on primary particle properties alone.

Another shortcoming is the fact that, by the nature of the way most models are derived, they are only applicable in a certain range of particle sizes. Given that models are typically validated by experimental data in a narrow size range, the actual range in which the model is accurate is usually unknown. Limited applicability is obvious for models which assume MSA to take place, since they predict that an increase in d_p leads to a decrease in agglomerate size, meaning at some point the predicted agglomerate is predicted to be smaller than the primary particle, which is a non-physical result. The regime in which the MSA assumption is valid is not well identified. An ideal model, predicting agglomerate sizes based on material properties, particle size, and fluidization conditions, should include a transition between single and multi-stage agglomeration based on a driving force. The underlying mechanism of MSA is, however, currently not fully understood. More research into this phenomenon is crucial for the further development of accurate models that are applicable over a larger size range.

Finally, in a balance, one equates attractive forces to repulsive ones, which implicitly assumes that an equilibrium between the forces exists in the bed. Given the fact that agglomerate sizes are known to change over time, as discussed in

Section 2.4.2, it can not be said that an equilibrium is present. This makes these balances inherently disputable for the prediction of agglomerate size.

2.6. CONCLUSIONS AND OUTLOOK

As shown in this study, the fluidization of cohesive powders is complex and contains many sub-fields of research. Though much is known, there are still fundamental issues that require more insight for further development of the field.
Current classifications of powders, although useful, have limited reliability when it comes to predicting the fluidization behaviour of cohesive powders. As shown in this work, several different behaviours are found for Type C powders alone. Furthermore, because cohesive powders form agglomerates, it is unclear whether the agglomerate properties or those of the primary particle should be used for predicting the fluidization behaviour. This is complicated even further when noting that the bed contains a distribution of agglomerate sizes, segregated over the bed height.
When it comes to predicting the sizes of formed agglomerates, multiple models have been proposed. They are however inconsistent with one another and at this time it cannot be said which are the more representative ones. The basic approach of balances to estimate agglomerate size is arguably flawed since this assumes an equilibrium to be present in the bed, whereas it is known that agglomerate sizes tend to change over time.
Overall it was found that micro- and nano-sized powders do indeed have some distinct characteristics and it is, to an extent, justified to treat them as such. The same inter-particle forces are dominant for both types of powders. The main difference is found in the way the powders form agglomerates: nano-sized particles form multi-stage agglomerates, whereas micro-sized ones do not. This results in differences in the way these powders fluidize too.
To push the field of cohesive powder fluidization further, certain topics require more research. First of all, consensus should be reached on how to measure agglomerate sizes accurately. This will allow for data to be compared between studies as well as provide a strong basis for model validation. In order to come to a standard for size measurements, the dependency of agglomerate size on fluidization time should be studied rigorously too. Secondly, the phenomenon of MSA requires a fundamental understanding to develop models to predict agglomerate sizes for nanoparticles. This will also open the door for the development of generalized models which predict agglomerate sizes of powders throughout larger size ranges including both nano- and microparticles.

REFERENCES

[1] A. Weir, P. Westerhoff, L. Fabricius, K. Hristovski, and N. von Goetz, *Titanium dioxide nanoparticles in food and personal care products,* Environmental Science and Technology **46**, 2242 (2012).

[2] S. Dekkers, H. Bouwmeester, P. M. Bos, R. J. Peters, A. G. Rietveld, and A. G. Oomen, *Knowledge gaps in risk assessment of nanosilica in food: evaluation of the dissolution and toxicity of different forms of silica,* Nanotoxicology **7**, 367 (2013).

[3] Y. Wang, L. Yuan, C. Yao, L. Ding, C. Li, J. Fang, K. Sui, Y. Liu, and M. Wu, *A combined toxicity study of zinc oxide nanoparticles and vitamin c in food additives,* Nanoscale **6**, 15333 (2014).

[4] S. Lehmann, E. U. Hartge, A. Jongsma, I. M. deLeeuw, F. Innings, and S. Heinrich, *Fluidization characteristics of cohesive powders in vibrated fluidized bed drying at low vibration frequencies,* Powder Technology **357**, 54 (2019), expanding Boundaries in Particle Technology: A select collision of papers from the World Congress in Particle Technology VIII.

[5] A. C. Burdușel, O. Gherasim, A. Grumezescu, L. Mogoantă, A. Ficai, and E. Andronescu, *Biomedical applications of silver nanoparticles: An up-to-date overview,* Nanomaterials **8**, 681 (2018).

[6] N. Aahin, R. Anwar, T. Twari, D. Kabir, A. Sajid, B. Mathew, S. Uddin, L. Aleya, and M. Abdel-Daim, *Nanoparticles and its biomedical applications in health and diseases: special focus on drug delivery,* Environ Sci Pollut Res **27** (2019), 10.1007/s11356-019-05211-0.

[7] H. Lu, J. Wang, M. Stoller, T. Wang, Y. Bao, and H. Hao, *An overview of nanomaterials for water and wastewater treatment,* Advances in Materials Science and Engineering **2016**, 1 (2016).

[8] S. Tesh and T. Scott, *Nano-composites for water remediation: A review,* Advanced Materials **26** (2014), 10.1002/adma.201401376.

[9] L. Chen, E. Hwang, and J. Zhang, *Fluorescent nanobiosensors for sensing glucose,* Sensors **18**, 1440 (2018).

[10] V. Khanna, *Nanoparticle-based sensors,* Defence Science Journal **58 (2018)** (2008), 10.14429/dsj.58.1683.

[11] N. A. Lah, M. N. Zubir, and M. A. Samykano, *Chapter 20 - engineered nanomaterial in electronics and electrical industries,* in *Handbook of Nanomaterials for Industrial Applications*, Micro and Nano Technologies, edited by C. Mustansar Hussain (Elsevier, 2018) pp. 324 – 364.

[12] I. Matsui, *Nanoparticles for electronic device applications: A brief review,* Journal of Chemical Engineering of Japan - J CHEM ENG JPN **38**, 535 (2005).

[13] J. R. Van Ommen, J. M. Valverde, and R. Pfeffer, *Fluidization of nanopowders: a review,* Journal of Nanoparticle Research **14** (2012), 10.1007/s11051-012-0737-4.

[14] F. Raganati, R. Chirone, and P. Ammendola, *Gas–solid fluidization of cohesive powders,* Chemical Engineering Research and Design **133**, 347 (2018).

[15] J. R. Grace, *Introduction, history, and applications,* in *Essentials of Fluidization Technology* (John Wiley and Sons, Ltd, 2020) Chap. 1, pp. 1–9.

[16] J. G. Yates and P. Lettieri, *Introduction,* in *Fluidized-Bed Reactors: Processes and Operating Conditions* (Springer International Publishing, Cham, 2016) pp. 1–21.

[17] J. Wang, S. Wu, X.-K. Suo, and H. Liao, *Chapter 2 - the processes for fabricating nanopowders,* in *Advanced Nanomaterials and Coatings by Thermal Spray*, Micro and Nano Technologies, edited by G.-J. Yang and X. Suo (Elsevier, 2019) pp. 13–25.

[18] S. Kang, M. Herzberg, D. F. Rodrigues, and M. Elimelech, *Antibacterial effects of carbon nanotubes: Size does matter!* Langmuir **24**, 6409 (2008).

[19] Y. Wang, L. Guohua, H. yu, and G. Gu, *The large-scale production of carbon nanotubes in a nano-agglomerate fluidized- bed reactor,* Chemical Physics Letters **364**, 568 (2002).

[20] A. P. Rood and R. M. Scott, *Size distributions of chrysottile asbestos in a friction products factory as determined by transmission electron microscopy,* The Annals of Occupational Hygiene **33**, 583 (1989).

[21] M. Harper, E. G. Lee, S. S. Doorn, and O. Hammond, *Differentiating non-asbestiform amphibole and amphibole asbestos by size characteristics,* Journal of Occupational and Environmental Hygiene **5**, 761 (2008).

[22] EU, *Commission recommendation of 18 october 2011 on the definition of nanomateria,* Official Journal of the European Union (2011).

[23] O. Amjadi, M. Tahmasebpoor, and H. Aghdasinia, *Fluidization behaviour of cohesive $Ca(OH)_2$ powders mixed with hydrophobic silica nanoparticles: Coverage quality effect,* Chemical Engineering and Technology **42**, 287 (2019).

[24] H. Liu, Y. Li, and Q. Guo, *Fluidization quality improvement for cohesive particles by fine powder coating,* Industrial and Engineering Chemistry Research **45**, 1805 (2006).

[25] L. Song, T. Zhou, and J. Yang, *Fluidization behavior of nano-particles by adding coarse particles,* Advanced Powder Technology **20**, 366 (2009).

[26] H. Mo, B. Xu, C. Luo, T. Zhou, and J. Kong, *Aggregation and fragmentation of agglomerates in a fluidized bed of mixed nanoparticles by adding fcc coarse particles,* Chinese Journal of Chemical Engineering **26**, 2531 (2018).

[27] J. R. Grace and G. Sun, *Influence of particle size distribution on the performance of fluidized bed reactors,* The Canadian Journal of Chemical Engineering **69**, 1126 (1991).

[28] G. Khoe, T. Ip, and J. Grace, *Rheological and fluidization behaviour of powders of different particle size distribution,* Powder Technology **66**, 127 (1991).

[29] R. Beetstra, J. Nijenhuis, N. Ellis, and J. R. van Ommen, *The influence of the particle size distribution on fluidized bed hydrodynamics using high-throughput experimentation,* AIChE Journal **55**, 2013 (2009).

[30] D. Geldart, *Types of gas fluidization,* Powder Technology **7**, 285 (1973).

[31] J. Valverde and A. Castellanos, *Extension of geldart's diagram to fluidizable fine and ultrafine particles,* AIP Conference Proceedings **1145**, 977 (2009).

[32] S. Morooka, K. Kusakabe, A. Kobata, and Y. Kato, *Fluidization state of ultrafine powders,* Journal of Chemical Engineering of Japan **21**, 41 (1988).

[33] A. Pacek and A. Nienow, *Fluidisation of fine and very dense hardmetal powders,* Powder Technology **60**, 145 (1990).

[34] W. Yao, G. Guangsheng, W. Fei, and W. Jun, *Fluidization and agglomerate structure of SiO_2 nanoparticles,* Powder Technology **124**, 152 (2002).

[35] C. Zhu, Q. Yu, R. Dave, and R. Pfeffer, *Gas fluidization characteristics of nanoparticle agglomerates,* AIChE Journal **51**, 426 (2005).

[36] J. R. Grace, *Contacting modes and behaviour classification of gas—solid and other two-phase suspensions,* The Canadian Journal of Chemical Engineering **64**, 353 (1986).

[37] W.-C. Yang, *Modification and re-interpretation of geldart's classification of powders,* Powder Technology **171**, 69 (2007).

[38] W. R. Goossens, *Classification of fluidized particles by archimedes number,* Powder Technology **98**, 48 (1998).

[39] N. Mostoufi, *Revisiting classification of powders based on interparticle forces,* Chemical Engineering Science **229**, 116029 (2020).

[40] S. Matsuda, H. Hatano, T. Muramoto, and A. Tsutsumi, *Modeling for size reduction of agglomerates in nanoparticles fluidization,* AIChE Journal **50**, 2763 (2004).

[41] L. de Martín and J. R. van Ommen, *A model to estimate the size of nanoparticle agglomerates in gas solid fluidized beds,* Journal of Nanoparticle Research **15** (2013), 10.1007/s11051-013-2055-x.

[42] H. Liu, L. Zhang, T. Chen, S. Wang, Z. Han, and S. Wu, *Experimental study on the fluidization behaviors of the superfine particles,* Chemical Engineering Journal **262**, 579 (2015).

[43] J. M. Valverde, M. A. S. Quintanilla, A. Castellanos, D. Lepek, J. Quevedo, R. N. Dave, and R. Pfeffer, *Fluidization of fine and ultrafine particles using nitrogen and neon as fluidizing gases,* AIChE Journal **54**, 86 (2008).

[44] S. V. Sokolov, E. Kätelhön, and R. G. Compton, *A thermodynamic view of agglomeration,* The Journal of Physical Chemistry C **119**, 25093 (2015).

[45] A. Fabre, A. Clemente, F. Balas, M. P. Lobera, J. Santamaría, M. T. Kreutzer, and J. R. van Ommen, *Correction: Entrainment of nanosized clusters from a nanopowder fluidized bed,* Environ. Sci.: Nano **4**, 1591 (2017).

[46] X. Zhang, Y. Zhou, and J. Zhu, *Enhanced fluidization of group a particles modulated by group c powder,* Powder Technology **377**, 684 (2021).

[47] A. Kamranian Marnani, A. Bück, S. Antonyuk, B. van Wachem, D. Thévenin, and J. Tomas, *The effect of the presence of very cohesive geldart c ultra-fine particles on the fluidization of geldart a fine particle beds,* Processes (2019), 10.3390/pr7010035.

[48] T. Zhou and H. Li, *Effects of adding different size particles on fluidization of cohesive particles,* Powder Technology **102**, 215 (1999).

[49] Z. Wang, M. Kwauk, and H. Li, *Fluidization of fine particles,* Chemical Engineering Science **53**, 377 (1998).

[50] S. Kaliyaperumal, S. Barghi, L. Briens, S. Rohani, and J. Zhu, *Fluidization of nano and submicron powders using mechanical vibration,* Particuology **9**, 279 (2011).

[51] C. Mogre, A. U. Thakurdesai, J. R. van Ommen, and S. Salameh, *Long-term fluidization of titania nanoparticle agglomerates,* Powder Technology **316**, 441 (2017), fluidization for Emerging Green Technologies.

[52] E. Hotze, T. Phenrat, and G. Lowry, *Nanoparticle aggregation: Challenges to understanding transport and reactivity in the environment,* Journal of environmental quality **39**, 1909 (2010).

[53] K. Rietema, *Theoretical Derivation of Interparticle Forces. In: The Dynamics of Fine Powders* (Springe - Dordrecht, 1991).

[54] M. Tahmasebpoor, R. Ghasemi Seif Abadi, Y. Rahimvandi Noupoor, and P. Badamchizadeh, *Model based on electrostatic repulsion and hydrogen bond forces to estimate the size of nanoparticle agglomerates in fluidization,* Industrial and Engineering Chemistry Research **55**, 12939 (2016).

[55] J. Seville, C. Willett, and P. Knight, *Interparticle forces in fluidisation: a review,* Powder Technology **113**, 261 (2000), neptis Symposium on Fluidization- Present and Future.

[56] M. Tahmasebpoor, L. de Martín, M. Talebi, N. Mostoufi, and J. R. van Ommen, *The role of the hydrogen bond in dense nanoparticle–gas suspensions,* Phys. Chem. Chem. Phys. **15**, 5788 (2013).

[57] S. Leroch and M. Wendland, *Influence of capillary bridge formation onto the silica nanoparticle interaction studied by grand canonical monte carlo simulations,* Langmuir : the ACS journal of surfaces and colloids **29** (2013), 10.1021/la402002f.

[58] S. C. Endres, L. C. Ciacchi, and L. Mädler, *A review of contact force models between nanoparticles in agglomerates, aggregates, and films,* Journal of Aerosol Science **153**, 105719 (2021).

[59] M. Capece, R. Ho, J. Strong, and P. Gao, *Prediction of powder flow performance using a multi component granular bond number,* Powder Technology **286**, 561 (2015).

[60] J. Chaouki, C. Chavarie, D. Klvana, and G. Pajonk, *Effect of interparticle forces on the hydrodynamic behaviour of fluidized aerogels,* Powder Technology **43**, 117 (1985).

[61] J. Shabanian, R. Jafari, and J. Chaouki, *Fluidization of ultrafine powders,* International Review of Chemical Engineering **4**, 16 (2012).

[62] P. Foscolo and L. Gibilaro, *A fully predictive criterion for the transition between particulate and aggregate fluidization,* Chemical Engineering Science **39**, 1667 (1984).

[63] M. R. Tamadondar, R. Zarghami, K. Boutou, M. Tahmasebpoor, and N. Mostoufi, *Size of nanoparticle agglomerates in fluidization,* The Canadian Journal of Chemical Engineering **94**, 476 (2016), https://onlinelibrary.wiley.com/doi/pdf/10.1002/cjce.22422 .

[64] O. Walton, *Review of adhesion fundamentals for micron-scale particles,* KONA Powder and Particle Journal **26**, 129 (2008).

[65] J. Israelachvili, *Intermolecular and Surface Forces* (Academic Press, 2011).

[66] H. Krupp, *Particle adhesion theory and experiment,* Advances in Colloid and Interface Science **1**, 111 (1967).

[67] K. Jiang and P. Pinchuk, *Temperature and size-dependent hamaker constants for metal nanoparticles,* Nanotechnology **27**, 345710 (2016).

[68] J. R. van Ommen and A. Goulas, *Atomic layer deposition on particulate materials,* Materials Today Chemistry **14**, 100183 (2019).

[69] R. Chirone, M. Poletto, D. Barletta, and P. Lettieri, *The effect of temperature on the minimum fluidization conditions of industrial cohesive particles,* Powder Technology **362**, 307 (2020).

[70] P. Lettieri and D. Macrì, *Effect of process conditions on fluidization,* KONA Powder and Particle Journal **33**, 86 (2016).

[71] L. Zhou, F. Zhang, H. Kage, and Y. Mawatari, *A model for estimating agglomerate sizes of nonmagnetic nanoparticles in magnetic fluidized beds,* Korean Journal of Chemical Engineering **30** (2013), 10.1007/s11814-012-0170-5.

[72] S. Matsuda, H. Hatano, and A. Tsutsumi, *Ultrafine particle fluidization and its application to photocatalytic NOx treatment,* Chemical Engineering Journal **82**, 183 (2001).

[73] M. Espín, J. M. Valverde, M. Quintanilla, and A. Castellanos, *Electromechanics of fluidized beds of nanoparticles,* Physical review. E, Statistical, nonlinear, and soft matter physics **79**, 011304 (2009).

[74] Y. I. Rabinovich, J. J. Adler, A. Ata, R. K. Singh, and B. M. Moudgil, *Adhesion between nanoscale rough surfaces: I. role of asperity geometry,* Journal of Colloid and Interface Science **232**, 10 (2000).

[75] K. Gong, L. Chen, H. Xia, H. Dai, X. Li, L. Sun, W. Kong, and K. Liu, *Driving forces of disaggregation and reaggregation of peanut protein isolates in aqueous dispersion induced by high-pressure microfluidization,* International Journal of Biological Macromolecules **130**, 915 (2019).

[76] P. Liu, C. Q. LaMarche, K. M. Kellogg, and C. M. Hrenya, *Dense versus dilute fluidization of cohesive particles: Reverse sensitivity to friction and restitution coefficient,* Physical Review Fluids **2**, 054302 (2017).

[77] H. C. H. Rumpf, *Zur theorie der zugfestigkeit von agglomeraten bei kraftübertragung an kontaktpunkten,* Chemie Ingenieur Technik **42**, 538 (1970).

[78] C. Q. LaMarche, S. Leadley, P. Liu, K. M. Kellogg, and C. M. Hrenya, *Method of quantifying surface roughness for accurate adhesive force predictions,* Chemical Engineering Science **158**, 140 (2017).

[79] J. E. Galvin and S. Benyahia, *The effect of cohesive forces on the fluidization of aeratable powders,* AIChE Journal **60**, 473 (2014).

[80] K. L. Johnson, K. Kendall, A. D. Roberts, and D. Tabor, *Surface energy and the contact of elastic solids,* Proceedings of the Royal Society of London. A. Mathematical and Physical Sciences **324**, 301 (1971).

[81] J. Yang, C.-Y. Wu, and M. Adams, *Three-dimensional dem–cfd analysis of air-flow-induced detachment of api particles from carrier particles in dry powder inhalers,* Acta Pharmaceutica Sinica B **4**, 52 (2014).

[82] J. Yang, C.-Y. Wu, and M. Adams, *Dem analysis of the effect of particle–wall impact on the dispersion performance in carrier-based dry powder inhalers,* International Journal of Pharmaceutics **487**, 32 (2015).

[83] M. W. Weber, D. K. Hoffman, and C. M. Hrenya, *Discrete-particle simulations of cohesive granular flow using a square-well potential,* Granular Matter **6**, 239 (2004).

[84] P. Liu, C. Q. LaMarche, K. M. Kellogg, and C. M. Hrenya, *A square-force cohesion model and its extraction from bulk measurements,* AIChE Journal **64**, 2329 (2018).

[85] S. Salameh, M. A. van der Veen, M. Kappl, and J. R. van Ommen, *Contact forces between single metal oxide nanoparticles in gas-phase applications and processes,* Langmuir **33**, 2477 (2017).

[86] H.-J. Butt and M. Kappl, *Normal capillary forces,* Advances in Colloid and Interface Science **146**, 48 (2009).

[87] Y. Li, J. Hu, and K. Bai, *Capillary and van der waals force between microparticles with different sizes in humid air,* Journal of Adhesion Science and Technology **30**, 1 (2015).

[88] O. Pakarinen, A. Foster, M. Paajanen, T. Kalinainen, J. Katainen, I. Makkonen, J. Lahtinen, and R. Nieminen, *Towards an accurate description of the capillary force in nanoparticle-surface interactions,* Modelling and Simulation in Materials Science and Engineering **13**, 1175 (2005).

[89] M. Dörmann and H.-J. Schmid, *Distance-dependency of capillary bridges in thermodynamic equilibrium,* Powder Technology **312**, 175 (2017).

[90] S. Salameh, J. Schneider, J. Laube, A. Alessandrini, P. Facci, J. W. Seo, L. Ciacchi, and L. Mädler, *Adhesion mechanisms of the contact interface of TiO_2 nanoparticles in films and aggregates,* Langmuir : the ACS journal of surfaces and colloids **28**, 11457 (2012).

[91] S. Plimpton, *Fast parallel algorithms for short range molecular dynamics,* Journal of Computational Physics **117**, 1 (1995).

[92] V. S. Sutkar, N. G. Deen, J. T. Padding, J. Kuipers, V. Salikov, B. Crüger, S. Antonyuk, and S. Heinrich, *A novel approach to determine wet restitution coefficients through a unified correlation and energy analysis,* AIChE Journal **61**, 769 (2015).

[93] B. Crüger, V. Salikov, S. Heinrich, S. Antonyuk, V. S. Sutkar, N. G. Deen, and J. Kuipers, *Coefficient of restitution for particles impacting on wet surfaces: An improved experimental approach,* Particuology **25**, 1 (2016).

[94] P. Darabi, K. Pougatch, M. Salcudean, and D. Grecov, *Dem investigations of fluidized beds in the presence of liquid coating,* Powder Technology **214**, 365 (2011).

[95] M. Farshchi-Tabrizi, M. Kappl, Y. Cheng, J. Gutmann, and H.-J. Butt, *On the adhesion between fine particles and nanocontacts: An atomic force microscope study,* Langmuir **22**, 2171 (2006), pMID: 16489804.

[96] H.-J. Butt and M. Kappl, *Surface and Interfacial Forces*, 2nd ed. (WILEY-VCH, 2010).

[97] N. V. Zarate, A. J. Harrison, J. D. Litster, and S. P. Beaudoin, *Effect of relative humidity on onset of capillary forces for rough surfaces,* Journal of Colloid and Interface Science **411**, 265 (2013).

[98] H.-J. Butt, W. J. P. Barnes, A. del Campo, M. Kappl, and F. Schönfeld, *Capillary forces between soft, elastic spheres,* Soft Matter **6**, 5930 (2010).

[99] T. Gröger, U. Tüzün, and D. M. Heyes, *Modelling and measuring of cohesion in wet granular materials,* Powder Technology **133**, 203 (2003).

[100] R. Pfeffer and J. A. Queyedo, *Systems and methods for reducing electrostatic charge in a fluidized bed,* (U.S. Patent 7905433, 2011).

[101] J. Peart, *Powder electrostatics: Theory, techniques and applications,* KONA Powder and Particle Journal **19**, 34 (2001).

[102] A. Bailey, *Charging of solids and powders,* Journal of Electrostatics **30**, 167 (1993).

[103] A. Bailey, *Electrostatic phenomena during powder handling,* Powder Technology **37**, 71 (1984).

[104] J. Valverde, M. Quintanilla, M. Espín, and A. Castellanos, *Nanofluidization electrostatics,* Physical review. E, Statistical, nonlinear, and soft matter physics **77**, 031301 (2008).

[105] Y. Mawatari, T. Ikegami, Y. Tatemoto, and K. Noda, *Prediction of agglomerate size for fine particles in vibro-fluidized bed,* Journal of Chemical Engineering of Japan **36**, 277 (2003).

[106] T. Zhou and H. Li, *Estimation of agglomerate size for cohesive particles during fluidization,* Powder Technology **101**, 57 (1999).

[107] Y. Horio, M.; Iwadate, *The prediction of sizes of agglomerates formed in fluidized beds,* Proceedings of the 5th World Congress of Chemical Engineering: 2nd International Particle Technology Forum; American Institute of Chemical Engineers: San Diego, California **V**, 571 (1996).

[108] X. Jiang, Q. Zeng, C. Chen, and A. Yu, *Self assembly of particles: Some thoughts and comments,* J. Mater. Chem. **21**, 16797 (2011).

[109] R. A. Bowling, *A theoretical review of particle adhesion,* in *Particles on Surfaces 1: Detection, Adhesion, and Removal*, edited by K. L. Mittal (Springer US, Boston, MA, 1988) pp. 129–142.

[110] J. Seville, T. U., and R. Clift, *Processing of particulate solids,* (Springer NL, 1997) pp. 120–125.

[111] B. van Wachem and S. Sasic, *Derivation, simulation and validation of a cohesive particle flow cfd model,* AIChE Journal **54**, 9 (2008).

[112] L. Niu, Z. Chu, M. Cai, and M. Liu, *Modified force balance model of estimating agglomerate sizes in a gas–solid fluidized bed,* Industrial and Engineering Chemistry Research **58**, 8472 (2019).

[113] A. A. Motlagh, J. R. Grace, M. Salcudean, and C. Hrenya, *New structure-based model for eulerian simulation of hydrodynamics in gas–solid fluidized beds of geldart group "a" particles,* Chemical Engineering Science **120**, 22 (2014).

[114] A. Teleki, R. Wengeler, L. Wengeler, H. Nirschl, and S. Pratsinis, *Distinguishing between aggregates and agglomerates of flame-made TiO_2 by high-pressure dispersion,* Powder Technology **181**, 292 (2008).

[115] C. Nam, R. Pfeffer, R. Dave, and S. Sundaresan, *Aerated vibrofluidization of silica nanoparticles,* AIChE Journal **50**, 1776 (2004).

[116] L. F. Hakim, S. M. George, and A. W. Weimer, *Conformal nanocoating of zirconia nanoparticles by atomic layer deposition in a fluidized bed reactor,* Nanotechnology **16**, S375 (2005).

[117] G. P. Cherepanov, *Physics of sintering,* in *Methods of Fracture Mechanics: Solid Matter Physics* (Springer Netherlands, Dordrecht, 1997) pp. 84–123.

[118] A. Gutsch, M. Krämer, G. Michael, H. Mühlenweg, M. Pridöhl, and G. Zimmermann, *Gas-phase production of nanoparticles,* KONA Powder and Particle Journal **20**, 24 (2002).

[119] F. E. Kruis, K. A. Kusters, S. E. Pratsinis, and B. Scarlett, *A simple model for the evolution of the characteristics of aggregate particles undergoing coagulation and sintering,* Aerosol Science and Technology **19**, 514 (1993).

[120] D. Walter, *Primary particles – agglomerates – aggregates,* in *Nanomaterials* (John Wiley and Sons, Ltd, 2013) Chap. 1.1, pp. 9–24.

[121] G. D. Ulrich and N. S. Subramanian, *3. coalescence as a rate-controlling process,* Combustion Science and Technology **17**, 119 (1977).

[122] M.-G. Li, C.-J. Sun, S.-H. Gau, and C.-J. Chuang, *Effects of wet ball milling on lead stabilization and particle size variation in municipal solid waste incinerator fly ash,* Journal of hazardous materials **174**, 586 (2009).

[123] L. Wang, S. Liu, Y. Hou, S. Lang, C. Wang, and D. Zhang, *Changes in particle size, structure, and physicochemical properties of potato starch after jet-milling treatments,* Journal of Food Processing and Preservation **44**, e14569 (2020).

[124] R. Sarrate, J. R. Ticó, M. Miñarro, C. Carrillo, A. Fàbregas, E. García-Montoya, P. Pérez-Lozano, and J. M. Suñé-Negre, *Modification of the morphology and particle size of pharmaceutical excipients by spray drying technique,* Powder Technology **270**, 244 (2015).

[125] J. Toro-Sierra, J. Schumann, and U. Kulozik, *Impact of spray-drying conditions on the particle size of microparticulated whey protein fractions,* Dairy Science and Technology **93** (2013), 10.1007/s13594-013-0124-7.

[126] S. S. Ali, A. Arsad, and M. Asif, *Effect of modified inlet flow strategy on the segregation phenomenon in pulsed fluidized bed of ultrafine particles: A collapse bed study,* Chemical Engineering and Processing - Process Intensification **159**, 108243 (2021).

[127] X. Wang, V. Palero, J. Soria, and M. Rhodes, *Laser-based planar imaging of nano-particle fluidization: Part 1—determination of aggregate size and shape,* Chemical Engineering Science **61**, 5476 (2006).

[128] J. Quevedo and R. Pfeffer, *In situ measurements of gas fluidized nanoagglomerates,* Industrial and Engineering Chemistry Research **49** (2010), 10.1021/ie9015446.

[129] L. de Martín, J. Sánchez-Prieto, F. Hernández-Jiménez, and J. R. van Ommen, *A settling tube to determine the terminal velocity and size distribution of fluidized nanoparticle agglomerates,* Journal of Nanoparticle Research **16** (2014), 10.1007/s11051-013-2183-3.

[130] R. Hong, J. Ding, and H. Li, *Fluidization of fine powders in fluidized beds with an upward or a downward air jet,* China Particuology **3**, 181 (2005).

[131] J. R. van Ommen, D. King, A. Weimer, R. Pfeffer, and B. van Wachem, *Experiments and modelling of micro-jet assisted fluidization of nanoparticles,* The 13th International Conference on Fluidization (2010).

[132] H. Nasri Lari, J. Chaouki, and J. R. Tavares, *De-agglomeration of nanoparticles in a jet impactor-assisted fluidized bed,* Powder Technology **316**, 455 (2017), fluidization for Emerging Green Technologies.

[133] J. Quevedo, A. Omosebi, and R. Pfeffer, *Fluidization enhancement of agglomerates of metal oxide nanopowders by microjets,* AIChE Journal **56**, 1456 (2009).

[134] Q. Guo, H. Liu, W. Shen, X. Yan, and R. Jia, *Influence of sound wave characteristics on fluidization behaviors of ultrafine particles,* Chemical Engineering Journal **119**, 1 (2006).

[135] E. AL-Ghurabi, M. Shahabuddin, N. Siva Kumar, and M. Asif, *Deagglomeration of ultrafine hydrophilic nanopowder using low-frequency pulsed fluidization,* Nanomaterials **10**, 388 (2020).

[136] S. Ali, E. AL-Ghurabi, A. Ajbar, Y. Mohammed, M. Boumaza, and M. Asif, *Effect of frequency on pulsed fluidized beds of ultrafine powders,* Journal of Nanomaterials **2016**, 1 (2016).

[137] S. S. Ali and M. Asif, *Fluidization of nano-powders: Effect of flow pulsation,* Powder Technology **225**, 86 (2012).

[138] F. Zhang, D. La Zara, F. Sun, M. J. Quayle, G. Petersson, S. Folestad, and J. R. van Ommen, *Fluidization of fine lactose for dry powder inhalation: A comparison of assisting methods,* The Canadian Journal of Chemical Engineering **99**, 1696 (2021).

[139] L. d. Martín, W. G. Bouwman, and J. R. van Ommen, *Multidimensionality in fluidized nanopowder agglomerates,* AIP Conference Proceedings **1542**, 82 (2013).

[140] A. Castellanos, J. M. Valverde, and M. A. S. Quintanilla, *Aggregation and sedimentation in gas fluidized beds of cohesive powders,* Phys. Rev. E **64**, 041304 (2001).

[141] J. Quevedo, R. Pfeffer, Y. Shen, R. Dave, H. Nakamura, and S. Watano, *Fluidization of nanoagglomerates in a rotating fluidized bed,* AIChE Journal **52** (2006), 10.1002/aic.10826.

[142] J. M. Valverde and A. Castellanos, *A modified richardson–zaki equation for fluidization of geldart b magnetic particles,* Powder Technology **181**, 347 (2008).

[143] M. A. S. Quintanilla, J. M. Valverde, M. J. Espin, and A. Castellanos, *Electrofluidization of silica nanoparticle agglomerates,* Industrial and Engineering Chemistry Research **51**, 531 (2012).

[144] J. M. Valverde and A. Castellanos, *Fluidization, bubbling and jamming of nanoparticle agglomerates,* Chemical Engineering Science **62**, 6947 (2007).

[145] A. Castellanos, J. M. Valverde, and M. Quintanilla, *Physics of compaction of fine cohesive particles,* Physical Review Letters **94**, 075501 (2005).

[146] O. Molerus, *Interpretation of geldart's type a, b, c and d powders by taking into account interparticle cohesion forces,* Powder Technology **33**, 81 (1982).

[147] M. Horio and H. Kuroki, *Three-dimensional flow visualization of dilutely dispersed solids in bubbling and circulating fluidized beds,* Chemical Engineering Science **49**, 2413 (1994).

[148] X. Wang, F. Rahman, and M. Rhodes, *Nanoparticle fluidization and geldart's classification,* Chemical Engineering Science **62**, 3455 (2007), frontier of Chemical Engineering - Multiscale Bridge between Reductionism and Holism.

[149] H. Barthel, L. Rösch, and J. Weis, *Fumed silica - production, properties, and applications,* in *Organosilicon Chemistry II* (John Wiley and Sons, Ltd, 1995) Chap. 91, pp. 761–778.

3

On the structure of nanoparticle clusters: effects of long-range interactions

We hypothesize that the differences in agglomerates formed by micro- and nanoparticles, as identified in Chapter 2, may be caused by the primary aggregate structures formed by nanoparticles during their production. This chapter takes an initial step toward (dis)proving this hypothesis. Using a 3D model we demonstrate how long-range forces influence the properties of nanoparticle aggregates. Furthermore, we show that these effects cannot be adequately recreated by 2D models, commonly used in similar studies.

This article has been published as "On the structure of nanoparticle clusters: effects of long-range interactions" by R. Kamphorst, M.F. Theisen, A.D. Bordoloi, S. Salameh, G.M.H. Meesters and J.R. van Ommen, Physical Chemistry Chemical Physics (2025)

The fractal structure of aggregates consisting of primary nanoparticles naturally arises during their synthesis. While typically considered to be a fully stochastic process, we suspect long-range interactions, in particular van der Waals forces, to induce an active pull on particles, altering the clustering process. Using an off-grid 3D model, we show that an active pull decreases the density and fractal dimension of formed clusters. These findings could not be reproduced by 2D models, which underestimate screening effects. Additionally, we determined the range within which van der Waals forces dominate the aggregation process.

3.1. INTRODUCTION

The famous artworks in the Chauvet Cave, drawn in charcoal, suggest intentional material production by pyrolysis dating back to at least 30,000 BCE, in the Upper Paleolithic. The first evidence of systematic particle production by pyrolysis appears around 1500 BCE with the manufacture of carbon black, which was used as a pigment [1]. However unintentional, this also marks the first large scale production of nanoparticles. Driven by the increasing interest in nanoparticles, the field has flourished over the past decades, expanding its repertoire to include a diverse array of materials with versatile applications, including photoelectric devices [2, 3], construction materials [4–6] and medicine [7, 8]. Most of these applications rely on the high specific surface area and low density of nanoparticle structures.

During the production of nanoparticles by pyrolysis, a precursor liquid is atomized at a high temperature, forming nano-sized droplets, which solidify upon cooling down, forming the primary nanoparticles [9]. In a typical modern aerosol-based nanoparticle manufacturing setup pyrolysis is performed in a flame reactor, usually enriched with oxygen, methane or hydrogen [10, 11]. The macro-properties, such as bulk density and surface area, of produced nanopowders arise from their multi-scale structure. While in the flame, exact droplet size is subject to process parameters, but is typically found in the range of 5–50 nm [12]. Outside of the flame, the temperature decreases, halting coalescence and making aggregation by sintering, where primary particles stick together due to surface diffusion, the dominant growth mechanism. When cooled to beyond the point where sintering occurs, agglomeration, induced by van der Waals forces, takes over as the main growth mechanism. The initially formed agglomerates are often referred to as 'simple agglomerates', as, upon further handling, they themselves can form even larger clusters called 'complex agglomerates' [13, 14]. Aggregate sizes typically span from 100 nm to 1 µm, whereas simple agglomerate sizes range from 1–100 µm [13–15]. While long-range interactions may contribute to the formation of larger structures too, in this work we exclusively consider the formation of aggregates.

The study of aggregate formation typically focuses on the emergence of fractal structures, that influence macro-scale properties like density and surface area. These structures arise from screening effects in the entropic process of cluster formation by Brownian droplets and particles [16, 17]. In addition to screening, the fractal dimension and eventual density of the formed aggregate may be subject to long and short-range interactions, in particular the van der Waals force. In the context of modelling the effect of attractive forces, the interactions can be represented by a capture distance, ℓ_c. This denotes the critical distance between two particles at which moving any closer leads to an inevitable collision induced

by attractive inter-particle forces scaling with distance. While the existence of such a zone is not established in relation to the clustering of nanoparticles, we deem its presence to be likely. There is a limited body of work that covers the potential effect of this region on the cluster structure. The classic work of Meakin [18] and a recent study by Nicolás-Carlock et al. [19], explored the impact of these interactions on the fractality of formed structures. Both studies used 2D random walk particle-cluster models with a variable capture distance to represent attractive forces. These works conclude that fractal dimension of clusters produced with and without capture effects end up having the same fractal dimension, provided the clusters are large enough. However, while not elaborated on in those works, cluster density is highly dependent on capture distance. This is easy to overlook as clusters with the same fractal dimension can still have vastly different densities, as fractal dimension relates to the change in density with respect to cluster size, not the absolute density itself. From the prior studies it can therefore already be inferred that long-range forces have the potential to affect macro properties, even while the fractality remains unchanged. Nevertheless, whether the magnitude of the forces acting on Brownian droplets and particles within flame pyrolysis is sufficient to induce any change in particle properties remains unexplored. Furthermore, it is unclear whether large enough clusters are actually attained during aggregate formation to reach a size at which fractal dimensions converge. Given the geometric nature of screening effects, examining their impact on structure formation in 2D may be an oversimplification. Given the small size of primary nanoparticles, we hypothesize an active capture zone to be present, which should in turn affect the macroproperties of formed aggregates.

In this work, we set out to determine the van der Waals-induced capture distance for Brownian nanoparticles. Additionally, using a model, we show the effect of capture effects on fractal dimensions and densities of 3D clusters.

Our results may also have implications for other systems of clustering particles subjected to long-range forces. For instance, magnetic nanoparticles tend to aggregate, causing issues in their application for magnetic resonance imaging [20]. Furthermore, in colloidal and biological systems exact interactions are highly dependent on surface groups and the nature of the surrounding medium [21, 22], but are known to act on distances exceeding 1 nm [23].

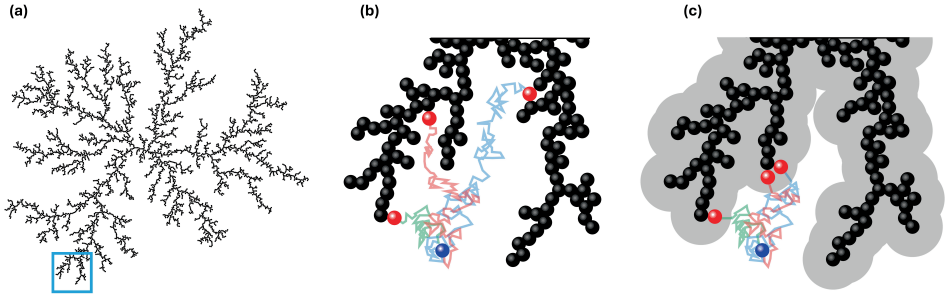


Figure 3.1: Overview of caption distance **(a)**, an aggregate, created without inclusion of a caption distance, **(b)**, three possible random walks of a particle entering the highlighted section of **(a)** without a caption distance, **(c)**, three possible random walks of a particle entering the highlighted section of **(a)** with a caption distance. The initial particle position is depicted in blue and final positions in red.

3.2. METHODS

In fig. 3.1, an overview of the representation and effect of the concept of a capture distance is provided. To enhance the clarity of the image, a 2D cluster is displayed. Here, and in the remainder of this work, a particle undergoing the random walk will be denoted with p_W, whereas we will use p_{Agg} for those that are part the aggregate. In fig. 3.1a, an aggregate is displayed, that was produced when assuming no capture effect to be present. The highlighted section of fig. 3.1a is displayed in fig. 3.1b with 3 random walks. The position of a wandering particle (p_W), is depicted by the blue particle, the lines representing paths the diffusing particle may take and the 3 corresponding locations the particle may end up in when no capture effects are present are shown in red. Figure 3.1c displays the same highlighted section in the presence of a capture zone. It can be seen that parts of the structure became inaccessible as a result of the screening effect of this region. When giving wandering particles the same initial paths as displayed in fig. 3.1b, the presence of an active pull in fig. 3.1c leads them to end up in different places as their path overlaps with the capture region in an earlier state of the random walk. As a result of the capture effect, particles are on average caught earlier, leading to less dense structures. We will use ℓ_c to represent the capture distance, which is defined as per eq. (3.1). Here, r_c denotes the radius of the capture distance and r_p is the particle radius. So $\ell_c = 1.0$ in the absence of screening effects, like in fig. 3.1b, whereas $\ell_c = 4.0$ was used in fig. 3.1c.

$$\ell_c = \frac{r_c}{r_p} \tag{3.1}$$

3.2.1. CAPTURE DISTANCE

To compute the effective van der Waals forces, F_{vdW}, of a cluster acting on a singular particle, we use the London-van der Waals equation for two identical spheres, eq. (3.2) [24]. Given the sensitivity of van der Waals forces with respect to particle distance, the closest particle within the cluster will induce the bulk of the pull. We can therefore simplify by only considering the forces between that particle, p_{Agg} and the wandering particle p_W. In the *Supplementary Materials*, we perform sensitivity analyses to validate this assumption.

$$F_{vdW} = \frac{A_H}{6D_p}\left(\frac{2(\gamma+1)}{\gamma^2+2\gamma} - \frac{\gamma+1}{(\gamma^2+2\gamma)^2} - \frac{2}{\gamma+1} - \frac{1}{(\gamma+1)^3}\right) \tag{3.2}$$

Here, A_H is the Hamaker constant, D_p is the particle diameter and γ denotes the ratio of surface distance d between the wandering particle and the closest particle within the cluster to the particle diameter:

$$\gamma_i = \frac{d}{D_p} \tag{3.3}$$

To find the location of the inter-particle capture distance, we use the Fluctuation Dissipation Theorem [25], based on the Langevin equation, eq. (3.4).

$$m\frac{dv}{dt} = f(t) - \xi v \tag{3.4}$$

Here, m is the mass of the singular particle, t is time, $f(t)$ represents the fluctuating forces acting on the body, ξ is the friction factor and v is the particle velocity. Using eq. (3.4), the correlation time, after which the current velocity of a particle became uncorrelated with its initial velocity, can be found as:

$$\tau = \frac{m}{\xi} \tag{3.5}$$

Where

$$\xi = \frac{k_b T}{\mathscr{D}} \quad with \quad \mathscr{D} = \frac{k_b T}{3\pi\mu D_p} \tag{3.6}$$

Where k_b is the Boltzmann constant, T is the temperature and $\mathscr{D}$ is the diffusion constant. To make this derivation leading from eq. (3.4) to eq. (3.5), the assumption that $\langle f(t)\rangle = 0$ has to be made. This assumption holds collectively for many particles, but is not necessarily true when considering a single particle at $t < \infty$.

To find the probability density of a Brownian particle in a constant drift, the Smoluchowski equation can be solved to find:

$$p(x,t|_{x_0}) = \frac{1}{\sqrt{4\pi\mathscr{D}t}} exp\left(-\frac{(x-x_0-vt)^2}{4\mathscr{D}t}\right) \tag{3.7}$$

Finally, to solve eq. (3.7) a velocity, describing the drift, is required. In our case, this drift is induced by F_{vdW}, which scales with surface distance, and therefore will change over time as the particle drifts towards or away from the cluster. To simplify, we assume v to remain constant within the correlation time, computed as per eq. (3.8). Here, we assume the effective F_{vdW} between the singular particle and cluster are equal to the force induced by the closest particle within the cluster. In the *Supplementary Materials* we perform a sensitivity analysis which validates this assumption.

$$v = \frac{F_{vdW}}{\xi}\tau \quad while \quad t \leqslant \tau \tag{3.8}$$

3.2.2. MODEL

Three types of aggregation dynamics are typically identified, reaction-limited, diffusion-limited and ballistic aggregation [15, 26]. In the reaction-limited regime, not all collisions lead to the particles sticking together. This can be modelled by introducing a sticking probability which is smaller than 1. Diffusion-limited and ballistic aggregation describe the path of a wandering particle by a random walk or a linear trajectory respectively. Collisions in these models do always result in aggregation.

As our work concerns the regime where primary particles are only just solidified and therefore still 'sticky', we consider our process to not be reaction limited. Furthermore, the particles considered in this study have such small volumes that they cannot build significant kinetic energy, needed to maintain a predictable direction of motion, therefore we model the system by using the diffusion-limited aggregation (DLA) approach.

A 3D off-grid DLA model, utilizing a random walk, was developed in Python to investigate our hypothesis. An initial, stationary, seed particle is introduced at (x,y,z) = (0,0,0) and new particles are introduced at a distance, scaling with current cluster size, and proceed with a random walk. New positions of wandering particles are computed using eq. (3.9). Here the displacement Δ is found by computing two random angles, θ and ϕ providing a direction to move in, and δ, the Euclidean distance between positions, which is kept constant.

$$(x,y,z)_{i+1} = (x,y,z)_i + \Delta \tag{3.9}$$

With

$$\Delta \in \mathbf{Perm}\Big(\delta sin(\theta)cos(\phi), \delta sin(\theta)sin(\phi), \delta cos(\theta)\Big) \tag{3.10}$$

The permutation performed by eq. (3.10) scrambles directions to eliminate biases that would otherwise be introduced if only randomizing the angles.
After every step, the Euclidean distance between the wandering particle and all particles within the cluster, e_i, is computed to see whether p_W entered the capture region, $e_i < \ell_c$. Upon entering this zone, the collision point is set as the location of a particle within the cluster with the smallest surface distance to the current position of the random walker.
To speed up the process, additional random walkers, that do not interact with one another, are added in parallel, the total simultaneously running particles scaling with aggregate size. To prevent chain-reactions, where one collision leads to all nearby wandering particles colliding too, all walkers within 2 particle sizes of a colliding one are killed off. As in the work of Nicolás-Carlock et al., we allow particles to wander away from the aggregate until twice the distance of their spawn point before removing them.

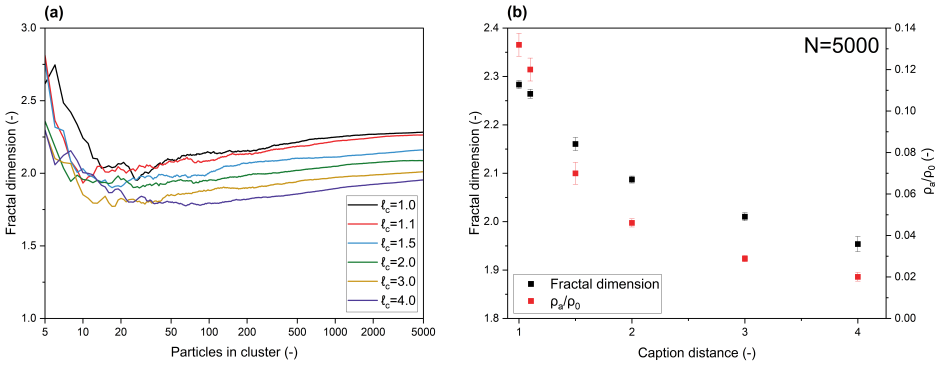


Figure 3.2: Effects of capture distance on properties of 3D aggregates, **(a)** development of fractal dimension of clusters produced with various capture distances, **(b)** obtained fractal dimensions and cluster densities of aggregates containing 5000 primary particles.

Fractal structures are typically described by eq. (3.11). Which, after rewriting, allows to find the fractal dimension, D_f, of an aggregate with known size.

$$N = k_f \left(\frac{R_g}{a} \right)^{D_f} \tag{3.11}$$

In eq. (3.11), N is the number of particles within the aggregate, a is the radius of the primary particles, k_f is the prefactor, assumed to be 1, and R_g is the effective radius of the gyration, which can be calculated as per eq. (3.12).

$$R_g^2 = \frac{1}{N}\sum_{i=1}^{N}\left(r_{i,j} - r_{0,j}\right)^2 \tag{3.12}$$

Here i indicates the particle number within the aggregate, j represents the x,y or z coordinate, $r_{i,j}$ is the position of the i^{th} particle and $r_{0,j}$ is the position of the center of the cluster, calculated as follows:

$$r_{0,j} = \frac{1}{N}\sum_{i=1}^{N} r_{i,j} \tag{3.13}$$

Since R_g is weighted, it is smaller than radii corresponding to the distance between the center of the cluster and the particle furthest removed from it, as one would determine from visual observation. Other works have not always explicitly mentioned how cluster radius was defined, but appeared to have used the approach analogous to visually observed radii (see *Supplementary Materials*). For an accurate assessment of D_f, that method works best when the aggregate is fairly circular in a 2D, or spherical in a 3D system. Given a large enough cluster, this assumption may be valid. In our work however, we do not allow clusters to grow indefinitely, the variations within the clusters leading to inaccurate results using that approach, especially in 3D systems, which is why we opt to use eq. (3.12).

3.3. RESULTS AND DISCUSSION

3.3.1. FRACTAL DIMENSION DEPENDENCY

In fig. 3.2, the properties of clusters produced with various capture distances are displayed. Figure 3.2a demonstrates the development of the fractal dimension, note the log scale on the x-axis. A consistently lower D_f is obtained when clusters are produced with an increased capture distance. Final cluster diameters ranged from 79.1 (ℓ_c=1.0) to 159.0 (ℓ_c=4.0) primary particle sizes. With regard to typically sized nanoparticles (5–50 nm), this puts the produced clusters among the larger ones that are experimentally observed. Considering the slope of the curves in fig. 3.2a, fractal dimensions of three dimensional clusters may indeed converge when building clusters with $N \to \infty$, as shown to be the case for 2D clusters [19]. On the scale in which the aggregates we are considering are typically found however, a pronounced difference in D_f, induced by long-range interactions, is evident. Coefficients of variation within the data were found to be $< 1\%$, and can be found the *Supplementary materials*.

The final fractal dimensions and densities of clusters containing 5000 primary particles are provided in fig. 3.2b. Densities are normalized by the density of a

primary particle. A clear decrease in cluster density is obtained when increasing the capture distance. Additionally, it can be observed that only minor variations are found among clusters created under the same conditions, highlighting the significance of our results. While less pronounced, the decreasing D_f with respect to capture distance is also found when using the approach used by Maekin, as demonstrated in the *Supplementary Materials*. Additionally, given that no such effect was obtained when using a 2D model, this underscores the limitations of studying screening effects in lower dimensions.

Collectively, the subfigures in fig. 3.2 demonstrate that, on the scale in which aggregates are typically found, increased capture distances lead to changes in the macro-properties of clusters as a result of more open structures being formed. A visualization of some produced clusters is provided in fig. 3.3. The axes are normalized to the diameter of a primary particle. As indicated by the cluster properties presented in fig. 3.2, it can be observed that increased capture distances lead to more open structures. It can be seen that our aggregates closely resemble those commonly observed by TEM. In particular, the 'net-like' structures, characteristic for nanoparticle aggregates are present in the model results as well.

3.3.2. CAPTURE DISTANCE

Next we determined the radius of the capture distance by using eq. (3.7) and material constants for SiO_2, listed in table 3.1. In fig. 3.4, the probability of a singular particle moving towards another one as a function of particle size and initial surface distance, Ω, is shown. In the context of our work this represents the probability of a wandering particle p_W colliding with a particle within the aggregate p_{Agg}. The region in deep blue represents the zone within which particle movement is completely stochastic, meaning the odds of the particle either approaching the cluster, or moving away from it are equal, hence the fraction of particles moving closer being 0.5. However, when the particle-cluster distance decreases, a transition region occurs, where the van der Waals force introduces a bias to the outcome of the stochastic Brownian motion. Finally, when surface distances are very small, particle movement is dominated by van der Waals forces, effectively rendering the process deterministic. Given the inevitability of a collision when particles reach beyond this capture distance, particle-cluster aggregation should be modelled by taking this region into account. It can be seen that the capture distance as determined by fig. 3.4 for a 10 nm particle adds about 1.2 nm to its radius. The simplification of using only 1 particle to represent the forces exerted by the cluster was found to introduce an error of $\ll 5\%$, as shown in the *Supplementary Materials*. Given this result, we conclude that a realistic value of ℓ_c is about 1.1 for nanoparticles in the 5–100 nm range. While not as extreme as some of the capture distances we used for the modelling, based fig. 3.2b we neverthe-

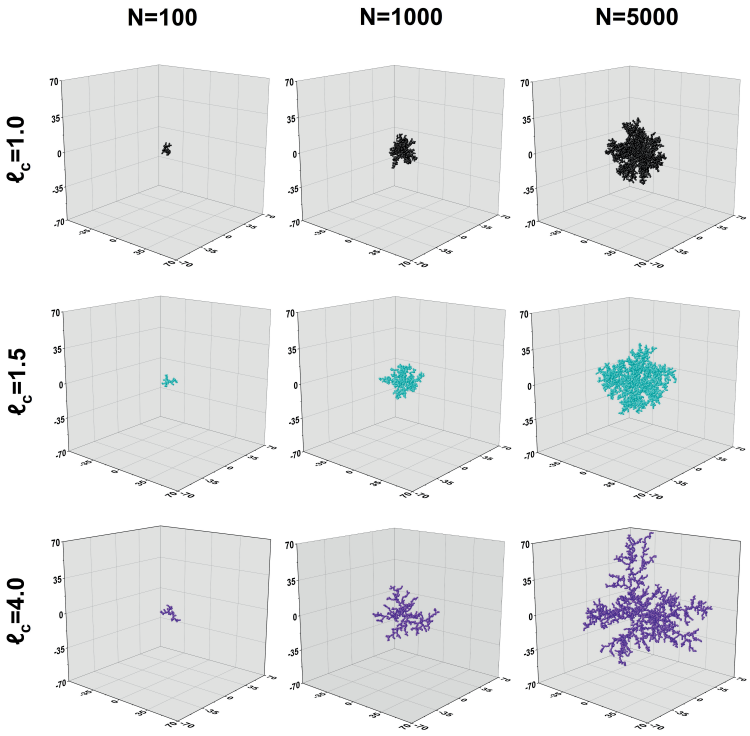


Figure 3.3: Development of aggregate structures produced with various capture distances.

less expect a decrease of about 10% in cluster density due to the capture effect. Confirming our findings by direct experimental observation is very difficult. Characterization methods often require sample preparation that may alter the aggregate structure, in particular by compaction and, in the presence of liquid, by capillary forces. Values of $D_f > 1.9$ are typically reported when considering aggregates formed by sintering particles [27]. However, reports using (small-echo) small-angle neutron scattering, which is less prone to alter aggregate features, indicate a wider range of fractal dimensions of ~1.1-2.1 [28–30] for nanoparticle aggregates. While lower than the ~2.3 predicted by a diffusion limited aggregation model in the absence of any capture effects, this is at least partially due to cluster-cluster aggregation. However, as these clusters are initially formed by particle-cluster interactions, a capture effect is still expected to contribute to even lower densities.

Parameter	Value	Unit
k_b	$1.38 \cdot 10^{-23}$	$m^2 kg s^{-1} K^{-1}$
ρ	2560	$kg m^{-3}$
T	700	K
μ	$3.45 \cdot 10^{-5}$	$kg m^{-1} s^{-1}$
A_H	$1.5 \cdot 10^{-19}$	$kg m^2 s^{-2}$

Table 3.1: Constants used to compute fig. 3.4

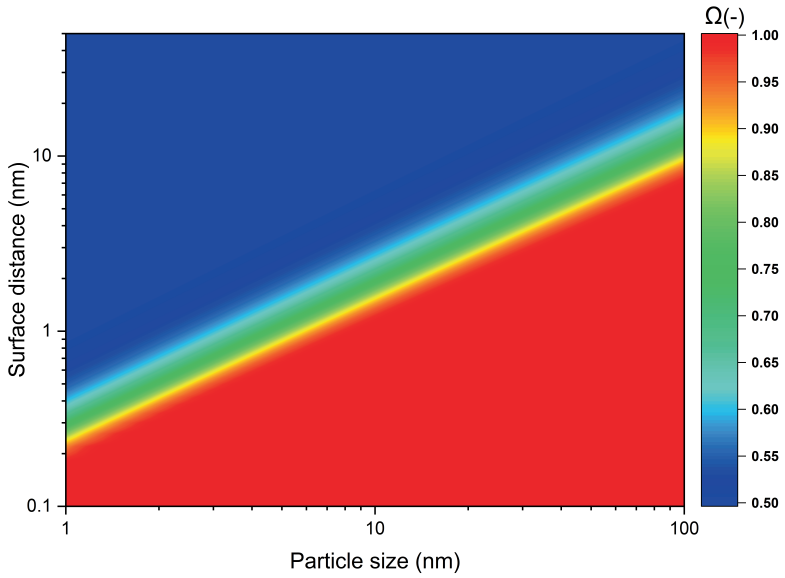


Figure 3.4: The probability of a particle moving towards another one as a result of van der Waals forces.

3.4. CONCLUSION

In this work, we assessed the effects of van der Waals interactions on the formation of nanoparticle aggregates. We hypothesized the existence of a critical distance between nanoparticles, beyond which collisions become inevitable as a result of attractive forces, affecting the aggregation process. Utilizing the Fluctuation Dissipation Theorem, we determined this region to extend about 10% beyond the particle radius for primary particles between 5–100 nm. Furthermore, we built a model to show that this effect alters the particle structure and results in a decrease in cluster density of ~10%. Additionally, deviations between the results obtained from 2 and 3 dimensional models show that screening effects can not be accurately studied in by using 2D models. Experimental validation of our

work is troublesome however, as it is unclear whether the predicted open structure is maintained upon further production and handling, especially in light of compaction. Furthermore, the complexity of accurately assessing structure on the aggregate scale, without affecting it, means very little experimental material is available for an accurate assessment.
While our work indicates capture effects to be present and significant, it relies on simplifications such as mono-sized spherical primary particles and a constant particle velocity within the correlation time. Furthermore, when determining the capture distance, we neglected all interactions besides van der Waals forces and Brownian motion. Additionally, used constants in this part of our work are subject to factors such as temperature and pressure, meaning that the outcome of this part of the work serves as an approximation. It would be interesting to see 3D models incorporating particle size distributions or allowing for different particle shapes. Furthermore, given that true systems are rarely fully ballistic or diffusion limited, the effect of combined particle dynamics in the context of screening effects would provide additional insight into real life systems.

REFERENCES

[1] S. Pratsinis, *18. history of manufacture of fine particles in high-temperature aerosol reactors,* (Research Triangle Institute, 2011) pp. 475–508.

[2] V. Singh, D. Joung, L. Zhai, S. Das, S. Khondaker, and S.Seal, *Graphene based materials: Past, present and future,* Progress in Materials Science **56**, 1178 (2011).

[3] Y. Wang and A. Hu, *Carbon quantum dots: synthesis, properties and applications,* J. Mater. Chem. C **2**, 6921 (2014).

[4] H. Allujami, M. Abdulkareem, T. Jassam, R. Al-Mansob, J. Ng, and A. Ibrahim, *Nanomaterials in recycled aggregates concrete applications: mechanical properties and durability. a review,* Cogent Engineering **9**, 2122885 (2022).

[5] W. Li, Z. Luo, C. Long, C. Wu, W. Duan, and S. Shah, *Effects of nanoparticle on the dynamic behaviors of recycled aggregate concrete under impact loading,* Materials & Design **112**, 58 (2016).

[6] G. Goel, P. Sachdeva, A. Chaudhary, and Y. Singh, *The use of nanomaterials in concrete: A review,* Materials Today: Proceedings **69**, 365 (2022).

[7] A. Rwei, W. Wang, and D. Kohane, *Photoresponsive nanoparticles for drug delivery,* Nano Today **10**, 451 (2015).

[8] A. Wang, R. Langer, and O. Farokhzad, *Nanoparticle delivery of cancer drugs,* Annual Review of Medicine **63**, 185 (2012).

[9] A. Workie, H. Ningsih, and S. Shih, *An comprehensive review on the spray pyrolysis technique: Historical context, operational factors, classifications, and product applications,* Journal of Analytical and Applied Pyrolysis **170**, 105915 (2023).

[10] H. Barthel, L. Rösch, and J. Weis, *Fumed silica - production, properties, and applications,* in *Organosilicon Chemistry Set* (John Wiley & Sons, Ltd, 2005) Chap. 91, pp. 761–778.

[11] S. Pratsinis, *Flame aerosol synthesis of ceramic powders,* Progress in Energy and Combustion Science **24**, 197 (1998).

[12] F. Meierhofer and U. Fritsching, *Synthesis of metal oxide nanoparticles in flame sprays: Review on process technology, modeling, and diagnostics,* Energy and Fuels **35** (2021).

[13] Y. Wang, G. Gu, F. Wei, and J. Wu, *Fluidization and agglomerate structure of SiO_2 nanoparticles,* Powder Technology **124**, 152 (2002).

[14] R. Kamphorst, K. Wu, S. Salameh, G. Meesters, and J. van Ommen, *On the fluidization of cohesive powders: Differences and similarities between micro- and nano-sized particle gas–solid fluidization,* The Canadian Journal of Chemical Engineering (2022).

[15] J. Van Ommen, J. Valverde, and R. Pfeffer, *Fluidization of nanopowders: a review,* Journal of Nanoparticle Research **14**, 737 (2012).

[16] P. Meakin and T. A. Witten, *Growing interface in diffusion-limited aggregation,* Phys. Rev. A **28**, 2985 (1983).

[17] T. Halsey, *Diffusion-limited aggregation as branched growth,* Phys. Rev. Lett. **72**, 1228 (1994).

[18] P. Meakin, *Diffusion-controlled flocculation: The effects of attractive and repulsive interactions,* The Journal of Chemical Physics **79**, 2426 (1983).

[19] J. Nicolás-Carlock, J. Carrillo, and V. Dossetti, *Fractality à la carte: a general particle-cluster aggregation model,* Scientific Reports **6** (2016).

[20] D. Fayol, N. Luciani, L. Lartigue, F. Gazeau, and C. Wilhelm, *Managing magnetic nanoparticle aggregation and cellular uptake: a precondition for efficient stem-cell differentiation and mri tracking,* Advanced Healthcare Materials **2**, 313 (2013).

[21] R. Kamphorst, P. Wanjari, S.Saedy, J. van Dam, A. Thijssen, P. Brüner, T. Grehl, G. Meesters, and J. van Ommen, *Enhancing colloid stability of polymer microspheres in water through SiO_2 coating: Effects of coating cycles and surface coverage,* Surfaces and Interfaces **45**, 103852 (2024).

[22] S. A. Hassan, *Computational study of the forces driving aggregation of ultrasmall nanoparticles in biological fluids,* ACS Nano **11**, 4145 (2017).

[23] L. Zhu, R. Tian, X. Liu, H. Xiong, and H. Li, *A general theory for describing coagulation kinetics of variably charged nanoparticles,* Colloids and Surfaces A: Physicochemical and Engineering Aspects **527**, 158 (2017).

[24] H. Hamaker, *The London—van der Waals attraction between spherical particles,* Physica **4**, 1058 (1937).

[25] R. Kubo, *The fluctuation-dissipation theorem,* Reports on Progress in Physics **29**, 255 (2002).

[26] S. Friedlander, *Smoke, dust and haze, fundamentals of aerosol dynamics,* (Oxford University Press, 2000) Chap. Dynamics of Agglomerate Formation and Restructuring, pp. 222–233, 2nd ed.

[27] P. Grammatikopoulos, M. Sowwan, and J. Kioseoglou, *Computational modeling of nanoparticle coalescence,* Advanced Theory and Simulations **2**, 1900013 (2019).

[28] L. de Martín, W. Bouwman, and J. van Ommen, *Multidimensional nature of fluidized nanoparticle agglomerates,* Langmuir **30**, 12696 (2014).

[29] A. Hurd, D. Schaefer, and J. Martin, *Surface and mass fractals in vapor-phase aggregates,* Phys. Rev. A **35**, 2361 (1987).

[30] A. Fabre, T. Steur, W. Bouwman, M. Kreutzer, and J. Van Ommen, *Characterization of the stratified morphology of nanoparticle agglomerates,* The Journal of Physical Chemistry C **120** (2016).

SUPPLEMENTARY MATERIALS

3.5. SENSITIVITY OF VAN DER WAALS INTERACTIONS

3.5.1. VAN DER WAALS FORCES

To compute the effective van der Waals forces, F_{vdW}, of a cluster acting on a singular particle, the London-van der Waals equation for two identical spheres was extended to include every particle within a cluster of N particles, shown in eq. (3.14).

$$F_{vdW} = \frac{A_H}{6D_p} \sum_{i=1}^{N} \left(\frac{2(\gamma_i + 1)}{\gamma_i^2 + 2\gamma_i} - \frac{\gamma_i + 1}{(\gamma_i^2 + 2\gamma_i)^2} - \frac{2}{\gamma_i + 1} - \frac{1}{(\gamma_i + 1)^3} \right) \tag{3.14}$$

Here, A_H is the Hamaker constant, D_p is the particle diameter and γ_i denotes the ratio of surface distance d_i between the singular particle and particle i within the cluster to the particle diameter:

$$\gamma_i = \frac{d_i}{D_p} \tag{3.15}$$

To compute d_i, we need to account for the position of each particle in the cluster, relative to the singular particle. To simplify, we consider linear strings of particles to represent the closest particles in a fractal structure. For the purposes of establishing the effective van der Waals forces between a single particle and a cluster, we consider two extreme cases, as demonstrated in fig. 3.5. The distance between particle A and the closest particle within the linear cluster (#1) is the same as the distance between particle B and the closest particle in the cluster (#3), however the distances between the other particles all differ, making the collective force acting on particle B larger.

For the extreme cases considered in this study, d_i is computed as per eq. (3.16).

$$d_i = \begin{cases} d_0 + D_p(i-1), \text{if parallel} \\ \\ \sqrt{d_0^2 + \left(D_p \frac{i-\lambda}{2}\right)^2}, \text{if perpendicular} \end{cases} \tag{3.16}$$

Here, d_0 denotes the surface distance to the singular particle and the closest particle in the cluster and λ takes values of 0 or 1 for clusters consisting of even and odd numbers of particles, respectively. Note that the computed surface distances for perpendicular clusters is only valid for clusters containing an

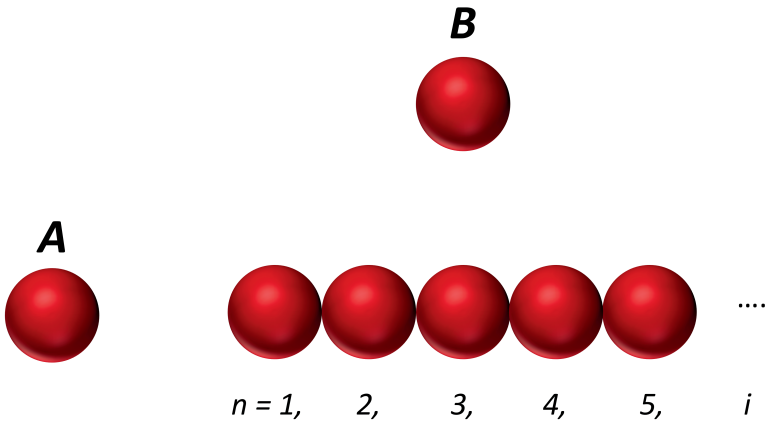


Figure 3.5: Particle-cluster configurations as considered for predicting effective van der Waals forces.

odd number of particles and the singular particle is always located in the middle of the cluster, slightly overestimating the effective van der Waals force. Finally, we need to account for the angle at which individual particles within the cluster pull on the singular particle. Since we always consider the singular particle to be located at the center of the string, the sideways components of the forces cancel out and the resulting force can be computed by multiplying eq. (3.14) by the correction factor α_i, where, as per eq. (3.17).

$$\alpha_i = cos\left(tan^{-1}\left(D_p \frac{i-\lambda}{2d_0}\right)\right) \tag{3.17}$$

3.5.2. RESULTS

Computing the forces acting on a singular particle by all particles within a cluster comes at a computational cost. Therefore, before we determine the capture distance in real life aggregation processes, we assess the need to do so. From eq. (3.14) it is evident that van der Waals forces scale with both current cluster size and surface distance between each particle within the cluster and the single particle. However, its extreme sensitivity with respect to surface distance may result in the effect of the particle within the cluster with the smallest surface distance to outweigh even the collective effect of all others. This can easily be shown to be true in extreme cases, as the ratio between the surface distance of the closest particle in the cluster and any other particle, Q, can be computed as:

$$Q = \frac{r_i}{r_0} = \frac{r_0 + x_i}{r_0} \tag{3.18}$$

Where r_0 and r_i are the distances to the closest particle and particle i respectively and x_i describes the absolute difference between them. Since $x_i > 0$, it is obvious that $\lim_{r_0 \to 0} Q = \infty$, meaning only the closest particle within the cluster is relevant upon close proximity. Furthermore, at $\lim_{r_0 \to \infty} Q = 1$, so at large distances, all particles become relevant. As demonstrated in section 3.5.2 and section 3.5.2, this is indeed the case for both parallel and perpendicular configurations. For these figures the normalized vdW forces are defined as the force acting on a cluster of a given number of particles divided by the force exerted by the closest particle within the cluster:

$$F_{vdW,norm} = \frac{\sum_i F_{vdW,n=i}}{F_{vdW,n=1}} \tag{3.19}$$

The solid black line indicates the combination of surface distance and particles within the cluster where the force induced by the entire cluster exceeds the one induced by the closest particle within it by 5%. Collectively, section 3.5.2 and section 3.5.2 demonstrate that multiple particles within a cluster should only be be taken into account when calculating the effective van der Waals forces on between a singular particle and a cluster when the cluster consists of many particles or when the distance between cluster and particle is $\gg 1$ nm.

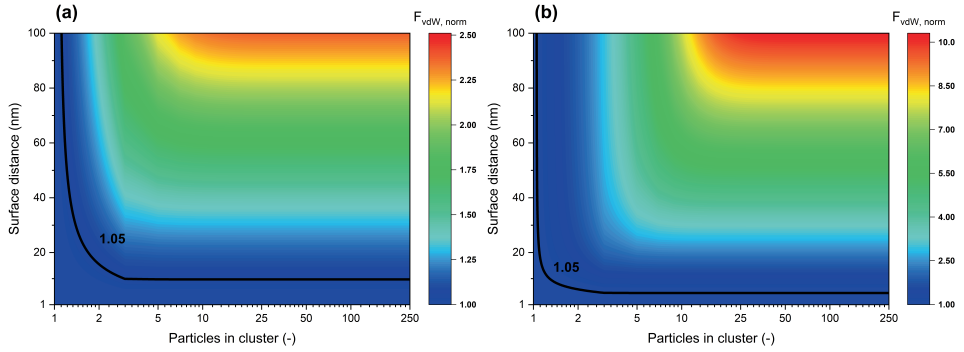


Figure 3.6: Normalized total forces acting between a singular particle and clusters of various surface distances and orientations: **(a)** Normalized van der Waals forces as a function of the number of particles in a cluster in parallel orientation and the surface distance between the closest particles within the cluster and a single particle, **(b)** Normalized van der Waals forces as a function of the number of particles in a cluster in perpendicular orientation and the surface distance between the closest particles within the cluster and a single particle, primary particle size = 10 nm, $A_H = 1.5 \cdot 10^{-19}$J

3.6. 2D MODEL

To validate our model, we adjusted it to produce 2D aggregates, which allowed for comparison of the output with previously published works. In fig. 3.7 and fig. 3.8 2D aggregates consisting of 1000 particles are displayed and compared to those of prior publications. It is evident that our output fully aligns with the one from the prior model, deviations arising from the stochastic nature of the aggregation process itself. Furthermore, fig. 3.9 demonstrates the same results are obtained when computing the fractal dimension using the approach by Meakin in the original work.



Figure 3.7: 2D aggregates containing 1000 particles produced from by Maekin[1] (left) and our model (right) with a capture distance of ℓ_c =1.0

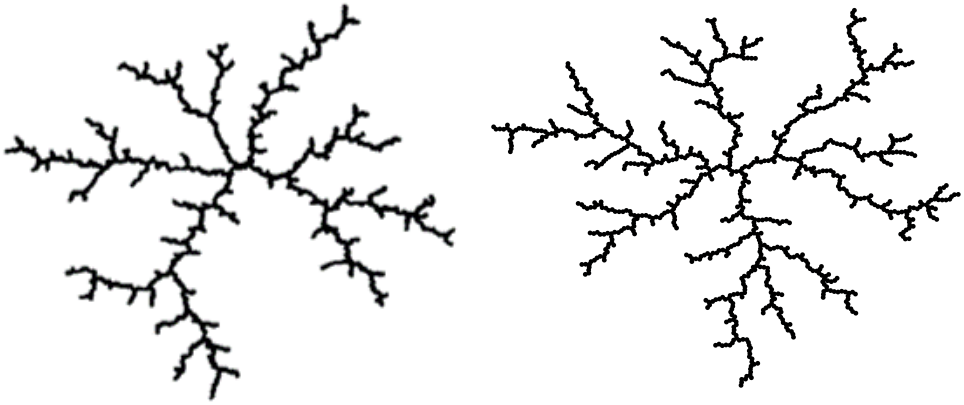


Figure 3.8: 2D aggregates containing 1000 particles produced from by Meakin[1] (left) and our model (right) with a capture distance of ℓ_c =4.0

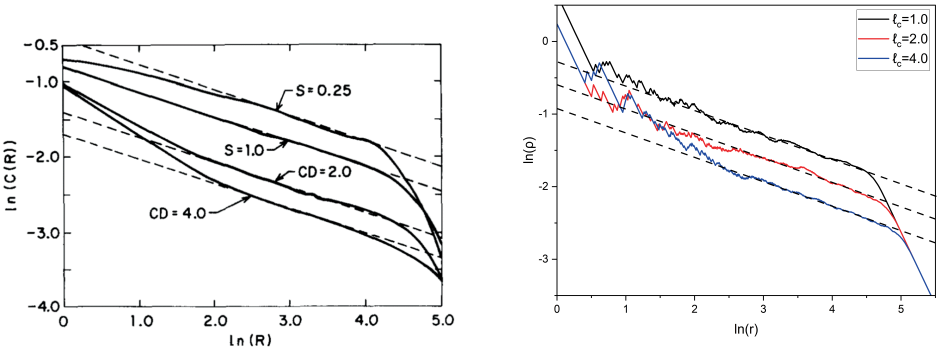


Figure 3.9: Density-radius correlation functions for various capture distances, obtained by 2D models. Left: Meakin[1] , right: our model. Aggregates consisted of 5000-8000 primary particles. The dashed lines in both figures have a slope of -1/3

3.7. ADDITIONAL 3D MODEL OUTPUT

For the 3D model, we also used the method from prior works to confirm our finding to not be an artifact of the method to find D_f. In fig. 3.10, the resulting dependencies of density and cluster size are provided. Here it can be seen that the slopes of curves obtained in 3D structures are indeed not parallel on the scale we consider. However, as we argue in the manuscript, this method is somewhat subjective, in particular for smaller structures, where the exact location of the

fully linear zone is not obvious.

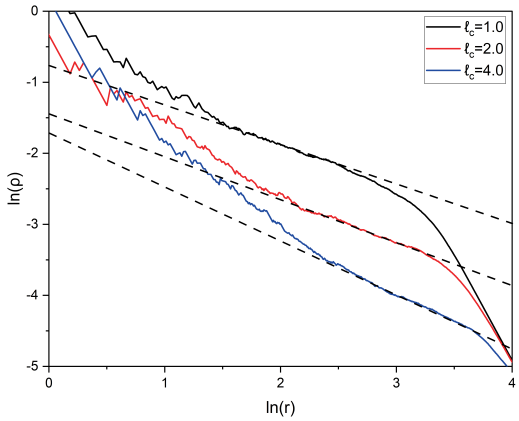


Figure 3.10: Density-radius correlation functions of 3D clusters, produced at various capure distances

In fig. 3.11, the coefficients of variation corresponding to Fig. 2a in the manuscript are provided. For the clusters of 5000 particles considered in the main text, it can be seen that none of the errors exceed 1 %, as indicated by the dashed line.

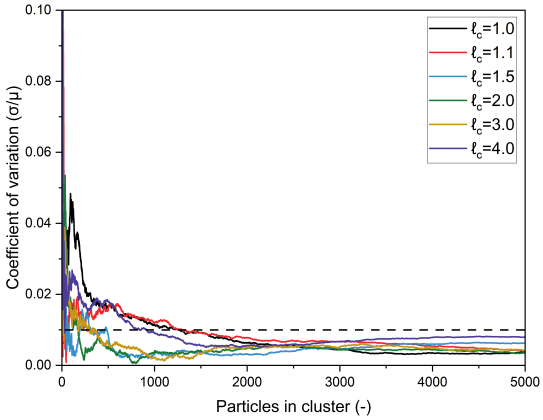


Figure 3.11: Coefficients of variation corresponding to sets of clusters produced under identical conditions. The horizontal dashed line indicates a value of 0.01

[1] Reprinted from 10.1063/1.446051, with the permission of AIP Publishing.

4

The Mechanism behind Vibration Assisted Fluidization of Cohesive Micro-Silica

In Chapter 2, we discussed literature on assistance methods. The development of assistance methods requires an understanding of the mechanism behind their functionality. Nevertheless, we found the explanations in much of the literature to be insufficient. We hypothesized that improvements or initiation of the fluidization of cohesive powders should be caused by the disruption of channels, whereas most publications claim the breakage of agglomerates to be the primary reason. In this chapter, we investigate our hypothesis by employing the X-ray imaging technique, which allowed to study the dynamics of the fluidized powder bed.

This chapter has been published as "The Mechanism behind Vibration Assisted Fluidization of Cohesive Micro-Silica" by R. Kamphorst, P.C. van der Sande, K. Wu, E.C. Wagner, M.K. David, G.M.H. Meesters and J.R. van Ommen, KONA Powder and Particle Journal **41**, 254 (2024)

Vibro-assisted fluidization of cohesive micro-silica has been studied by means of X-ray imaging, pressure drop measurements, and off-line determination of the agglomerate size. Pressure drop and bed height development could be explained by observable phenomena taking place in the bed; slugging, channeling, fluidization or densification. It was observed that channeling is the main cause of poor fluidization of the micro-silica, resulting in poor gas–solid contact and little internal mixing. Improvement in fluidization upon starting the mechanical vibration was achieved by disrupting the channels. Agglomerate sizes were found to not significantly change during experiments.

4.1. INTRODUCTION

Fluidization of cohesive powders has seen significant interest in the last decades, fueled by the increase in applications of powders with a small particle size. Cohesive micro- and nanopowders find their use in medical applications [1, 2], catalysis [3] and coatings [4] for example.

Due to their small particle size, the attractive van der Waals forces between these particles are dominant, in the absence of moisture, making them hard to fluidize [5]. Two main complications are seen: channelling and agglomeration. Channelling is the phenomena where a gas bypass, or channel, is formed through the bed in the vertical direction upon the introduction of gas. Gas mainly flowing through a channel has poor interaction with the powder bed, meaning less drag is created and no fluidization takes place. Agglomeration is the formation of particle clusters as a result of dominant cohesive forces. Whereas agglomerates can sometimes be fluidized without assistance [6], gas-solid contact is reduced due to the surface area of particles being inside the agglomerate and gas mostly passing outside of it, with diffusion into the agglomerates pores. A phenomenon that is also sometimes observed, at start-up, for cohesive powder is slugging or plugging, here the entire bed is pushed up through the fluidization column. While one could argue this to be a third complication of cohesive powder fluidization, we consider this an extreme form of agglomeration, where the entire bed acts as one large cluster. Slugging is typically not seen in industrial size beds.

In order to fluidize cohesive powders, assistance methods can be employed, which introduce an additional manipulation. For most assistance methods it was concluded, by one or more studies, mostly done on nano-particles, that the mechanism by which fluidization was improved is by breaking up agglomerates; mechanical vibration [7, 8], acoustic vibration [9], magnetic field [10], stirring [11], micro-jet [12, 13] and pulsed flow [14–16]. This conclusion is based on smaller agglomerate sizes being measured in beds that have been fluidized, using an assistance method, than one that could not be fluidized. However, the mechanism of agglomerate breakage should be taken into account. First of all, they can break as a result of collisions, either with other agglomerates or with the column wall. However, in an unfluidized bed, agglomerates will be (mostly) static, meaning no collisions take place. Another way for agglomerates to decrease in size is due to shear with the fluidizing gas, though simulations for nanoparticle fluidization have shown this effect to be minor, even at high gas velocities [17]. For this to happen at a significant scale, there should be significant gas-solid contact, which is also absent before fluidization is initiated.

Based on this, we hypothesize that agglomerates break as a result of initiated fluidization, but this agglomerate breakage is not the cause of the improvement. Rather than the agglomeration, we propose channelling is the major hur-

dle to overcome to achieve fluidization of cohesive powders. By introducing additional manipulation, from an assistance method, the channels can be destabilized and will collapse. Note that mechanical vibration, acoustic vibration, magnetic fields, pulsed flow, stirring and a (micro)jet all introduce additional motion of gas, column or internals into the bed, providing a mechanism by which the channelling can be disrupted. In the absence of channels, all fluidizing gas has to flow through the bed, creating drag. When sufficiently large drag is created, the particles or agglomerates will be fluidized. This reasoning leaves one to conclude that the best assistance methods are not the ones which are best at breaking agglomerates, but those which most effectively destroy channels. For further development and optimization of assistance methods it is essential to have a complete understanding of the mechanism by which the fluidization is improved.

Characterization of the fluidization quality is often done by measuring bed height expansion and pressure drop [7, 8, 18]. These two measurements alone are insufficient when it comes to analyzing the cause of poor fluidization. Visualization of the temporal evolution of hydrodynamics, going from poor fluidization with channeling to bubbling fluidization under the influence of an assistance method, could provide better understanding of the mechanism. Simple optical techniques that are typically used to visualize hydrodynamics in two-phase systems are, however, limited to acquiring information close to the wall region, because the large solid fraction of the dispersion phase makes the dense flow opaque to visible light. X-ray imaging, on the other hand, has been demonstrated to be a valuable technique to study dynamics in opaque systems, such as fluidized beds with nanoparticles [19], irregular particles [20], sintering [21] internals [22, 23], and spouts [24].

This study aims to characterize the hydrodynamics of a gas-solid fluidized bed, consisting of cohesive micro-silica, with and without vibration applied to it. This is done by means of X-ray imaging, pressure drop and bed height extension measurements. Channel formation and disruption are shown and agglomerate sizes are measured to elucidate the mechanism behind the employed assistance method.

4.2. ASSISTANCE MECHANISM

For most of the studied assistance methods, except dry particle coating, it was concluded, by one or more studies, that the mechanism by which fluidization was improved is by breaking up large agglomerates (Mechanical vibration [7], Acoustic vibration [9], magnetic field [10], Stirring [11], micro-jet [12, 13], Pulsed flow [14–16]). This conclusion is based on smaller agglomerate sizes being measured in a bed which has been fluidized using an assistance method compared

to an un-fluidized bed.

Something to consider here is how agglomerates can be broken. First of all, they can break as a result of collisions, either with other agglomerates or with the column wall. However, in an unfluidized bed agglomerates will be (mostly) static, meaning no collisions take place. Another way for agglomerates to decrease in size is due to shear with the fluidizing gas. For this to happen at a significant scale, there should be significant gas-solid contact, which is absent before fluidization is initiated. Based on this, we hypothesize that fluidization is a requirement for breaking up agglomerates. The fact that smaller agglomerate sizes are measure are therefore thought to not the cause, but the result, of improved fluidization.

We hypothesize that assistance methods work in another way. Rather than the agglomeration, we think channelling is the major hurdle to overcome to achieve fluidization of cohesive powders. Channels are mostly stable with respect to superficial gas velocity, therefore increasing the velocity usually not effective to induce fluidization. By introducing additional motion, from an assistance method, the channels can be destabilized and will collapse. Note that mechanical vibration, acoustic vibration, magnetic fields, stirring and a (micro)jet all introduce additional motion of gas, column or internals into the bed, providing a mechanism by which the channelling can be disrupted. In the absence of channels, all gas flows through the particle bed, creating drag. When enough enough drag is created, the particles will be fluidized. This reasoning leaves one to conclude that the best assistance methods are not the ones which are best at breaking agglomerates, but those which most effectively destroy channels. The measured smaller agglomerate sizes are thought merely a result increased collisions in the fluidized phase after the channels are broken and fluidization takes place. On top of that, agglomerates might also break from the shear, created by the increased amount gas that is now flowing through the bed.

For further development and optimisation of assistance methods it is of course essential to have a complete understanding of the mechanism by which fluidization is improved.

4.3. EXPERIMENTAL AND METHODOLOGY

4.3.1. FLUIDIZATION PROCEDURE

A perspex column with inner diameter of 9 cm and sample ports at 2.5, 6.5 and 13.5 cm from the distributor plate was used as the fluidized bed column. The pressure drop was measured from the surface of distributor plate to the breakout box, using OMEGA PX409-10WG5V pressure transducers. The static pressure

of the powder was 2.3 mbar ($2.3 \cdot 10^2 Pa$) for all experiments. The column was mounted on a vibration table, a frequency of 30 Hz and a vertical amplitude of 1 mm was used for all experiments with vibration. For this study, two gas velocities were used, 1.8 and 3.1 $cm\,s^{-1}$. During the X-ray experiments, a remotely controlled camera was used to capture images of the column from which the bed height was measured.

The used powder, Köstropur 050818, consists of SiO_2 particles with a volume-averaged primary particle size of 9.7 µm (as measured by laser diffraction); particle size distribution is shown in Figure 4.1. The powder was sieved beforehand (mesh size 1.25 mm). Note that this is orders of magnitude larger than the primary particle size, meaning it did not affect the size distribution of the powder, but was done to establish an equal state of aeration at the start of each experiment, ensuring reproducibility. The bulk density after sieving was measured to be 134 $kg\,m^{-3}$.

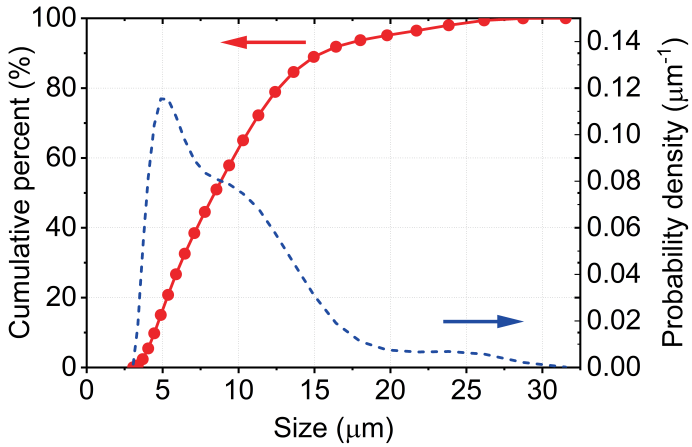


Figure 4.1: Volume based size distribution of micro silica powder acquired with the Coulter LS230 particle size analyzer.

After each experiment, powder samples were taken from the plane center of the collapsed bed at heights 2.5, 6.5 and 13.5 cm from the distributor plate. A Zeiss Colibri 7 Axio Observer microscope, equipped with Orca Flash 4.0 Hamamatsu V2 camera was used for imaging. The images were analysed using ImageJ. The equivalent circle diameter of the agglomerates was calculated from the projected area of the agglomerates on the image. To avoid including primary particles too, which will drastically shift the number-based distribution, agglomerates

with a diameter smaller than 35 µm were excluded. A minimum of 800 agglomerates was measured for each sample.

To be able to distinguish between the effect of 1) agglomerate breaking and 2) disrupting of channels on the fluidziation quality, three sets of experiments were conducted. One where no vibration was used, one where vibration was used for 8 min and finally one where vibration was used for 5 s before the inlet gas and vibration were switched off, all at the two aforementioned gas velocities.

4.3.2. X-RAY IMAGING SETUP

The gas-solids distribution inside the fluidized bed column was measured using an in-house fast X-ray analysis set-up. The complete set-up consists of three standard industrial type X-ray sources (Yxlon International GmbH) with a maximum energy of 150 keV working in cone beam mode. The sources are placed at 120° around a common center, which forms the field of view. Three 2D detectors (Teledyne Dalsa Xineos) are placed opposite of the sources. The sources and detectors are attached to a hexagonal support frame that enables translation of the detectors. By changing the distance between the source and detector, or the relative position of the column, the magnification of the image of the column can be adjusted. In this study the experiments were performed with one X-ray source-detector pair to obtain a projected 2D output from the 3D column as shown in Figure 4.2. The column was fixed to a vibration table which was positioned in the center of the setup. The distance between the source and the detector was 128.8 cm.

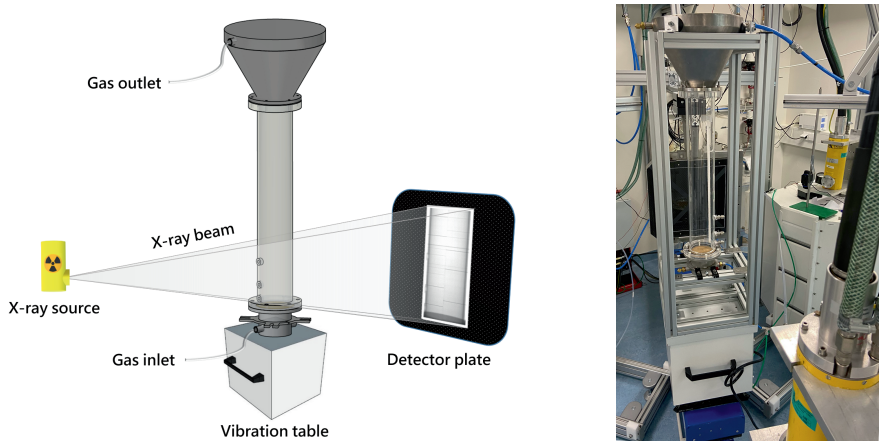


Figure 4.2: Experimental X-ray imaging setup showing the x-ray source and detector plate, fluidized bed column and the vibration table.

The experimental procedure was controlled from a workstation outside the

setup room, guaranteeing a safe working environment. The workstation was used to trigger the X-ray source and read out the signals from the detector plate. The theoretical spatial resolution of the X-ray detector was 0.15 mm per pixel. During all experiments the X-ray images were recorded with a frequency of 50 Hz for a measurement time of 200 s for the channel-breaking experiments or 600 s for the full experiment, which corresponded to the acquisition of respectively 10,000 and 30,000 images per experiment. The measured data was stored for further digital image analysis.

4.3.3. X-RAY IMAGE PROCESSING

For each experiment, the attenuation of the X-ray beam was measured at the detector plate to obtain the time-resolved projected 2D intensity map of the reactor. The raw images acquired were corrected for dead-pixels, originating from the construction of the detector plate, by means of interpolation to give pre-processed images.

In order to convert the measured X-ray attenuation to a solids concentration, a two points calibration protocol was performed. First, a reference image was acquired of the empty column. Then, the column was completely filled with the powder and vibrated for 10 minutes to approach the maximum packing density. After packing, the full reference image was acquired. The X-ray measurement principle is based on the attenuation of X-rays that travel through a material in a straight line from an X-ray source to a scintillation detector. The law of Lambert-Beer describes the transmission of a monochromatic beam of high energy photons with initial intensity I_0 through a material of constant density:

$$I(x) = I_0 \, exp(-\mu x) \tag{4.1}$$

where $I(x)$ represents the intensity measured at the detector, μ the attenuation coefficient and x the thickness. In case of a varying attenuation, the measured intensity is the integral effect of the local attenuation with the local attenuation coefficient. By applying the Lambert-Beer law the measurement gas-fraction map was obtained from the measurement intensity map by using the empty and full reference. The normalized solids fraction α was calculated as follows:

$$\alpha = 1 - \frac{log(I_{measured} \,/\, I_{full})}{log(I_{empty} \,/\, I_{full})} \tag{4.2}$$

Note the range of normalized solid fraction used in this work is between 0 to 1, with 0 representing pure gas and 1 representing close packing of the solids. For the solid fraction map, low attenuation of X-rays is represented by light colours and indicates low solid concentrations. By contrast, high attenuation of X-rays

is represented by the dark colours and indicates a high solids concentration.The acquired images obtain time-resolved, or dynamic, information of the gas-solids distribution in the column.

4.3.4. PRESSURE DATA PROCESSING

Pressure drop over the whole fluidized bed, or over part of it, is commonly used to evaluate the fluidization. When mechanical vibration is applied, the periodic oscillation of mass and gas induced is significantly greater than that caused by rising bubbles and suspension of solids. These driven oscillations affect the measured time series of bed pressure drop, greatly complicating the analysis of fluidization state. For example, Figure 4.3a plots the time series of bed pressure drop sampled over 600 s. The vibration was introduced at around 120 s, after which the measured signal (black) fluctuates largely with an amplitude of up to triple the theoretical bed pressure drop. To further determine the components of such oscillations, one could analyse the signal in the frequency domain [25]. Figure 4.3b demonstrates the power spectrum for the signal sampled between 120 – 600 s. The dominant peaks occur at 30 Hz, corresponding to the vibration frequency adopted in the experiment, as well as its sub-harmonic frequencies with a reduced intensity. As a result, in the following sections, the 10 s time-averaged pressure drop is used to assess fluidization quality during vibration, such as the red lines in Figure 4.3a, while its standard deviation mainly associated to the vibration is therefore neglected. For the experiments where vibration was only used for 5 s, averages over 1 s were taken.

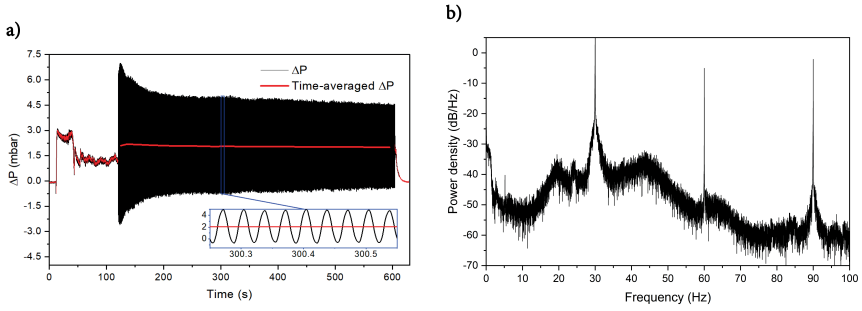


Figure 4.3: **(a)** Pressure drop series and **(b)** power spectrum of the vibrated bed at1.8 cm s^{-1}

4.4. RESULTS AND DISCUSSION

4.4.1. CHANNEL BREAKAGE BY VIBRATION

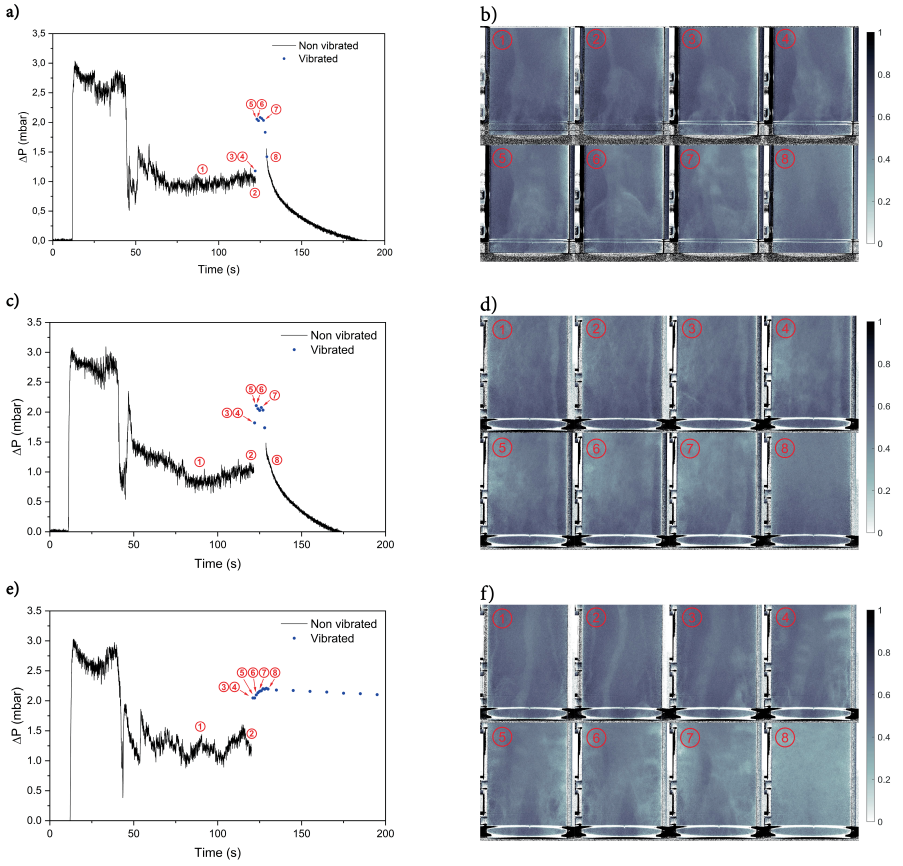


Figure 4.4: Images corresponding to channel breakage experiments at 1.8 cm s^{-1} gas velocity, in all images: ① = 90 s, ② = 120 s, ③ = 120.5 s, ④ = 121 s, ⑤ = 121.5 s, ⑥ = 122 s, ⑦ = 123 s and ⑧ = 130 s into the experiment. **(a)** Pressure drop of experiment 1; **(b)** X-ray images of experiment 1; **(c)** Pressure drop of experiment 2; **(d)** X-ray images of experiment 2; **(e)** Pressure drop of experiment 3; **(f)** X-ray images of experiment 3.

PRESSURE DROP AND X-RAY IMAGES

In Figure 4.4 the pressure drop and X-ray images of the experiments where vibration was used are shown. Experiment 1 and 2 were terminated after 5 s of vibration. The third one was vibrated for 8 min after vibration started, in order to demonstrate the long-term fluidization behaviour. The initial pressure drop fluctuations, seen in all pressure graphs, are caused by slugging which is discussed in detail in Section 4.4.2. For each experiment it can be seen that a semi-stable pressure drop was achieved after roughly 75 s. The P/P_0, the ratio of measured pressure drop over theoretical pressure drop of full fluidization (the static pressure exerted by the powder), after 90 s was found to be low. The chan-

neling, causing the low pressure drops, can clearly be seen. Comparing these images to Figure 4.4b-2, Figure 4.4d-2 and Figure 4.4f-2 it can also be seen that these channels were stable with time, as the images with sub-labels 1 and 2 were taken 30 s apart. The relatively high and unstable pressure drop seen from 50 s to 120 s in Figure 4.4e are explained by the collapse and reforming of unstable channels, in Figure 4.4f-2 the channel structure can be seen to have changed compared to Figure 4.4f-1. We consider this occurs simply as a matter of chance, since up to 120 s there is no difference in operation between the three experiments. In the following images the effect of vibration, within the first seconds of initiation, can be seen. For all experiments, two types of channeling were observed: rat-holes and vein-like channels. Where rat-holes run almost vertically from bottom to top of the bed, creating a large gas bypass, vein-like channels branch out in several directions, resulting in a network of thinner interconnected channels. Not enough data was acquired to reliably assess what causes either type of channeling to occur. It was consistently observed that the vein-like channels disappear by merging together, due to the powder barriers, initially separating them, crumbling. The rat-holes, persist longer and are destroyed by powder falling into them, disrupting the gas flow and creating bubble-like gas pockets. In Figure 4.4a, Figure 4.4c and Figure 4.4e it can be seen that the P/P_0 spiked to 0.89, 0.79 and 0.89 after 1 s, and kept increasing to 0.91, 0.88 and 0.94 after 5 s, of vibration respectively. Note that this increase over the first 5 s corresponds to more and more channels breaking, as seen in the X-ray images. The increase in the fluidized fraction of powder, as measured by pressure drop, is in all experiments clearly correlated to the breaking of channels.

AGGLOMERATE SIZES

For the experiments displayed in Figure 4.4 the agglomerate sizes were measured after ending the experiment for the top, middle and bottom of the bed (as described in Section 4.3.1). The resulting number-based d_{10}, d_{50} and d_{90}, are shown in Figure 4.5. First comparing the two runs in which vibration only lasted for 5 s, labeled 1 and 2 in Figure 4.5, no significant difference between them can be seen, showing the data is reproducible. Also, comparing the sizes in both of these experiments to the un-fluidized powder, no significant change is observed. Looking at the sizes found after 8 min of vibro-fluidizing, labeled 3 in Figure 4.5, no big change in agglomerate sizes was found compared to the un-fluidized powder or compared to the other experiments.

It was hypothesized that channel disruption is the cause of initiated fluidization upon the introduction of vibration. It was expected to find a decreased agglomerate size after 8 min of vibro-fluidization compared to 5 s, where virtually no decrease was expected. While no significant change in agglomerate sizes was

found for any of the experiments, it can still be concluded that the break-up of agglomerates does not play a role in initiating fluidization of the cohesive powder.

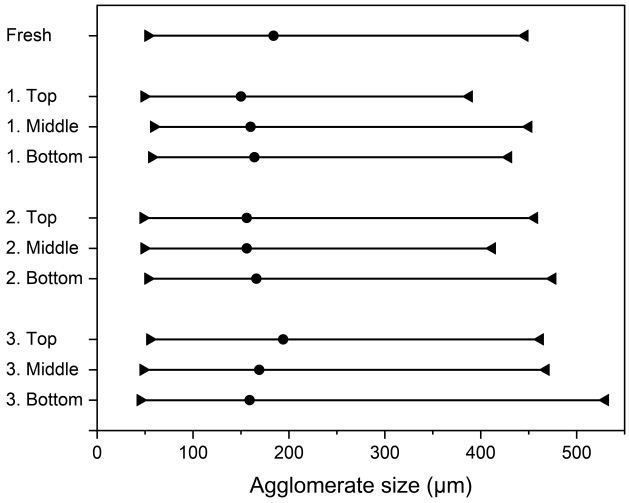


Figure 4.5: Agglomerate sizes after vibration all with gas velocity of 1.8 cm s^{-1}; 1) vibrated for 5 s; 2) vibrated for 5 s; 3) vibrated for 8 min; ▶=d_{10} •=d_{50} ◀=d_{90}, number based.

4.4.2. INFLUENCE OF VIBRATION AND GAS VELOCITY

CASE I: NO VIBRATION, 1.8 cm s^{-1}

In Figure 4.6 the bed height, pressure drop and X-ray images from the experiment without vibration and 1.8 cm s^{-1} gas velocity are shown. It can be seen that the bed was initially lifted as a plug, which corresponded to a large pressure drop over the column. The plug eventually broke and fell down in pieces, as seen in Figure 4.6c-3, which led to heavy pressure swings in the system. Note that in this image most of the powder bed is still out of frame, higher up in the column. Right after, some fluidization took place, as seen by the pressure drop, significant bed height expansion and dilute X-ray image. Within 45 s after the plug fell down, stable channels had formed (Figure 4.6c-5), that did not significantly change over time anymore. The pressure drop remained constant over this time with an average P/P_0 of 0.57. Bed height was decreasing slowly due to the bed compacting from its initial fluidized state. Still, an expansion ratio of 1.2 was maintained, caused by the added volume of the channels now present in the bed and the looser packing state of the powder. This experiment shows all the

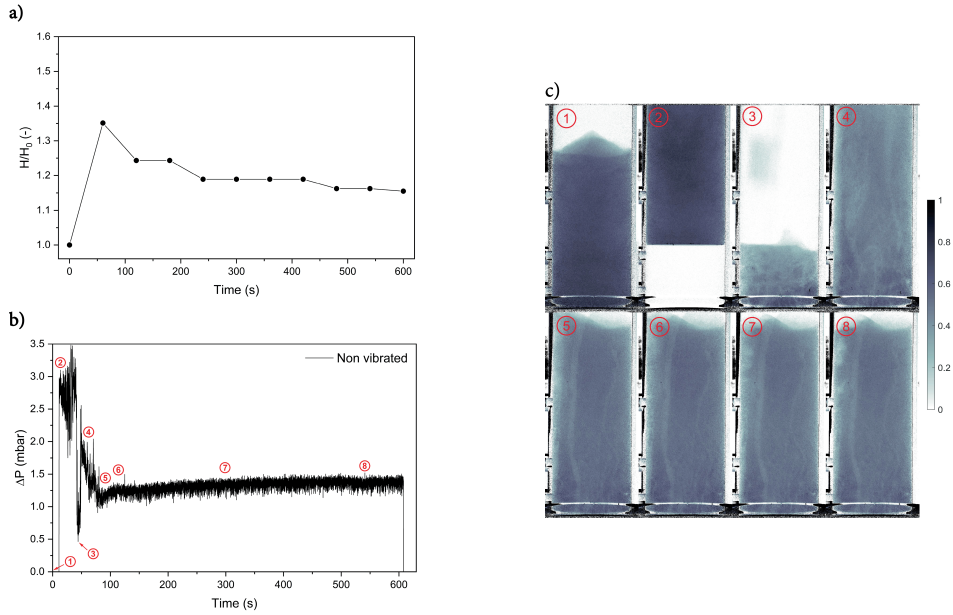


Figure 4.6: Results of fluidization experiments, 1.8 cm s^{-1} without vibration, in all images: ① = 0 s, ② = 15 s, ③ = 45 s, ④ = 60 s, ⑤ = 90 s, ⑥ = 120 s, ⑦ = 300 s and ⑧ = 540 s into the experiment. **(a)** Bed height; **(b)** Pressure drop; **(c)** X-ray images.

expected behaviour of a cohesive powder upon the introduction of a gas flow.

CASE II: VIBRATION, 1.8 cm s^{-1}

The results shown in Figure 4.7 are of the same experiment shown in Figure 4.4e and Figure 4.4f, but extended to the full experimental time to assess the effect of vibration over time. The bed initially rose as a plug again, the X-ray images corresponding to this were omitted since they are virtually identical to the experiment previously described in Section 4.4.2 and the focus here is on the effect of vibration, which started at 120 s. In Figure 4.7c-1 to Figure 4.7c-5, the initial stable channel collapsing and the initiation of fluidization are shown. Over time, compaction and partial de-fluidization took place. It can be seen that the bed height decreased, coupled with a decrease in P/P_0 from 0.93 in the first minute after vibration started to 0.87 in the last minute of the run. From the X-ray images it could also be observed that the bed was densifying during this time, with a compacted region being present, dominantly at the bottom of the bed.

CASE III: NO VIBRATION, 3.1 cm s^{-1}

The obtained results for the 3.1 cm s^{-1} experiment without vibration are shown in Figure 4.8. As in the other experiments, the bed initially formed a plug. In

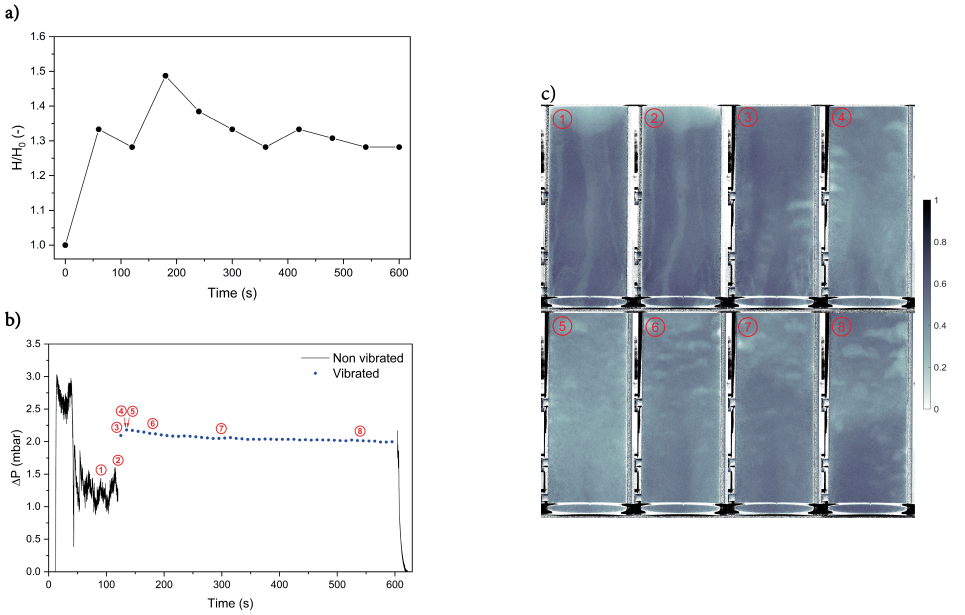


Figure 4.7: Results of fluidization experiments, 1.8 cm s^{-1} wit vibration, in all images: ① = 90 s, ② = 120 s, ③ = 121 s, ④ = 125 s, ⑤ = 130 s, ⑥ = 180 s, ⑦ = 300 s and ⑧ = 540 s into the experiment. **(a)** Bed height; **(b)** Pressure drop; **(c)** X-ray images.

Figure 4.8c-3 the fragments of the broken plug can be seen falling down, corresponding with the pressure swing seen at 30 s in Figure 4.8b. This was followed by some degree of fluidization, giving a bed height expansion ratio of 1.5 and a P/P_0 of 0.89 at the peak, 115 s. The dip in bed height and pressure drop that followed is explained by the formation of two rat-holes, seen in Figure 4.8c-5, which collapsed later leading to vein-like channel formation and some spouting and bubbling in top of the bed, coupled with stable P/P_0 of 0.77.

CASE IV: VIBRATION, 3.1 cm s^{-1}

Figure 4.9 shows the data from the experiment at 3.1 cm s^{-1} with vibration. As for all experiments, slugging occured initially, followed by some degree of fluidization before stable channels formed, which are seen in Figure 4.9c-1 and Figure 4.9c-2. After 10 s of vibration (Figure 4.9c-5), no long-term structures could be observed anymore and the bed was homogeneously fluidized. In the remaining time that the experiment was running, densification was observed, mainly at the bottom of the bed, as when 1.8 cm s^{-1} gas velocity was used. The densifying resulted in a lower bed height expansion ratio, eventually even lower than when no vibration was used at 3.1 cm s^{-1}, and a slight reduction in P/P_0 from 0.91 of in the first minute after vibration started, to 0.87 after 8 min.

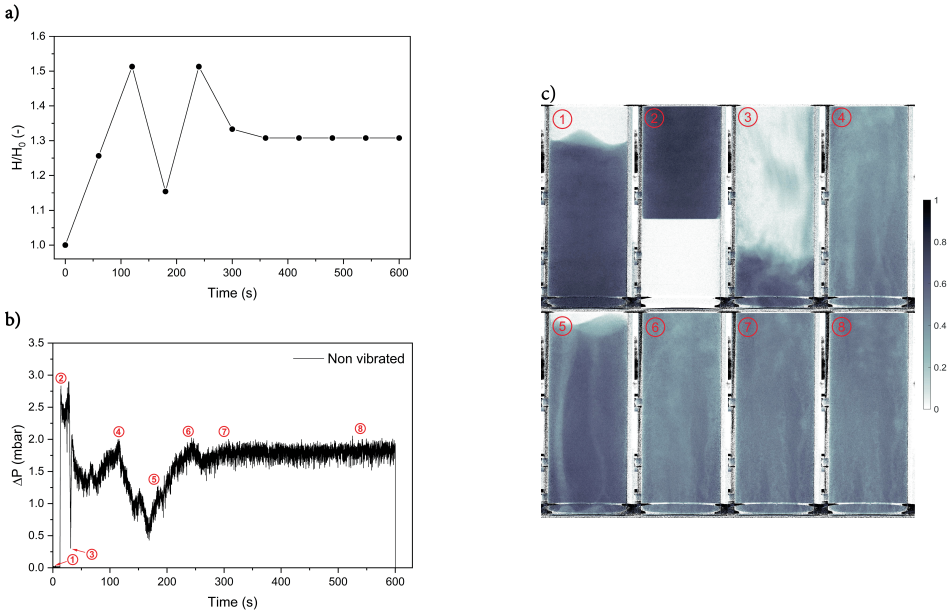


Figure 4.8: Results of fluidization experiments, 3.1 cm s^{-1} without vibration, in all images: ① = 0 s, ② = 15 s, ③ = 115 s, ④ = 120 s, ⑤ = 180 s, ⑥ = 240 s, ⑦ = 300 s and ⑧ = 540 s into the experiment. **(a)** Bed height; **(b)** Pressure drop; **(c)** X-ray images.

AGGLOMERATE SIZES

For each 10 min experiment, the agglomerate sizes (d_{10}, d_{50} and d_{90}, number-based), at all sample heights, are shown in Figure 4.10. Comparing the results, across gas velocities and with or without vibration to fresh powder, the differences are minor. Influence of vibration and gas velocities, within the ranges used in this study, on agglomerate sizes is therefore concluded to be insignificant. The densification of the bottom bed - as observed after several minutes of vibration - is not reflected by the agglomerate size.

4.4.3. CHANNEL FORMATION

Channeling took place in all the experiments conducted, either without vibration or before vibration was switched on. From the X-ray images shown in the previous sections, the variety of the formed channels across different experiments is obvious. The diversity which is seen, even under identical conditions, underlines the random nature of channel formation. It also shows no bias from the used experimental method, since no preferential place for the channels to form is observed. The results also suggest that even the formation of rat-hole like or vein-like channeling is random and not affected by gas velocity within the range

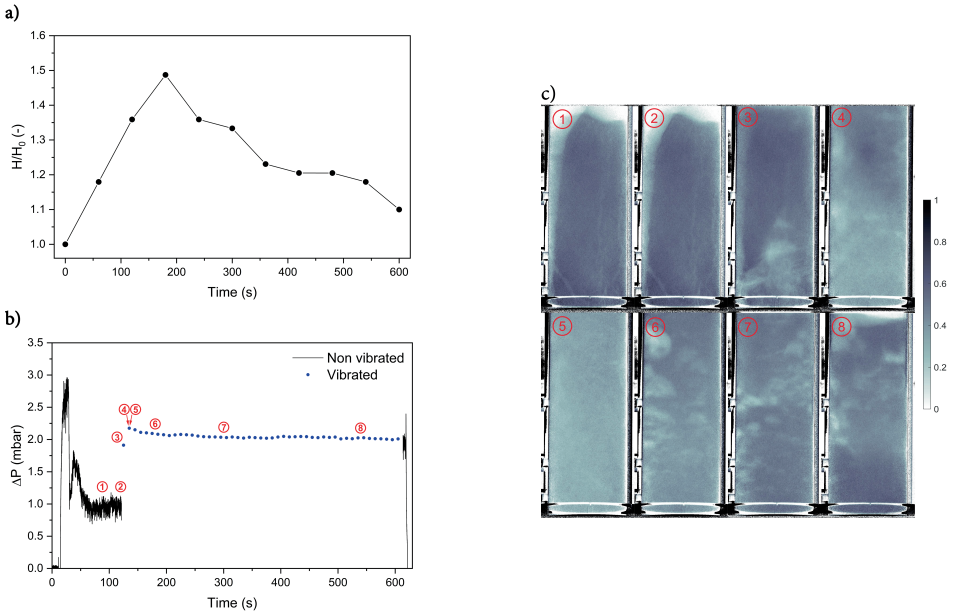


Figure 4.9: Results of fluidization experiments, 3.1 cm s^{-1} with vibration, in all images: ① = 90 s, ② = 120 s, ③ = 121 s, ④ = 125 s, ⑤ = 130 s, ⑥ = 180 s, ⑦ = 300 s and ⑧ = 540 s into the experiment. **(a)** Bed height; **(b)** Pressure drop; **(c)** X-ray images.

used for this study.

4.5. CONCLUSIONS

In this work, the mechanism behind the initiation of fluidization of cohesive micro-sized powder, by vibrations, was studied by means of X-ray imaging, pressure drop and bed height measurements. Agglomerate sizes were measured to decouple the phenomena of channel disruption and agglomerate breakage. When no vibration was used, the powder could not be properly fluidized at either 1.8 or 3.1 cm s^{-1} and severe channeling was observed, which was not always clearly reflected in the pressure drop or bed height, showcasing the limitations of these techniques when it comes to assessing the dynamics of complex systems. Gas velocity, vibration and vibration time were not found to have any significant effect on agglomerate sizes, within the parameter ranges applied in this work. From this it is concluded that vibrations initiate fluidization not by breaking agglomerates, but by disrupting channels. Furthermore, it was found that narrow, vein-like channels are disrupted significantly faster than the larger rat-holes. Finally, when vibration was employed, bed compaction was observed over time, as a dense phase formed on top of the distributor plate, causing a decrease in bed

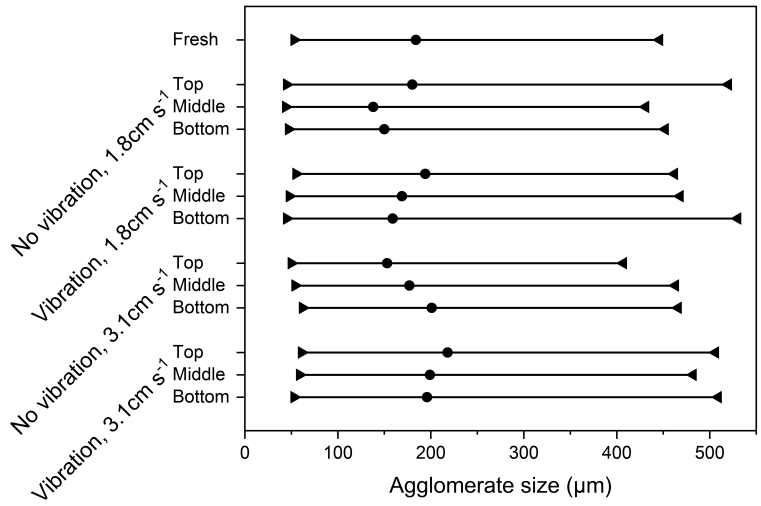


Figure 4.10: Agglomerate sizes for experiments ran at 1.8 and 3.1 $\mathrm{cm\,s^{-1}}$, with and without vibration for 8 min; ► = d_{10} • = d_{50} ◄ = d_{90}, number based.

height and pressure drop. The study was carried out using a single micro-silica powder, meaning material- and size-specific influences, which might influence results, were not investigated. While variations are deemed likely when using other powders, based on the described mechanism by which assistance methods work and the absence of a mechanism by which agglomerates can be broken before fluidizaiton is iniated, it is expected that the disruption of channels is the cause of initiated fluidization for other cohesive powders too. This study is a first step towards a better understanding of the mechanism behind vibro-assisted fluidizaton of cohesive powder and may contribute to the further development and optimization of assistance methods.

REFERENCES

[1] P. Sukumaran and E. Poulose, *Silver nanoparticles: Mechanism of antimicrobial action, synthesis, medical applications, and toxicity effects,* International Nano Letters **2** (2012), 10.1186/2228-5326-2-32.

[2] L. Guo, W. Yuan, Z. Lu, and C. M. Li, *Polymer/nanosilver composite coatings for antibacterial applications,* Colloids and Surfaces A: Physicochemical and Engineering Aspects **439**, 69 (2013).

[3] P. Li, D. E. Miser, S. Rabiei, R. T. Yadav, and M. R. Hajaligol, *The removal of carbon monoxide by iron oxide nanoparticles,* Applied Catalysis B: Environmental **43**, 151 (2003).

[4] N. Mahato and M. H. Cho, *Graphene integrated polyaniline nanostructured composite coating for protecting steels from corrosion: Synthesis, characterization, and protection mechanism of the coating material in acidic environment,* Construction and Building Materials **115**, 618 (2016).

[5] R. Kamphorst, K. Wu, S. Salameh, G. M. H. Meesters, and J. R. van Ommen, *On the fluidization of cohesive powders: Differences and similarities between micro- and nano-sized particle gas–solid fluidization,* The Canadian Journal of Chemical Engineering **101**, 227 (2023), https://onlinelibrary.wiley.com/doi/pdf/10.1002/cjce.24615 .

[6] S. Morooka, K. Kusakabe, A. Kobata, and Y. Kato, *Fluidization state of ultrafine powders,* Journal of Chemical Engineering of Japan **21**, 41 (1988).

[7] C. Nam, R. Pfeffer, R. Dave, and S. Sundaresan, *Aerated vibrofluidization of silica nanoparticles,* AIChE Journal **50**, 1776 (2004).

[8] D. Barletta and M. Poletto, *Aggregation phenomena in fluidization of cohesive powders assisted by mechanical vibrations,* Powder Technology **225**, 93 (2012).

[9] Q. Guo, H. Liu, W. Shen, X. Yan, and R. Jia, *Influence of sound wave characteristics on fluidization behaviors of ultrafine particles,* Chemical Engineering Journal **119**, 1 (2006).

[10] L. Zhou, F. Zhang, H. Kage, and Y. Mawatari, *A model for estimating agglomerate sizes of nonmagnetic nanoparticles in magnetic fluidized beds,* Korean Journal of Chemical Engineering **30**, 501 (2013).

[11] X. Zhang, Y. Zhou, and J. Zhu, *Enhanced fluidization of group a particles modulated by group c powder,* Powder Technology **377**, 684 (2021).

[12] J. A. Quevedo and R. Pfeffer, *In situ measurements of gas fluidized nanoagglomerates,* Industrial & Engineering Chemistry Research **49**, 5263 (2010).

[13] H. N. Lari, J. Chaouki, and J. R. Tavares, *De-agglomeration of nanoparticles in a jet impactor-assisted fluidized bed,* Powder Technology **316**, 455 (2017).

[14] E. Al-Ghurabi, M. Shahabuddin, N. Siva Kumar, and M. Asif, *Deagglomeration of ultrafine hydrophilic nanopowder using low-frequency pulsed fluidization,* Nanomaterials **10**, 388 (2020).

[15] S. Ali, E. AL-Ghurabi, A. Ajbar, Y. Mohammed, M. Boumaza, and M. Asif, *Effect of frequency on pulsed fluidized beds of ultrafine powders,* Journal of Nanomaterials **2016**, 1 (2016).

[16] S. S. Ali and M. Asif, *Fluidization of nano-powders: Effect of flow pulsation,* Powder Technology **225**, 86 (2012).

[17] J. van Ommen, D. King, A. Weimer, R. Pfeffer, and B. van Wachem, *Experiments and modelling of micro-ject assisted fluidization of nanoparticles,* The 13th International Conference on Fluidization (2010).

[18] Y. Mawatari, T. Koide, T. Ikegami, Y. Tatemoto, and K. Noda, *Characteristics of vibrofluidization for fine powder under reduced pressure,* Advanced Powder Technology **14**, 559 (2003).

[19] J. Gómez-Hernández, S. Sánchez-Delgado, E. Wagner, R. F. Mudde, and J. R. van Ommen, *Characterization of TiO_2 nanoparticles fluidization using x-ray imaging and pressure signals,* Powder Technology **316**, 446 (2017).

[20] I. Mema, E. C. Wagner, J. R. van Ommen, and J. T. Padding, *Fluidization of spherical versus elongated particles-experimental investigation using x-ray tomography,* Chemical Engineering Journal **397**, 125203 (2020).

[21] D. Macrì, S. Sutcliffe, and P. Lettieri, *Fluidized bed sintering in tio2 and coke systems,* Chemical Engineering Journal **381**, 122711 (2020).

[22] S. Maurer, E. C. Wagner, J. R. van Ommen, T. J. Schildhauer, S. L. Teske, S. M. A. Biollaz, A. Wokaun, and R. F. Mudde, *Influence of vertical internals on a bubbling fluidized bed characterized by x-ray tomography,* International Journal of Multiphase Flow **75**, 237 (2015).

[23] A. Helmi, E. C. Wagner, F. Gallucci, M. van Sint Annaland, J. R. van Ommen, and R. F. Mudde, *On the hydrodynamics of membrane assisted fluidized bed reactors using x-ray analysis,* Chemical Engineering and Processing: Process Intensification **122**, 508 (2017).

[24] F. Barthel, M. Bieberle, D. Hoppe, M. Banowski, and U. Hampel, *Velocity measurement for two-phase flows based on ultrafast x-ray tomography,* Flow Measurement and Instrumentation **46**, 196 (2015).

[25] K. Wu, F. Galli, J. de Tommaso, G. S. Patience, and J. R. van Ommen, *Experimental methods in chemical engineering: Pressure,* The Canadian Journal of Chemical Engineering **101**, 41 (2023), https://onlinelibrary.wiley.com/doi/pdf/10.1002/cjce.24533 .

5

EFFECT OF VIBRATIONAL MODES ON FLUIDIZATION CHARACTERISTICS AND SOLID DISTRIBUTION OF COHESIVE MICRO-AND NANO-SILICA POWDERS

In the previous chapter, we demonstrated that assistance methods enhance fluidization primarily by disrupting channels within the powder bed. Based on these findings, and considering that channels run vertically, we suspect that horizontal motion of the bed may be favorable over vertical motion. In this chapter we explore the effects of combined horizontal and vertical vibration on the fluidization quality of micro- and nanopowder. We also show how fractional pressure drop measurements provide additional insight into fluidization quality

This chapter has been published as "Effect of vibrational modes on fluidization characteristics and solid distribution of cohesive micro-and nano-silica powders" by R. Kamphorst, K. Wu, M. van Baarlen, G.M.H. Meesters and J.R. van Ommen, Chemical Engineering Science **291**, 119911 (2024)

In this study, the impact of different vibrational modes on the fluidization characteristics of cohesive micro-and nano-silica powder was examined. Fractional pressure drop, bed expansion measurements, and X-ray imaging were utilized to characterize the fluidization quality. The densities of the emulsion phase at the top and bottom of the column were quantified and compared, providing insights into the solid distribution within the fluidized bed. In the absence of vibration, neither powder could be fluidized within the considered range of superficial gas velocities. Vertical vibration was found to initiate fluidization for both powders. In contrast, elliptical vibration failed to overcome the channelling behavior when fluidizing the micro-powder. For nano-powder, combined channelling and powder compaction occurred when the bed was subjected to elliptical vibration. For the micro-powder, it was observed that bed homogeneity was independent of vertical vibration intensity but improved with increasing superficial gas velocity. For nano-powder, intensifying vertical vibration led to segregation, likely due to agglomerate densification. Furthermore, fractional pressure drop measurements proved to be a strong tool in assessing fluidization quality, providing insights that could not be attained by conventional indicators.

5.1. INTRODUCTION

In recent years, there has been a growing interest in cohesive micro- and nano-powders due to their diverse applications across a range of fields, including catalysis [1, 2], electronic devices [3, 4] and food production [5, 6]. Fluidization is often the preferred method for processing powders [7, 8]. However, powders consisting of primary particles smaller than 30 µm are typically cohesive, complicating the fluidization process. The cohesive nature of these powders stems from the scaling of inter-particle forces, with respect to particle size [8–10]. Upon decreasing the particle size, the attractive van der Waals forces start dominating (in the absence of moisture), introducing complications for fluidization. Conventional fluidization of such powders is typically characterized by channelling and excessive agglomeration, severely limiting gas-solid contact and internal mixing [11–13]. If present, these phenomena dominate the often poor fluidization behaviour [14–16]. The reduced gas-solid interactions in such systems undermine applications targeted at the high surface-to-volume ratio of (ultra-)fine particles. Additionally, a homogeneous solid distribution within the bed - indicating superior internal mixing as well as inter-phase heat and mass transfer - is beneficial for most applications and is severely lacking when utilizing conventional fluidization with such powders. To improve the fluidization quality of cohesive powders, various techniques, such as pulsed flow [17, 18], mechanical agitation [13] and mechanical vibration [19, 20], are described in literature. These assistance methods have been demonstrated to disrupt channelling and reduce agglomerate sizes. Out of the assistance methods found in literature, mechanical vibration has seen the most interest from researchers. Commonly listed benefits of this technique include the lack of internals and its applicability for a broad range of powders. The vast majority of studies on this method focus solely on vertical vibration, with only a few studies considering horizontal motion. Considering that a combination of horizontal and vertical motion, resulting in an elliptical trajectory, is often applied in industrial fluidized bed dryers [21–23], this vibration orientation begs to be explored.

Previous research has shown that stratification of agglomerates occurs within the fluidized bed [24], with larger agglomerates predominantly found in the bottom and smaller ones in the top of the emulsion phase. Since bed homogeneity is desirable, optimizing assistance methods necessitates insight and quantification of solid distribution. While bed homogeneity is a common focus in studies on assistance methods [25–27], there is a lack of quantitative assessment in this regard.

In this study, the impact of elliptical vibration, as well as the effect of the intensity of vertical vibration, on the fluidization of cohesive micro- and nano-silica were studied. Total pressure drop and bed height expansion measurements, as well as

X-ray imaging, were employed. Furthermore, we evaluated the solid distribution within vibro-fluidized beds, subjected to various vibration modes. This analysis was performed by examining the density distribution alongside the bed height, calculated from fractional pressure drop measurements.

5.2. MATERIALS AND METHODS

5.2.1. EXPERIMENTAL

For all fluidization experiments, a glass column with an inner diameter of 2.5 cm was used. Similar column sizes are commonly found in literature, both for studying the fundamentals [28, 29] and applications of fluidized beds [30–32]. The column was filled with powder reaching a bed height of either 5.0 cm (with a ratio of initial bed height to column inner diameter $H_0/D = 2.0$), denoted as 'low', or 7.5 cm ($H_0/D = 3.0$), denoted as a 'high' initial bed height. Prior to each experiment, the powder sample was weighed on an ABJ 320-4NM scale, allowing to calculate the static pressure exhibited by a given sample in the absence of a gas flow. Dry nitrogen was supplied through a SIKA-R 3 AX distributor plate. Two pressure sensors utilized during each experiment, one of which measured the pressure drop, ΔP, from the bottom to the top of the column, the other measuring from $2/3^{rd}$ of the initial bed height to the top, as depicted in Figure 5.1**a**. FSM DPS pressure sensors were used for the micro-sized particles, whereas Siemens QBM2030-1U pressure sensors were employed for the nano-powder. The setup was mounted on a PTL-40/40 vibrating table. When operating in the vertical orientation, two distinct modes were used, which will be referred to as a 'low' setting and a 'high' setting throughout this work. The 'low' intensity corresponds to the lowest setting at which the micro-powder could consistently be fluidized within the range of superficial gas velocities considered in this study. The same vibrating table was used to create both vertical and horizontal vibrations simultaneously, resulting in an elliptical motion. The relevant parameters of the selected vibrational modes are provided in Table 5.1.

Vibrational settings				
Label	A_x (mm)	f_x (Hz)	A_y (mm)	f_y (Hz)
Low vertical	0	0	0.20	36
High vertical	0	0	0.30	51
Elliptical	0.15	36	0.14	36

Table 5.1: Amplitudes and frequencies of studied vibrational modes

Both powders used in the experimental investigation are SiO_2 based. The micro-

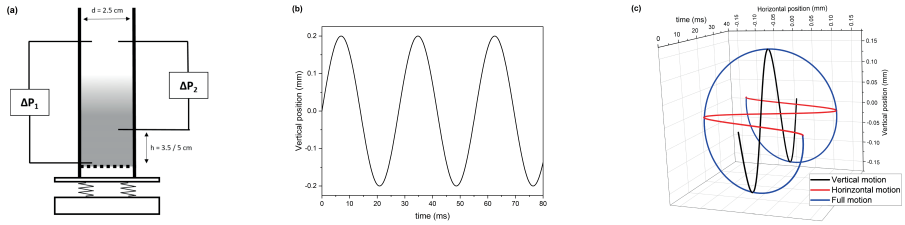


Figure 5.1: **(a)** experimental vibro-fluidization setup with location of pressure sensors, depending on initial powder bed height, **(b)** vertical and **(c)** elliptical vibration trajectories

sized powder, Köstropur 050818, has a number-based primary particle size of 4.4 µm (d_{50}), as measured by laser diffraction (see Figure 5.2**a**). The nano-sized powder, Aerosil 300, is characterized by a number-based primary particle size of 6.7 nm (d_{50}), as obtained from analysis of TEM images (see Figure 5.2**b**). The dominant difference in fluidization behaviour observed within cohesive powders originates from the different agglomerate structures formed by micro- and nano-powders, being single-stage or multi-stage agglomerates respectively [8]. Therefore, the powders considered in this study offer insights that are broadly applicable to cohesive powders as a whole.

Previous studies have shown that powder history, particularly slow compaction during storage, significantly affects the fluidization behaviour of cohesive powders [33, 34]. To ensure reproducibility of our work, fresh powder was used for each experiment. Additionally, the powder was sieved (mesh size of 600 µm for micro- and 224 µm for nano-powder) prior to any measurement. This procedure maintained a consistent state of aeration for the powder bed prior to conducting experiments. Note that the used pore sizes are orders of magnitude larger than the primary particle size of the respective powders, therefore having a negligible impact on the particle size distributions. Moreover, since prior studies have shown fluidization behaviour to change over time [35, 36], each measurement was taken 10 min after the initiation of gas flow. Unless stated otherwise, the presented data points represent the average of three separate experiments.

5.2.2. DENSITY CALCULATIONS

The theoretical maximum pressure drop over a fluidized bed can be calculated as per Equation (5.1). Here, ΔP_0 represents the maximum theoretical pressure drop, m_{bed} the mass of powder in the column, g the gravitational acceleration, and S_{column} the cross-sectional area of the column. The fraction of fluidized ma-

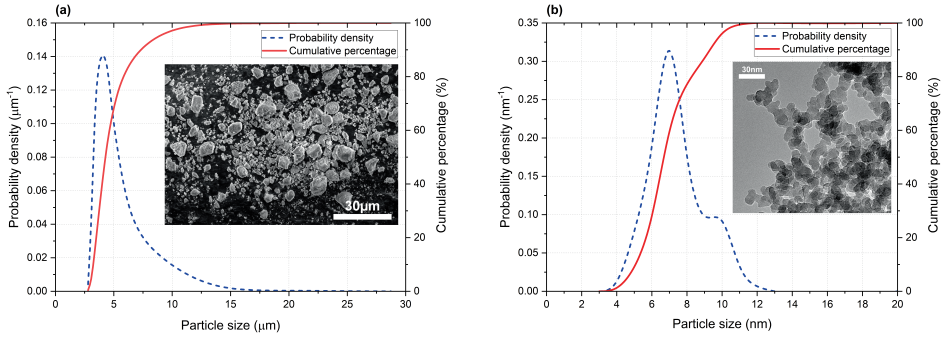


Figure 5.2: Number-based particle size distributions of the used **(a)** micro- and **(b)** nano-powder

terial, X_f, is calculated as per Equation (5.2), where P_{tot} represents the measured pressure drop over the entire bed. For the fractional measurements, the bed was divided into a bottom and top section. The bottom phase runs from the distributor plate to the location of the pressure sensor at 3.5 cm for low and 5 cm for high bed initial height, as shown in Section 5.2.1a. The top phase spans from the bottom sensor location to the top of the emulsion phase. The pressure drop in the top section was measured directly, while the ΔP of the bottom section was obtained by the difference between the entire bed and the top section. For calculation of the emulsion density in the top of the bed, Equation (5.3) was used. Here, ΔP_{top} represents the pressure drop measured over the top section of the bed and H_{top} the height of the bed in the top section, which is equal to the total bed height, H_{bed}, minus the height of the bottom pressure sensor, H_{bot}. Note that Equation (5.3) implicitly assumes the powder present above the top pressure sensor to be fully fluidized. If this condition is not fulfilled, the equation can still be used to calculate a surrogate top density. While the calculated value may not provide an adequate assessment of the fluidized state in the top section by itself in such case, the ratio between top and bottom bed densities, will still provide valuable insights into the quality of fluidization as will be shown in the result section.

$$\Delta P_0 = \frac{m_{\text{bed}} \cdot g}{S_{\text{column}}} \tag{5.1}$$

$$X_f = \frac{\Delta P_{\text{tot}}}{\Delta P_0} \tag{5.2}$$

$$\rho_{\text{top}} = \frac{\Delta P_{\text{top}}}{H_{\text{top}} \cdot g} \tag{5.3}$$

Additional considerations are required to calculate the density of the emulsion phase in the bottom section of the bed. The fluidized fraction is typically less than unity, meaning a fraction of the powder unagitated, not contributing to the pressure drop. This stagnant powder occupies space in the bottom section, which needs to be corrected for. Equation (5.4) was used to calculate ρ_{bot}, the density in the bottom section of the bed. In this equation, ΔP_{bot} represents the pressure drop over the bottom section of the bed and ρ_b the bulk density of the powder. The ρ_{b} after sieving is 134 kg m^{-3} for micro-silica and 50 kg m^{-3} for nano-silica. For the density ratios presented in this work, the calculated bottom density was divided by the (surrogate) top density.

$$\rho_{\text{bot}} = \frac{S_{\text{column}} \cdot \Delta P_{\text{bot}}}{g \cdot \left(S_{\text{column}} \cdot H_{\text{bot}} - \frac{m_{\text{bed}}(1-X_f)}{\rho_b} \right)} \tag{5.4}$$

5.2.3. X-RAY IMAGING

To provide additional insight in the gas-solid distribution within the fluidized bed and verify the results obtained by the fractional pressure drop measurements, X-ray imaging was performed. Experiments were performed using an in-house fast X-ray imaging set-up, utilising a single standard industrial type X-ray tube source (Yxlon International GmbH) with a maximum energy of 150 keV working in cone beam mode and a Teledyne Dalsa Xineos 2D detector. A detailed description of this setup can be found in our previous work [14].

5.3. RESULTS AND DISCUSSION

5.3.1. UNASSISTED FLUIDIZATION

Previous research findings indicated that cohesive powders, with particle sizes comparable to those used in our study, may exhibit fluidization without the need for assistance methods [37, 38]. However, as can be seen in Figure 5.3, unassisted operation did not yield desirable fluidization quality for the powders considered in this study. The bed expansion was observed to be relatively modest in all experiments. This expansion primarily resulted from the formation of gas channels, looser packing, and sporadic particle spouting. The significant initial pressure drop ratio, observed for all experiments, was attributed to plugs which did not break at low gas velocities, consistent with our earlier work [14]. At higher gas velocities, the $\Delta P/\Delta P_0$ exhibited high fluctuations due to the formation and subsequent collapse of channels coupled with occasional spouting in the upper section of the bed. Given the inherent unpredictability of the channelling behaviour in unassisted fluidization of cohesive powder, attaining reproducible

data becomes challenging. Therefore, the data points presented in Figure 5.3 are of single experiments. Nevertheless, repeated runs yielded similarly fluctuating profiles.

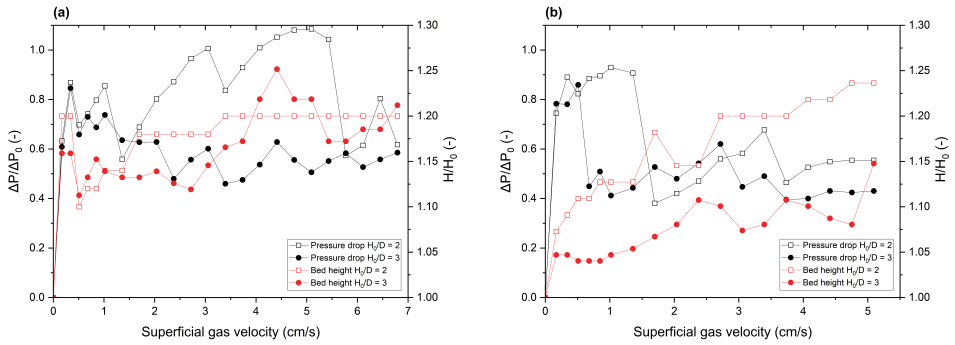


Figure 5.3: Normalized pressure drop and bed expansion data from unassisted fluidization of **(a)** micro and **(b)** nano-powder

5

5.3.2. VIBRO-FLUIDIZATION OF MICRO-POWDER

The normalized pressure drop values of micro-powder beds under different vibrational modes are depicted in Figure 5.4. The dashed vertical lines indicate minimum fluidization velocities, corresponding to the first pressure drop value that falls within a 1% range of the average of the five consecutive data points. At low-intensity vertical and elliptical vibration, the values appear to be irregular at low gas velocities, irrespective of initial bed height. This behaviour corresponds to slugging as well as the formation and subsequent collapse of gas channels, comparable to unassisted fluidization. For vertical vibration, the final $\Delta P/\Delta P_0$ all range from 0.88 to 0.91, indicating no significant dependency on vibrational intensity or initial bed height. In our prior research, utilizing the same micro-powder in a 9 cm column, vibrated at f=50 Hz and A=1 mm, $\Delta P/\Delta P_0$ values of up to 0.93 were found [14]. The similar final normalized pressure drop values, while utilizing vastly different column sizes, suggests that wall effects played not significant role during these experiments. Furthermore, the $\Delta P/\Delta P_0$ is comparable to those reported by other studies on cohesive micro powders in vibro-fluidized beds, ranging from 0.7 to 1.0 [25, 26, 39–41]. A decrease in minimum fluidization velocity with respect to initial bed height can be observed, which was also found during the experiments with nano-particles. This can be explained by considering the channel dimensions. To provide a consistent gas bypass, a channel

needs to span the entire bed height. A taller bed will produce longer, and comparatively more slender, channels, which are more easily disrupted, leading to improved fluidization (i.e., a lower minimum fluidization velocity). Consistent with earlier studies, an increase in vertical vibrational intensity was found to decrease the minimum fluidization velocity [20, 25]. In the case of elliptical vibration, the $\Delta P/\Delta P_0$ values remain consistently low, compared to vertical vibration. Some degree of stable fluidization is achieved, as indicated by the smooth pressure drop curve at high superficial gas velocities, compared to the one found for unassisted fluidization. However, the presence of gas channels is visually observed throughout all experiments.

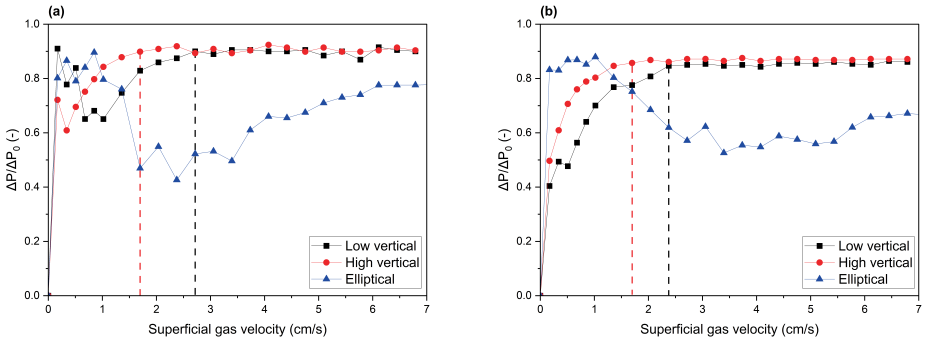


Figure 5.4: Normalized pressure drop of vibro-fluidized beds consisting of micro-powder with **(a)** low and **(b)** high initial bed heights, the dashed lines indicate the minimum fluidization velocities

Contrary to the expectation of enhancing fluidization through the introduction of additional energy, the horizontal component of elliptical vibration was found to counteract the disruptive effects of vertical vibrations. This is apparent from the comparatively low $\Delta P/\Delta P_0$ data obtained while introducing elliptical vibrations, as shown in Figure 5.4. The same can be seen by considering the coefficients of variation of the obtained data, which can be found in the supplementary materials. Furthermore, looking at Figure 5.4, lowering the vibrational intensity shifts the obtained results, delaying the pressure plateau at which fluidization occurs, while the trend itself is preserved, the same was demonstrated by earlier studies [25, 42, 43]. When considering the results of elliptical vibration however, it can be seen that no such trend is visible at all, suggesting the underlying phenomena dominating this system are fundamentally different. Note that full fluidization can sometimes be obtained when applying vertical vibration of a lower intensity than used in this study. Therefore, the absence of full fluidization

in all experiments conducted with elliptical vibration cannot be explained by the lower amplitude in the vertical direction considered in isolation.

It was hypothesized that this phenomenon may be attributed to the compaction of powder against the column wall induced by the horizontal motion, similar to the effect of vertical vibration in creating a dense layer near the distributor plate [19]. In order to investigate this hypothesis, additional experiments were performed, using the X-ray imaging technique, to inspect the flow patterns. The results of these experiments are depicted in Figure 5.5. The displayed images represent an average of 650 frames (10 s) captured 10 min after the initiation of gas flow. First of all, Figure 5.5a shows channelling in the absence of any vibration applied to the system. Furthermore, since structures can be seen, even while the images are time-averaged, it can be concluded that these structures are mostly stable. In Figure 5.5b and c the gas fractions of fluidized beds subjected to low and high intensity vertical vibration are displayed. These beds demonstrate significant bed expansion and a fairly homogeneous emulsion phase, indicating the absence of permanent structures. However, the bottom region of the bed is significantly denser than the top section for either vibration intensity. This phenomenon was also observed in a study by Wu et al. utilizing a significantly higher amplitude for the vibration [19]. The consistent appearance of this region at the lowest intensity at which consistent fluidization can be achieved, as well as at significantly higher frequencies and amplitudes of vibration, indicates its presence to be unavoidable. The lack of long-term structures in the bottom sections does however indicate that this region is still fluidized under influence of either vertical vibration intensity. Finally Figure 5.5d provided insight in the bed operated at elliptical vibration. Long-term structures can be observed with only a small fraction of the powder being fluidized. Based on the similarity observed in the flow patterns between elliptically vibrated and non-vibrated beds, it can be concluded that elliptical vibration does not have a discernible influence on the channel formation or disruption. Furthermore, these findings highlight the mitigation of vertical vibrations, when horizontal motion is employed, in a manner resulting in an elliptical motion of the system. However, these experiments do not provide conclusive evidence to determine whether this phenomenon is solely due to horizontal vibrations or the specific combination of horizontal and vertical vibrations employed in our experiments. The persistent channelling also explains the relatively low and stable normalized pressure drop values observed in Figure 5.4. Additionally, the anticipated compaction of particles near the column walls was not obvious, and an accurate assessment of compaction at the bottom cannot be fully realized, as the presence of a clamp obstructed part of the view of the lower section.

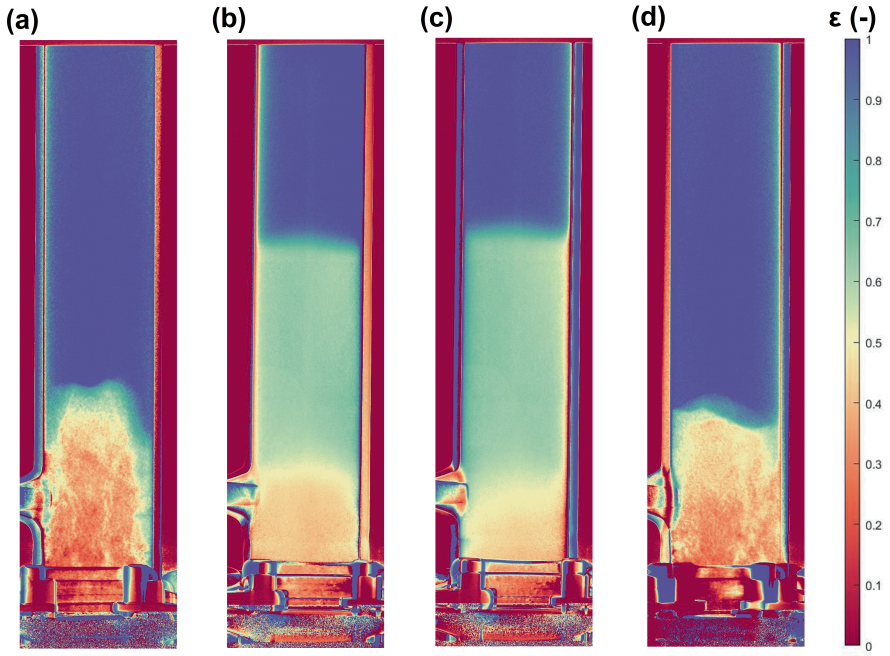


Figure 5.5: 10 second average X-ray images of the bed of micro particles in a fluidized bed column with a superficial gas velocity of 3.0 $\mathrm{cm\,s^{-1}}$, subjected **(a)** no vibration, **(b)** low intensity vertical vibration, **(c)** high intensity vertical vibration and **(d)** elliptical vibration, the legend on the right provides the gas fraction corresponding to each color

The bed expansion of the micro-powder reached a plateau across all experimental conditions, as shown in Figure 5.6. The comparison of the $\Delta P/\Delta P_0$ and H/H_0 graphs also reveals that the plateau in bed expansion typically occurs at higher gas velocities. This observation suggests that the expansion of the bed between the minimum fluidization velocity and the velocity at maximum bed expansion is primarily influenced by the increased dilation of the emulsion phase, rather than the additional fraction of powder becoming fluidized. Moreover, a comparison between Figure 5.6a and Figure 5.6b illustrates that lower initial bed heights result in higher bed expansion ratios across all vibration modes investigated. This finding indicates a potential correlation between the attenuation of vibrations throughout the powder bed, resulting in the vibrations having a greater impact on shallower powder beds. However, this limitation may be partially overcome by increasing the vibrational intensity, thereby increasing the penetration depth of the effective vibration into the bed, as suggested in Figure 5.6b.

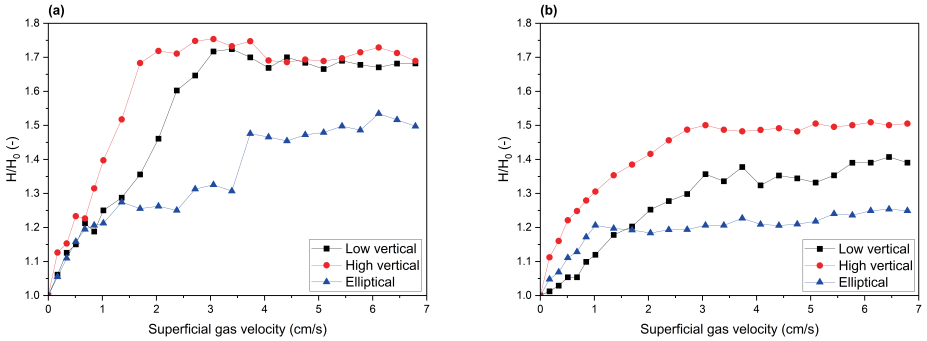


Figure 5.6: Normalized bed expansions of vibro-fluidized beds consisting of micro-powder with **(a)** low and **(b)** high initial bed heights

5

The density ratios between the bottom and top sections of the micro-powder bed, as defined in Section 5.2.2, are displayed in Figure 5.7. The data related to vertical vibration modes spans from the minimum fluidization point to the maximum gas velocity at which experiments were performed. Across these cases, it can be observed that the density in the bottom region of the bed is approximately twice that of the top section. Previous research has indicated the occurrence of agglomerate stratification in fluidized beds containing micro- and nano-particles [24]. Provided that larger agglomerates are more often found in the bottom of the bed, it is expected that the density of the emulsion phase is higher in this region since smaller agglomerates, experiencing the same gas velocity are more likely to be lifted by the gas flow, due to their lower terminal velocity. This results in a higher inter-agglomerate voidage and therefore a less dense phase. However, as mentioned earlier, the vibration itself induces the formation of a dense phase in the bottom region of a vibro-fluidized bed. Rather than segregation based on agglomerate size, the bottom phase getting hit repeatedly by the distributor plate appears to be the dominant factor leading to this dense phase. An increase in the gas velocity was found to mitigate this issue, independent of vibration intensity. It is important to note that this information cannot be deduced from the total pressure drop or bed expansion measurements. Solely relying on these indicators, one would find no further improvements in fluidization quality after $3.0\,\mathrm{cm\,s^{-1}}$, as both $\Delta P/\Delta P_0$ and H/H_0 reach a plateau at this point, which underscores the benefits of fractional pressure drop measurements. For the elliptically vibrated beds, exhibiting no significant degree of fluidization at any of the experimental conditions, density ratios were plotted from $4\,\mathrm{cm\,s^{-1}}$

onward. The results for both initial bed heights may suggest a completely homogeneous mixture. However, effective fluidization did not occur as indicated by the pressure drop and by X-ray imaging. Instead, these results indicate persistent channelling in the bottom section of the bed, resulting in a low pressure drop within that region, while occasional spouting behavior in the top of the bed causes a relatively high pressure drop in that section, resulting in a ratio less than 1. Moreover, higher initial bed heights lead to even lower density ratios due to the instability of taller and slender channels, which are more prone to collapse in the top of the bed, leading to enhanced spouting and local pressure drop values in this region. These findings reinforce the conclusion that elliptical vibration does not consistently eliminate channelling. Additionally, these results demonstrate the capability of fractional pressure drop measurements to indicate the presence of channels within the powder bed by obtaining density ratio approaching or below unity.

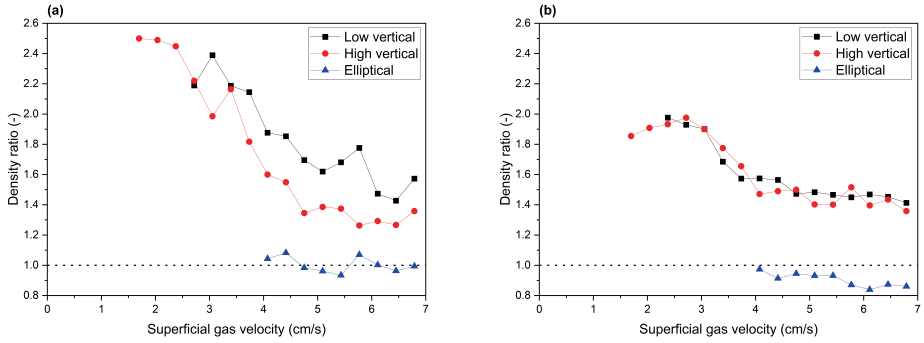


Figure 5.7: Density ratios between top and bottom sections of vibro-fluidized beds consisting of micro-powder with **(a)** low and **(b)** high initial bed heights

5.3.3. VIBRO-FLUIDIZATION OF NANO-POWDER

The pressure drop values observed during experiments conducted with nano-powder are displayed in Figure 5.8. Similar to the micro-powder results, the fluctuations in some of the data at low gas velocities can be attributed to slugging and channelling phenomena. Moreover, all vibration modes exhibit a plateau in the pressure drop ratio, the elliptically vibrated bed at significantly lower values than both vertically vibrated ones. High intensity vertical vibrations consistently exhibit the lowest minimum fluidization velocity, followed by low intensity vertical vibrations, due to its low normalized pressure drop value, the elliptically

vibrated bed is not considered to be adequately fluidized. A discussion on the coefficients of variation corresponding to the pressure drop data can be found in the supplementary materials. As for the micro-powder, an increased aspect ratio of the bed lowers the minimum fluidization velocity due to the presence of less stable channels.

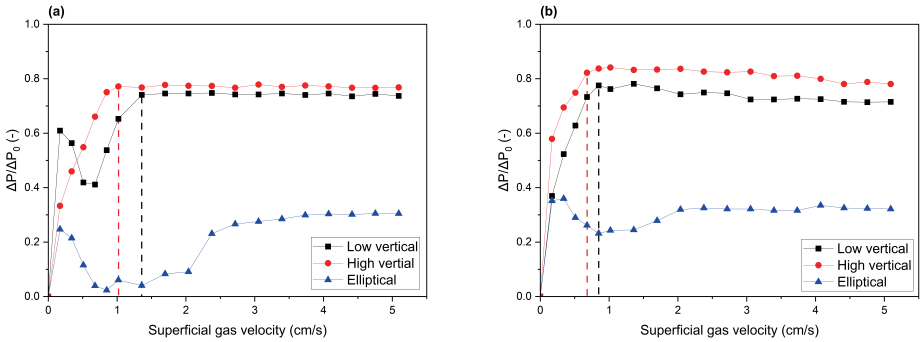


Figure 5.8: Normalized pressure drop of vibro-fluidized beds consisting of nano-powder with **(a)** low and **(b)** high initial bed heights, the dashed lines indicate the minimum fluidization velocities

According to Figure 5.8 and Figure 5.9, high pressure drop values are accompanied by high bed expansion ratios. As for the micro-powder, the peak values of H/H_0 are attained at gas velocities beyond u_{mf} and higher initial bed heights result in lower bed expansion ratios, indicating signal attenuation throughout the beds. Additionally, while the pressure drop values were low, substantial bed expansion is observed with elliptical vibration. Zhang et al. reported similar bed expansions for a horizontally vibrated bed of Aerosil 300 at 33.4 Hz [44], which aligns with our findings for elliptical vibration. In that study, the conclusion that the Aerosil 300 was well-fluidized was solely based on bed expansion as no pressure drop values were reported. Our pressure drop results do however indicate that only a limited amount of powder is agitated, highlighting the limitations of bed expansion data in reliably assessing the fluidization quality of cohesive powders. The normalized pressure drop plateau values for vertical vibration found in this work range from 0.75 to 0.85. This is reasonably close to the range of 0.82–1.1 found in other studies on vibro-fluidization of nanopowders [26, 35, 45].

While the low pressure drop values observed with elliptical vibration can be partially explained by ineffective channel disruption, as discussed in Section 5.3.2, the existence of a plateau in normalized pressure drop, accompanied by a significant bed expansion, suggests at least part of the bed is fluidized. It is therefore

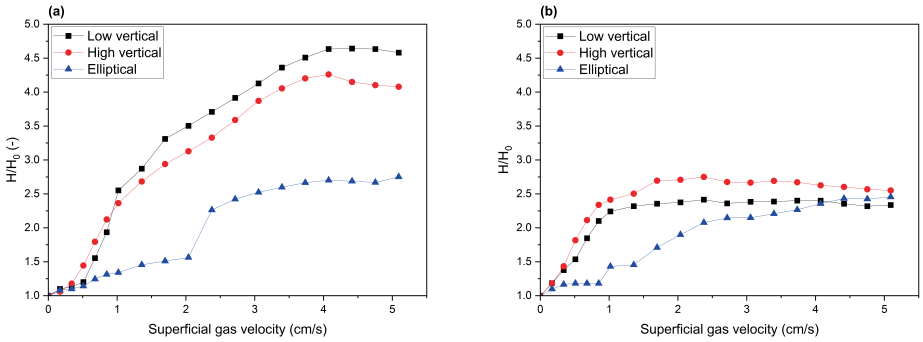


Figure 5.9: Normalized bed expansions of vibro-fluidized beds consisting of nano-powder with **(a)** low and **(b)** high initial bed heights

anticipated that channel destabilization is not the sole contributing factor. To elucidate, additional experiments were conducted. Similar to how vertical vibration induces compaction of the bottom fraction of the bed, we hypothesized that the column walls would provide an additional source of compaction due to the horizontal component of the elliptical motion. The low bulk density of the silica nano-powder complicates the exact determination of density differences with X-ray imaging, necessitating the use of alternative methods. To this end, nano-powder was fluidized at $3\,\mathrm{cm\,s^{-1}}$ for 10 min with an initial H/D of 2.0 for each vibration mode. After terminating the gas flow, loose powder was carefully extracted using a suction probe, inserted from the top of the column. Subsequently, the windbox was then removed, and all remaining powder, compacted on the column wall and distributor plate, was collected. The weight fraction of the collected powders were presented in Figure 5.10, each data point representing an average of five measurements. The results indicate no significant difference between low and high intensity vertical vibrations. The nano-powder being predominantly found at the bottom of the column after employing either vertical vibration mode, supports the idea that this compaction results from tapping by the distributor plate. In contrast, when elliptical vibration was employed, the amount of compacted powder nearly triples compared to that observed in vertical vibrations. Although not quantified, visual observations confirm a substantial amount of powder adhering to the column walls. It should be noted that triboelectric forces, causing the nano-powder to adhere to the column walls, may contribute to this phenomenon as well. The observed compaction can account for the relatively low pressure drop observed during the fluidization of the nano-powder with elliptical vibration, as depicted in Figure 5.8, as this fraction of pow-

der does not actively participate in the fluidization process.

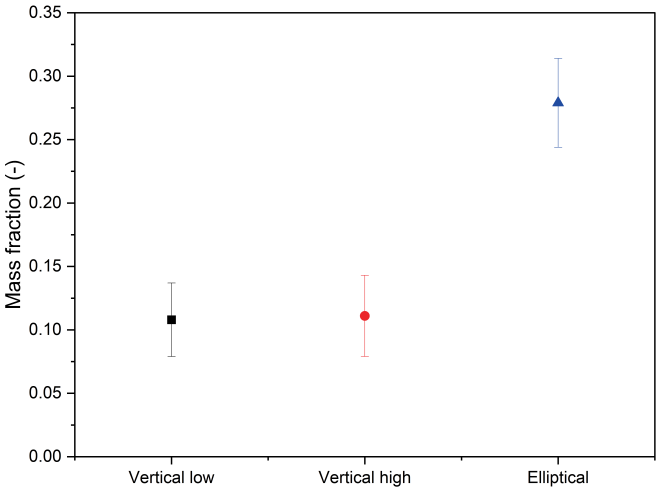


Figure 5.10: Fraction of compacted nano-powder present in the system after fluidizing under different vibration conditions, averages of 5 measurements, error bars correspond to the standard deviation

In Figure 5.11, the influence of gas velocity on the density ratios of nano-powder under the selected vibration modes is presented. As with the micro-powder analysis, the ratios are plotted from u_{mf} onwards for vertical vibrations, while for elliptical vibration, the gas velocities corresponding to the pressure drop plateaus are displayed. The density ratios under both vertical intensities are 1.5 to 2 times higher than those for the micro-powder. This observation can be attributed to the relatively denser bottom section of the nano-powder, stemming from its higher compactability. Furthermore, higher intensities were found to depress the bed homogeneity. However, based on the findings presented in Figure 5.10, this is not attributable to variations in compacted regions with increased vibration intensity. Rather, we hypothesize that agglomerates densify, leading to enhanced stratification within the emulsion phase. Existing literature indicates that nanoparticle agglomerates undergo densification over time, the higher vibration intensity is expected to increase agglomerate-agglomerate and agglomerate-wall collisions, amplifying this densification. The densification process is associated with a decrease in agglomerate size [36], which, combined with other studies demonstrating reduced agglomerate size with increased vibration intensities [26, 40], substantiates this hypothesis. In the case of elliptical vibration, the den-

sity ratios are significantly higher (note the axis break in Figure 5.11b), indicating poor internal mixing within the emulsion phase. It is important to note that the observed poor solid distribution cannot be attributed to the compacted fractions shown in Figure 5.10, as they were measured to exhibit a minimal pressure drop. Instead, it is suspected that the increased particle-wall collisions resulting from the horizontal component of the elliptical motion results in denser agglomerates, amplifying the density gradient along the bed height. Additionally, the considerable portion of un-fluidized powder introduces sensitivity to the calculated density ratios, as these results rely on the correction method for the volume of the bottom section, as seen in Equation (5.4). It is suspected that the density of the un-fluidized fraction may deviate from the bulk density, possibly reflecting a tapped density. It is worth noting that such a deviation may lead to the results presenting an exaggerated representation of the actual density ratio.

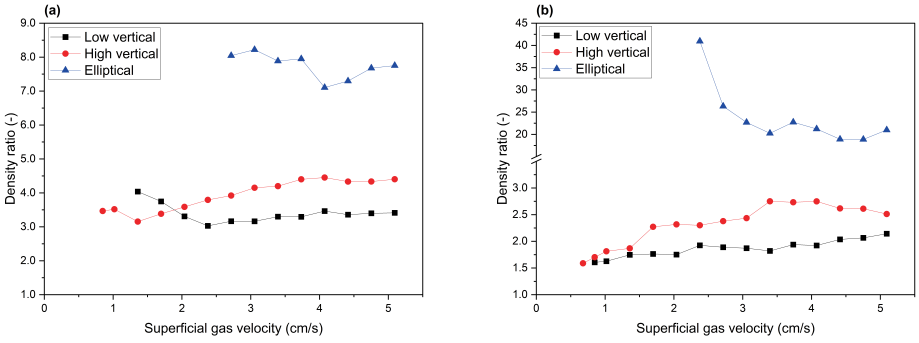


Figure 5.11: Density ratios between top and bottom sections of vibro-fluidized beds consisting of nano-powder with **(a)** low and **(b)** high initial bed heights

5.3.4. COMPARATIVE ANALYSIS OF MICRO- AND NANO-SILICA VIBRO-FLUIDIZATION

Upon examining the datasets obtained from all experiments collectively, several overarching conclusions can be drawn. Neither powder could be fluidized without the aid of an assistance method, while high and low intensity vertical vibrations were effective in achieving a fluidized state for both powders. Comparing beds with high and low initial bed heights, the latter consistently demonstrated higher bed expansion ratios, suggesting attenuation of the vibration signal through the bed. Furthermore, higher initial bed heights consistently corresponded with lower minimum fluidization velocities, attributed to less channel integrity in taller bed. However, notable differences are found when considering

the density ratios of the respective powders. With increasing vibration intensity, the fluidized nano-powder exhibited reduced homogeneity, whereas no significant effect was observed for micro-powder. This discrepancy can be explained by the distinctive agglomeration processes inherent to micro- and nano-powders. Micro-powders undergo agglomeration through the clustering of primary particles, driven by attractive inter-particle forces, often referred to as 'single-stage agglomeration' [8]. In contrast, nano-particles form multi-staged agglomerates, wherein primary particles are sintered into aggregates during the production process. These aggregates can then cluster together to form simple agglomerates, which further stick together to create complex agglomerates [8, 38]. Importantly, each stage of this multi-stage agglomeration incorporates additional voids into the structure, resulting in a lower density and increased compactability. The difference in behavior of the two powders when subjected to increased vibration intensity is therefore attributed to the disparities in agglomerate structure and characteristics, particularly the compactability of the formed agglomerates. It is worth noting that the exact particle size at which single-stage transitions into multi-stage agglomeration is not well-defined [8], limiting the predictability of fluidization behaviour.

5.4. CONCLUSION

In this study, we investigated the impact of vibrational orientation and intensity on the bed homogeneity of fluidized micro- and nano-silica. Bed expansion and fractional pressure drop values were collected to quantify fluidization quality. In the absence of mechanical vibration, both powders exhibited slugging and channelling, resulting in poor fluidization. However, vertical vibration enabled fluidization of both micro- and nano-powders, as evidenced by increased pressure drop ratios and significant bed expansions. The solid distribution of micro-powder is enhanced by increasing the superficial gas velocity. In contrast, bed homogeneity was unaffected by superficial gas velocity when considering nano-particles. Furthermore, increasing the vertical vibration intensity in such systems led to large density differences within the bed, attributed agglomerate compaction. Elliptical vibration, already applied in industry for non-cohesive powder fluidization, did not yield a desirable fluidization quality for either powder. For micro-particles, this mode was incapable of adequately disrupting channels, whereas for nano-particles, this orientation additionally led to a significant increase in powder compaction. Furthermore, vertical vibration introduces an unavoidable high-density region in the bottom of the bed, restricting the effectiveness of this assistance method. Combined with indicated signal attenuation over the system, it is implied that mechanical vibration, of any orientation, has

limited benefits for the fluidization of cohesive powders at large scale. Therefore, research into other assistance methods, that may avoid these specific issues, is encouraged. Additionally, while the elliptical orientation was found to be inefficient, fundamental understanding of its ineffectiveness is incomplete. Combinations of horizontal and vertical motion resulting in other trajectories, may still provide benefits; further research into these methods is required to allow for generalization of the results regarding the field vibro-fluidization of cohesive powders as a whole. Specifically, a study on sole horizontal vibration, utilizing fractional pressure drops to assess the solid distribution throughout the column would provide valuable insights, especially considering the few available studies on this topic and their limited assessment of fluidization quality.
Finally, our findings emphasize the limitations of relying on total pressure drop and bed extension as indicators of fluidization quality. Fractional pressure drop measurements are recommended for studying fluidized beds and optimizing assistance methods as they provide insight into solid distribution, while being easy to implement. Additionally, fractional pressure drop measurements were found to be a useful tool to indicate the presence of channels within the system.

REFERENCES

[1] L. Qu, Y. Liu, J.-B. Baek, and L. Dai, *Nitrogen-doped graphene as efficient metal-free electrocatalyst for oxygen reduction in fuel cells,* ACS nano **4**, 1321 (2010).

[2] L. Feng and Z. Liu, *Graphene in biomedicine: Opportunities and challenges,* Nanomedicine (London, England) **6**, 317 (2011).

[3] Z. He, Z. Zhang, and S. Bi, *Nanoparticles for organic electronics applications,* Materials Research Express **7** (2020), 10.1088/2053-1591/ab636f.

[4] I. Matsui, *Nanoparticles for electronic device applications: A brief review,* Journal of Chemical Engineering of Japan **38**, 535 (2005).

[5] S. Dekkers, H. Bouwmeester, P. M. Bos, R. J. Peters, A. G. Rietveld, and A. G. Oomen, *Knowledge gaps in risk assessment of nanosilica in food: evaluation of the dissolution and toxicity of different forms of silica,* Nanotoxicology **7**, 367 (2013).

[6] Y. Wang, L. Yuan, C. Yao, L. Ding, C. Li, J. Fang, K. Sui, Y. Liu, and M. Wu, *A combined toxicity study of zinc oxide nanoparticles and vitamin c in food additives,* Nanoscale **6**, 15333 (2014).

[7] J. R. Van Ommen, J. M. Valverde, and R. Pfeffer, *Fluidization of nanopowders: a review,* Journal of Nanoparticle Research **14** (2012), 10.1007/s11051-012-0737-4.

[8] R. Kamphorst, K. Wu, S. Salameh, G. M. H. Meesters, and J. R. van Ommen, *On the fluidization of cohesive powders: Differences and similarities between micro- and nano-sized particle gas–solid fluidization,* The Canadian Journal of Chemical Engineering (2022), 10.1002/cjce.24615.

[9] F. Raganati, R. Chirone, and P. Ammendola, *Gas–solid fluidization of cohesive powders,* Chemical Engineering Research and Design **133**, 347 (2018).

[10] J. Seville, C. Willett, and P. Knight, *Interparticle forces in fluidisation: a review,* Powder Technology **113**, 261 (2000), neptis Symposium on Fluidization- Present and Future.

[11] Y. Iwadate and M. Horio, *Prediction of agglomerate sizes in bubbling fluidized beds of group c powders,* Powder Technology **100**, 223 (1998).

[12] P. Chen and D. C. T. Pei, *Fluidization characteristics of fine particles,* The Canadian Journal of Chemical Engineering **62**, 464 (1984).

[13] S. Alavi and B. Caussat, *Experimental study on fluidization of micronic powders,* Powder Technology **157**, 114 (2005), 4th French Meeting on Powder Science and Technology.

[14] R. Kamphorst, P. C. van der Sande, K. Wu, E. C. Wagner, M. K. David, G. M. Meesters, and J. R. van Ommen, *The mechanism behind vibration assisted fluidization of cohesive micro-silica,* KONA Powder and Particle Journal , 2024007 (2023).

[15] S. Morooka, K. Kusakabe, A. Kobata, and Y. Kato, *Fluidization state of ultrafine powders,* Journal of Chemical Engineering of Japan **21**, 41 (1988).

[16] C. Zhu, Q. Yu, R. Dave, and R. Pfeffer, *Gas fluidization characteristics of nanoparticle agglomerates,* AIChE Journal **51**, 426 (2005).

[17] E. AL-Ghurabi, M. Shahabuddin, N. Siva Kumar, and M. Asif, *Deagglomeration of ultrafine hydrophilic nanopowder using low-frequency pulsed fluidization,* Nanomaterials **10**, 388 (2020).

[18] S. Ali, E. AL-Ghurabi, A. Ajbar, Y. Mohammed, M. Boumaza, and M. Asif, *Effect of frequency on pulsed fluidized beds of ultrafine powders,* Journal of Nanomaterials **2016**, 1 (2016).

[19] K. Wu, E. Wagner, O. Ochkin-Koenig, M. Franck, D. Weis, G. Meesters, and J. R. Van Ommen, *Time-resolved x-ray study of assisted fluidization of cohesive micron powder: On the role of mechanical vibration,* Chemical Engineering Journal **470**, 143936 (2023).

[20] Y. Mawatari, Y. Hamada, M. Yamamura, and H. Kage, *Flow pattern transition of fine cohesive powders in a gassolid fluidized bed under mechanical vibrating conditions,* Procedia Engineering **102**, 945 (2015), new Paradigm of Particle Science and Technology Proceedings of The 7th World Congress on Particle Technology.

[21] S. Satija and I. Zucker, *Hydrodynamics of vibro-fluidized beds,* Drying Technology **4**, 19 (1986).

[22] W. Han, B. Mai, and T. Gu, *Residence time distribution and drying characteristics of a continous vibro-fluidized bed,* Drying Technology **9**, 159 (1991).

[23] M. Mohseni, A. Kolomijtschuk, B. Peters, and M. Demoulling, *Biomass drying in a vibrating fluidized bed dryer with a lagrangian-eulerian approach,* International Journal of Thermal Sciences **138**, 219 (2019).

[24] Z. Wang, M. Kwauk, and H. Li, *Fluidization of fine particles,* Chemical Engineering Science **53**, 377 (1998).

[25] J.-R. Lee, N. Hasolli, K.-S. Lee, K.-Y. Lee, and Y. O. Park, *Fluidization of fine powder assisted by vertical vibration in fluidized bed reactor,* Korean Journal of Chemical Engineering **36**, 1548 (2019).

[26] S. Kaliyaperumal, S. Barghi, L. Briens, S. Rohani, and J. Zhu, *Fluidization of nano and submicron powders using mechanical vibration,* Particuology **9**, 279 (2011).

[27] E. Jaraiz, S. Kimura, and O. Levenspiel, *Vibrating beds of fine particles: Estimation of interparticle forces from expansion and pressure drop experiments,* Powder Technology **72**, 23 (1992).

[28] P. Zeng, T. Zhou, and J. Yang, *Behavior of mixtures of nano-particles in magnetically assisted fluidized bed,* Chemical Engineering and Processing: Process Intensification **47**, 101 (2008).

[29] J. Yang, T. Zhou, and L. Song, *Agglomerating vibro-fluidization behavior of nano-particles,* Advanced Powder Technology **20**, 158 (2009).

[30] J. Li, X. Liang, D. M. King, Y.-B. Jiang, and A. W. Weimer, *Highly dispersed pt nanoparticle catalyst prepared by atomic layer deposition,* Applied Catalysis B: Environmental **97**, 220 (2010).

[31] D. Shen and S. Gu, *The mechanism for thermal decomposition of cellulose and its main products,* Bioresource Technology **100**, 6496 (2009).

[32] R. Kamphorst, P. Wanjari, S. Saedy, J. F. van Dam, A. Thijssen, P. Brüner, T. Grehl, G. M. Meesters, and J. R. van Ommen, *Enhancing colloid stability of polymer microspheres in water through sio2 coating: Effects of coating cycles and surface coverage,* Surfaces and Interfaces **45**, 103852 (2024).

[33] A. Bailey, *Electrostatic phenomena during powder handling,* Powder Technology **37**, 71 (1984).

[34] J. M. Valverde and A. Castellanos, *Effect of compaction history on the fluidization behavior of fine cohesive powders,* Phys. Rev. E **73**, 056310 (2006).

[35] C. Nam, R. Pfeffer, R. Dave, and S. Sundaresan, *Aerated vibrofluidization of silica nanoparticles,* AIChE Journal **50**, 1776 (2004).

[36] C. Mogre, A. U. Thakurdesai, J. R. van Ommen, and S. Salameh, *Long-term fluidization of titania nanoparticle agglomerates,* Powder Technology **316**, 441 (2017), fluidization for Emerging Green Technologies.

[37] A. Pacek and A. Nienow, *Fluidisation of fine and very dense hardmetal powders,* Powder Technology **60**, 145 (1990).

[38] W. Yao, G. Guangsheng, W. Fei, and W. Jun, *Fluidization and agglomerate structure of SiO_2 nanoparticles,* Powder Technology **124**, 152 (2002).

[39] Y. Mawatari, T. Koide, T. Ikegami, Y. Tatemoto, and K. Noda, *Characteristics of vibrofluidization for fine powder under reduced pressure,* Advanced Powder Technology **14**, 559 (2003).

[40] D. Barletta and M. Poletto, *Aggregation phenomena in fluidization of cohesive powders assisted by mechanical vibrations,* Powder Technology **225**, 93 (2012).

[41] Z. Jiang and N. Fatah, *New investigation of micro-fluidized bed: The effect of wall roughness and particle size on hydrodynamics regimes,* Chemical Engineering Journal **430**, 133075 (2022).

[42] E. Zhou, Y. Zhang, Y. Zhao, Z. Luo, J. He, and C. Duan, *Characteristic gas velocity and fluidization quality evaluation of vibrated dense medium fluidized bed for fine coal separation,* Advanced Powder Technology **29**, 985 (2018).

[43] E. Marring, A. Hoffmann, and L. Janssen, *The effect of vibration on the fluidization behaviour of some cohesive powders,* Powder Technology **79**, 1 (1994).

[44] W. Zhang and M. Zhao, *Fluidisation behaviour of silica nanoparticles under horizontal vibration,* Journal of Experimental Nanoscience **5**, 69 (2010).

[45] K. An and J. M. Andino, *Enhanced fluidization of nanosized tio2 by a microjet and vibration assisted (mva) method,* Powder Technology **356**, 200 (2019).

SUPPLEMENTARY MATERIALS

5.5. COEFFICIENTS OF VARIATION WITHIN PRESSURE DROP DATA

In Figure 5.12 and Figure 5.13 the coefficients of variation (CV), also known as "normalized standard deviation", of the pressure drop signals, defined as $\frac{\sigma}{\mu}$, are presented for the micro- and nano-particle fluidization respectively. When applying vertical vibration to either powder at either bed height, it can be seen that the CV values stay comparatively low after the minimum fluidization velocities was reached (indicated by the dashed vertical lines), irrespective of vibration intensity. This is to be expected as prior to this point, the fluidization is incomplete, introducing randomness into the system, whereas full fluidziaiton provides a fairly stable pressure drop. In contrast, the data corresponding to the unassisted experiments and those where elliptical vibration was applied do not show any clear trend, indicating no consistent fluidization to take place during these experiments. For nano-particle fluidization with low initial bed heights subjected to ellipitical vibration, the average ΔP values were small at low gas velocities. As a result of this low μ, the CV values corresponding to these experiments, presented in Figure 5.13a, are magnified.

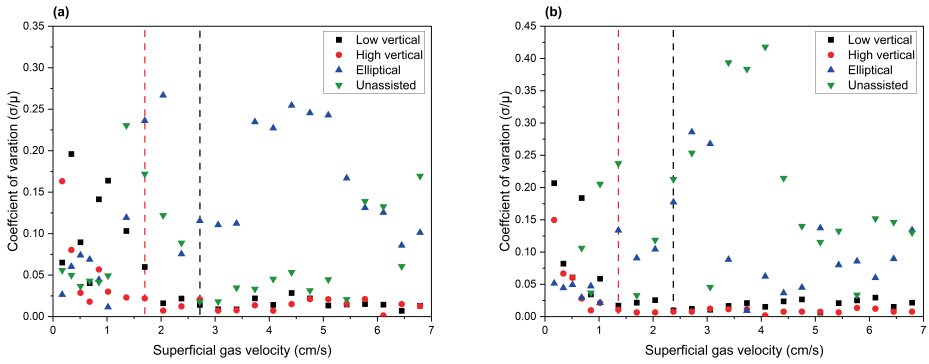


Figure 5.12: Coefficients of variation corresponding to the normalized pressure drop of vibro-fluidized beds of micro-powder with **(a)** low and **(b)** high initial bed heights. The dashed vertical lines indicate the minimum fluidization velocities found for the setting of the corresponding color.

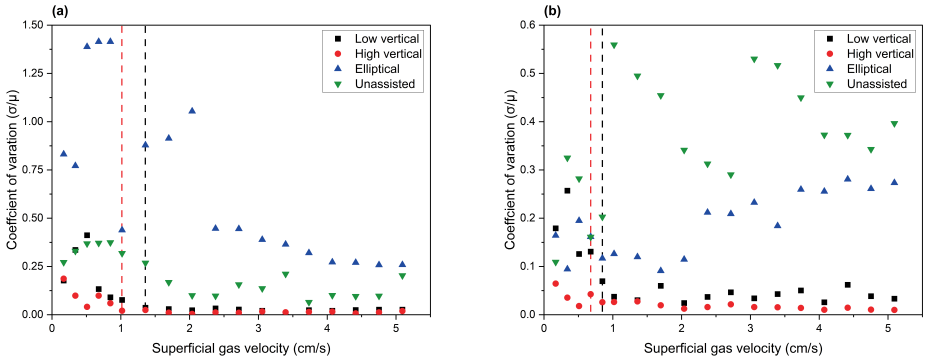


Figure 5.13: Coefficients of variation corresponding to the normalized pressure drop of vibro-fluidized beds of nano-powder with **(a)** low and **(b)** high initial bed heights. The dashed vertical lines indicate the minimum fluidization velocities found for the setting of the corresponding color.

6

STIRRER DESIGN FOR IMPROVING FLUIDIZATION OF COHESIVE POWDER: A TIME-RESOLVED X-RAY STUDY

In Chapter 4 and Chapter 5, we explored mechanical vibration as a method for improving the fluidization of cohesive powders. We identified several shortcomings of this approach, like the appearance of compacted regions within the powder bed. We therefore decided to look into mechanical agitation, the results of which are presented in this chapter. We test various impeller designs to determine their impact on fluidization quality and, based on our findings, propose design criteria that can guide future applications of this method.

This chapter has been published as "Stirrer design for improving fluidization of cohesive powder: A time-resolved X-ray study" by K. Wu, R. Kamphorst, A. Bakker, J. Ford, E.C. Wagner, O. Ochkin-Koenig, M. Franck, D. Weis, G.M.H. Meesters and J.R. van Ommen, Chemical Engineering Science **294**, 120069 (2024)

Stirring has been recognized in the literature as a promising technique for facilitating fluidization of cohesive powders, via inputting additional energy to counteract interparticle forces. However, the influence of operating conditions and stirrer configurations on flow behavior remains largely unknown, which impedes the practical implementation of stirred fluidization. Utilizing X-ray imaging, this research demonstrates that stirring enhances fluidization in cohesive micron-silica powder (Sauter mean diameter 7.9 µm) by collapsing the powder packing structure, and transitioning channeling beds into bubbling states. Comb-like configurations featuring fewer stirrers and blades, placed in the bottom region, have shown to be highly effective. Excessive stirring can lead to air pockets and a compacted phase of particles on the column walls, undermining the interaction between particles and stirrers. Additionally, the experiments show that maximizing the sweeping coverage, employing complex asymmetrical configurations, and avoiding tortuous gas pathways are preferable.

6.1. INTRODUCTION

Fluidization is a popular technique to process solids for various applications in industry, where exceptional interphase mixing and heat and mass transfer are paramount. Smooth fluidization is easily attainable with sand-like particles, whereas it becomes rather troublesome to effectively aerate fine particles because of their intrinsic cohesiveness. Strong interparticle forces, such as capillary and van der Waals forces, dominate the collective behaviour of fine particles, resulting in the formation of agglomerates [1, 2]. When fluidizing fine powders, individual particles or agglomerates tend to adhere together, forming internal cracks and channels, which results in a substantial portion of the fluidizing gas to bypass, undermining the gas-solids interaction [3].

Incorporating additional degrees of freedom allows for enhanced flexibility in manipulating fluidization. A range of assistance methods, imposing various forces and forms of energy on the system, has been demonstrated to be effective in improving fluidization of fine powders [3–5]. These approaches can be classified based on the mode of manipulation, which involves imposing dynamic or geometrical constraints on the gas or solid phase, and modifications to forces, such as contact force (e.g., particle-particle and particle-wall), surface force (e.g., particle-fluid), or body force (e.g., external force fields and gravitational pull) [6]. External actuators have been explored, with numerous successful attempts documented in the literature, including vibration [7–9], pulsation [10, 11], stirrer mixing [7, 12], high-speed jet flow [13–15], and doping of flow conditioner [16–18]. Nonetheless, devising a universal method for fluidizing cohesive powders remains a challenge, as the type of cohesion, scalability, energy consumption, and instrumentation requirements varies between different applications.

In comparison to other assistance techniques, stirring offers advantages in terms of scale-up practices, operation and effective length, and practicality of integration with existing reactor units. Stirrers function as moving internals to agitate particulate flows, transmitting mechanical energy through particle-boundary interaction. Nevertheless, their performance largely relies on the operating conditions and stirrer configurations. For instance, there is no universally applicable rotation speed. Previous research reports that, in columns with diameters ranging between 3 cm and 7 cm, increasing stirring speed mitigates agglomeration and channelling, resulting in a reduced terminal velocity and minimum fluidization velocity for Geldart C micro-powders [19], while improving bed dilation [12] and promoting a vigorous bubbling fluidization state for nano-powders [7]. However, in columns of similar sizes, excessively high rotation speeds (e.g., faster than 100 rpm) have been found to significantly increase the particle entrainment rate in fluidizing Geldart C type micro-powders [20]. Additionally, a tendency to compress particles against the column walls was observed, result-

ing in the formation of the compact layers of solids,indicated by an overshoot in the bed pressure drop signal [16]. On the other hand, a low rotation speed (e.g., 30 rpm), irrespective of stirrer geometries, has been observed to yield insufficient impact on agglomerates to overcome interparticle forces of micro-powders larger than 1 µm [16], although such a speed has been shown fast enough to promote fluidization of sub-micron and nano-powders smaller than 1 µm [21]. The placement of the stirrer also plays a crucial role. An impeller-type stirrer was investigated and considered most effective when positioned in the bottom region of the bed, e.g., within approximately 1 cm from the base of a 45 cm deep column [22]. It is hypothesized that the stirrers sweep particles into the initial channels, which subsequently break down. However, in half a column (semi-circle or a 'D' shape when viewed from above) with a diameter of 20 cm, improved fluidization quality and reduced minimum fluidization velocity of micron cohesive particles (16 µm LiF powder used in the study) were also found with the impeller placed at a higher position (e.g., at 70% static bed height) [23]. This study also concluded that gas channels develop and become too persistent to break when the stirrer is mounted too high (e.g., at 86% static bed height), as indicated by a significant reduction in the measured pressure drop. Studies on stirred fluidization of fine, cohesive powders are scarce, and primarily rely on pressure drop measurements and visualization on the surface layers through transparent walls. Nevertheless, the local gas channeling and powder structures complicate the interpretation of pressure signals, making it challenging to associate with the impact induced by stirring on the hydrodynamics. Furthermore, surface layers, which experience significant boundary effects, do not accurately represent the bulk flow behaviour, and fine particle clouds have a tendency to adhere to walls, rapidly causing blurred or obstructed visibility.

Non-intrusive imaging and tomography techniques, extensively applied in medical and technical practices, such as electrical capacitance tomography [24, 25], magnetic resonance imaging [26, 27], and X-ray imaging and computational tomography (XRT) [28], offer opportunities to overcome the constraints of observational limitation and access into system hydrodynamics [29]. These technologies allow for a direct visual exploration into the bed characteristics in 3-D opaque systems, not only monitoring the detailed time evolution of apparent phenomena, such as flow pattern and bubble motion, but also quantitatively measuring particle-level features, including solid fraction distribution and particle segregation. Consequently, they facilitate understanding of systems with complex hydrodynamic behaviors and fundamental mechanisms. In terms of studying gas-solid system, among the mentioned techniques, X-ray imaging excels by offering a higher spatial resolution and identification of material contrast [29]. This technique has been widely applied since the 90s to study the gas-solid

fluidization of various powders [30, 31] and structural geometries [32, 33]. With the X-ray beams attenuating according to the local solid fraction, it is possible to attain a temporally resolved solid distribution of fluidization, which allows for the direct inspection and tracking of local hydrodynamic events within a cylindrical apparatus, like the one employed in this study [34].

In this study, a comprehensive experimental investigation into the effects of stirring on the fluidization of cohesive powders by varying design parameters and operating conditions was conducted. The fluidization behaviour is thoroughly compared across various design variables, including the number of stirrers, number of blades, rotation speed and geometry. Two-dimensional (2D) fast X-ray imaging was performed in conjunction with pressure drop and bed expansion measurements to capture the temporal evolution of flow patterns and identify in-situ hydrodynamic events, such as solid distribution, gas bubble development, and channel formation. The results serve as a valuable guide for designing optimal stirrers for applications of solid processing and provides opportunities for validating models of simulating fluidization of cohesive powders.

6.2. EXPERIMENTATION AND METHODOLOGY

6.2.1. EXPERIMENTAL SETUP

Figure 6.1 depicts a schematic representation of the experimental arrangement. Experiments were conducted using a Plexiglas column with an inner diameter D of 5 cm. Two 3 mm thick porous plates (SIKA-R 3 AX, Sintertech) were used to couple the column to a plenum chamber situated below and a breakout box positioned above. The porous plates were cleaned using an ultrasound bath before use. Furthermore, particles entrained within the fluidized bed were captured by the porous plate positioned at the top of the column. To ensure safety, a wash bottle and a HEPA powder filter were installed downstream prior to discharging the fluidizing gas into the atmosphere.

The column was mounted onto a vibration table, which was utilized for initialization of fluidization in certain experiments. The particles were fluidized at room temperature with dry nitrogen gas, which was regulated using a mass flow controller (Bronkhorst F-202AV). An in-house LabVIEW program managed the data acquisition system, which connected to both the flow controller and pressure transducers (OMEGA-PX419). A motor was placed on top of the breakout box, with the lowest tip of the shaft mounted 5 mm above the distributor. The shaft used in this study was made of metal, effectively functioning as a grounding rod and mitigating the triboelectric charging of particles induced by stirring. It is therefore expected that the contribution of electrostatic forces to the observed fluidizaiton behavior to be minimal.

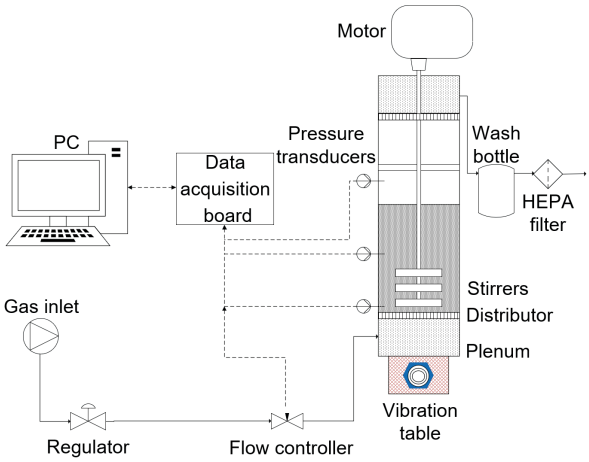


Figure 6.1: Schematic representation of the experimental setup.

6.2.2. X-RAY IMAGE PROCESSING

Fast X-ray imaging serves as a non-invasive and hard field technique to effectively monitor system hydrodynamics. The column was positioned in between an X-ray generation tube and a scintillation detector panel, as shown in Figure 6.2. The distance between the source tube and center of the column was set at 100 cm. The X-ray source used was YXLON Y.TU 160-D06 tube with a maximum voltage of 150 kV and a maximum anode current of 12 mA. In this study, a voltage of 120 kV and a current of 1.9 mA were selected to ensure the X-ray intensity remained sufficiently high after passing though the full bed, yet did not surpass the maximum limit of the detector when passing through an empty column. The X-ray detector plate utilized is a Theledyne Dalsa Xineos-3131 model, featuring a sensitive area measuring 307 mm× 302 mm and a resolution of 1548 × 1524 pixels. Each pixel has dimensions of 198 µm × 198 µm. In this work, a field of view of 1548 × 500 pixels is used. The raw images were acquired at a frame rate of 65 Hz, which is considered sufficient for monitoring the system hydrodynamics, as the majority of hydrodynamic events occur below 10 Hz [35].

X-ray beams pass through gas-solid suspensions, their attenuation being directly proportional to the mass of the material present within the pathway [28]. For each experiment, the attenuated X-ray beams were measured at the detector panel to construct a 2D intensity map of the field of view. The attenuation of X-ray beams follows the Lambert-Beer law:

$$I = I_0 \exp(-\mu d) \tag{6.1}$$

where I_0 and I are the intensity of X-ray beams before and after penetrating loaded material of a thickness d, μ is the attenuation coefficient associated with the material properties. Theoretically, deviation from the correlation is expected, as X-rays are poly-chromatic. However, a calibration test shows that this deviation is minimal (see section 1 of the Supplementary Material for the calibration procedure).

The X-ray attenuation provides a map of the gas fraction. Considering the same solid material, the local normalized gas fraction, denoted as ε, is expressed as a line integral extending from the X-ray source to the specific pixel on the detector:

$$\varepsilon = \frac{d_f - d_m}{d_f} \tag{6.2}$$

where d_f and d_m represent the solid length (i.e., the distance of the X-ray beam travelling through solids) of the full bed and measurement, respectively. As per Equation (6.1), these solid lengths can be obtained by measuring two reference intensity profiles:

$$\begin{aligned} d_f &= \mu^{-1} \ln\left(\frac{I_{empty}}{I_{full}}\right) \\ d_m &= \mu^{-1} \ln\left(\frac{I_{empty}}{I_{meas}}\right) \end{aligned} \tag{6.3}$$

where I_{empty} is for an empty column, and I_{full} is for a fully loaded column. I_{meas} is for the measurement column. By employing a two-point calibration protocol with these two reference profiles of X-ray intensity, the gas fraction ε can be computed using the following expressions:

$$\varepsilon(I_{meas}) = \frac{\ln(I_{meas} \,/\, I_{\text{full}})}{\ln(I_{\text{empty}} \,/\, I_{\text{full}})} \tag{6.4}$$

Note that the range of ε, as per the definition, lies between 0 and 1, standing for the close packing of the powder and pure gas, respectively. In order to obtain a reproducible full reference, the loaded powders were vibrated for 10 min to approach a close packing state without the presence of stirrers. In the subsequent gas fraction maps, low attenuation of X-rays is represented by deep blue colors, signifying low solid concentrations. On the other hand, high attenuation of X-rays is represented by red colors, denoting high solid concentrations. The projected area of both the stirrers and shaft consistently appearing in deep red, due to higher attenuation, have been excluded from the analysis.

Given a symmetrical configuration, the projections obtained from various angles are expected to be identical. Validation experiments were conducted by

shooting X-ray simultaneously from three detector-source pairs, with each pair being evenly spaced by 120 degrees. The outcomes confirmed that the flow patterns are indeed symmetrical, and that a projection from a single angle is sufficiently representative (see section 2 of the Supplementary Material for the validation experiments).

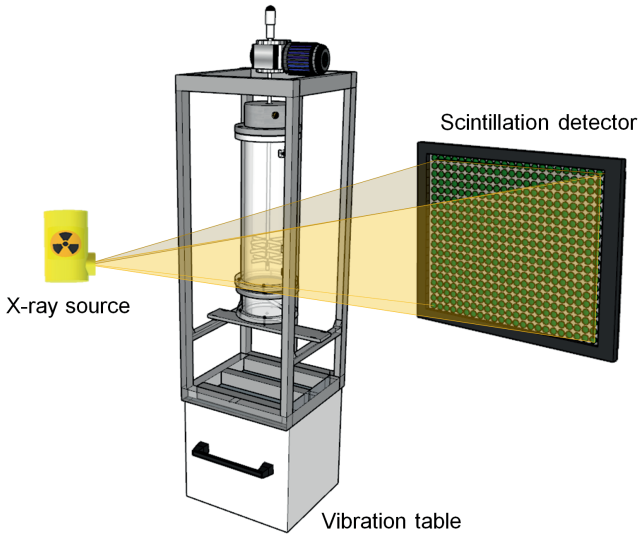


Figure 6.2: Schematic representation of the X-ray imaging setup. The column is placed in between the X-ray source and detector.

6.2.3. POWDER PROPERTIES

Commercially available Geldart C Silica powder (CWK Bad Köstritz) was employed in this study. Laser diffraction particle analyser measurements reveal a mono-peak size distribution, characterized by a Sauter mean diameter of 7.9 µm, as depicted in Figure 6.3. The cohesive silica powder tends to form agglomerates upon close contact. The scanning electron microscopy (SEM) images of the fresh powder confirm the presence of intricately shaped primary agglomerates (see figures inserted in Figure 6.3). The silica powder is porous, with a skeletal density of 1900 kg/m^3. The theoretical minimum fluidization velocity U_{mf} is determined to be 0.002 cm/s as per the Gidaspow correlation [36]. However, preliminary tests show channeling in the powder bed up to 7 cm/s, making it impractical to determine the experimental U_{mf}. The bulk density is 134 kg/m^3, determined by filling a measuring column without consolidation. The dynamic angle of repose is measured to be 50°, using a rotating drum at 30 revolutions per minute. This angle indicates poor flowability according to the Carr classification [37].

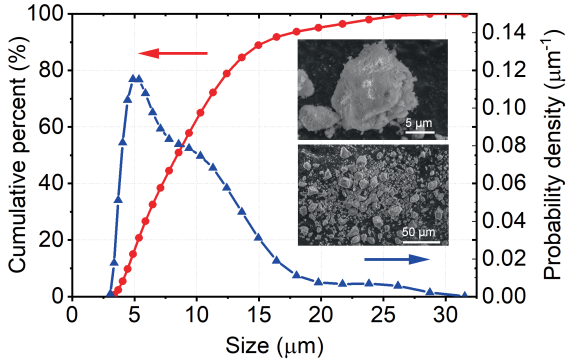


Figure 6.3: Volume-based particle size distribution and cumulative distribution of the silica powder. Sauter mean diameter D_{32} is 7.9 μm. The inserted photos are the SEM images of the silica powder.

6.2.4. FLUIDIZATION PROPERTIES

To facilitate the evaluation of fluidization, the pressure drop across both the entire and lower section (8.5 cm above the distributor plate) of the fluidized powder bed was continuously monitored using two pressure transducers. Pressure oscillations were recorded at a sampling rate of 1000 Hz. Oscillations in the pressure time series are induced by the periodic rotation of stirrers and the bubbling events. Signal analysis is conducted in both time and frequency domains, as illustrated by time-averaged and power-spectrum plots [35, 38]. Furthermore, for fluidization, dominant hydrodynamic events typically occur at frequencies below 10 Hz [38].

For a 2D projection of the flow pattern, a bubble is defined as the area consisting of pixels where the gas fraction exceeds a threshold determined from the surroundings. An in-house MATLAB code is used to identify the bubbles by adaptive thresholding [39]. The bubbling probability density is constructed:

$$p_b(x,y) = \frac{1}{N_{\Delta t}\Delta x \Delta y} \sum_{t=t_0}^{t_0+\Delta t} F_b(x,y,t) \tag{6.5}$$

where F_b is the bubble flag, which is equal to one for a bubble pixel and zero for an emulsion pixel. $N_{\Delta t}$ is the number of X-ray imaging frames between t_0 and $t_0 + \Delta t$.

In addition, with the gas fraction ε obtained from the X-ray imaging, a time-averaged gas fraction profile $\overline{\varepsilon}$ can be computed as follows:

$$\overline{\varepsilon}(x,y) = \frac{1}{N_{\Delta t}} \sum_{t=t_0}^{t_0+\Delta t} \varepsilon(x,y,t) \tag{6.6}$$

6.2.5. STIRRER CONFIGURATIONS

Various stirring parameters were investigated independently using a (comb-form configuration) modular design that allows decoupling design parameters and producing measurable effects. The modular design employs basic axial blade stirrers as building blocks, inspired by the work conducted by Kuipers et al. [40], in which the authors investigated the impact of various axial stirrers on the fluidization of heavy potato starch (mean volume-based diameter around 50 µm). The dimensions of the stirrer were adapted to suit the column in this study, and set to a diameter of 41 mm, which considers a certain shaft wobble and results in a gap of 4.5 mm between the blade tip and the column wall for each side. All stirrers were 3D-printed with Polylactic Acid-Polymer (PLA) material. An additional ring disc was affixed to the shaft to minimize the wobbling effect, located at 30 cm above the distributor plate, which is beyond the maximum bed height reached by the bed. Multiple stirrers could be flexibly mounted and stacked with a separation of 6 mm between the neighbouring stirrers, secured by two nuts. Example stirrers are depicted in Figure 6.4.

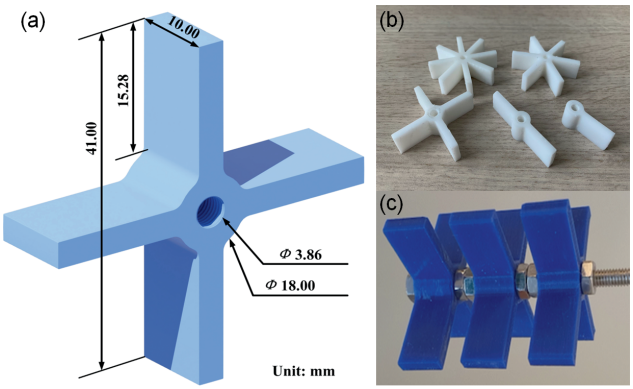


Figure 6.4: 3D-printed modular stirrers: (a) dimensions of the four-bladed modular design, (b) modular stirrers with different number of blades, and (c) an example of stacked stirrers.

6.2.6. EXPERIMENTAL DESIGN

To prepare for the experiments, the unfluidized powder was initially sieved through a 600 µm mesh to collapse any large, existing agglomerates and ensure an equal state of initial aeration. For each experiment, a new batch of sieved powder of 21 g was loaded, constituting a static bed height H_0 of approximately 10 cm ($H_0/D = 2$). The performance of the stirrer design is evaluated from two different perspectives: the ability to initialize and sustain fluidization. The initialization phase concerns the stirrer configuration's effectiveness in disrupting pre-existing

bed structures, such as cracks and channels induced by the shaft placement and powder loading protocols, and initiating the aeration of particles. Conversely, the maintenance phase focuses on the stirrer's capacity to sustain a consistent state of complete fluidization. The detailed operating protocols are listed in Figure 6.5.

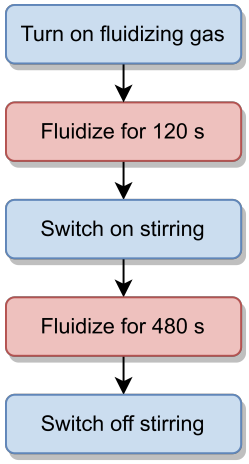


Figure 6.5: Operating procedures for the stirring fluidization experiments. $U = 3.1$ cm/s.

To comprehensively identify the influence of various stirrer configurations on fluidizing cohesive powder, a series of experiments was conducted under different conditions, including rotation speeds, number of blades, and stirrer arrangements. Other design variables, such as attachment angle of blades and length of blade, while important, are less contentious in designing and fall outside the scope of this study to determine the optimal stirrer dimensions or test every possible configurations. The observed fluidization was compared to evaluate the significance of each parameter on flow behaviour. The experiment conditions tested are listed in Table 6.1. The fluidization observed in the highlighted experiment (conditions marked in bold in Table 6.1) serves as a reference for comparing the effects of various stirring conditions. Each experiment was conducted at least in duplicate to ensure reliability and reproducibility of the results.

6.3. RESULTS AND DISCUSSION

A comparative study of the stirrers' capability to initialize and sustain effective fluidization is conducted concerning the key fluidization properties, such as flow pattern, solid distribution, bed expansion, and pressure drop. Based on the analysis, a set of criteria for stirrer design is proposed and then examined based on the improved stirrer configurations.

Table 6.1: Experimental conditions investigated.

Stirring parameter*	Value
Rotation speed [rpm], N	35;70;**130**;160;230
Number of blade [-], B	1;2;**4**;6;8
Number of stirrer [-], S	1;2;**3**;6

* The conditions of the reference case are present in bold.

6.3.1. HYDRODYNAMICS OF THE UNASSISTED AND VIBRO-FLUIDIZED BEDS

For comparison purpose, unassisted and vibro-fluidization experiments were carried out, with no stirrer present in the system. The fluidizing gas was introduced at the beginning in both experiments. For vibro-fluidization, the vibration was activated at 120 s. Notable differences in the flow patterns arise between the unassisted and vibro-fluidization of cohesive powder. When subjected to dry nitrogen gas without vibration, micron-silica particles initially form a plug and the entire powder bed rises in the column. Subsequently, upon hitting the top plate, this plug collapses, causing the elevated powders to fall and settle on the distributor plate, resulting in a slightly dilated bed with disorganized internal cracks.

Figure 6.6 shows the time-evolving flow patterns over a 540 s fluidization with a superficial gas velocity U = 3.1 cm/s after the plug has collapsed, and the powder has settled. In absence of external assistance, the powders remain predominantly stationary, despite the presence of a fluidizing gas. Mechanical vibration is shown able to initiate fluidization, resulting in significant bed expansion and bubbling. Nevertheless, stratification of the powder occurs rapidly, with two distinct flow regions appearing over time, as depicted in Figure 6.6b. Due to vibration, the bottom layer of powders progressively compacts against the distributor plate, causing a significant reduction in the gas fraction ε at normalized Y-position, Y/D = 1.0. In addition, the dilute phase in the top bed also decreases in depth and gas fraction, eventually leading to incomplete fluidization, showing poor sustainability. Similar fluidization behaviour has been observed in a larger vibrated column [41].

6.3.2. EFFECT OF ROTATION SPEED

To investigate the impact of rotation speed on fluidization, experiments were conducted employing a configuration consisting of three stirrers, each with four

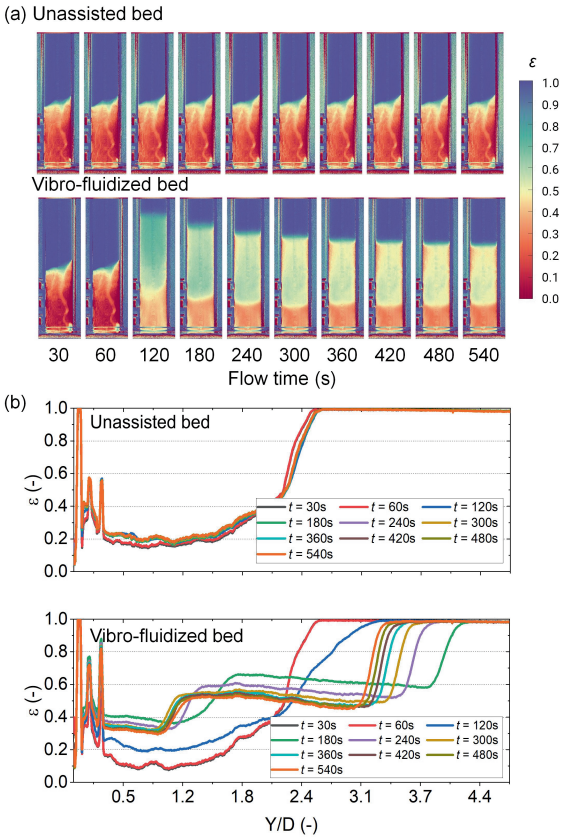


Figure 6.6: (a) Time-averaged flow patterns and (b) gas fraction profile in the unassisted and vibro-fluidized beds. Each flow pattern is obtained by averaging 10 s of frames at each time. Vibration starts at 120 s after the fluidization process begins. $U = 3.1$ cm/s; $f = 30$ Hz; $A = 1.0$ mm, $D = 5$ cm, $H = 10$ cm.

radial blades (as displayed in Figure 6.4c), operating at speeds of 35 rpm, 70 rpm, 130 rpm, 160 rpm and 230 rpm. The results reveal that varying rotation speed has distinct effects on the initialization of fluidization, as shown in Figure 6.7.

For the beds initiated by stirring, it was observed that as the stirrer begins to rotate, the rotating blades disrupt and break up the primary packed structure within the sweeping region into fragments or agglomerates. These fragments subsequently become fluidized, traveling towards the upper region of the bed. Simultaneously, the structure of packed particles located above the sweeping region descends and collapses layer by layer upon contact with the blades. A good representation of this phenomenon can be seen in Figure 6.7a for 160 rpm at 120 s, where the bottom section of the bed is agitated by the sitter, yet a slug

initially persists above it. Such a continuous process subsequently leads to the initial expansion of the bed, and causes a delay of at least 30 s between the beginning of stirring and initiation of fluidization.

Increasing rotation speed results in a more pronounced development of fluidization. The flow patterns presented in Figure 6.7a demonstrate that a rotation speed of 35 rpm is insufficient to achieve a homogeneous fluidization state in the bed. The gas flow tends to concentrate towards the central region, where the shaft is located, indicating that the existing powder structure remains largely intact. Figure 6.7b displays an overshoot of bed expansion at 130 rpm, reaching a peak approximately 60 s after the stirring begins. The results suggest the existence of a threshold rotation speed required for initiating a fully developed fluidization state, which in this set-up was observed above 70 rpm, corresponding to a tip speed of 10.5 cm/s. However, excessively high rotation speeds led to the rapid displacement of particles, preventing them from entering the sweeping zone. This separation results in the formation of an air pocket - a stable, particle-free region around the stirrer stack - which greatly reduces the contacts between particles and stirrers, as shown at 180 s for 160 rpm, therefore delaying the initialization of fluidization. At larger rotation speeds, such as 230 rpm, an air pocket forms and persists, and the primary bed structure remains largely untouched, since the blade rotates without impacting powder or inputting any mechanical energy. Consequently, the gas flow tends to bypass the central region around the shaft, continuously propelling particles to both sides and creating a funnel-like configuration at the top of the bed.

Additionally, the flow patterns show that, over time, particles tend to accumulate along the sidewalls of the column, resulting in reduced bed expansion. Although there are variations in the maximum expansion levels, the bed expansion at all tested rotation speeds eventually converges to a similar H/H_0 of approximately 1.5, with the exception of the bed at 160 rpm, which experienced delayed fluidization initiation, as shown in Figure 6.7c. This is consistent with the previously reported bed expansions for this powder in a vibro-fluidized bed [42]. On the other hand, Figure 6.7b displays that at rotation speeds of 70 rpm and above, the beds exhibit similar gas fractions around $\varepsilon = 0.5$, despite the slight differences in bed expansion, suggesting the attainment of comparable fluidization with each other.

6.3.3. EFFECT OF NUMBER OF BLADES

Increasing the number of blades makes the initialization of fluidization more challenging. As depicted in Figure 6.8a, a single-bladed stirrer leads to immediate collapse of the existing powder structure, resulting in rapid bed expansion. However, such a dilated state is not sustained, and the bed quickly contracts.

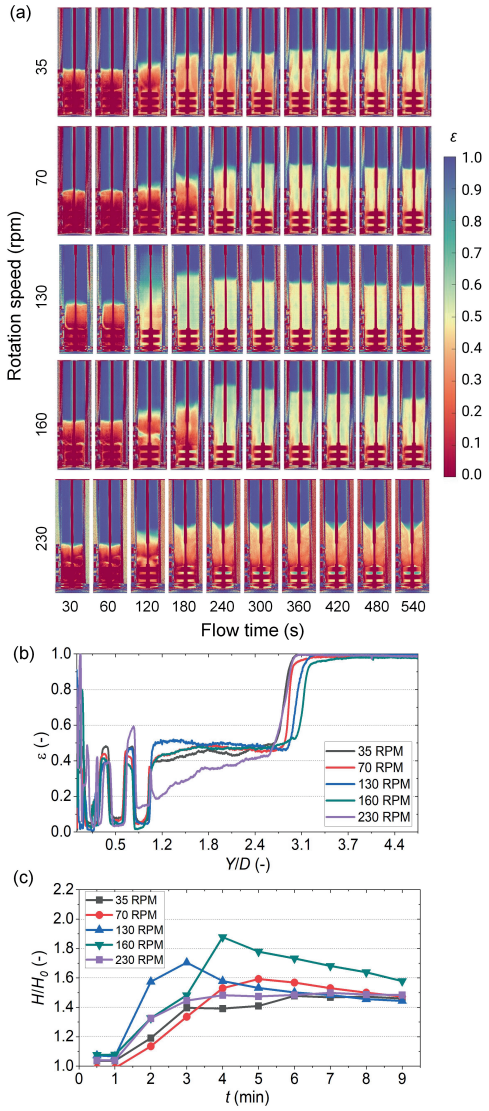


Figure 6.7: (a) Time-averaged flow patterns in stirred beds of varying rotation speed from 35 rpm to 230 rpm, and (b) the gas fraction at 540 s and (c) bed expansion profiles. Stirring starts at 120 s after the fluidization process begins. The flow pattern and profiles are obtained by averaging 10 s of frames at each selected time. Three stirrers of four blades are used. $U = 3.1$ cm/s, $D = 5$ cm, $H_0 = 10$ cm.

In contrast, stirrers equipped with eight blades initially render an air pocket (as shown at 180 s), and gradually cause the bed to spout, with a substantial number of particles being directed towards the walls, which impairs the interphase con-

tacts. Consequently, instead of evolving into an effective fluidization state, the bed creates a pronounced preferential path for gas to bypass around the shaft in the central region.

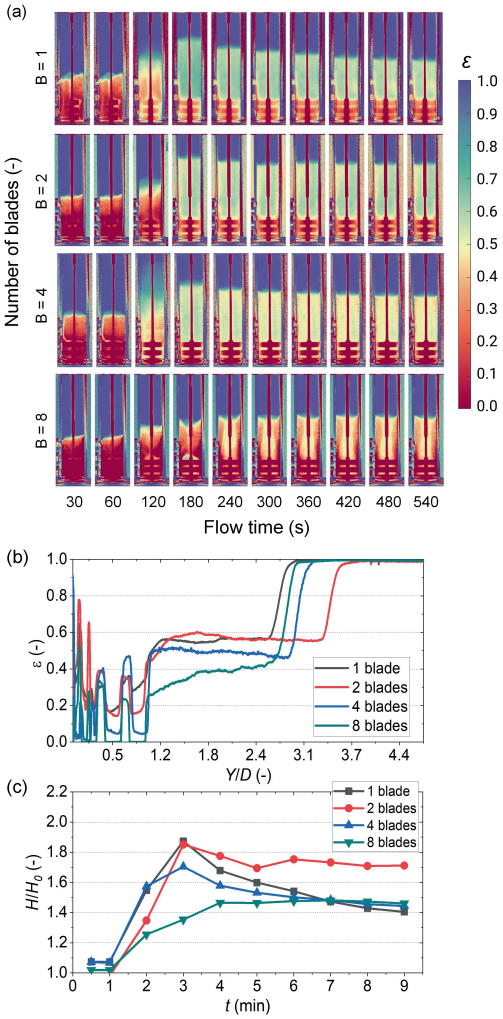


Figure 6.8: (a) Time-averaged flow patterns in stirred beds of varying number of blades from one to eight, and (b) the gas fraction at 540 s. Stirring starts at 120 s after the fluidization process begins. The flow pattern and profiles are obtained by averaging 10 s of frames at each selected time. A stack of 3 stirrers is used, operating at 130 rpm. $U = 3.1$ cm/s, $D = 5$ cm, $H = 10$ cm.

According to Figure 6.8b and Figure 6.8c, configurations with double-bladed stirrers outperforms others in terms of bed expansion and gas fraction. For the configurations with one and four blades, despite achieving initial fluidization,

bed expansion begins to decline over time, eventually converging to a similar bed expansion, indicative of poor sustaining fluidization. Based on the flow patterns, an increased number of blades leads to more pronounced stratification in the gas-solid suspension, creating preferential gas pathways at the center and reduced particle dilation.

However, increasing the number of blades at a fixed rotation speed has a twofold effect: it enhances the disturbance frequency (a product of the blade number and rotation speed), but also increases obstruction in the cross-sectional area for gas distribution. Fluidization behavior cannot be solely characterized by disturbance frequency, as detailed in Table 6.2. For instance, the configuration with two blades at 130 rpm and the configuration with four blades at 70 rpm yield comparable disturbance frequencies, yet the latter displays much inferior fluidization. The performance is influenced by both the absolute impact speed (e.g., tip speed) and the coverage of the cross-sectional area.

Table 6.2: Disturbance frequencies tested.

		Rotation speed, R [rpm]				
Blade number B [-]	Area blockage A_B [-]	35	70	130	160	230
1	15.97%	-	-	130	-	-
2	18.97%	-	-	260	-	-
4	24.98%	140	280	520	640	920
8	37.00%	-	-	1040	-	-

6.3.4. EFFECT OF NUMBER OF STIRRERS

To determine the influence of stirrer number on fluidization, experiments were performed at a consistent rotation speed of 130 rpm, while varying the number of stirrers from one to six. Stacks of four-blade stirrers were used as the basic stirrer block. Increasing the number of stirrers occupies more space inside the powder bed, slightly elevating the static bed height, but also results in a decrease in bed expansion, as shown in Figure 6.9.

With the use of more stirrers, a greater fraction of particles is swept across the bed. It is noteworthy that, with six stirrers, the sweep length approaches the static bed height. This increased effective stirring volume creates a taller compacted phase within the bed induced by the stirrer blades. Consequently,

it promotes the formation of the central gas pathway. Figure 6.9c shows a rapid decline in bed expansion after only 120 s of stirring. The flow pattern is similar to the one obtained with an eight-blade configuration in Figure 6.8a, where the preferential pathway allows upward spouting of particles, eventually leading to a funnel-like bed surface. Conversely, fewer stirrers develop higher initial bed expansion as well as sustaining a more homogeneous fluidization. The bed expansion ratios of the one and three stirrer configurations approach approximately the same value after 540 s, whereas the double-stirrer configuration demonstrates enhanced maintenance of effective bed fluidization. Single- and double-stirrer configurations were observed to initiate fluidization rapidly, resulting in a steadily homogeneous fluidization state. Overall, an increase in the number of stirrers has a tendency to lead to degraded and more inhomogeneous fluidization.

In several experiments, such as those combining one or three stirrers with four or eight blades, a persistent air pocket formed, remaining stable throughout the experiment and hindering the initiation of fluidization. It is noteworthy that the single-blade stirrer configuration did not result in the formation of an air pocket in any scenario. In particular, the flow pattern observed with a single stirrer configuration exhibits less particle accumulation on the walls. This phenomenon is potentially attributed to its asymmetric design, which facilitates more complex gas and bubbles distribution and encourages particle recirculation. Therefore, it is likely that an asymmetrical stirrer design is advantageous for sustaining fluidization, while a suitable combination of sufficient tip speed and cross-section opening is crucial to disrupt existing structures in the bed, such as channels and air pockets, thereby initiating fluidization. Furthermore, stirring the bottom region is of critical importance, as demonstrated by the experiment shown in Figure 6.10, in which a two-bladed stirrer positioned in the middle of the static bed was ineffective in initiating fluidization. Such a mid-level stirring only led to the formation of an air pocket in the stirred area, aligning with the conclusions in [22].

Additionally, brief episodes of vertical vibration (with an amplitude of 1 mm and a frequency of 30 Hz) have shown effective in initiating fluidization, preventing the formation of air pockets regardless of the stirrer configurations; however, it was discovered that vibration induces significant powder stratification within the bed, which depresses the maintenance of the fluidized state. Therefore, such a combination of stirring and vibration is not is not considered favorable (See section 3 of the Supplementary Material for the experimental results).

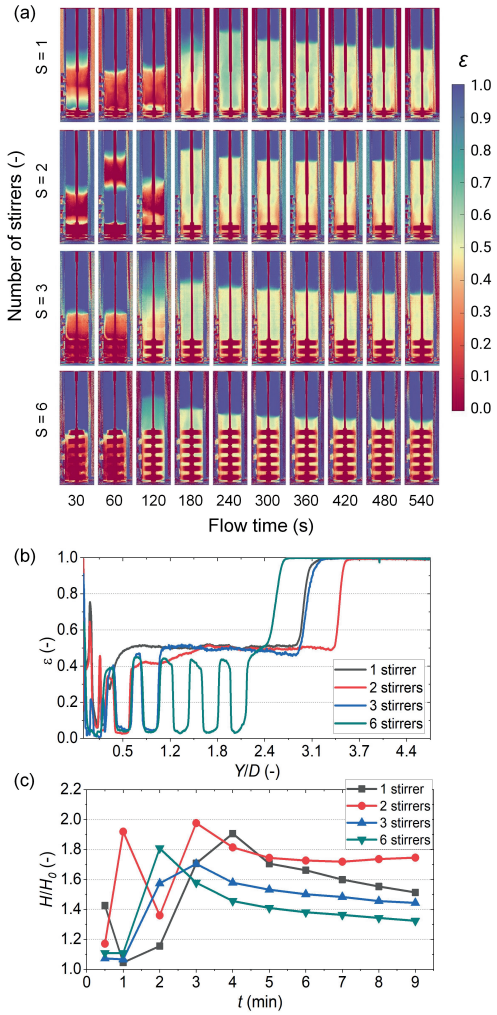


Figure 6.9: Time-averaged flow patterns in stirred beds of varying number of stirrers from one to six, and (b) the gas fraction at 540 s. Stirring starts at 120 s after the fluidization process begins. The flow pattern and profiles are obtained by averaging 10 s of frames at each selected time. Four-bladed stirrers are used, operating at 130 rpm. $U = 3.1$ cm/s, $D = 5$ cm, $H = 10$ cm.

6.3.5. ADVANCED DESIGN OF STIRRER

The flow patterns observed show that most modular designs, following the shape shown in Figure 6.4, are not capable of maintaining a highly expanded state. Overall, the modular stirrers exhibit a tendency to press the particles against the walls, inducing poor interphase contact. For demonstration purpose, Figure 6.11a and Figure 6.11b illustrate various stages of flow patterns and the bub-

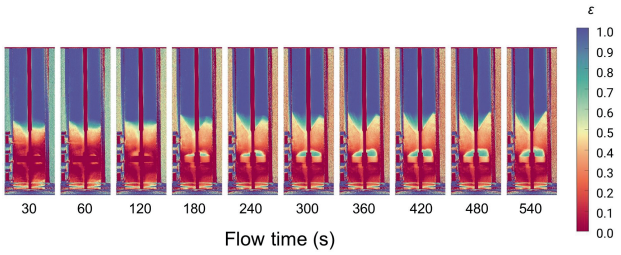


Figure 6.10: Time-averaged flow patterns in the stirred bed. The stirrer is positioned in the middle of the static bed ($Y = 5$ cm). Stirring starts at 120 s after the fluidization process begins. The flow pattern and profiles are obtained by averaging 10 s of frames at each selected time. A two-bladed stirrer is used, operating at 130 rpm. $U = 3.1$ cm/s, $D = 5$ cm, $H = 10$ cm.

bling probability density of a stirred bed operating at 175 rpm with three stirrers of two blades, where this issue is particularly pronounced. The observed flow patterns show that, following the initial bed expansion, particles begin to accumulate along the walls and directly above the distributor plate in regions not reached by the stirrers. Subsequently, the particles form a stable structure that restricts gas flow, causing bubbles and gas to divert towards the bed central regions, as shown in Figure 6.11a with added illustrated bubbles and streamlines for clearer understanding of the gas pathways. Meanwhile, bubble-free regions in close proximity to the sidewall continue to develop. Eventually, the particle structure becomes stable, without recirculation of solids in the side and bottom regions of the bed, forming an annular ring of the stagnant particle phase. In contrast, the gas flow and bubbles consistently travel the central region and spout particles upwards, creating a funnel-like surface at the top of the bed. Overall, the bed deteriorates into a radially stratified system characterized by insufficient interphase contacts.

In Figure 6.11c and Figure 6.11d, the time series of normalized pressure drops and their power spectra are displayed, respectively. The pressure drop of both the bottom section and the total bed sharply increases upon the initiation of the mechanical agitation at 120 s. In the subsequent 20 s, a decrease in the pressure drop in the bottom bed is noted, whereas the total pressure drop increases, indicating dilution of the bed and internal mixing. However, for the remaining duration of the experiment, the opposite was observed: the total pressure drop decreases, whereas it increases in the bottom section, suggesting a densification of the bed, specifically in the bottom section, as shown in Figure 6.11a. Additionally, the power spectra of the pressure drop signals exhibit distinct peaks at the frequency of full stirrer rotation ($f = 2.92$ Hz), and the disturbance frequency linked with individual blades passing by the probe ($f = 5.84$ Hz).

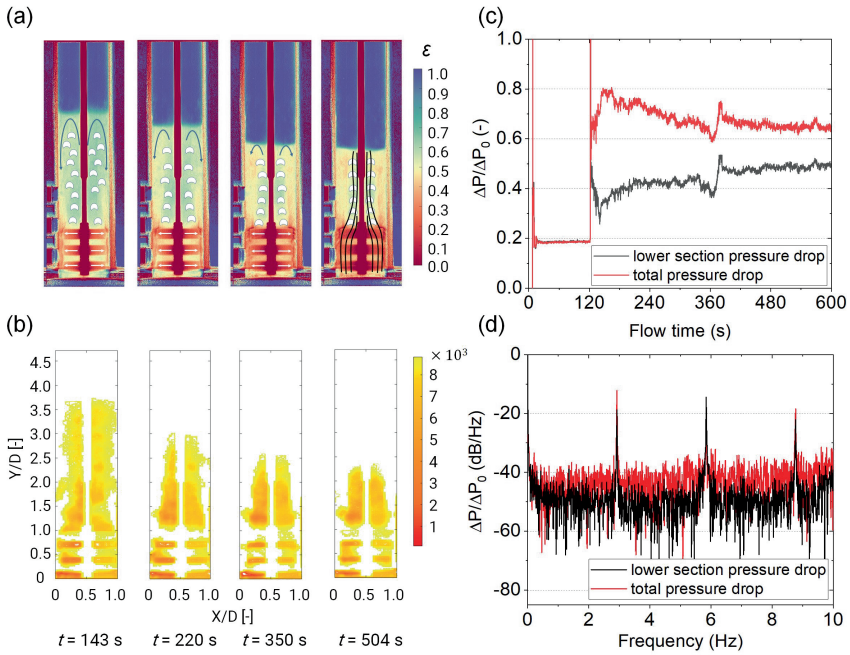


Figure 6.11: Example flow behaviour in a stirred bed with three double-bladed stirrers at 175 rpm: (a) Time-averaged flow patterns with indicative bubbles, and arrows suggesting the solid circulation routes, and streamlines showing the gas and bubbles routes; (b) the corresponding bubble probability density map; (c) the corresponding pressure series, measured over the entire bed and the bottom to $2/3^{rd}$ of initial bed height and (d) power spectrum. The flow pattern and profiles are obtained by averaging 10 s of frames at each selected time. $U = 3.1$ cm/s, $D = 5$ cm, $H = 10$ cm.

The witnessed fluidization behaviour provides insight into several design criteria for improving stirrer configurations. Firstly, the stirrer design should aim to maximize the sweep area to ensure consistent mobility of the powder, particularly in the bottom and wall regions of the bed. To corroborate this hypothesis, a modification to the stirrer is proposed, designed to reactivate particles that have settled in these critical regions. Lowering the stirrers is not feasible, since the tip of the bottom shaft was already positioned close to the distributor plate, only 5 mm away. As an alternative, attaching a soft brush to the lowest stirrer enables gently contacts with the plate and column walls, sweeping the deposited particles. Such a modification would facilitate in reciculating the powder into the fluidization process. A modular design consisting of three stirrers, each with four blades, served as the reference geometry, and experiments were conducted at a rotation speed of 130 rpm. From this reference configuration, two variations of soft brush arrangements were tested. The first design positions the soft brushes

solely on the bottom surface of the lowest stirrer, and the second layout features soft brushes affixed to both the side and bottom of the lowest stirrer, allowing for the simultaneous sweeping of the wall and bottom areas above the distributor plate, as shown in Figure 6.12.

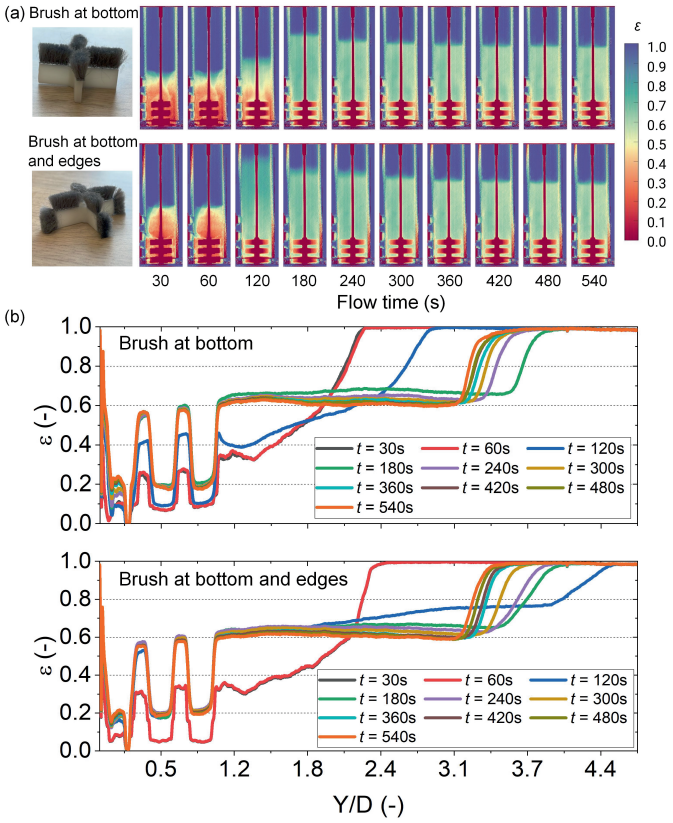


Figure 6.12: (a) Time-averaged flow patterns and (b) gas fraction profile in the stirred beds with brushes attached. Stirring starts at 120 s after the fluidization process begins. Each flow pattern is obtained by averaging 10 s of frames at each time. $U = 3.1$ cm/s, $N = 130$ rpm, $D = 5$ cm, $H = 10$ cm.

An improvement in fluidization is discernible with the integration of soft brushes, as depicted in Figure 6.12b. Both brush designs result in a similar initial bed expansion, and fluidization degradation is considerably reduced with the brush implementation. The bed stabilized after 300 s, and maintained a consistent, homogeneous state of fluidization. Compared to the experiments shown in Figure 6.7, the flow patterns displayed a much more uniform fluidization across the entire bed. Furthermore, the flow patterns revealed particle accumulation along the sidewalls, where brushes are absent, but notably, particles at the bed

bottom are effectively recirculated in both scenarios, promoting sustainable solid circulation. While the difference between the two brush designs is marginal, there is an improvement in terms of particle aeration, as indicated by the increased gas fraction. In contrast, experiments with non-brush modular stirrers showed a continuous compaction of solids. The successful implementation of brushes, as proof of concept, highlight the importance of thoroughly sweeping the bottom region to ensure effective circulation of particles. It is worth noting that in large-scale applications, the volume beneath the stirrers may only constitute a relatively small portion of the total powder load. Nonetheless, this region plays a crucial role in shaping the gas distribution, making it imperative to avoid any structured accumulation of particles.

In addition, the stirrer design should promote a more even distribution of bubbles and gas throughout the bed. while also preserving as much of the cross-sectional area as possible. This approach enables high shear interactions between gas and solids and minimizes the likelihood of air pocket formation. In addition to the modular design analysis, various modifications and several advanced stirrer configurations were also explored, as a proof of concept. These are depicted in Figure 6.13. The designs aim to fulfill the identified design criteria for enhanced fluidization performance by introducing both radial and axial disturbances. Specifically, three intricate configurations: the helical ribbon, spiral ribbon, and double spiral ribbon stirrer, were tested. These stirrers maintain a height comparable to the stacked three-stirrer modular configurations, but feature a curved spine and ribbon geometry. This design is anticipated to lift particles, instead of pressing them to the sides. The spiral ribbon mixers modify the gas pathway with cone-shaped rings positioned centrally, effectively redirecting gas streams and bubbles to create a more dynamic gas distribution. For consistency, all comparisons were also conducted at a rotation speed of 130 rpm, allowing for a direct comparison of their effectiveness in fluidization against the standard modular configurations.

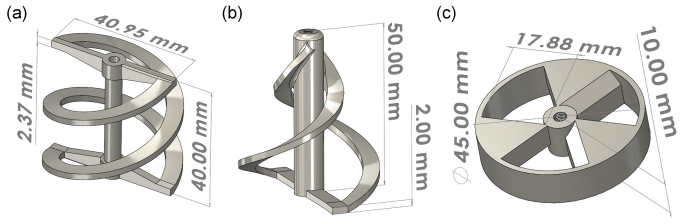


Figure 6.13: Configurations of advanced stirrers (a) ribbon type stirrer (b) spiral type stirrer (c) rotary disc.

The experimental results shown in Figure 6.14 reveal that the ribbon stirrer

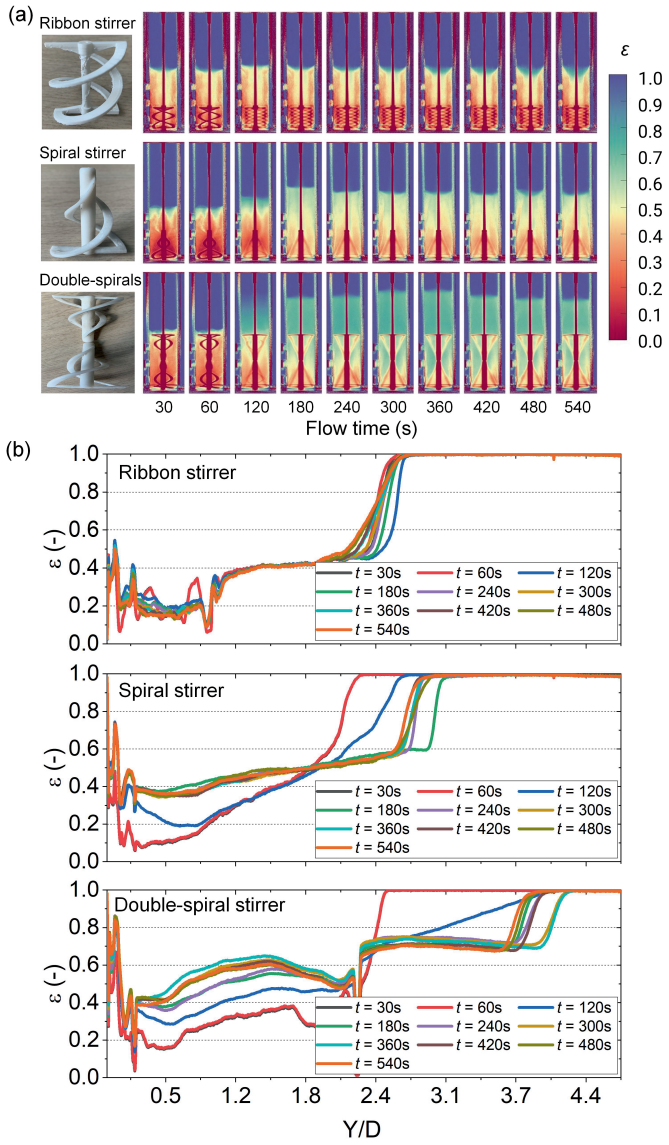


Figure 6.14: (a) Time-averaged flow patterns and (b) gas fraction profile in the unassisted and vibro-fluidized beds. Each flow pattern is obtained by averaging 10 s of frames at each time. Stirring starts at 120 s after the fluidization process begins. $U = 3.1$ cm/s, $N = 130$ rpm, $D = 5$ cm, $H = 10$ cm.

falls short in promoting bed expansion or disrupting the existing bed structure. Despite the stirring, gas continues to bypass through the central region, similar to the flow pattern obtained with the three-stirrer eight-blade configuration in

Figure 6.8, which is attributed to its relatively hollow and symmetrical configuration, coupled with gas blockage near the edges. In contrast, the use of a single spiral stirrer is able to trigger an initial bed expansion, while the particles quickly begin to accumulate, clearly visible along the cone edges. The results indicate that the single spiral stirrer converges gas streams at the tip of its cone, leading to a stable state with a slightly higher gas fraction of 0.5, compared to the ribbon stirrers, in which the gas fraction remains at 0.4. In an effort to redistribute gas flow, a configuration featuring two opposing spiral stirrers mounted in an inverted arrangement was tested. This configuration is anticipated to redistribute the merged gas flow from the tip of the lower spiral stirrer. The flow patterns reveal that such a configuration rapidly initiated bed expansion, and the top region was fluidized with a more uniform distribution of gas and bubbles, thereby maintaining a high level of bed expansion. Despite some particles settling from the gap between the stirrer edge and column wall, the enhanced distribution results in less particle accumulation along the sidewalls. The fluidization achieved with this configuration remains stable over time, exhibiting a significant dilated bed with a gas fraction ε exceeding 0.7.

Lastly, the influence of cross-sectional area openings on fluidization was investigated using different arrangements of rotary discs. The designs feature three triangular-shaped openings, as shown in Figure 6.13c. Both aligned and alternating arrangements were assessed, accounting for 50% and 100% of cross-sectional area obstruction, respectively. In the case of the 100% obstruction arrangement, the gas is unable to pass axially through the column, but navigates tortuously through the gaps between adjacent stirrers.

Figure 6.15 illustrates the effect of stirrer-induced cross-sectional area blockage on fluidization behavior. Fluidization becomes increasingly challenging, as the level of obstruction increases. Beds stirred by rotary discs in both the aligned and alternating arrangements are incapable of achieving a homogeneous state of fluidization. The aligned configuration is able to trigger initial bed expansion, but instead of improving fluidization by redistributing gas flow, fluidization rapidly deteriorates as particles accumulate along the sides, resulting in a spouting state. The half-opening configuration, designed to continuously redirect gas streams through the available openings, also shows it is ineffective in assisting fluidization. In contrast, the alternating arrangement faces greater challenges in initiating fluidization. Air pockets remain prevalent throughout the fluidization process, leading to a significant spouted bed state, as shown in Figure 6.15b. This comparison suggests that the tortuous gas pathways created in this setup are detrimental to initiating fluidization. These findings align with the observations of increased blockage when the number of blades is increased, as previously shown in Figure 6.8.

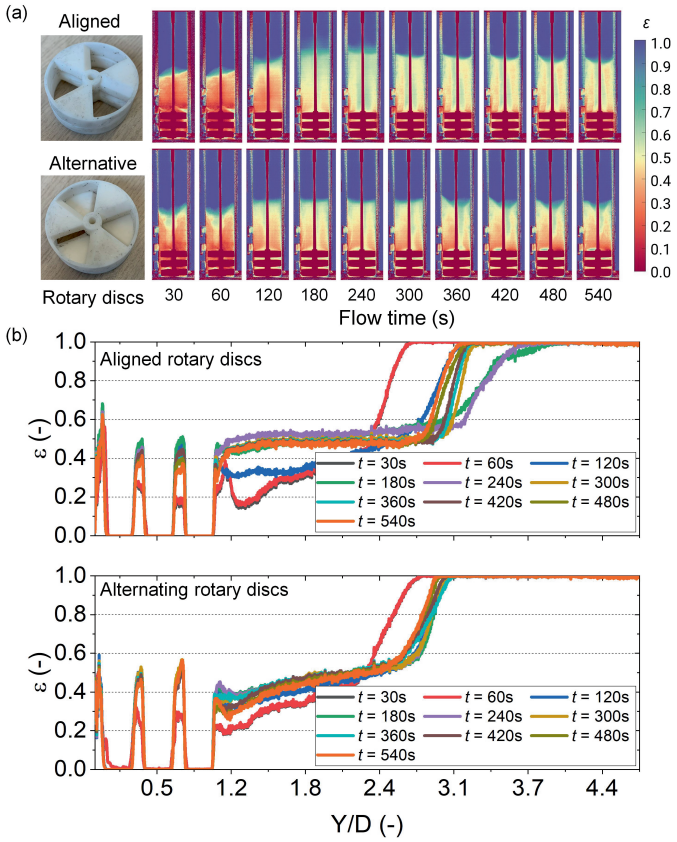


Figure 6.15: (a) Time-averaged flow patterns and (b) gas fraction profile in the bed with different cross-section blockage. Each flow pattern is obtained by averaging 10 s of frames at each time. Stirring starts at 120 s after the fluidization process begins. $U = 3.1$ cm/s, $N = 130$ rpm, $D = 5$ cm, $H = 10$ cm.

The conducted experiments showcase that the proposed design criteria for stirrers are promising. Notable improvements were observed in both bed expansion and sustained aeration in comparison to modular designs. However, practical applications present additional concerns. Scaling up stirrers is not trivial and can be approached either through employing multiple stirrers in specific areas or a single, larger-sized stirrer. Therefore, replicating these experiments in a larger column would yield valuable insights.

In addition to stirrer configurations, the observed flow patterns reveal that the presence of the shaft throughout the bed is problematic. Its substantial size (10% of the bed diameter) is promoting a preferential pathway for gas-bypass. It might be preferable to introduce the shaft from the bottom of the bed, thereby

avoiding the formation of a central gas pathway. Nevertheless, such a negative effect is anticipated to diminish if a larger bed diameter is employed, which would proportionally reduce the relative size of the shaft.

Moreover, achieving a balance between the blade length and volume swept by the blades is crucial. An excessively long blade could continuously press particles towards the bed boundaries, leading to inefficient mixing and potential compaction. In contrast, a blade that is too short may be inadequate for effectively sweeping the powder bed and initiating fluidization.

6.4. CONCLUSIONS

Stirring assistance has been shown to be an effective method for initiating fluidization by collapsing the existing bed structure, expanding the bed, and converting a channeling bed into a bubbling one by reactivating settled particles. The fluidization of cohesive micron-silica powders is heavily influenced by the stirring conditions and the configuration of the stirrer. Designs with the comb-configuration featuring fewer stirrers and blades, particularly when positioned in the bottom region of the bed, are more effective than those with a larger number of stirrers and blades in both initiating and sustaining fluidization. It has been observed that an increased number of stirrers tends to sweep more particles towards the column walls, resulting in a compacted layer of stagnant solids. This layer restricts the effective cross-sectional area, and redirects gas and bubbles towards a central pathway alongside the shaft. Besides, stirring agitation should be sufficiently vigorous to disrupt the internal structure of the bed, while excessive stirring can prevent particles from entering the stirring zone and quickly push them towards the sides, causing poor contact between the stirrer and the particles.

The analysis of flow patterns highlights that the compacted phase of solids is detrimental to effective fluidization. It is essential to either prevent the formation of stagnant zones or reactivate settled solids to sustain a fluidized state. Consequently, it is advisable to maximize sweep coverage to reduce stagnant areas and prevent compaction and deposition of solids. In addition, implementing more intricate designs, especially those that are asymmetrical, can facilitate the redistribution of gas and bubbles, and thereby promoting solid circulation. The configurations should also preserve an adequate opening in the cross-sectional area and avoid creating tortuous gas pathways. To formulate a more quantitative assessment, future research can focus on measuring the torque exerted by the stirrer on the system. This measure could serve as an additional indicator for optimizing stirrer configurations, potentially correlating it with the minimum mechanical energy input necessary to initiate and sustain an effective fluidization state. Moreover, to further understand radial and axial mixing within this system,

particle tracking techniques could be employed.

REFERENCES

[1] F. Raganati, R. Chirone, and P. Ammendola, *Gas-solid fluidization of cohesive powders,* Chemical Engineering Research and Design **133**, 347 (2018).

[2] R. Kamphorst, K. Wu, S. Salameh, G. M. H. Meesters, and J. R. van Ommen, *On the fluidization of cohesive powders: Differences and similarities between micro- and nano-sized particle gas–solid fluidization,* The Canadian Journal of Chemical Engineering **101**, 227 (2023).

[3] J. R. van Ommen, J. M. Valverde, and R. Pfeffer, *Fluidization of nanopowders: a review,* Journal of Nanoparticle Research **14**, 737 (2012).

[4] W. Zhang, *A review of techniques for the process intensification of fluidized bed reactors,* Chinese Journal of Chemical Engineering **17**, 688 (2009).

[5] J. R. van Ommen, J. Nijenhuis, and M.-O. Coppens, *Reshaping the structure of fluidized beds,* Chemical Engineering Progress , 49 (2009).

[6] V. Francía, K. Wu, and M.-O. Coppens, *Dynamically structured fluidization: oscillating the gas flow and other opportunities to intensify gas-solid fluidized bed operation,* Chemical Engineering and Processing - Process Intensification **159**, 108143 (2021).

[7] Z. Zhao, D. Liu, J. Ma, and X. Chen, *Fluidization of nanoparticle agglomerates assisted by combining vibration and stirring methods,* Chemical Engineering Journal **388**, 124213 (2020).

[8] M. A. A. Cruz, M. L. Passos, and W. R. Ferreira, *Final drying of whole milk powder in vibrated-fluidized beds,* Drying Technology **23**, 2021 (2005).

[9] R. Kamphorst, K. Wu, M. van Baarlen, G. M. Meesters, and J. R. van Ommen, *Effect of vibrational modes on fluidization characteristics and solid distribution of cohesive micro- and nano-silica powders,* Chemical Engineering Science **291**, 119911 (2024).

[10] K. Wu, L. de Martín, and M.-O. Coppens, *Pattern formation in pulsed gas-solid fluidized beds: the role of granular solid mechanics,* Chemical Engineering Journal **329**, 4 (2017).

[11] H. Khosravi Bizhaem and H. Basirat Tabrizi, *Experimental study on hydrodynamic characteristics of gas-olid pulsed fluidized bed,* Powder Technology **237**, 14 (2013).

[12] A. Kariman, V. Rao, and M. Farjpourlar, *Fluidization characteristics of nano particles with the assist of stirrer,* IOSR Journal of Applied Physics **5**, 24 (2013).

[13] R. Hong, J. Ding, and H. Li, *Fluidization of fine powders in fluidized beds with an upward or a downward air jet,* Particuology **3**, 181 (2005).

[14] J. R. van Ommen, D. M. King, A. Weimer, R. Pfeffer, B. van Wachem, S. Johnson, and N. Looije, *Experiments and modelling of micro-jet assisted fluidization of nanopowder,* in *10th international conference on circulating fluidized beds and fluidization technology (CFB-10)*, ECI Symposium Series, edited by P. E. T. Knowlton (2013).

[15] J. A. Quevedo, A. Omosebi, and R. Pfeffer, *Fluidization enhancement of agglomerates of metal oxide nanopowders by microjets,* AIChE journal **56**, 1456 (2010).

[16] S. Alavi and B. Caussat, *Experimental study on fluidization of micronic powders,* Powder Technology **157**, 114 (2005).

[17] Y. Zhou and J. Zhu, *Group C+ particles: Enhanced flow and fluidization of fine powders with nano-modulation,* Chemical Engineering Science **207**, 653 (2019).

[18] S.-W. Yin, L. Wang, and C.-P. Liu, *Study on agglomerate breaking and feeding of superfine particles in fluidized bed,* Chinese Journal of Process Engineering **8**, 230 (2008).

[19] J. Kim and G. Y. Han, *Effect of agitation on fluidization characteristics of fine particles in a fluidized bed,* Powder Technology **166**, 113 (2006).

[20] F. Yang, L. Wang, S. Yin, Y. Li, C. Liu, and L. Tong, *Experimental study on the entrainment characteristics of ultrafine powder in a fluidized bed with vibrator and agitator,* Industrial & Engineering Chemistry Research **52**, 1359 (2013).

[21] D. M. King, X. Liang, Y. Zhou, C. S. Carney, L. F. Hakim, P. Li, and A. W. Weimer, *Atomic layer deposition of tio2 films on particles in a fluidized bed reactor,* Powder Technology **183**, 356 (2008).

[22] K. Godard and J. Richardson, *The use of slow speed stirring to initiate particulate fluidisation,* Chemical Engineering Science **24**, 194 (1969).

[23] C. Hu, P. Zhang, X. Wang, X. Yang, L. Yang, Z. Zhang, and X. Kong, *Improvement of fluidization quality of a lif bed using internal blades,* Powder Technology **362**, 817 (2020).

[24] Y. Makkawi and P. Wright, *Fluidization regimes in a conventional fluidized bed characterized by means of electrical capacitance tomography,* Chemical Engineering Science **57**, 2411 (2002).

[25] T. Chandrasekera, A. Wang, D. Holland, Q. Marashdeh, M. Pore, F. Wang, A. Sederman, L. Fan, L. Gladden, and J. Dennis, *A comparison of magnetic resonance imaging and electrical capacitance tomography: An air jet through a bed of particles,* Powder Technology **227**, 86 (2012), emerging Particle Technology.

[26] C. M. Boyce, N. P. Rice, A. Ozel, J. F. Davidson, A. J. Sederman, L. F. Gladden, S. Sundaresan, J. S. Dennis, and D. J. Holland, *Magnetic resonance characterization of coupled gas and particle dynamics in a bubbling fluidized bed,* Physical Review Fluids **1**, 074201 (2016).

[27] A. Penn, C. M. Boyce, N. Conzelmann, G. Bezinge, K. P. Pruessmann, and C. R. Müller, *Real-time magnetic resonance imaging of fluidized beds with internals,* Chemical Engineering Science **198**, 117 (2019).

[28] R. F. Mudde, *Time-resolved x-ray tomography of a fluidized bed,* Powder Technology **199**, 55 (2010).

[29] J. R. van Ommen and R. F. Mudde, *Measuring the gas-solids distribution in fluidized beds – A review,* International Journal of Chemical Reactor Engineering **6** (2008), 10.2202/1542-6580.1796.

[30] J. Ma, J. R. van Ommen, D. Liu, R. F. Mudde, X. Chen, E. C. Wagner, and C. Liang, *Fluidization dynamics of cohesive geldart B particles. part I: X-ray tomography analysis,* Chemical Engineering Journal **359**, 1024 (2019).

[31] I. Mema, E. C. Wagner, J. R. van Ommen, and J. T. Padding, *Fluidization of spherical versus elongated particles - experimental investigation using X-ray tomography,* Chemical Engineering Journal **397**, 125203 (2020).

[32] S. Maurer, E. C. Wagner, J. R. van Ommen, T. J. Schildhauer, S. L. Teske, S. M. A. Biollaz, A. Wokaun, and R. F. Mudde, *Influence of vertical internals on a bubbling fluidized bed characterized by X-ray tomography,* International Journal of Multiphase Flow **75**, 237 (2015).

[33] A. Helmi, E. C. Wagner, F. Gallucci, M. van Sint Annaland, J. R. van Ommen, and R. F. Mudde, *On the hydrodynamics of membrane assisted fluidized bed reactors using x-ray analysis,* Chemical Engineering and Processing: Process Intensification **122**, 508 (2017).

[34] J. Saayman, W. Nicol, J. R. van Ommen, and R. F. Mudde, *Fast x-ray tomography for the quantification of the bubbling-, turbulent- and fast fluidization-flow regimes and void structures,* Chemical Engineering Journal **234**, 437 (2013).

[35] K. Wu, F. Galli, J. de Tommaso, G. S. Patience, and J. R. van Ommen, *Experimental methods in chemical engineering: Pressure,* The Canadian Journal of Chemical Engineering **101**, 41 (2023).

[36] D. Gidaspow, R. Bezburuah, and J. Ding, *Hydrodynamics of circulating fluidized beds: Kinetic theory approach,* in *Proc. of 7th Eng. Found. Conf. on Fluidization* (1991) pp. 75–82.

[37] H. M. Beakawi Al-Hashemi and O. S. Baghabra Al-Amoudi, *A review on the angle of repose of granular materials,* Powder Technology **330**, 397 (2018).

[38] J. R. van Ommen, S. Sasic, J. van der Schaaf, S. Gheorghiu, F. Johnsson, and M.-O. Coppens, *Time-series analysis of pressure fluctuations in gas-solid fluidized beds - A review,* International Journal of Multiphase Flow **37**, 403 (2011).

[39] D. Bradley and G. Roth, *Adaptive thresholding using the integral image,* Journal of Graphics Tools **12**, 13 (2007).

[40] N. Kuipers, E. Stamhuis, and A. Beenackers, *Fluidization of potato starch in a stirred vibrating fluidized bed,* Chemical Engineering Science **51**, 2727 (1996).

[41] K. Wu, E. C. Wagner, O. Ochkin-Koenig, M. Franck, D. Weis, G. M. H. Meesters, and J. Ruud van Ommen, *Time-resolved x-ray study of assisted fluidization of cohesive micron powder: On the role of mechanical vibration,* Chemical Engineering Journal , 143936 (2023).

[42] R. Kamphorst, P. C. van der Sande, K. Wu, E. C. Wagner, M. David, G. M.H.Meester, and J. R. van Ommen, *The mechanism behind vibration assisted fluidization of cohesive micro-silica,* KONA Powder and Particle Journal , 2024007 (2023).

SUPPLEMENTARY MATERIALS

6.5. VALIDATION OF TWO-POINT CALIBRATION

To specifically assess the deviation in two-point calibration due to beam hardening, we conducted validation experiments using lactose, characterized by a bulk density of 280 $kg\,m^{-3}$. Lactose is a food-grade powder and can be safely handled. While its density is still about twice as high as the silica powder employed in the study. Using the cascade container shown in Figure 6.16a, we monitored the X-ray intensity on the detector decreases as the material length increases. The results in Figure 6.16b show that the two-point calibration fitting remains valid, showcasing a minimal margin of error (the largest recorded deviation being less than 5%). Due to the lower bulk density than the lactose powder, it is expected that the silica powder will exhibit an even smaller deviation. It should be noted that such a deviation encompasses both measurement errors and the effects of beam-hardening, implying that the errors specifically due to potential beam-hardening effect is even smaller. Additionally, the multi-point fitting results presented in Figure 6.16c demonstrate essentially the same parameters and an R-squared value comparable to the two-point calibration fitting. The only notable difference is a marginally higher root mean squared error (RMSE) in the two-point fitting. Consequently, the validation test shows that two-point calibration fitting is sufficient.

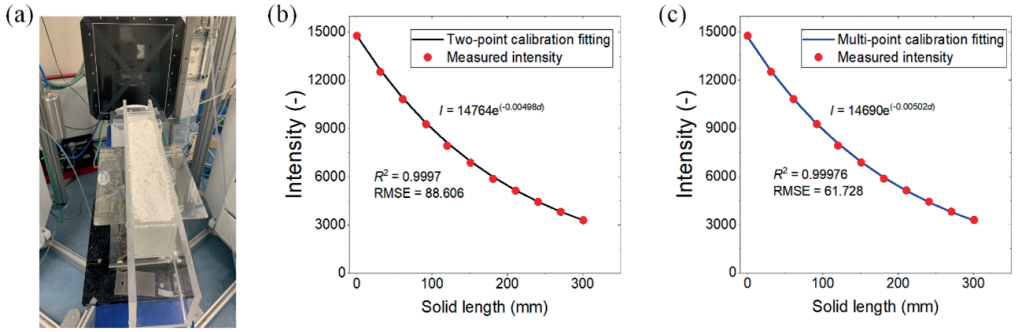


Figure 6.16: **(a)** Experimental setup for calibration process; **(b)** two-point calibration fitting, and **(c)** multi-point calibration fitting. Lactose powder is used in the experiments.

6.6. VALIDATION OF SINGLE ANGLE PROJECTION

Given a symmetrical configuration, the projections obtained from various angles are expected to be identical. Validation experiments were conducted using

three detector-source pairs simultaneously, which were evenly spaced around the setup, therefore encircling the entire fluidized bed, as illustrated in Figure 6.17a. The experimental conditions are outlined in the manuscript section Section 6.2. The results, shown in Figure 6.17b, align closely with the flow behaviour presented in Figure 6.11 of the manuscript. Observations from three different angles consistently reveal identical flow patterns, affirming the symmetry within the system. These patterns consistently showed regions near the sidewalls becoming denser over time, while the central regions remained a more dilute state. This consistency across different viewpoints confirms the symmetrical nature of the flow patterns and validates that a projection from a single angle is adequately representative of this system.

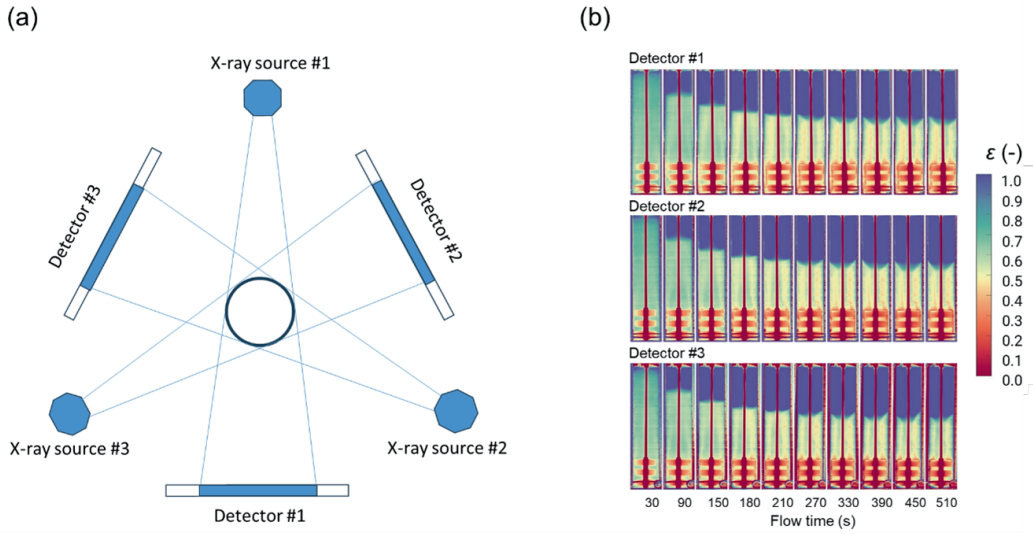


Figure 6.17: **(a)** The configuration of three detector-source pairs for the validation experiments; **(b)** Time-averaged flow patterns in a stirred fluidized bed. The flow patterns are recorded from three different angles simultaneously, each separated by 120°, providing a comprehensive 360°. Stirring starts at 30 s after the fluidization process begins. The flow pattern and profiles are obtained by averaging 10 s of frames at each selected time. Three stirrers of two blades are used. U = 3.1 cm s^{-1}. The rotational speed is 175 rpm.

6.7. STIRRED FLUIDIZED BEDS WITH VIBRATION INITIALIZATION

To initiate fluidization and achieve satisfactory bed expansion, vertical vibration was applied for the initial 30 s, followed by stirring for a duration of 480 s. The detailed operating protocols are outlined in Figure 6.18. Employing a vertical vibration with a frequency of 30 Hz and an amplitude of 1 mm the input momentum was transmitted throughout the particle bed. This helped in overcoming

interparticle forces and disrupting the internal structure of the bed [42]. After this vibro-initialization phase, a rapid stratification of the powder bed was observed. A significant portion of the bed mass settled in the lower section, resulting in a flow pattern comparable to the vibrated bed illustrated in Figure 6.6 of the manuscript.

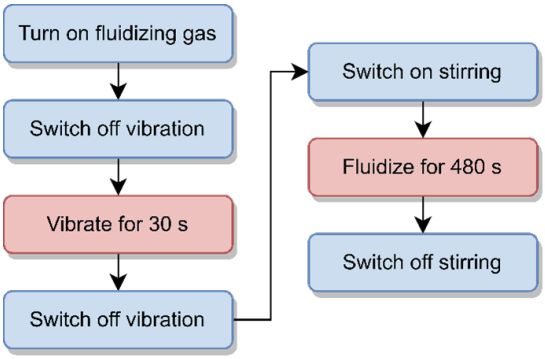


Figure 6.18: Operating procedures for the vibration-initialized fluidization experiments

This observed phenomenon is attributed to the frequent oscillation and tapping on the bottom layer particles, leading to bed compaction, a subject we explored in our previous work [41]. Such inhomogenity greatly impedes the ability of stirring to sustain fluidization. The flow patterns show that, in general, the fluidization degrades more rapidly and manifests similar temporal pattern of bed expansion, independent of the stirrer configuration, as shown in Figure 6.19. Moreover, the attained bed expansion is lower than that achieved in fluidization using the same stirrer configuration but without vibration. Nevertheless, the effectiveness of different stirrers in sustaining fluidization is not conclusively determined by these observations. The comparison clearly demonstrates that stirring alone is superior in creating a homogeneous mix of gas and solids. On the other hand, vibration assistance outperforms in promoting rapid bed expansion and development of fluidization.

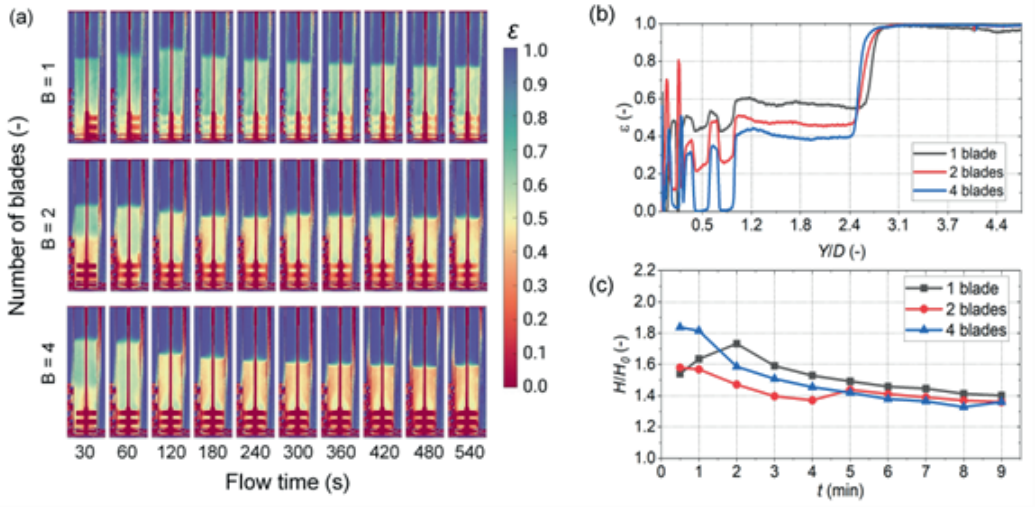


Figure 6.19: **(a)** Time-averaged flow patterns in vibro-fluidized beds, stirred with varying number of blades from one to four; **(b)** the gas fraction at 540 s, and **(c)** bed expansion profiles. Stirring starts at 120 s after the fluidization process begins. The flow pattern and profiles are obtained by averaging 10 s of frames at each selected time. Vertical vibration is used to initialize the fluidization at beginning, with the conditions of f = 30 Hz, A = 1 mm, U = 3.1 cm s^{-1}, N = 130 rpm

7

ENHANCING COLLOID STABILITY OF POLYMER MICROSPHERES IN WATER THROUGH SiO_2 COATING: EFFECTS OF COATING CYCLES AND SURFACE COVERAGE

Employing the acquired knowledge on fluidization gained in the previous chapters, we employed ALD in mechanically vibrated fluidized beds to improve the wettability of polymer microspheres. We show that low temperature deposition leads to coverage of the entire surface of particles after only two deposition cycles. Furthermore, it is shown that colloid stability is highly improved by the presence of an ultra-thin layer of SiO_2 and that film thickness plays a minor role compared to surface coverage.

This chapter has been published as "Enhancing colloid stability of polymer microspheres in water through SiO_2 coating: Effects of coating cycles and surface coverage" by R. Kamphorst, P. Wanjari, S. Saedy, J.F.K. van Dam, A. Thijssen, P. Brüner, T. Grehl, G.M.H. Meesters and J.R. van Ommen, Surfaces and Interfaces **45**, 103852 (2024)

In this study, we investigated the wettability and agglomeration characteristics of polymer microspheres coated with low-temperature deposited SiO_2 in a fluidized bed atomic layer deposition (ALD) setup. Surface characterization revealed the presence of a significant amount of deposited Si-OH groups within the first cycles. A drastic decrease in agglomerate size, water contact angle (WCA), and droplet absorption time of the powder was observed when coating was applied. Furthermore, we observed an increase in the amount of Si-OH present on the particle surface with increasing coating cycles, while no significant improvement in water affinity was found after the first coating cycles. Our findings suggest that surface coverage is the primary factor in improving the colloid stability of particles, coated at low temperatures. The low temperature operation of our system introduced a chemical vapor deposition (CVD) component to our coating process, which allowed full surface coverage to be achieved within the first two coating cycles.

7.1. INTRODUCTION

Fine particles dispersed in a liquid medium have extensive applications in various fields, examples of which are food [1, 2], drug-delivery [3], composites [4], and paints [5]. Due to their small size, the gravitational force acting on these particles is negligible, the stability of a colloidal suspension containing such particles is predominantly determined by the affinity of the solid surface groups with the liquid medium [6]. In the absence of adequate repulsion forces, van der Waals forces are dominant, causing particle clustering and eventual growth to a size where buoyancy induces phase segregation.

Since the affinity of the solid particles with the liquid medium is a surface characteristic, manipulating the surface groups is an effective lever to control the stability of liquid-solid dispersions. Various coating techniques have demonstrated their potential to stabilize the solid-liquid mixture without the need for a surfactant [7]. Of these techniques, atomic layer deposition (ALD) is an attractive option since it can deposit conformal, ultra-thin films, preserving the bulk properties of the coated substrate [8]. In this coating process, one or more precursor(s) and oxidiser(s) are introduced sequentially, with a purge step in between. The reactants are carefully chosen, such that they react in a self-limiting way with the substrate surface, depositing no more than one monolayer per coating cycle [9]. Coating thickness is controlled by selecting the amount of cycles. To obtain complete self-limiting behavior, the coating should take place within the ALD temperature window, which is typically at elevated temperatures. This limits the applicability and precursor options of the ALD process when dealing with temperature-sensitive substrates.

ALD is often seen as a specific type of chemical vapor deposition (CVD)[10]. In standard CVD, the precursor and oxidiser are typically introduced simultaneously. In the absence of a purge step, the reactants tend to physisorb onto the substrate surface and directly react with on another. This typically results in faster deposition and thicker coatings compared to ALD. Coating thickness is controlled by reaction time. CVD has the benefit of faster growth rates, but provides limited coating uniformity [11].

The application of such coating techniques on flat substrates is relatively straightforward. When dealing with particles however, a fluidized bed is often employed [12, 13]. Here, the powder is present in a column and gas in introduced from the bottom, creating drag and lifting up the particles, provided the system is operated above the so called minimum fluidization velocity. When in the fluidized state, gas-solid contact is maximized, allowing for efficient coating deposition on the particles. Due to the cohesive nature of small particles, fluidization becomes troublesome as slugging, channeling and excessive agglomeration can occur [14, 15], all of which limit gas-solid interactions. To overcome these

issues, assistance methods, like mechanical vibration [16, 17] and pulsed flow operation[18], can be introduced, which can break pre-existing structures and maintain a well-mixed emulsion phase.
In the present study, we improved the wettability of temperature sensitive polymer microspheres by depositing an SiO_2 coating, employing an fluidized bed ALD setup. The temperature sensitive substrate we aim to modify, necessitates operating at low temperatures. Consequently, not all reactants adsorbed on the substrate surface will be removed during the pruge steps, resulting in CVD behaviour, drastically increasing the deposition per coating cycle. We expect this to result in faster complete surface coverage, which we anticipate to be beneficial for this particular application. By operating in a pulsed, ALD-like, manner, we maintain control over the amount of deposition on the polymer particles. We demonstrate complete surface coverage was obtained within the first two deposition cycles. Furthermore, it is shown that the introduction of functional surface groups improved wettability and colloid stability. Our results provide insight into the dominant parameters of improved colloid stability by surface modification when applying coatings on temperature-sensitive substrates.

7.2. METHODS AND MATERIALS

7.2.1. SUBSTRATE

For this study, Expancel® polymer micro-spheres (provided by Nouryon) were used. An SEM image of the Expancel particles is show in in Figure 7.1. These particles are a methylmethacrylate-acrylonitrile co-polymer, which has a glass transition temperature of 90 °C, necessitating low temperature operation when depositing functional surface groups. The polymer shell encloses a driving gas, making that heating this powder to temperatures beyond 90 °C induces swelling of the particles, resulting in a volume increase of up to 60 times the initial volume. This property makes for a versatile product, which is, among other applications, used in paint, shoe soles, artificial leather, and printing ink. In Figure 7.2 the volume-based particle size distribution, as determined by a Malvern3000 particle size analyser, is shown.

7.2.2. DEPOSITION SETUP

The particles were coated in a fluidized bed ALD setup, utilising $SiCl_4$ and H_2O as reactants. A vibrating table was employed, operated at a frequency of 50 Hz and 0.015 mm amplitude to mitigate channel formation of the cohesive powder. Furthermore, since this powder proved to be exceptionally cohesive, we sieved with a 600 µm mesh size to remove pre-existing agglomerates and increase aeration of the bulk powder prior to fluidization. A glass column, with an inner diameter

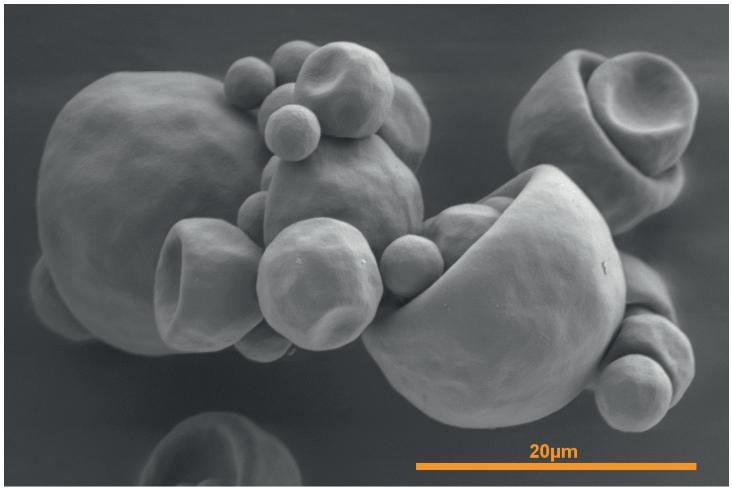


Figure 7.1: SEM image of Expancel® polymer microspheres

of 2.5 cm equipped with a heating jacket to maintain a constant temperature of 50 °C, as measured in the core of the reactor column, was used. The precursor bubblers were not heated (the ambient temperature was 25 °C), while the outlet lines of the bubblers and makeup stream line were heated to 30 °C, as was the windbox. Pulse times of 30 s for $SiCl_4$ and 45 s for H_2O were used with dry nitrogen as carrying gas; a N_2 purge time of 5 min was maintained between pulse steps. Additionally, a N_2 makeup stream was employed to maintain an equal gas flow during pulse and purge steps, assuring stable fluidization at constant a superficial gas velocity of 17 $cm\,s^{-1}$. During pulse steps, the ratio of pulse to makeup stream was 1:10. After every pulse step, the gas flow was interrupted for 15 s to allow for a back-pulse, preventing clogging of the top distributor plate, after which the fluidization was initiated again. After the final pulse step, the bed was purged for an additional 10 min before terminating the experiment. About 5 g of powder was coated during each experiment.

7.2.3. CHARACTERIZATION

Fourier Transform Infrared Spectrometry Attenuated Total Reflection (FTIR-ATR) was employed to identify surface groups on both coated and uncoated samples using the Nicolet 6700 spectrometer by ThemoFischer.

Additionally, the surface chemistry of uncoated and coated substrates was studied using X-ray photoelectron spectroscopy (XPS). For this purpose, a Thermo Scientific K-Alpha spectrometer, utilizing a monochromatic aluminum Kα radiation with a photon energy of 1486.7 eV, was used. An elliptical X-ray spot of 700

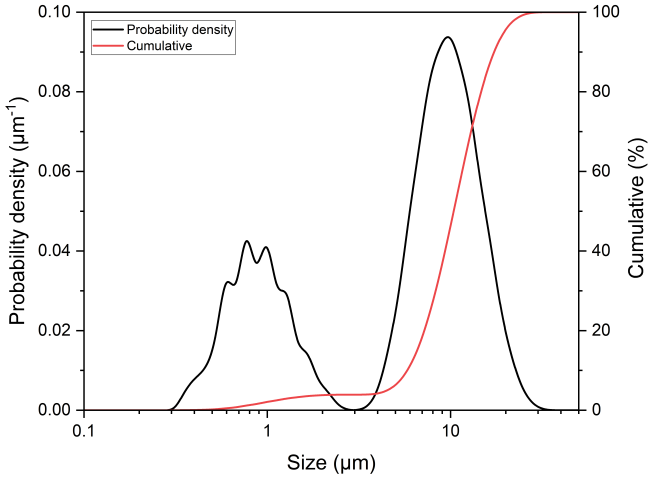


Figure 7.2: Volume-based particle size distribution of Expancel® polymer microspheres

x 400 µm^2 was radiated to the surface of the samples, and the differential charging was compensated using a flood gun. Using such a large probe size, compared to the individual Expancel® particle size, results in proper signal quality, statistically representing the average of the samples. The pristine and as-coated samples were stabilized on the sample holder using conductive carbon tape and transferred into the measurement chamber of the machine. The survey scans with a resolution of 1.0 eV were acquired to have an overall view of the surface chemistry of the sample and high-resolution spectra of the elements of interest (C, O, N, Si, and Cl) with a resolution of 0.1 eV. The obtained XPS spectra were analyzed using CasaXPS software. The peak positions were calibrated with reference to the aliphatic carbon 1s peak (284.8 eV). The chemical composition of the surface of investigated samples was quantified by taking into account the peak area (peak integration) of the studied elements after defining the quantification regions for each element, in CasaXPS.

To assess the surface coverage attained after coating we employed Low Energy Ion Scattering (LEIS). This technique offers the unique quality of having virtually no penetration depth, the measured signal originating the very top layer of a substrate surface [19]. This allows to establish whether full surface coverage is achieved, even if by a very thin layer of deposited material, from disappearance of substrate related peaks. The experiments were carried out using a Double Toroidal Energy Analyser by IONTOF, which used Helium ions and operated at an incident ion energy of 3000 eV, scattering angle of 145°.

Environmental Scanning Electron Microscopy (ESEM) was utilized to image the particles in the presence of moisture. To this end, a FEI Quanta FEG 650 was employed utilising a peltier cooling stage, operated at 0.5 °C, and operating pressures between 6–8 mbar to obtain water condensation.

Focused Beam Reflectance Measurements (FBRM) were performed for in-situ agglomerate size measurements, using the FBRM G400 by Mettler Toledo. The measured cord lengths were converted to diameters, using the ratio between the average cord length of a circle to its diameter. The powder sample was suspended in ultra-pure (Milli-Q) water at a loading of 20 $g L^{-1}$. For each experiment, the mixture was sonicated for 10 min prior to measuring the cluster size. Measurements were performed at room temperature, and a magnetic stirrer, rotating at 100 rpm, was employed during the entire runtime of the experiment. Data points were collected every 10 s; experiments lasted for a total of 60 min.

The water contact angle (WCA) was measured using the Drop Shape Analysis System by Kruss Scientific GmbH. To obtain a flat surface, (coated) powder was compressed into 1.0 cm diameter tablets by applying 1.0 tonne of pressure for 15 s, and droplets of 5 µL were placed onto the tablets at room temperature. The angle was measured immediately after the water-tablet contact. In addition, the duration of droplet infiltration into the tablet pores was recorded to yield supplementary insights on the affinity between the water and the substrate.

7.3. RESULTS AND DISCUSSION

7.3.1. SURFACE CHARACTERIZATION

The particles were subjected to FTIR-ATR to investigate the presence of Si surface species on coated substrates. To demonstrate the presence of SiO_2 after deposition, an isolated signal, originating from the applied coating, obtained by subtracting the signal from the uncoated sample from the coated one (10C raw), resulting in a differential signal (10C differential), is displayed in Figure 7.3. The highlighted regions of interest indicate the formation of Si-related groups and suppression of substrate-related peaks. The inverse peak observed in the differential signal in region **A** is caused by attenuation of the C=O response by the coating layer formed on top of the pristine sample. This region offers insights into film growth, as displayed in Figure 7.4. Note that the absorbance is plotted on the y-axis. We de-convoluted the raw signal by peak-fitting to determine the area of the C=O peak in each sample respectively (note the slight peak at 1630 cm^{-1} and the right shoulder to the C=O peak for the pristine sample). This area, normalized to the area peak of uncoated powder is shown in the inset. The coating layer reduced the peak intensity by each additional cycle. The inset in Figure 7.4 depicts a steep decrease in peak area upon the first cycle, with additional atten-

uation upon further deposition. Furthermore, the inset displays a considerably higher decrease in peak area upon the first coating cycle, compared to the near linear decrease found for consecutive cycles.

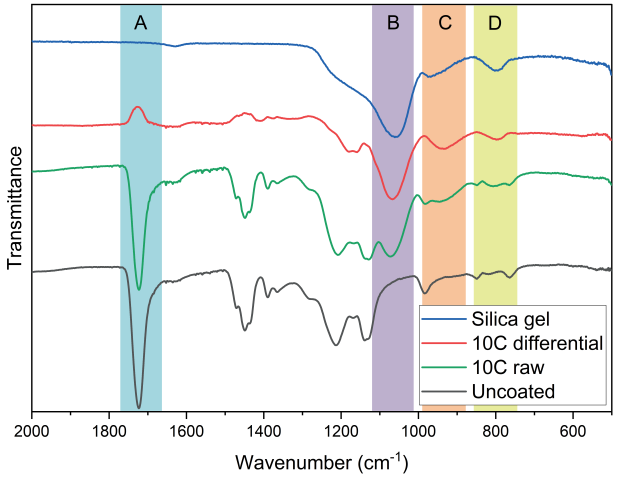


Figure 7.3: FTIR-ATR spectrum overview, **A** : C=O stretch, **B** : asymmetric Si–O–Si stretch, **C** : Si–OH bend , **D** : symmetric Si–O–Si

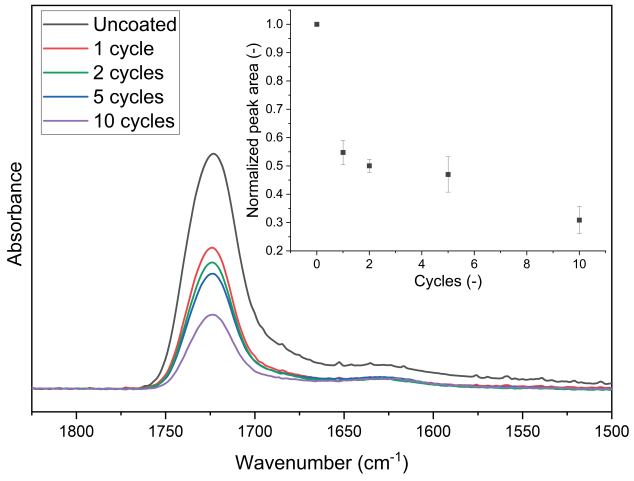


Figure 7.4: FTIR-ATR spectra showing decreasing intensity of C=O peak, due to signal attenuation when increasing the amount of coating cycles. In the inset normalized C=O peak areas after various amounts of deposition cycles are displayed.

In Figure 7.5, we present the FTIR-ATR spectra within the region where Si-related peaks occur. It can be observed that the peak heights found at 930 cm^{-1} and 1070 cm^{-1} grow with increasing deposition cycles. The 930 cm^{-1} peak is attributed to Si-OH bending [20–22] and the 1070 cm^{-1} peak corresponds to asymmetric Si-O-Si stretching [23]. Furthermore, for 5 and 10 cycles of deposition, an additional peak becomes visible at 800 cm^{-1}, which corresponds to symmetric stretching Si-O-Si [23]. This peak is partially obscured at lower amount of cycles due to the substrate peaks at 760 cm^{-1} and 850 cm^{-1}. These peaks, as well as the one at 980 cm^{-1} again show signal suppression of the substrate when the amount of coating cycles is increased. The inset in Figure 7.5 provides insight into the relative growth rate of Si-O-Si and Si-OH groups (normalized to the area underneath the C=O peak of the pristine sample, for Si-O-Si only the area of the peak corresponding to asymmetric stretching is considered). Since Si-OH groups are anticipated to be present mostly on the surface of the sample, and are expected to be consumed in the precursor step by forming O-Si-Cl bonds, the observed lower relative value is expected. The continuous growth of this peak during the first 10 cycles indicates coating deficiencies, where not all Si-OH groups react upon the introduction of $SiCl_4$ during the precursor step and some are built into the coating. The inset also shows a pronounced initial slope for both Si-groups, followed by a, less steep, linear growth upon additional deposition cycles.

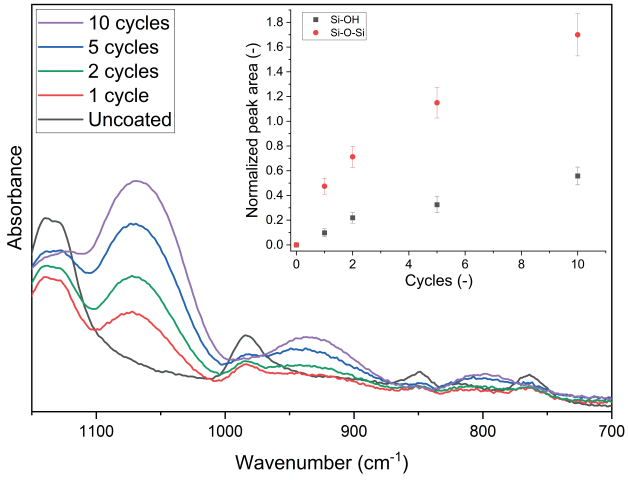


Figure 7.5: FTIR-ATR spectra showing growth of Si-related peaks when increasing the amount of coating cycles. In the inset normalized areas of O-Si-O and Si-OH peaks after various amounts of deposition cycles are displayed.

The XPS experimental results are presented in Figure 7.6. First of all, it is

evident that the coating incorporates negligible amounts of chlorine. This finding indicates that the oxidizer step of the coating cycles reaches full completion. However, considering the results presented in Figure 7.5, the precursor step does not reach completion, as the amount of Si-OH groups keeps increasing with additional coating cycles. Additionally, the atomic percentage of Si and O demonstrates an initial increase in the first coating cycle, followed by a stable composition in subsequent deposition cycles. This observation leads us to conclude that a coating layer thicker than the XPS signal's penetration depth (approximately 4 nm) is deposited during the first coating cycle. This outcome aligns with the FTIR-ATR data, although the greater penetration depth of that technique allows for subsurface information to be obtained, even after multiple coating cycles. Finally, the presence of carbon (note the double y-axis) originates from incidental groups formed due to sample exposure to the atmosphere.

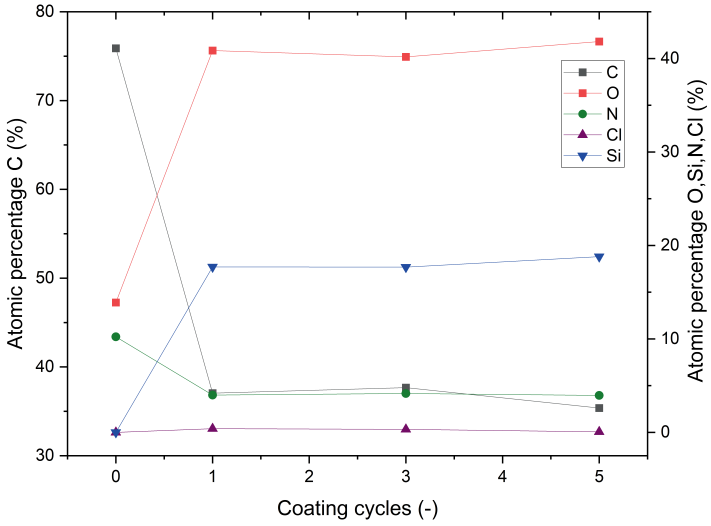


Figure 7.6: Atomic percentage of elements found on the particle surface, obtained via XPS

LEIS experiments were performed to assess the surface coverage of coated samples, the results of which are displayed in Figure 7.7. Here it is demonstrated that the spectra of the coated particles did not change with an increasing number of coating cycles; note that we tested a sample coated with 100 cycles to assure of no changes upon excessive additional deposition. Furthermore, in contrast to the signal obtained by XPS, the carbon related signal found by LEIS is absent after a single coating cycle already. Additionally, the absence of a chlorine peak, which would appear at 1950 eV if present, re-affirms completion of the oxidizer step of the coating process. Our findings indicate that full surface coverage was

achieved after a single coating cycle. Furthermore, the non-zero signal between the O and Si peaks originates from subsurface Si. Note that this is observed after 1 coating cycle and is not changing with additional deposition. This confirms the conclusions drawn earlier from the XPS data that more than a mono-layer of coating is deposited after in the first coating cycle. From additional experiments utilizing focused ion beam SEM, it was found that the coating thickness of all samples in this study was well below 80 nm, though an exact thickness could not be obtained, see the supplementary materials for more details.

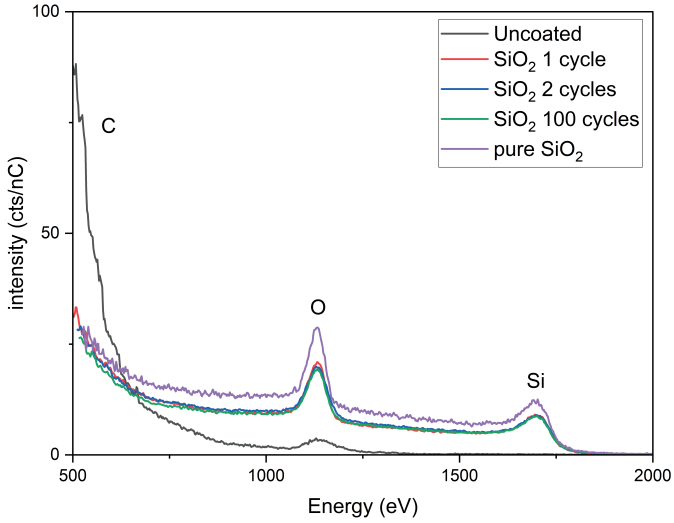


Figure 7.7: LEIS results of pristine sample, coated samples and SiO_2 powder

Based on the analysis of FTIR-ATR, XPS, and LEIS results, we expect the presence of adsorbed moisture on the particle surface during the initial coating cycle, which could not entirely be removed due to the low temperature operation. Adsorption of ultra-thin layers of moisture is known to occur on hydrophilic, and even to some extent on hydrophobic particles [24]. When present, this moisture contributes to the formation of a comparatively thick and conformal coating during the first deposition cycle, which subsequently increases in thickness with additional coating cycles. This observation provides a plausible explanation for several findings. Firstly, LEIS analysis indicates complete surface coverage following the first cycle. Secondly, XPS analysis confirms a substantial deposition thickness after the initial cycle. Lastly, FTIR-ATR data reveals a higher deposition amount in the first cycle compared to subsequent cycles. These observations collectively highlight key distinctions between the conventional ALD coating process and the pulsed CVD coating process employed in our study.

7.3.2. WETTABILITY AND AGGLOMERATION

In order to provide a qualitative evaluation of the improved wettability of the coated particles, we utilized ESEM to visualize the particles in the presence of moisture. The image of uncoated particles, Figure 7.8, demonstrates limited affinity with water, as the surface of the particles appear completely devoid of moisture. In contrast, the coated particles, seen in Figures 7.9 to 7.11 display a marked affinity with water. The imaged agglomerates tended to absorb water to a high extent, resulting in their entire surface being covered by water. Furthermore, individual particles were observed to adsorb water, and form a layer of water onto their surfaces too. Based on these images, it is evident that there is a discernible distinction in behaviour between the coated and uncoated particles when brought in contact with water. It should be noted that the clustering of the coated particles observed in the images is a result of the coating process, in which agglomerates are formed in the fluidized bed. All of the agglomerates imaged in this study were present prior to the introduction of moisture in the ESEM.

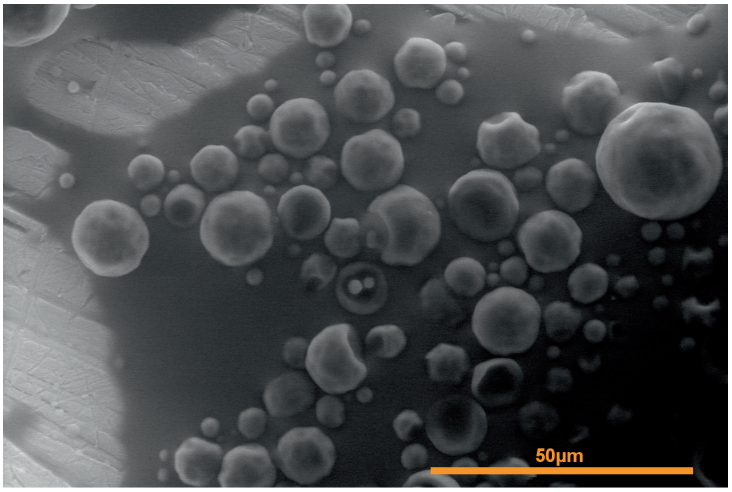


Figure 7.8: ESEM image of uncoated powder in the presence of moisture showing limited water-sample affinity

To gain further insight into the phenomenon observed in the ESEM images, and to allow the results to be quantified, we also considered the results of the FBRM. Figure 7.12 illustrates the development of the agglomerate size distribution in water of the experiment where uncoated particles are studied. Note that the vast majority of primary particles of the pristine powder were found to have a size below 20 µm (Figure 7.2). Therefore, only the measured entities with a diameter above 20 µm can reliably be identified as agglomerates. It was observed that

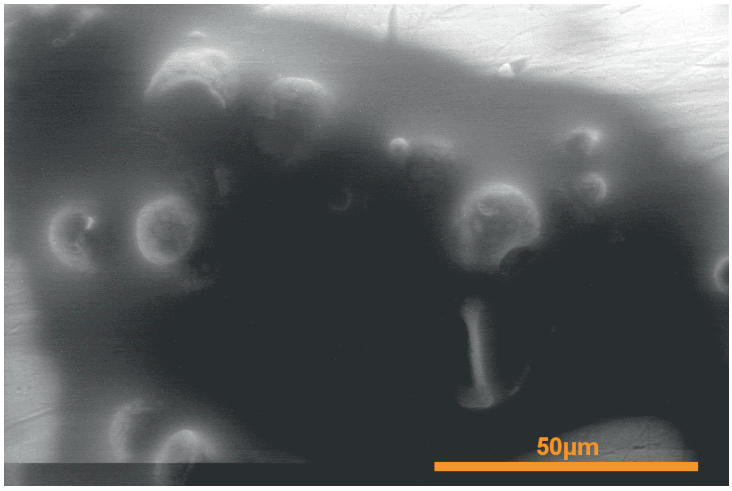


Figure 7.9: ESEM image of powder, coated with 1 cycle of SiO_2, in the presence of moisture

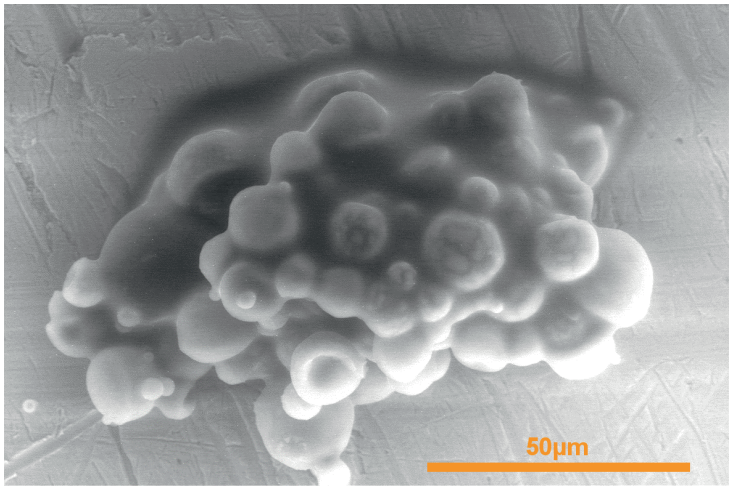


Figure 7.10: ESEM image of powder, coated with 5 cycles of SiO_2, in the presence of moisture

the agglomerates initially grow upon contact with water, which is highlighted in the inset of Figure 7.12. This behaviour re-establishes the limited affinity of the pristine powder with water. In contrast, particles coated with SiO_2 for only 1 cycle show no significant change in agglomerate size formation over time, when brought in contact with water, as can be observed in Figure 7.13. Furthermore, when 2 coating cycles are deposited, the agglomerate size even decreases initially before reaching a stable size, as seen in Figure 7.14. After the first two coating cycles, subsequent deposition yielded no significant changes in agglomerate

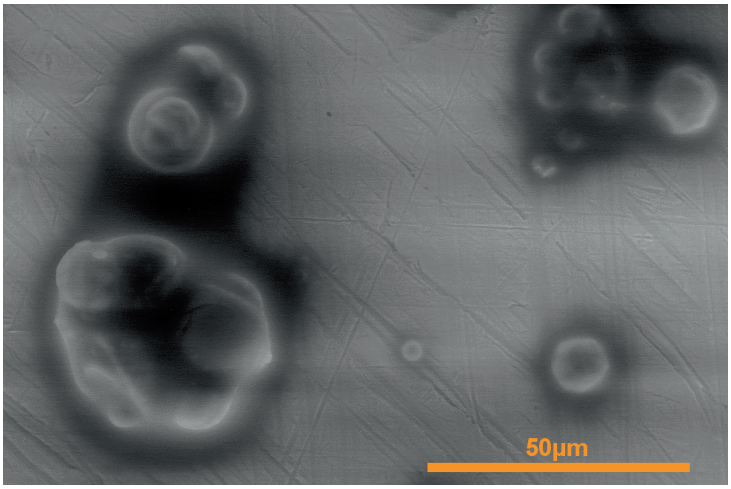


Figure 7.11: ESEM image of powder, coated with 10 cycles of SiO_2, in the presence of moisture

size distribution. Moreover, the uncoated particles exhibited a broader peak in comparison to those coated with one or two cycles, inidicating the formation of a significant quantity of agglomerates smaller than 20 µm (note in Figure 7.2 that a considerable amount of small primary particles are present in the powder; clustering of these particles can result in agglomerates of less than 20 µm). The relatively sharp peak observed in particles coated with two cycles suggests a reduction these smaller agglomerates, although we were not able to quantify the extent of their suppression. Furthermore, the emergence of a new peak at approximately 10 µm aligns with the second peak of the bimodal distribution of the primary particles, providing further evidence of successful de-agglomeration of both large and small particle clusters.

The number-based d_{50} and d_{90} of the coated particles, as measured after 30 min in water, when the agglomerate sizes of all samples have stabilized, are presented in Figure 7.15. The d_{50} remains nearly unchanged between samples due to its correspondence to the larger primary particles found in the powder, as observed in Figure 7.2, potentially including some agglomerates formed by the clustering of smaller particles. The diameter of the largest clusters found in the samples, d_{90}, decreases during the first two coating cycles and remains stable after subsequent deposition. Note that in Figure 7.5 we showed additional Si-OH groups to keep forming after the first coating cycle, and Figure 7.7 showed full surface coverage after the first coating cycle. These results, combined with the FBRM data imply that surface coverage is the dominant parameter to reduce the agglomerate formation of the polymer micro spheres. We conclude that no additional benefit is gained from increasing the coating thickness and additional

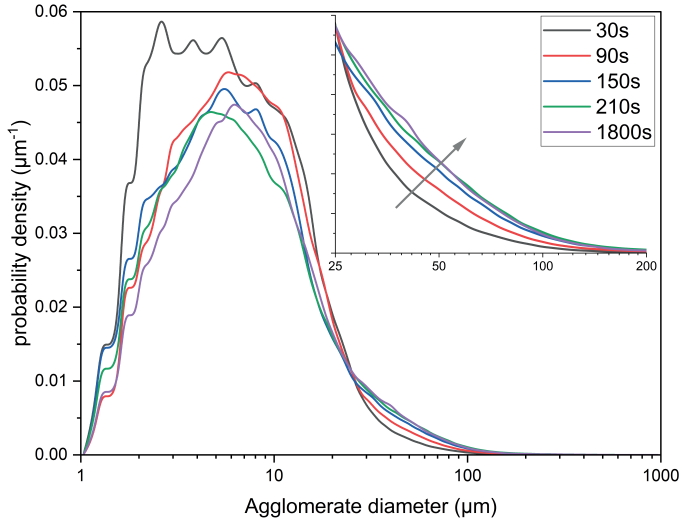


Figure 7.12: Number-based agglomerate size distribution development over time of uncoated polymer microspheres in water, measured by FBRM

functional Si-OH groups once full surface coverage has been achieved. It should be noted that agglomeration occurring during the coating process can hinder the complete surface coverage of individual particles in a single cycle, leaving certain regions of particle contact uncoated. During prolonged fluidization agglomerates can break and reform in a dynamic equilibrium, exposing uncoated areas and facilitating the complete coating of all particles over time. The prior discussion of ESEM images taken of coated particles already touched on the presence of this agglomeration. It is anticipated that these agglomerates are stable under normal handling conditions, clarifying why this effect cannot be seen when employing the previously discussed characterization techniques. However, fully submerging the particles in water is anticipated to cause their disintegration, thereby exposing the uncoated regions, affecting the agglomeration behavior. This explains the additional decrease in d_{90} observed in Figure 7.15 with the application of the second deposition cycle, as it promotes complete coating of all particles.

To substantiate this claim, SEM images of coated particles are provided in Figure 7.16 (additional images are provided in the supplementary materials). Particle clusters were intentionally broken up before imaging to reveal uncoated areas resulting from agglomeration. Considering samples, coated with only a single cycle of SiO_2, many non-fully coated particles could be observed, as demonstrated in Figure 7.16a. The gaps being circular, implies that the coating was in-

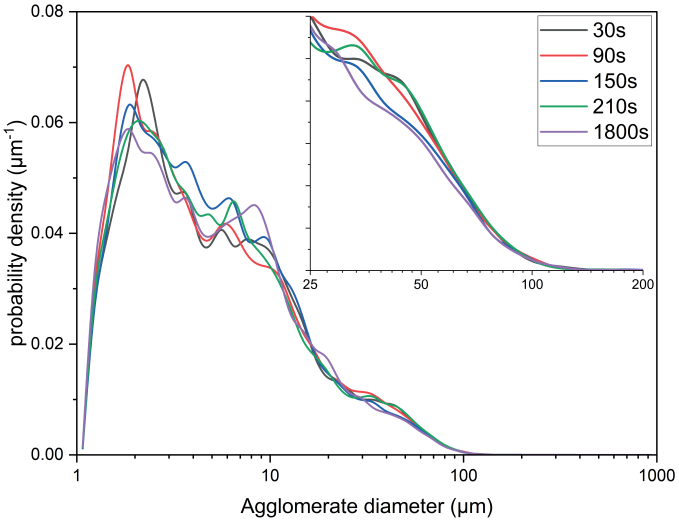


Figure 7.13: Number-based agglomerate size distribution development over time of polymer microspheres coated with 1 cycle of SiO_2 in water, measured by FBRM

deed blocked by the presence of particles, attached to the surface by van der Waals forces. Significant gaps were not observed in samples that were subjected to multiple coating cycles. Furthermore, all images in Figure 7.16 display a non-uniform coating thickness, which is expected to result from the CVD component within our system.

Additionally, in Figure 7.17, we present the findings from the WCA measurements, as well as the measured time for the porous tablet to absorb the entire droplet. The results indicate that the affinity towards water increases after the initial coating cycles, with limited benefits from subsequent deposition. The tested particles were compressed into a tablet prior to experimentation, therefore their mobility was limited. This explains why the effects of exposure of uncoated areas upon the presence of water, as seen during the FBRM experiments, was not observed here. It is important here to note that the preparation of the samples introduces cracks in the coating due to the application of mechanical stress on the particles to pelletize them. This exposes the substrate underneath and alters the surface roughness of the sample, thus contributing to some of the variability in the data. Additionally, we wish to emphasize that the WCA and absorption time measured on pelletized powder substrates should be treated with care since the results might not always be representative of individual particle behaviour. These results, however, do confirm the trend observed in the other discussed outcomes, where additional deposition, after achieving full surface

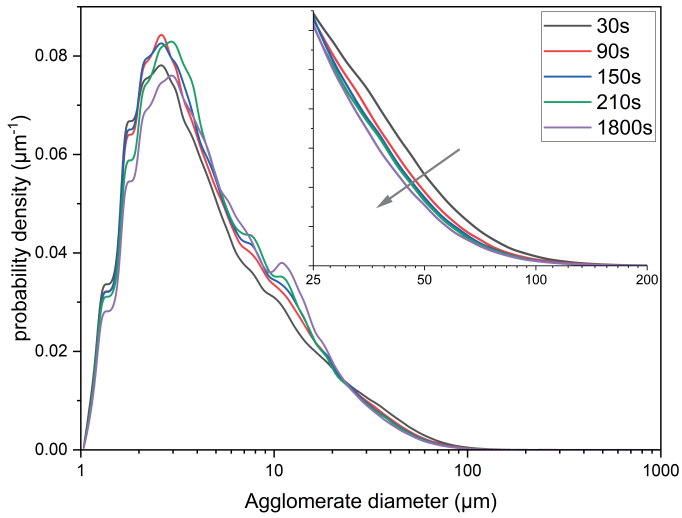


Figure 7.14: Number-based agglomerate size distribution development over time of polymer microspheres coated with 2 cycles of SiO_2 in water, measured by FBRM

coverage, has no significant impact on the substrate's affinity towards water.

7.4. CONCLUSION

In this investigation, we assessed the impact of a SiO_2 coating, deposited at low temperature in a fluidized bed ALD setup, on the wetting properties of polymer microspheres. Our objective was to introduce hydrophilic Si-OH groups to the particle surface. Their presence was confirmed by FTIR-ATR analysis of the coated substrate. Combined FTIR-ATR, XPS, LEIS and SEM results indicated that a film of SiO_2, covering the entire particle surface, was deposited within the first two coating cycles, with additional cycles thickening this film. Furthermore, insights from applying these techniques demonstrated that the selected conditions under which our system was operated resulted in non-ideal ALD behaviour (i.e. pulsed CVD). This led to the deposition of a film with a considerable thickness (>4 nm) within the first coating cycle due to the presence of a large CVD component. ESEM imaging demonstrated that the coated agglomerates had a higher tendency to absorb water compared to the uncoated particles. Additional insight from FBRM data indicated that a second coating cycle provided benefits in reducing agglomerate sizes when brought in contact with water. We anticipate this to be caused by uncoated regions which were subjected to particle-particle

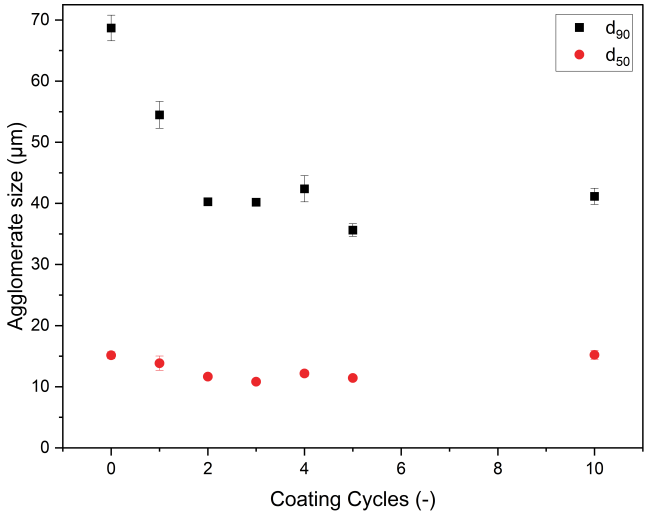


Figure 7.15: Agglomerate sizes of pristine and coated powder in water, as measured after 30 min by FBRM (number-based)

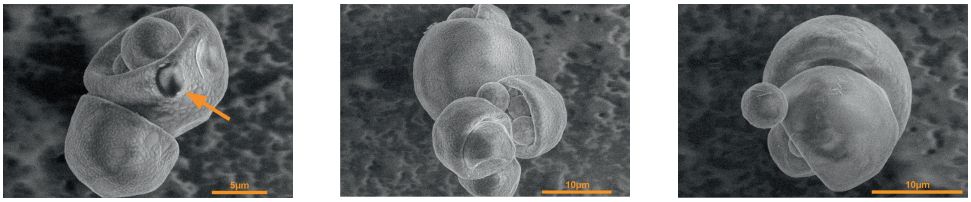


Figure 7.16: SEM images of Expancel® powder, coated with **(a)** 1 cycles, **(b)** 2 cycles and **(c)** 10 cycles of SiO_2, the arrow in **(a)** indicates the position of an uncoated spot

contact during the first coating cycle. These regions are revealed upon disintegration of the agglomerates in the presence of water. The uncoated areas can be filled in by consecutive coating cycles, however. More than two coating cycles did not lead to any significant gains in affinity with water, indicating the majority of gaps to have been coated by then. This hypothesis is supported by SEM images of coated samples. Our findings indicate that surface coverage is the key factor in enhancing the stability of a particle-water dispersion by depositing a hydrophilic nanocoating.

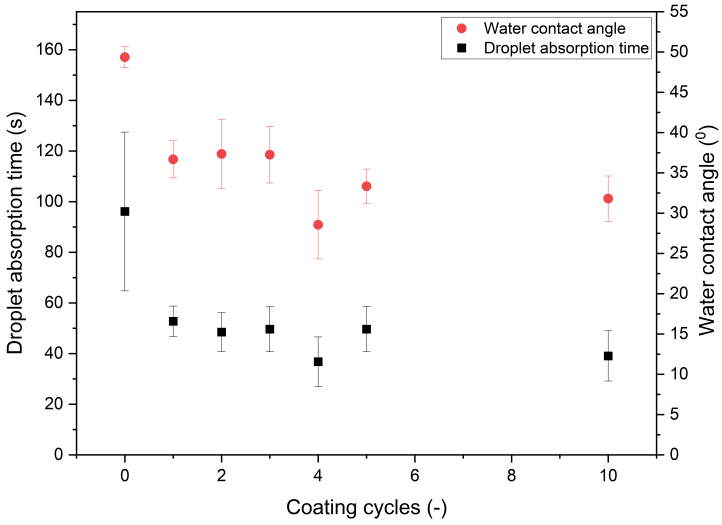


Figure 7.17: Water contact angles and absorption time of uncoated and coated sample

REFERENCES

[1] N. Garti and I. Yuli-Amar, *6 - micro- and nano-emulsions for delivery of functional food ingredients*, in *Delivery and Controlled Release of Bioactives in Foods and Nutraceuticals*, Woodhead Publishing Series in Food Science, Technology and Nutrition, edited by N. Garti (Woodhead Publishing, 2008) pp. 149–183.

[2] A. Sullo and I. Norton, *Food colloids and emulsions,* in *Encyclopedia of Food and Health*, edited by B. Caballero, P. M. Finglas, and F. Toldrá (Academic Press, Oxford, 2016) pp. 7–15.

[3] N. Singh, A. Joshi, A. Toor, and G. Verma, *Chapter 27 - drug delivery: advancements and challenges,* in *Nanostructures for Drug Delivery*, Micro and Nano Technologies, edited by E. Andronescu and A. M. Grumezescu (Elsevier, 2017) pp. 865–886.

[4] M. Agrawal, S. Gupta, and M. Stamm, *Recent developments in fabrication and applications of colloid based composite particles,* J. Mater. Chem. **21**, 615 (2011).

[5] T. Tadros, *Colloids in paints,* in *Colloids in Paints* (John Wiley and Sons, Ltd, 2010) Chap. 1, pp. 1–9, https://onlinelibrary.wiley.com/doi/pdf/10.1002/9783527631179.ch1 .

[6] H. Butt and M. Kappl, *Surface and Interfacial Forces*, 2nd ed. (WILEY-VCH, 2010).

[7] J. Schubert and M. Chanana, *Coating matters: Review on colloidal stability of nanoparticles with biocompatible coatings in biological media, living cells and organisms,* Current medicinal chemistry **25** (2018), 10.2174/0929867325666180601101859.

[8] H. Van Bui, F. Grillo, and J. R. van Ommen, *Atomic and molecular layer deposition: off the beaten track,* Chem. Commun. **53**, 45 (2017).

[9] R. W. Johnson, A. Hultqvist, and S. F. Bent, *A brief review of atomic layer deposition: from fundamentals to applications,* Materials Today **17**, 236 (2014).

[10] L. Sun, G. Yuan, L. Gao, J. Yang, M. Chhowalla, K. Heydari Gharahcheshmeh, M.and Gleason, Y. Choi, B. Hong, and Z. Liu, *Chemical vapour deposition,* **1**, 5 (2021).

[11] D. Muñoz-Rojas, V. Nguyen, C. Masse de la Huerta, S. Aghazadehchors, C. Jiménez, and D.Bellet, *Spatial atomic layer deposition (sald), an emerging tool for energy materials. application to new-generation photovoltaic devices and transparent conductive materials,* Comptes Rendus Physique **18**, 391 (2017), demain l'énergie.

[12] J. van Ommen and A. Goulas, *Atomic layer deposition on particulate materials,* Materials Today Chemistry **14**, 100183 (2019).

[13] J. Guo, D. Benz, T.-T. Doan Nguyen, P.-H. Nguyen, T.-L. Thi Le, H.-H. Nguyen, D. La Zara, B. Liang, H. T. B. Hintzen, J. R. van Ommen, and H. Van Bui, *Tuning the photocatalytic activity of tio2 nanoparticles by ultrathin sio2 films grown by low-temperature atmospheric pressure atomic layer deposition,* Applied Surface Science **530**, 147244 (2020).

[14] R. Kamphorst, K. Wu, S. Salameh, G. H. Meesters, and J. van Ommen, *On the fluidization of cohesive powders: Differences and similarities between micro- and nano-sized particle gas–solid fluidization,* The Canadian Journal of Chemical Engineering **101**, 227 (2023), https://onlinelibrary.wiley.com/doi/pdf/10.1002/cjce.24615 .

[15] D. Geldart, N. Harnby, and A. Wong, *Fluidization of cohesive powders,* Powder Technology **37**, 25 (1984).

[16] R. Kamphorst, P. van der Sande, K. Wu, E. Wagner, M. David, G. Meesters, and J. van Ommen, *The mechanism behind vibration assisted fluidization of cohesive micro-silica,* KONA Powder and Particle Journal **advpub**, 2024007 (2023).

[17] H. Azizpour, M. Talebi, F. Tichelaar, R. Sotudeh-Gharebagh, J. Guo, J. van Ommen, and N. Mostoufi, *Effective coating of titania nanoparticles with alumina via atomic layer deposition,* Applied Surface Science **426**, 480 (2017).

[18] S. Ali, E. AL-Ghurabi, A. Ajbar, Y. Mohammed, M. Boumaza, and M. Asif, *Effect of frequency on pulsed fluidized beds of ultrafine powders,* Journal of Nanomaterials **2016**, 1 (2016).

[19] S. Ebnesajjad, *Chapter 4 - surface and material characterization techniques,* in *Surface Treatment of Materials for Adhesive Bonding (Second Edition)*, edited by S. Ebnesajjad (William Andrew Publishing, Oxford, 2014) second edition ed., pp. 39–75.

[20] P. Launer and B. Arkles, *Infrared analysis of organosilicon compounds,* (2013) pp. 175–178.

[21] M. Omar, K. Ismail, A, I. Sumpono, E. Albert Alim, M. Nawi, M. Mukri, Z. Othaman, and S. Sakrani, *Ftir spectroscopy characterization of si-c bonding in sic thin film prepared at room temperature by conventional 13.56 mhz rf pecvd,* Malaysian Journal of Fundamental and Applied Sciences **8** (2012), 10.11113/mjfas.v8n4.156.

[22] F. Yan, J. Jianguo, X. Chen, S. Tian, and K. Li, *Synthesis and characterization of silica nanoparticles preparing by low-temperature vapor-phase hydrolysis of sicl4,* Industrial and Engineering Chemistry Research **53**, 11884 (2014).

[23] P. Pinto, L. Mendes, M. Dias, and C. Azuma, *Synthesis of acrylic-modified sol–gel silica,* Colloid and Polymer Science **284**, 529 (2006).

[24] S. Salameh, M. van der Veen, M. Kappl, and J. van Ommen, *Contact forces between single metal oxide nanoparticles in gas-phase applications and processes,* Langmuir **33**, 2477 (2017), pMID: 28186771, https://doi.org/10.1021/acs.langmuir.6b02982 .

SUPPLEMENTARY MATERIALS

7.5. SEM

Additional images of coated and uncoated particles were obtained. A FEI FIB/SEM Helios G4 CX was employed for imaging. All images were taken at high vacuum and an accelerating voltage of 3.0 kV. This comparatively low voltage was required to mitigate charging tendency of the particles and limited the obtainable resolution of the acquired images. To adequately image the deposited SiO_2 film we chose not to sputter-coat the substrates, which could otherwise have been employed to reduce charging.

7.5.1. IMAGES OF COATED PARTICLES

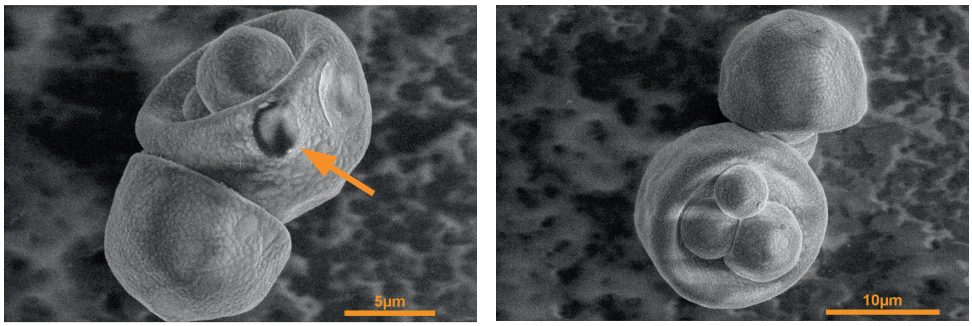


Figure 7.18: SEM images of particles, coated with 1 cycle of SiO_2, the arrow in sub-figure **a** indicates an uncoated spot

The images presented in Figures 7.18 to 7.21 show the development of the coating on the particles upon additional deposition cycles. In Figure 7.18, particles can be seen that were subjected to only a single coating cycle. In sub-figure (a), a spot can be seen where no coating appears to be present, as indicated by the arrow. While by no means copious, particles with such deficiencies were common in this sample. Sub-figure (b) shows particles that appear to be fully coated, indicating that not all particles had significant cavities. The spotted appearance of the particle surface is a result of electron beam penetration, providing subsurface information, it indicates a non-uniform coating thickness.
The samples that were coated with 2 cycles, shown in Figure 7.19, show a complete coating coverage. Additionally the varying coating thickness can be observed again. The same holds for the substrates coated with 5 Figure 7.20 and 10

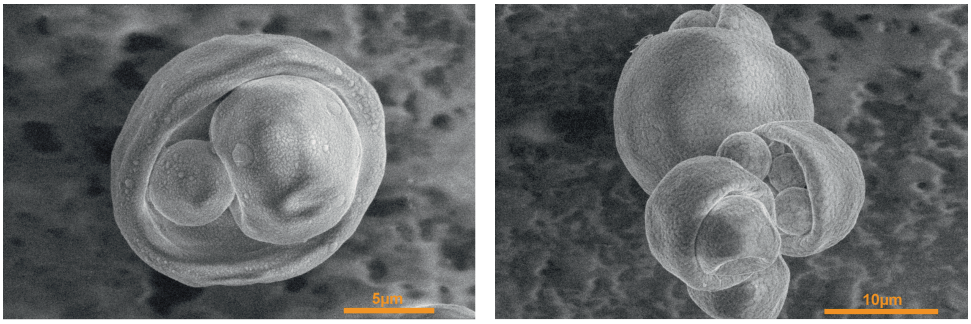


Figure 7.19: SEM images of particles, coated with 2 cycles of SiO_2

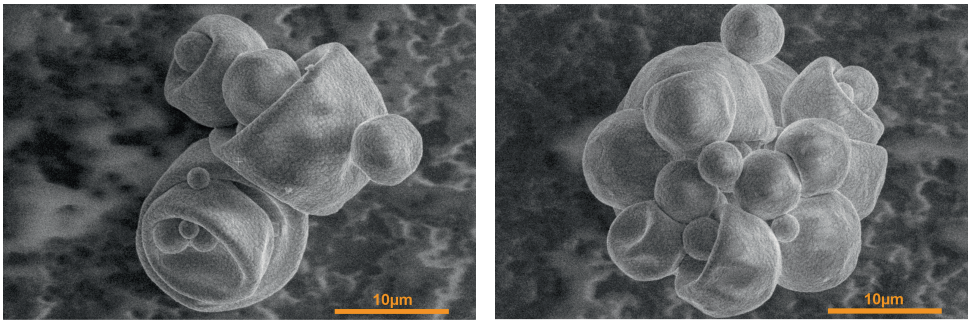


Figure 7.20: SEM images of particles, coated with 5 cycles of SiO_2

cycles Figure 7.21; no obvious gaps are observed and the coating appears to be of non-uniform thickness.

7.5.2. IMAGES OF EXPANDED PARTICLES

To assure that the coating process does not interfere with the expansion, characteristic of the used substrate, an uncoated sample and one coated by 10 cycles were heated to 110 °C for 1 h. After heating the particles were collected and SEM images were taken. The images are presented in Figure 7.22 and Figure 7.23.

Collectively, the images presented in Figure 7.22 and Figure 7.23 demonstrate the expanding capability of the particles to be retained after being subjected to several coating cycles.

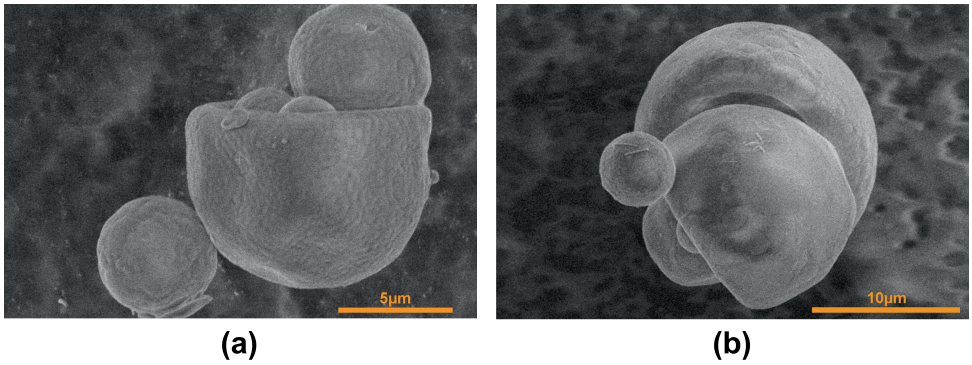


Figure 7.21: SEM images of particles, coated with 10 cycles of SiO_2

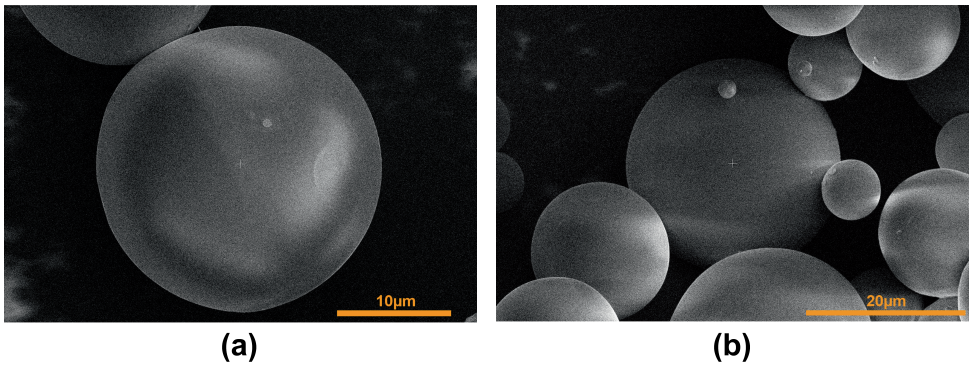


Figure 7.22: SEM images of pristine particles after being subjected to heat

7.5.3. Focussed Ion Beam Scanning Electron Microscopy

To attain information on the coating thickness of the samples produced in our study, we utilized the Focussed Ion Beam SEM (FIB-SEM) technique. Using the destructive nature of the ion-beam an incision can be made in the particle surface, which can subsequently be imaged by the electron beam. To minimize damage to the coating itself during the cutting process, a protective Pt layer with a thickness of ~0.5 µm was deposited on the particle first. Furthermore, after making the initial cut, an edging step was performed at low ion-beam currency. The coating thickness of samples, subjected to only a couple of coating cycles, could not be accurately assessed due to the limitations of magnification by the SEM technique. However, a sample coated by 100 cycles could be successfully cut and imaged, and is displayed in Figure 7.24. The non-uniform coating thick-

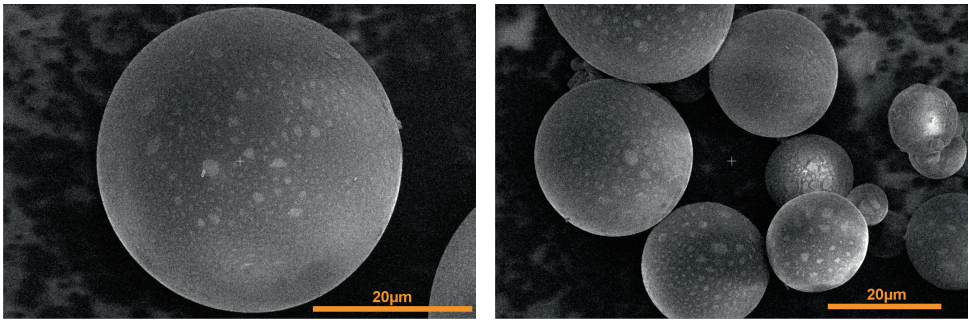


Figure 7.23: SEM images of particles, coated with 10 cycles of SiO_2, after being subjected to heat

ness was found to vary from 25 to 80 nm (reported thickness is corrected for the 52° tilt of the cut with respect to electron-beam). Since the samples discussed in the manuscript were subjected to only 1, 2, 5 or 10 cycles respectively, it is concluded that all coating thicknesses of these samples are well below 80 nm. Given a coating thickness of >4 nm after the first deposition cycle, it is expected that the growth per cycle quickly drops to resemble more ideal atomic layer deposition behaviour after initial deposition.

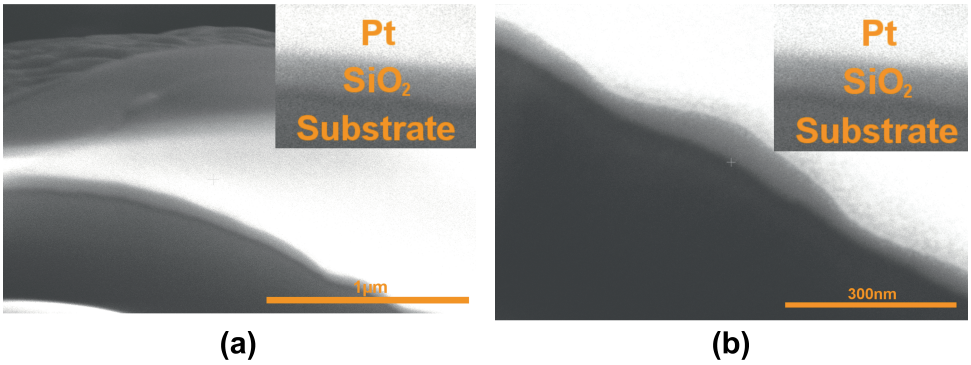


Figure 7.24: SEM image of a particle, coated with 100 cycles of SiO_2, cut in-situ by a focused ion beam.

7.6. XPS

Full XPS spectra are provided in Figure 7.25, all apparent peaks are identified. The absence of any non-substrate or coating-related peaks indicates the absence

of contamination. Furthermore, as highlighted in the manuscript, the chlorine peaks are virtually non-existent, indicating a complete oxidation step of the coating cycles.

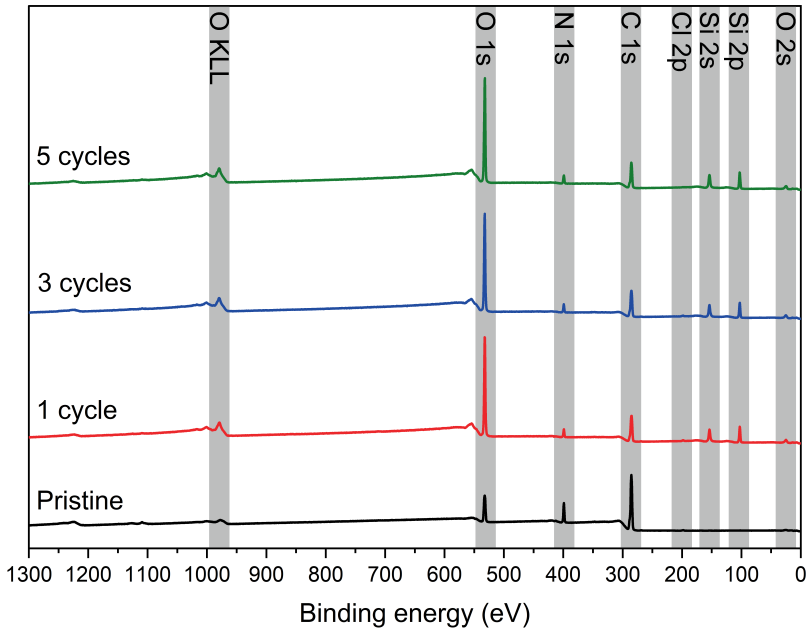


Figure 7.25: Full spectra of pristine and coated samples

8

RESEARCH IMPLICATIONS AND OUTLOOK

Collectively, the prior chapters demonstrated that the surface properties of cohesive micro-particles can be favorably altered by fluidized bed atomic layer deposition. In this chapter, the main conclusions of our work are laid out, as well as a perspective of where to go from here. Topics may span multiple manuscripts, meaning chapters are not necessarily discussed in chronological order.

8.1. AGGREGATE AND AGGLOMERATE FORMATION

In our literature review, presented in Chapter 2, several research gaps in relation to the fluidization of cohesive particles were identified. In particular, these are related to the differences between nano- and microparticle agglomeration, being multi-stage or single-stage respectively. It is suspected that this distinction arises from structure and density differences between simple agglomerates formed by nano- or micro-particles. Upon two simple agglomerates colliding, ones with a higher density, carrying enough kinetic energy, will lead to breakages or simply bounce off, where those with a lower density carry very little kinetic energy and are likely to stick together under the influence of van der Waals interactions.
In Chapter 3, the first steps were taken towards proving this hypothesis by studying the formation of aggregates, which serve as the building blocks for simple agglomerates of nanoparticles. It was shown that van der Waals induced interactions result in an active pull on primary nanoparticles. The range within which this pull is potent enough to make collisions inevitable scales drastically with primary particle size. Additionally, an off-gird 3D random walk model was built, to show that this active pull indeed alters the cluster formation of nano-particles. For 10 nm particles, an estimated 10% decrease in cluster density is expected due to this capture effect. Furthermore, the screening effects could not be replicated by a 2D model, highlighting the importance of using 3D models. This work enables future steps in the larger context of multi-stage agglomeration, by providing insight into the very first step of the process.
As only part of the entire concept of single and multi-stage agglomeration was studied within the context of this work, additional research onto this topic is highly encouraged. As the very open aggregate structures are highly susceptible

to deformation upon collisions, increasing aggregate-aggregate contact formed agglomerates may be strengthened by this effect. We therefore encourage future work to delve into the deformation characteristics of aggregates. Furthermore, it would be interesting to see additional work on the effects of density and elasticity of various cluster structures on likeliness of collisions leading to breakage, bounce-off or merger. Apart from addressing scientific curiosity, it is expected that the results of such work will aid in improving operations of existing fluidized bed applications as well as enabling new applications or processes to emerge, especially in the context of particle surface modifications.

8.2. MECHANISM OF ASSISTANCE METHODS

As the fluidization of cohesive particles is troublesome, assistance methods have been developed and researched for over half a century. As of date, the bulk of literature is dedicated to assessing the effectiveness of a particular method, by pressure drop, bed expansion and agglomerate size measurements. Based on these results, the consensus was that assistance methods initiate fluidization by breaking up agglomerates. We however hypothesized that it is the disruption of gas channels that enables fluidization of cohesive powders when subjected to an assistance method, the decrease in agglomerate size being a mere result of subsequent collisions.

In Chapter 4, X-ray imaging was employed to confirm this hypothesis. It is shown that the collapse of gas channels initiates homogeneous fluidization of mechanically vibrated beds of micro-silica. It was also demonstrated that the agglomerate sizes remain unchanged within very short time frames after fluidization was initiated, proving that their breakage is a result rather than a cause of the improved fluidization quality.

In unpublished follow-up work, the development of agglomerate size, density and fractal dimension within mechanically vibrated fluidized beds were studied over time. It was found that an equilibrium agglomerate size is only reached after prolonged fluidization (> 90 min), limiting the insights that can be gained by the many reported agglomerate sizes that are typically measured within 30 min. Additionally, agglomerate sizes were observed to decrease by both breakage and compaction during the fluidization process.

These insights allow for development and optimization of assistance methods, specifically targeting the disruption of gas channels. Future work on the dynamics of agglomerate properties within fluidized beds would, both experimental and computational could provide additional insight into these phenomena.

8.3. SCALE-UP POTENTIAL OF ASSISTANCE METHODS

A significant part of this research was dedicated to study assistance methods and in particular their potential to be scaled up. Whereas it was found that a range of methods work on lab-scale, complications are expected for most of them when applied to larger scale systems.

In Chapter 5, the effectiveness of mechanical vibration in various directions was discussed. Vertical vibration was found to result in high fluidization qualities. However, as first identified by our collaborator K. Wu in a prior publication [1], a densified region within the bottom of the bed emerged as well. As agglomerates are, by their nature, highly compactable, this zone appears as a result of the bottom distributor plate repeatedly hitting the powder bed. Since most of the powder resides in this region, where gas-solid contact is limited, this phenomenon highly mitigates the effectiveness of this assistance method. Furthermore, as shown in Chapter 4, gas channels are the cause of the troublesome fluidization of cohesive powder, the indiscriminate approach of vibrating the entirety of the bed, column and internals is highly energy inefficient. Finally, on industrial scale, vibrating systems are known to cause damage over time to nearby equipment as a result of resonance. Regardless, studies that consider sole horizontal vibration would be interesting to see.

In work not included in this dissertation, the effects of pulsed flow operation were also assessed. However, here it was found that the potency of pulses quickly diminishes as they rise through the column. In the context of scalability, this suggests that this technique is only feasible in shallow beds.

Finally, in Chapter 6, mechanical agitation was assessed as a scalable method by which to improve the fluidization of cohesive powders. Various shape parameters as well as amounts of stirrers were employed to attain insights into the potential of this method. It was found that the effectiveness of this method is highly dependent on shape of the stirrer. As for mechanical vibration, compaction can be an issue for stirrers. As layed out in this study, an ideal stirrer has a low cross-sectional surface area, minimizing dead zones, where gas is blocked by the presence of the stirrer itself. Furthermore, the stirrer should be shaped such that the entire cross-sectional area bed is exposed to the gas flow within a full rotation of the stirrer. Furthermore, the stirrer should be positioned as close to the bottom distributor plate as possible and span the entire diameter of the column. Additionally, major benefits of adding soft brushes to the bottom and edges of the stirrer were observed. These allow for the reintroduction of powder that otherwise can get stuck at the column wall and distributor plate. Regarding scalability, mechanical agitation is regarded as having high potential, as the main complications encountered in our lab-scale experiments are expected to decrease upon scaling up. Studies utilizing stirring to initiate the fluidization of cohesive pow-

der beds in larger columns are highly encouraged.

8.4. IMPROVED COLLOID STABILITY BY SURFACE MODIFICATION

In Chapter 7, hydrophilic surface groups, namely –Si–OH, were deposited to improve the stability of Expancel-water suspensions. Typically, the Expancel particles would cluster together and, upon reaching a large enough size where buoyancy becomes significant, segregate. Utilizing the attained insights from the prior chapters allowed us to perform atomic layer deposition in fluidized bed reactors. In Chapter 7, it was demonstrated that coated particles remain as singular entities within the colloid. Furthermore, signs of preexisting particle clusters disintegrating as a result of the deposited surface groups were found as well. Similar results were obtained for TiO_2 coated particles, though these findings are unpublished. Additionally, surface coverage was shown to be a more important parameter than coating thickness when it comes to improving colloid stability. This final finding ties into the dynamic nature of agglomeration during the fluidization process. As a result of agglomeration, the vast majority of the substrate surface is present within the agglomerate and is therefore only accessible for reactants by means of diffusion. However, collisions within the fluidized bed cause constant breakage and reforming of agglomerates, dynamically exposing and covering up surfaces. Provided this process occurs on a reasonable time-scale, this allows for conformal coating of agglomerating particles. In the study, it was shown that a full surface coverage was attained within 2 deposition cycles. As agglomerates dynamically break and reform during the deposition process, exposing and obstructing particle surface area, this implies our initial pulse times of 45 s may have been insufficient.

Furthermore, it was found that the presence of physisorbed H_2O, caused by the low temperature operation, led to increased deposition rates. In unpublished follow-up work, the drying dynamics of this particle bed were assessed and purge times were tuned in order to deposit a predetermined coating thickness within a single coating cycle. Future research which further explores this system's operation is highly encouraged.

REFERENCES

[1] K. Wu, E. Wagner, O. Ochkin-Koenig, M. Franck, D. Weis, G. Meesters, and J. R. Van Ommen, *Time-resolved x-ray study of assisted fluidization of cohesive micron powder: On the role of mechanical vibration,* Chemical Engineering Journal **470**, 143936 (2023).

LIST OF COMMON SYMBOLS

α	normalized solid fraction
γ	surface tension (chapter 2)
	specific surface distance (chapter 3)
γ_s	surface energy
δ	deformation (chapter 2)
	Euclidean distance (chapter 3)
Δ	displacement
$\mathscr{D}$	diffusion constant
ϵ	bed voidage
μ	viscosity (chapter 2 & 3)
	attenuation coefficient (chapter 4,5 & 6)
ξ	friction factor
ρ	density
τ	correlation time
A	surface area
A_H	Hamaker constant
A_r	Archimedes number
Bo	Bond number
D_f	fractional dimension
d	diameter
F	force
f	frequency
g	gravitational acceleration
H	bed height
H_0	minimum inter-particle distance
H_r	hardness
I	intensity
l	azimuthal radius
ℓ_c	capture distance
N	number of particles
P	pressure
r	particle radius
T	Temperature
t	time
u	superficial gas velocity
X_f	fluidized fraction

ACKNOWLEDGEMENTS

First and foremost, I want to thank my sister. She taught me lessons that don't come in books and somehow found the patience to put up with me for all these years. You are a pillar in my life, I am blessed to have you.
Further gratitude goes to my parents who gave me the tools and opportunity to chase my goals.

Additionally, I want to thank **Ruud** and **Gabrie**. You have supported and guided me throughout these four years and made it a truly satisfying ride. I value the relationship we built over the years and am grateful for the freedom you granted me throughout the project. In an ideal world all PhD students would be supervised by people like you.

Furthermore, I owe a big thanks to **Elwin** and **Richard** from Nouryon whom provided me with feedback and research directions during our progress meetings. I also want to thank **Hannah Anita** and **Jeroen** from ARC-CBBC for their organizational work.

The (ex-)colleagues and guest researchers within the PPE and PSE elevated the experience of the PhD. Of course I value all work-related input and suggestions, of which I was given many. However, the non-work conversations during lunch (12.00) and coffee breaks (10.00 and 15.00) are what will really stick with me. Addressing you as colleagues feels awkward, you are friends, and I feel blessed to have gotten to work with you all.
Christian, we started at almost the same time, and both finished the ride together, thank you for the good times.
Emma, thank you so much for the fun and thought-provoking talks we had. You taught me a lot. You were an amazing addition to the group, and I hope you will continue being your wonderful self in the new job.
Saeed, you're one of the first friends I made in the PPE group, and possibly responsible for my caffeine addiction. Thank you for your guidance and the good conversations we had.
Kaiqiao, thank you so much the collaborations and the frenetic texting during champions league games.
Zaid, thank you for providing our group with some much-needed cat sounds and for being such a great friend. I am super happy you decided to stay in the Netherlands, there are so many albums we need to listen to together still.
Lena, in the short time you've been part of the group you already feel like a vital

part of it. Thank you for your inspiring positivity, your special dance move and for the way you pronounce the word 'fucker'.
Nasim, you're an amazingly kind person and I'm looking forward to work with you on multiphase reactor engineering for one final time in the coming year!
Ruben, thank you for the many (often heated) discussions and more importantly, for the great fun we had both in and outside of the office. Sorry for leaving a chicken in your apartment.
Pranav, I am sorry that I can never handle any of the food you cook, I am however grateful that you keep offering.
Max, don't let me catch you sitting in my chair again.
Ankur, I value our cinema trips and movie discussions. Your new job is going to be so exciting, I hope to get to visit you there someday.
Qinghe, I hope we get to go to a concert together some day. Also, keep making those lines move up.
Margherita, we went a long way from the first time we met in an online meeting where I could not figure out how to un-mute myself. Thank you for the fun we had during the slightly escalating evenings making tiramisu and paella.
Lukas, thank you for your ever-positive presence in the group. Due to the pouring rain, our first sailing trip was not exactly what I hoped it would be, let's try again next summer!
Peter, you taught me the term 'swamped', which I love using now. I'm looking forward to working with you on the next project.
Albert, I cherish the memories we made on our trip to Naples, thank you for being so unapologetically you.
Riccardo, you may be the only one in the group who actually knows what everyone else is doing. Thank you for being a great friend, your random drops of Dutch words in our conversations will never not be funny to me.
Sophie, I started to miss getting my legs kicked every once in a while since you changed offices. Thank you for being such a kind and fun person; I will never forget the moment you joined our coffee break rocking the carrot suit.
Tanuj, a small confession: the very first time we met, having drinks and playing pool, I was unsure whether I was going to like you. I was very wrong, you are an amazing person and I'm happy you're part of the group.
Qing, you're a wonderful addition to the group, please keep showing me your nail art in the future.
Bhavesh, I enjoyed watching the Olympic Games together and am still unsure whether sprinters breathe during the 100m.
Athina, I'm happy we get to share offices for another year.
Dominik, the nerf gun office fights may not have been the best idea, but I did enjoy them.

Ignasi, never forget: I beat you to 750 blitz!
Sophia, I bet you still have not watched the video by the time you read this.
Christine, though you were only officially part of the group for a short while, you remain ever so in my view. I will not rest untill I get revenge on our UNO game!

During the project I had loads of help from bachelor and master students In order of starting dates: **Matthijs**, **Taco**, **Jasper**, **Julia van Dam**, **Huib**, **Teun**, **Pratyush**, **Anna**, **Irem**, **Julia Everard**, **Arvin** and **Jelle**. I want to thank all of you for your respective contributions to this work, and more importantly, for the passion and fun you brought to your projects.

A big thanks to the technicians and other supporting staff, namely to **Evert**, **Mojgan**, **Arjan**, **Kristen**, **Duco**, **Stefan**, **Cas**, **Aleksandra**, **Sietse**, **Leslie** and **Leonie**. You all played crucial roles which made this work possible in both direct and indirect ways.

Work is fun and rewarding, but enjoying free time is even more so. I want to thank my friends from university, **Stef**, **Simone**, **Kosta**, **Christel** and **Elise**. Thanks to our movie nights, covid times remained somewhat tolerable and thanks to the party nights, post-covid times were actually amazing. Furthermore, I am blessed to have **Manon**, **Ingo**, **Mats**, **Kevin**, **Ramon** and **Enzo**. You were around when I needed it most, it still means a lot to me. Finally, I cherish the holidays and weekends I spent with my sailing friends, **Nádja**, **Dennis**, **Simon**, **Maarten**, **Gerard**, **Tim**, **Jelle**, **Wilfred** and **Menno**. Our weekends on the sailing club and holidays on the Sneekermeer provided enough amazing stories to easily double the page count of this booklet. I am deeply grateful for the amazing and meaningful moments we have spent together.

Saskia, I am so happy that you became part of my life. Some may think I was a mostly happy and non-complaining person during the PhD. Truth is, I saved most of the complaining for you. Now that you are entering the second half of your PhD, you're very welcome to return the favor. You are a source of stability and happiness in my life, I am deeply grateful to have you.

CURRICULUM VITÆ

Rens KAMPHORST

27-02-1995	Born in Spijkenisse, The Netherlands.

EDUCATION

2014-2018	Bachelor of Chemical Engineering Hogeschool Rotterdam
2018-2020	Master of Chemical Engineering Delft University of Technology
2020-2024	PhD. Chemical Enginering Delft University of Technology *Thesis:* Tuning the surface properties of polymer microspheres by means of Atomic Layer Depsosition in fluidized beds *Promotor:* Prof. dr. J. R. van Ommen *Promotor:* Dr. G.M.H. Meesters

LIST OF PUBLICATIONS

6. **R. Kamphorst**, M.F. Theisen, A.D. Bordoloi, S. Salameh, G.M.H. Meesters and J.R. van Ommen *On the structure of nanoparticle clusters: effects of long-range interactions*, Physical Chemistry Chemical Physics (2025)

5. K. Wu, **R. Kamphorst**, A. Bakker, J. Ford, E.C. Wagner, O. Ochkin-Koenig, M. Franck, D. Weis, G.M.H. Meesters and J.R. van Ommen *Stirrer design for improving fluidization of cohesive powder: A time-resolved X-ray study*, Chemical Engineering Science **294**, 120069 (2024).

4. **R. Kamphorst**, K. Wu, M. van Baarlen, G.M.H. Meesters and J.R. van Ommen *Effect of vibrational modes on fluidization characteristics and solid distribution of cohesive micro-and nano-silica powders*, Chemical Engineering Science **291**, 119911 (2024).

3. **R. Kamphorst**, P. Wanjari, S. Saedy, J.F.K. van Dam, A. Thijssen, P. Brüner, T. Grehl, G.M.H. Meesters and J.R. van Ommen *Enhancing colloid stability of polymer microspheres in water through SiO_2 coating: Effects of coating cycles and surface coverage*, Surfaces and Interfaces **45**, 103852 (2024).

2. **R. Kamphorst**, P.C. van der Sande, K. Wu, E.C. Wagner, M.K. David, G.M.H. Meesters and J.R. van Ommen *The Mechanism behind Vibration Assisted Fluidization of Cohesive Micro-Silica*, KONA Powder and Particle Journal **41**, 254 (2024).

1. **R. Kamphorst**, K. Wu, S. Salameh G.M.H. and J.R. van Ommen *On the fluidization of cohesive powders: Differences and similarities between micro- and nano-sized particle gas–solid fluidization*, The Canadian Journal of Chemical Engineering **101**, 227 (2023).

Not included in this thesis:

2. K. Wu, **R. Kamphorst**, P.C. van der Sande, E.C. Wagner, G.M.H. Meesters and J.R. van Ommen *Gas pulsation-assisted fluidization of cohesive micron powder: An X-ray imaging study*, Under review

1. P.C. van der Sande, K. Wu, **R. Kamphorst**, E.C. Wagner, G.M.H. Meesters and J.R van Ommen *On the inherent correlation between the fluidization and flow properties of cohesive powders*, AIChE Journal (2024).

